

2

# SRI International

**AD-A264 210**



Final Report • March, 1993

## OPTICAL AND KINETIC PROCESSES IN EXCIMER LASERS

David L. Huestis, M. J. Dyer, W. K. Bischel, D. C. Lorents, and G. Black  
Molecular Physics Laboratory

SRI Project No. PYU-7123  
Contract No. N00014-84-C-0256

MP 92-279

Prepared for:

Office of Naval Research  
800 North Quincy Street  
Arlington, VA 22217

DTIC  
ELECTE  
MAY 12 1993  
S B D

Attn: Dr. Vern N. Smiley

DISTRIBUTION STATEMENT A  
Approved for public release  
Distribution Unlimited

**93-10531**

93 5 11 19 8

# **OPTICAL AND KINETIC PROCESSES IN EXCIMER LASERS**

**D. L. Huestis, Associate Director  
M. J. Dyer, Physics Specialist  
W. K. Bischel, Program Manager  
D. C. Lorents, Sr. Staff Scientist  
G. Black, Sr. Physicist**

**SRI Project PYU 7123  
MP 92-279**

**Contract No. N00014-84-C-0256**

**Prepared for:**

**Office of Naval Research  
800 North Quincy Street  
Arlington, VA 22217**

**Attn: Dr. Vern N. Smiley**

**Approved:**

**Donald J. Eckstrom, Laboratory Director  
Molecular Physics Laboratory**

**David M. Golden  
Vice President  
Physical Sciences Division**

**REPORT DOCUMENTATION PAGE**Form Approved  
OMB No. 0704-0188

Public reporting burden for this collection of information is estimated to average 1 hour per response, including the time for reviewing instructions, searching existing data sources, gathering and maintaining the data needed, and completing and reviewing the collection of information. Send comments regarding this burden estimate or any other aspect of this collection of information, including suggestions for reducing this burden, to Washington Headquarters Service, Directorate for Information Operations and Reports, 1215 Jefferson Davis Highway, Suite 1204, Arlington, VA 22202-4302, and to the Office of Management and Budget, Paperwork Reduction Project (0704-0188), Washington, DC 20503.

1. AGENCY USE ONLY (Leave blank)		2. REPORT DATE 921214	3. REPORT TYPE AND DATES COVERED Final 840329-890301	
4. TITLE AND SUBTITLE Optical and Kinetic Processes in Excimer Lasers			5. FUNDING NUMBERS Contract No. N00014-84-C-0256	
6. AUTHOR(S) D. L. Huestis, M. J. Dyer, W. K. Bischel, D. C. Lorents, and G. Black				
7. PERFORMING ORGANIZATION NAME(S) AND ADDRESS(ES) SRI International Molecular Physics Laboratory 333 Ravenswood Avenue Menlo Park, California 94025-3493			8. PERFORMING ORGANIZATION REPORT NUMBER MP 92-279 PYU-7123	
9. SPONSORING/MONITORING AGENCY NAME(S) AND ADDRESS(ES) Office of Naval Research 800 North Quincy Street Arlington, VA 22217 Attn: Dr. Vern N. Smiley (619) 553-6128			10. SPONSORING/MONITORING AGENCY REPORT NUMBER 290384010389	
11. SUPPLEMENTARY NOTES				
12a. DISTRIBUTION/AVAILABILITY STATEMENT Approved for public release; distribution unlimited			12b. DISTRIBUTION CODE Unlimited	
13. ABSTRACT (Maximum 200 words) This report summarizes a program of research on optical and kinetic processes of importance for excimer laser systems. The research consists of four major topics: (1) investigations of the spectroscopy and chemical kinetics of XeF and XeCl lasers using theoretical techniques, synchrotron radiation excitation, and laser-induced fluorescence, (2) measurement of the angle, wavelength, temperature, and density dependencies of vibrational and rotational Raman gain in H <sub>2</sub> , D <sub>2</sub> , and N <sub>2</sub> , (3) studies of stimulated Rayleigh-Brillouin scattering in gases, and (4) investigation of other topics in lasers and nonlinear optics.				
14. SUBJECT TERMS Excimer Lasers, Laser Kinetics, XeF and XeCl Lasers, Nonlinear Optics, Raman and Brillouin Scattering			15. NUMBER OF PAGES	
			16. PRICE CODE	
17. SECURITY CLASSIFICATION OF REPORT Unclassified	18. SECURITY CLASSIFICATION OF THIS PAGE Unclassified	19. SECURITY CLASSIFICATION OF ABSTRACT Unclassified	20. LIMITATION OF ABSTRACT UL	



## **SUMMARY**

This report describes the results of a five-year research program to provide the basic information needed to design and develop high performance lasers systems, operating in the visible and near ultraviolet, for use in blue-green optical communication systems and in weapon systems. All such systems require a reliable, scalable, and efficient laser. In several applications, operation within a specific wavelength range is required, along with narrow spectral output to improve optical conversion efficiency or to match fixed-frequency narrow-band receivers.

Over the past twenty years, the search for and development of efficient, high energy, visible and ultraviolet lasers have been extremely productive. This phenomenally rapid progress was made possible by exploiting the previously established base of molecular concepts and experimental data. Detailed understanding of the kinetic and optical processes operating within the laser medium is needed to identify new molecules, pumping mechanisms, or optical conversion schemes that could lead to high performance lasers and to guide the achievement of the best possible performance. Sustaining the accelerated pace of development requires a continuously improving description of the microscopic processes within the laser medium, which in turn requires continuing research programs to investigate these processes.

During the period covered by this contract, our research program emphasized the quantitative characterization of optical and kinetic processes important for XeCl and XeF excimer laser systems. The documents included in this report as Appendices describe our major research accomplishments. These may be divided into four areas, as briefly outlined below.

### **EXCIMER LASER SPECTROSCOPY AND KINETICS**

Excimer lasers are among the most complicated of gas lasers because many chemical reactions are involved in production, relaxation, and quenching of the upper and lower laser levels.

Nevertheless, rare gas halide excimer lasers are remarkably efficient. The complicated chemical pathways are, in fact, very selective.

The kinetics of the XeCl laser are especially worthy of investigation. Even after years of study, significant inconsistencies and contradictions remain. We have used vacuum ultraviolet synchrotron radiation from the Spear storage ring at the Stanford Synchrotron Radiation Laboratory to excite Xe atoms and halogen-containing molecules. The resulting fluorescence was time resolved and analyzed to derive rate coefficients for production and quenching of XeCl and Xe<sub>2</sub>Cl. These experiments provided branching ratios for production of XeCl from various Xe\* states reacting with a number of chlorine donors. These studies show that pathways that might have been expected to dominate, e.g., Xe\*(6s) + HCl, in fact have a low probability for producing XeCl\*. These results strongly support the need for developing a consistent understanding of the role of moderate energy electrons in mixing the excited states of the Xe atom and in exciting the higher vibrational levels of HCl.

The XeF laser is unusual among the rare gas halide lasers in that the ground state of XeF is bound. Nonterminating laser action requires that the lower laser level be removed, in this case by collisional vibrational relaxation and dissociation. We measured the rates of collision-induced dissociation of XeF(X) by He, Ne, Ar, Kr, Xe, N<sub>2</sub>, SF<sub>6</sub>, and XeF<sub>2</sub>, and of vibrational relaxation by XeF<sub>2</sub>. In our experiment XeF(X<sub>v</sub>') was produced by KrF or ArF excimer laser photodissociation of XeF<sub>2</sub> and then excited by a doubled dye laser to XeF(B<sub>v</sub>'), whose fluorescence was detected. The time-evolution of the XeF(X<sub>v</sub>') population was monitored by varying the time delay between the excimer and dye lasers.

Our work on excimer laser spectroscopy and kinetics is described in Appendices A through G.

## **STIMULATED VIBRATIONAL AND ROTATIONAL RAMAN SCATTERING**

Stimulated Raman scattering (SRS) is a convenient means of frequency shifting of ultraviolet excimer lasers to permit transmission through the atmosphere. Stimulated Raman

scattering is also useful for improving the optical beam quality of excimer lasers by combining several excimer laser beams at small angles in a Raman conversion cell. Finally, the atmosphere itself can lead to stimulated Raman scattering, which can limit the power density of lasers beams propagating through the atmosphere.

Our research program was intended to obtain the detailed quantitative experimental data required to design practical frequency converters and beam combiners and to quantify the effects of Raman scattering in the atmosphere. Our work on vibrational Raman scattering in H<sub>2</sub> included measurement and modeling of the angular dependence of the Raman linewidth, measurement and *ab initio* calculation of the Raman scattering cross sections of the fundamental and overtone transitions, and determination of the refractive index or polarizability of H<sub>2</sub> in its first vibrationally excited level. We investigated rotational Raman scattering in considerable detail. Our nearly complete determination of the Raman scattering parameters allowed us to develop a comprehensive model of Raman gain coefficients for N<sub>2</sub> in the atmosphere. This work had a substantial influence on development of strategies for using power lasers in the atmosphere.

Our work on stimulated vibrational and rotational Raman scattering is described in Appendices H through M.

## **STIMULATED RAYLEIGH-BRILLOUIN SCATTERING**

Stimulated Brillouin scattering (SBS) is used in optical phase-conjugation mirrors to compensate for refractive distortions in the excimer laser medium. We developed a high-resolution (10-MHz) coherent Brillouin spectrometer that, for the first time, clearly resolves the Rayleigh and Brillouin components of the low frequency scattering spectrum of gases. We measured the SBS gain coefficients, linewidths, and line shifts for Xe and SF<sub>6</sub>, improved the accuracy of previous measurements, and illustrated the power of the technique for characterizing potential SBS media. Our work is described in Appendices N and O.

## OTHER TOPICS IN LASERS AND NONLINEAR OPTICS

The SRS and SBS measurements described above require lasers with a combination of narrow spectral width and relatively high power. To perform such measurements, we developed a Nd:YAG laser with exceptional performance characteristics: 80-ns pulse duration, 8-MHz bandwidth, 300-mJ pulse energy and 10-Hz pulse repetition frequency. The laser system has formed the basis of numerous state-of-the-art experiments in nonlinear optics. It is described in Appendix P.

The high efficiency of the KrF laser has led to numerous schemes to convert its wavelength from 248 nm to the visible, which would allow it to propagate through the atmosphere. Such a conversion of a 248-nm photon to a 400 - 600-nm photon results in a loss of at least 40%-60% of the photon's energy. We have investigated a new scheme by which a single KrF photon would be converted into two visible photons, by four-wave mixing with a 10- $\mu$ m photon from a CO<sub>2</sub> laser:

$$248 \text{ nm} + 10 \text{ } \mu\text{m} \rightarrow 484 \text{ nm} + 484 \text{ nm} .$$

This process, which we called frequency halving, could accomplish the conversion to the visible with, in principle, no loss of energy. Generation of two waves at the same frequency is known to occur in a number of parametric processes in solids. Appendix Q describes our first attempt at frequency halving-in barium vapor.

**Appendix A**

**EXCITED STATE KINETICS FOR XeCl**

International Conference on Lasers '84  
26-30 November 1984, San Francisco, CA

EXCITED STATE KINETICS FOR XeCl<sup>†</sup>

Donald C. Lorents  
Chemical Physics Laboratory  
SRI International  
Menlo Park, California

Although the XeCl laser has operated with e-beam and discharge pumping for nearly 10 years now several intriguing mysteries remain in both the ion and excited state kinetic behavior of its medium. In the positive ion chemistry the pathways to the formation of xenon ions in a neon buffer are complex and ill defined. In mixtures containing HCl the negative ion formation processes are still confronted with apparently contradictory experimental results.

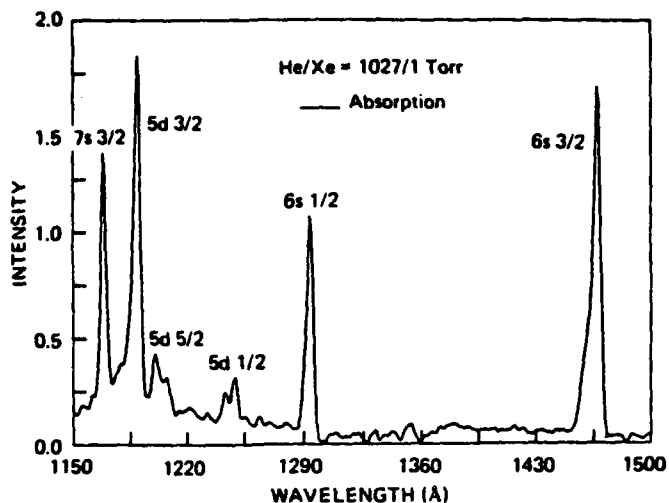
Although the excited state kinetics of XeCl are understood on a qualitative basis, many of the important kinetic rate constants remain uncertain or unmeasured. As we look in more detail at the various kinetic pathways more questions arise in the overall model of XeCl formation, radiation, and quenching particularly as it pertains to laser performance and modeling. Such issues as the collisional mixing and vibrational relaxation of the B and C states remain highly uncertain in spite of their importance to the understanding of laser performance. Indeed the spectroscopic location of the C state relative to the B state remains uncertain by about  $200 \text{ cm}^{-1}$ . Evidence of the poor understanding of the XeCl laser medium is particularly clear for the case where HCl is used as the Cl donor. In e-beam pumped XeCl a vexing question is why the laser turns off before the pump pulse does while the fluorescence continues, indicating that the cause is not depletion of the donor. The laser behavior at low HCl concentrations giving high initial peak power and rapid termination is not understood. These problems are frequently assigned to unidentified absorbers formed through some unknown kinetic reaction scheme. These characteristics pose difficult problems which the current models find difficult to reproduce.

At LASERS '80 the first results of our synchrotron studies of the kinetics of XeCl were presented. In the intervening time we have extended, and improved the measurements, the data analysis, and ability to extract rate constants based on an improved understanding of the overall excited state kinetics of XeCl.

We present here results of our extended set of excited state kinetics measurements using the tunable uv synchrotron source at SSRL which has ideal temporal and intensity characteristics for such studies. These experiments provide a means for obtaining in a simple reliable and readily interpretable manner many of the important kinetic parameters. Very briefly, uv photons of specified energy are used to excite an atom or molecule to a desired electronic state in a gas mixture containing the desired reactants and or quenchers. The formation and decay of a fluorescing excimer is followed in time and intensity as a function of the concentration of individual components of the gas as well as the total pressure. As far as possible an individual reaction is isolated by arranging the gas mixtures and excitation conditions to make it the dominant process in which case its reaction rate can be determined uniquely. When that proves impossible it becomes necessary to model the several processes involved using initial estimated rates and a large set measurements taken over a large range of gas mixtures and pressures.

These measurements were done on the 8 degree port of the SSRL facility which delivers 0.3 ns pulses at 1.28 MHz tunable from 40 to 300 nm. The gas cell is equipped with entrance and exit windows to transmit the uv radiation and a third window looking perpendicular to the beam to monitor the fluorescence. Filtered photomultipliers were used to detect the fluorescent photons. MgF<sub>2</sub> windows used on the gas cell limit the short wavelength transmission to 115 nm. Gas mixtures are made up in advance of a measurement using a ballast tank and a well passivated gas mixing apparatus. Gas pressures are measured with calibrated capacitance manometers.

An absorption scan of a He/Xe mixture at 1027/1 Torr is shown in Figure 1 for the wavelength range of 115-150 nm taken with a resolution of 0.25 nm. The intensity scale is



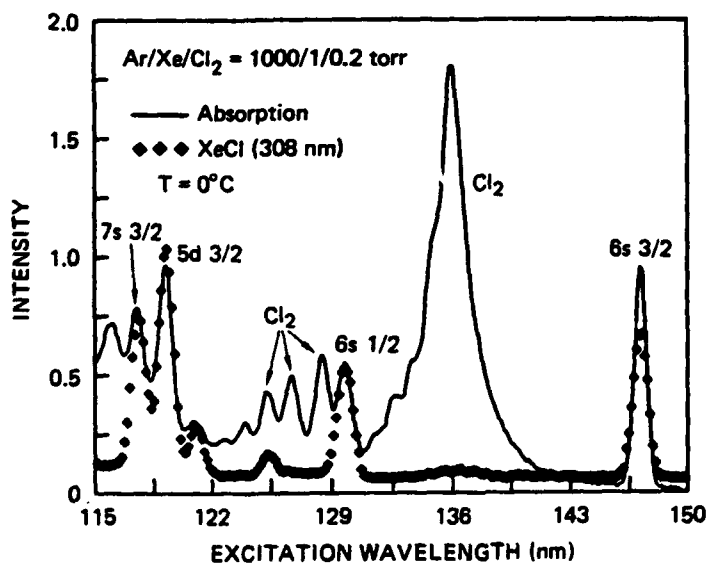
JA-7123-15

Figure 1 Absorption scan of 1 Torr Xe in 1027 Torr He.

at 308 nm was monitored and the intensity was normalized to the absorption spectrum at the Xe( $7s_{3/2}$ ) state. It is clear that the major XeCl 308 nm fluorescence is due to excitation of the Xe states and very little comes from the  $Cl_2$  excitation. However it is important to note that there is some fluorescence signal at 136 nm where the major  $Cl_2$  absorption lies. This signal increases as the Xe concentration increases and is clearly due to the reaction of  $Cl_2^*$  with Xe to produce  $XeCl^*$ . The chlorine excitation at 136 nm is rapidly quenched by Ar to lower states so that this mechanism of XeCl formation is kinetically fast and thus a very useful means of producing it for rate measurements on other kinetic reactions. In Figure 3 the XeCl 308 signal is plotted together with an absorption scan of Ar/Xe containing no  $Cl_2$  and shows that the Xe excited states give high but not 100% yields for the lower

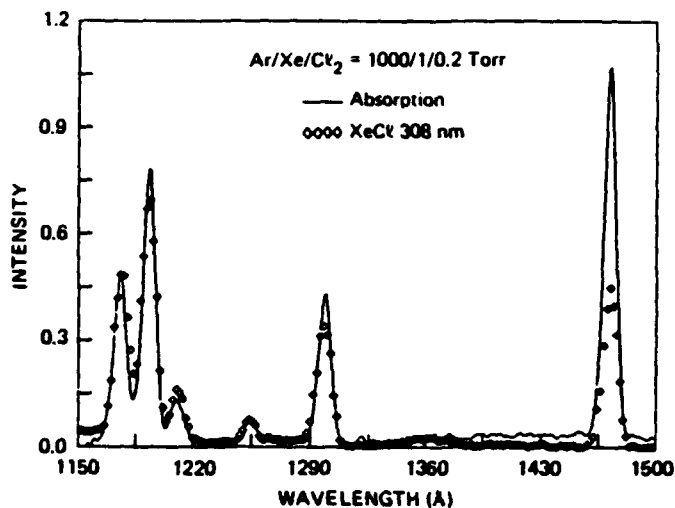
proportional to the absorption cross section having been normalized to the beam intensity profile obtained from a scan at zero pressure. All of the absorption lines observed are identifiable Xe lines collision broadened by the high density He. It is noteworthy that not only are the allowed transitions broadened but also some transitions normally disallowed in atomic Xenon are observed to absorb in the presence of high density buffer (e.g.  $5d_{1/2}$  and  $5d_{5/2}$ ). A similar scan for an Ar/Xe mix at 1021/1 Torr shows that the broadened structure of the lines differs from those observed in He but otherwise is similar. These collision induced absorption features have been observed and analyzed in higher resolution by Castex.<sup>1</sup>

In Figure 2, 0.2 torr of  $Cl_2$  has been added to an Ar/Xe mix of 1000/1 Torr producing a very complex absorption spectrum. In addition to the Xe lines, strong absorption features are observed that have been identified in higher resolution studies<sup>2</sup> as transitions to various Rydberg states of  $Cl_2$ . In this measurement the fluorescence



JA-1822-105

Figure 2 Absorption/Fluorescence scan of an Ar/Xe/ $Cl_2$  mix.



JA-7123-19

Figure 3 Fluorescence data of Figure 2 normalized to an absorption scan in Ar/Xe.

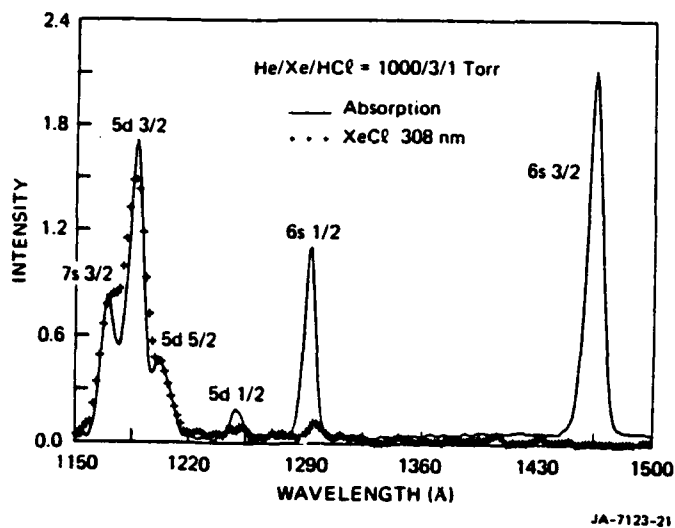


Figure 4 Absorption/Fluorescence scan of a He/Xe/HCl mix.

indicating that the harpoon reaction is strongly influenced by the higher electron affinity of the Cl atom.

Kinetic information is obtained from measurements of the time history of the fluorescence signal as a function of total and component gas pressures for each gas mixture. To obtain unique kinetic information on a specific reaction it is necessary to

lying states. The yield for the  $6s_{3/2}$  state which is  $53 \pm 5\%$  is surprising in view of the 100% yield reported<sup>3</sup> for the nearby but lower lying  $6s_{3/2}$  metastable level ( $J = 2$ ). In Figure 4 an absorption/fluorescence scan is shown for a mixture of He/Xe/HCl of 1000/3/1 Torr. This shows that HCl which is commonly used for the Cl donor in XeCl lasers gives good fluorescence yields only for the 5d and 7s and presumably higher states lying above about 10 eV. At this energy the reaction is about 1.5 eV exothermic which seems to be a typical requirement for a high yield harpoon reaction. This reaction is thermo-neutral for  $Xe(6s_{3/2})$  where the yield is zero.

Fluorescence yields obtained by the technique described above for several fluorine and chlorine donors are shown in Table 1. The quantities in parentheses indicate where the yields have been normalized. In the cases of ClF and HCl the  $XeCl^*$  yields were normalized to the  $Xe(7s_{3/2})$  yield in  $Cl_2$ . It is interesting that ClF reacting with  $Xe^*$  has a strong preference to form XeCl relative to XeF

Table 1

QUANTUM YIELDS FOR  $Xe^* + RX \rightarrow XeX^* + R$

$Xe^*$	XeF				XeCl		
	F <sub>2</sub>	NF <sub>3</sub>	N <sub>2</sub> F <sub>4</sub>	ClF	ClF	HCl	Cl <sub>2</sub>
$6s_{3/2}$	0.45	0.05	0.21	0.02	0.29	0.0	0.53
$6s_{1/2}$	0.75	0.50	0.58	0.04	0.46	0.05	0.95
$5d_{1/2}$	1.0	0.70	1.0	?	0.60	0.30	1.00
$5d_{5/2}$	1.0	1.0	1.0	0.05	0.60	0.7	1.00
$5d_{3/2}$	0.90	0.90	0.90	0.04	0.50	0.65	0.95
$7s_{3/2}$	(1.0)	(1.0)	(1.0)	0.05	0.60	0.72	(1.0)

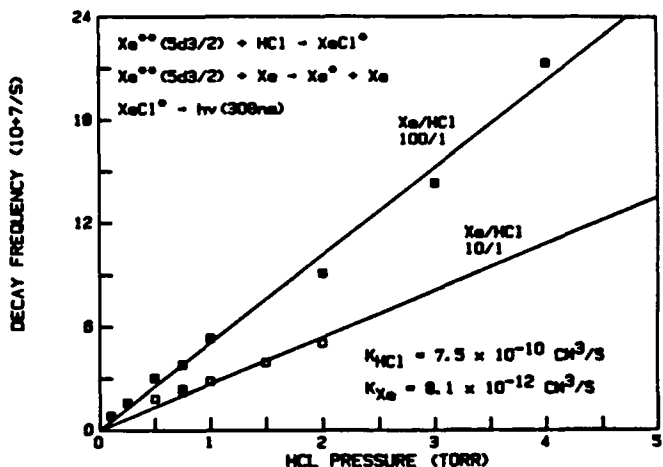
isolate that reaction as much as possible by arranging the gas mixture and pressures such as to make it the dominant process controlling either the fast or slow component of the signal. It is also important that the rates of the fast and slow components are well separated if a realistic exponential fit is to be obtained from a least squares fitting routine.

In Figure 5 is shown the results of a measurement of the rate of formation of  $\text{XeCl}^*$  from  $\text{Xe}(5d_{3/2})$  reacting with HCl. This rate is found to be dependent on both the HCl and Xe concentrations. Evidently the  $5d_{3/2}$  state is collisionally deactivated by Xe to a lower state that does not produce  $\text{XeCl}^*$  giving a Xe pressure dependence which appears very clearly by using two different Xe/HCl ratios. The decay frequencies as a function of HCl pressure shown for 100/1 and 10/1 Xe/HCl ratios are observed to be linearly dependent on pressure within the error limits. Thus we can readily assign the slope of these as the sum of the HCl and Xe reaction rates and using the two equations, derive the two rate constants shown on the figure.

To obtain the  $\text{XeCl}^*$  quenching rate due to HCl we used a constant mixture of Xe/ $\text{Cl}_2$  to which HCl was added. In this case the  $\text{XeCl}^*$  was formed from the  $\text{Cl}_2^*$  reaction with Xe in order to produce the  $\text{XeCl}^*$  fast compared to its radiative and quenched lifetime. The decay rates as a function of HCl are displayed in Figure 6 for Xe/ $\text{Cl}_2$  pressures of 200/0.3 and 50/0.3 and in each case a linear dependence on HCl is observed with a common slope but differing asymptotes. An accurate HCl quenching rate constant is easily derived from the slope of the two straight line least squares fits. In addition the two asymptotic values give the  $\text{XeCl}^*$  decay rate for the respective Xe/ $\text{Cl}_2$  mixtures indicating a strong dependence of this rate on the Xe concentration.

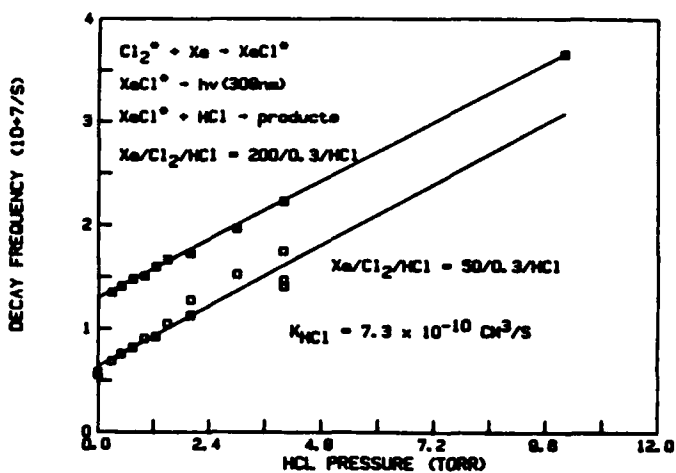
Similar measurements using a 450 nm filter were carried out to obtain the lifetime and quenching of  $\text{Xe}_2\text{Cl}$ . In this case it was found that the decay rate of  $\text{Xe}_2\text{Cl}$  was independent of the Xe pressure and only dependent on the  $\text{Cl}_2$  and HCl concentrations permitting a direct measure of the halogen quenching. The measurements shown in Figure 7 carried out in Xe/ $\text{Cl}_2$  mixtures at various Xe pressures from 50 to 2000 torr gives the  $\text{Cl}_2$  quenching rate. The asymptote gives the radiative decay rate of  $\text{Xe}_2\text{Cl}^*$  of  $3.8 \times 10^6 \text{ s}^{-1}$  corresponding to a lifetime of about 260 ns, a value longer than any previously reported. The HCl quenching rate was derived from a measurement of the 450 nm decay in a Xe/ $\text{Cl}_2$  mixture of 212/0.3 Torr to which HCl was added.

Finally the decay and quenching of  $\text{XeCl}$  itself is more complex because of the involvement of the two close lying electronic B and C states. Since the B and C states of  $\text{XeCl}$  are known to lie within  $\sim 200 \text{ cm}^{-1}$  of each other they are strongly coupled by collisions and thus at most pressures act as a single state with an intermediate lifetime. Our measurements



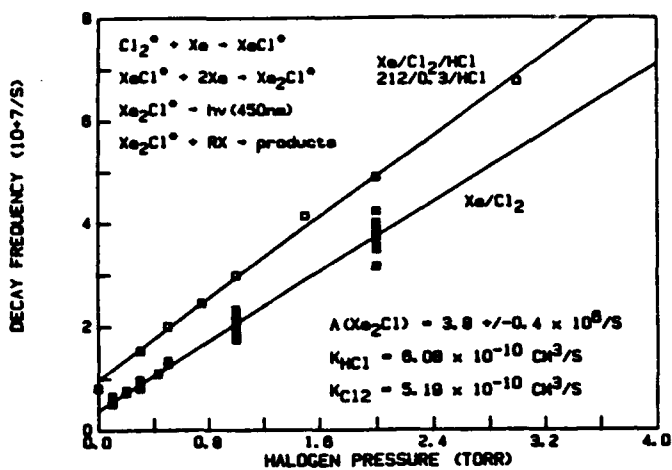
JA-7123-31

Figure 5 Formation rate of  $\text{XeCl}$  from  $\text{Xe}(5d_{3/2}) + \text{HCL}$  and removal rate of  $\text{Xe}(5d_{3/2})$  by Xe.



JA-7123-33

Figure 6 Quenching rate of  $\text{XeCl}$  by HCl.



JA-7123-34

Figure 7 Radiative and quenching rate of  $Xe_2Cl^*$  by  $HCl$  and  $Cl_2$ .

routine to determine the  $K_1$ 's. This fit for the  $Xe/Cl_2$  case indicated that the linear  $Xe$  term is small but that the three-body quenching is predominant even at low pressures. This is illustrated in Figure 8 where the  $XeCl^*$  decay frequency measurements corrected for the  $Cl_2$  quenching rates are plotted versus the square of the  $Xe$  pressure. The plot clearly exhibits a linear dependence that indicates that the two-body  $Xe$  quenching is very small even at low pressures. Additional data not shown, extending a factor of 6 high in (pressure)<sup>2</sup> fits the same function. Nevertheless the least squares fitting does give a small positive value for the linear  $Xe$  term with a large (factor of 2) uncertainty. The value we quote is the upper limit that the statistical analysis on our data allows.

Finally an additional large set of data for mixtures of  $Ar/Xe/Cl_2$  was combined with the  $Xe/Cl_2$  data set and a least squares fitting of the total set was performed to an  $R$  function with an additional term in  $Ar^*Xe$ . The resulting fit gave essentially the same parameter values as found for the  $Xe$  data with the addition of the term for  $Ar^*Xe$ . The fit for this total data set of 87 points is excellent and clearly indicates that the overall model describes the decay processes of  $XeCl$  very well. This model that prescribes slow 2-body and fast 3-body removal of  $XeCl$  by  $Xe$  differs from the recent measurements of the Kansas group<sup>4</sup> who determined a 2-body rate a factor of ten larger than our measurements indicate. However a recent set of measurements carried out by a European group<sup>7</sup> using synchrotron radiation in an experiment very similar to ours has produced  $Xe$  and  $Cl_2$  removal rates nearly identical to those reported here.

An additional important parameter that results from these measurements is the mixed state radiative rate of  $XeCl^*$ . This quantity is given by the pressure independent term in the least squares fitting and is interpreted as the mixed state lifetime. This lifetime obtained from the fitting of the total data set described above taken together with the individual B and C state lifetimes<sup>4</sup> can be used to determine energy separation of the two

reflect this by the observation that the C-A and B-X transitions at 340 nm and 308 nm respectively have identical decay rates. The radiative lifetimes of each of these states have been recently measured under collision free conditions<sup>4</sup> but the mixed state lifetime and the equilibrium constant are not yet well established for this excimer; the reported energy separations vary from 0 to  $-200 \text{ cm}^{-1}$ .<sup>5,6</sup> Because the mixed state is quenched by both  $Xe$  and  $Cl_2$ , and the dependence on  $Xe$  could be both linear and quadratic corresponding to quenching and to  $Xe_2Cl$  formation respectively, it was necessary to obtain a large data set with a large range of pressures and mixture ratios. The decay rate,  $R$ , was assumed to obey a four parameter function  $R$  given as equation (1).

$$R = K_1 + K_2Cl_2 + K_3Xe + K_4Xe^2 \quad (1)$$

Some 47 sets of data were fit to  $R$  with a multi-parameter least squares fitting routine

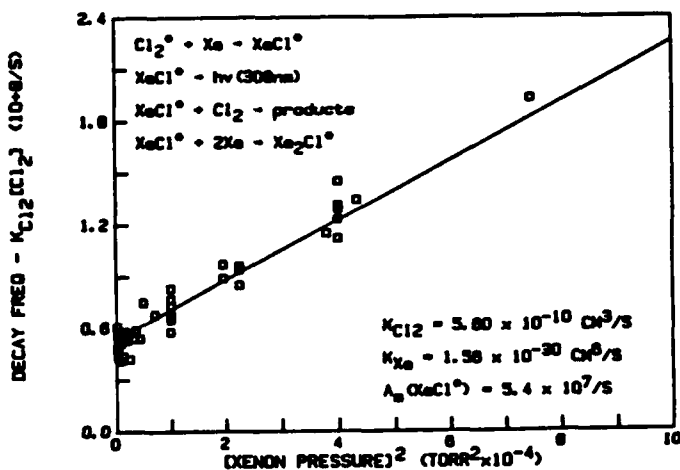


Figure 8 Three body removal rate of  $XeCl^*$  by  $Xe$ . Note that the  $Cl_2$  quenching rate has been subtracted from the total decay rate.

electronic states. The mixed state radiative rate  $A_m$  is given in terms of the B and C state rates and the equilibrium constant  $K_e$  in equation (2)

$$A_m = (A_B K_e + A_C) / (K_e + 1) \quad (2)$$

Using the recently measured rates for  $A_B$  and  $A_C$  and our value for  $A_m$  of  $5.0 \times 10^7/s$  we find that  $K_e = \sim 1$  indicating an energy separation near zero. This finding is consistent with the recent work of the European group<sup>7</sup> but differs from other observations.

The rate constants and lifetimes derived from the present analysis of our synchrotron data are presented in the Table II. In these table KSU refers to Kansas State University, SAC refers to reference,<sup>7</sup> and RICE to reference 8.

Table II  
RATE CONSTANTS FOR XeCl KINETICS  
FORMATION

REACTION	RATE CONSTANT	REF
$Xe(^3P_2) + Cl_2 \rightarrow XeCl^*$	$7.2 \times 10^{-10} \text{ CM}^3/\text{S}$	KSU
$Xe(^3P_1) + Cl_2 \rightarrow XeCl^*$	$7.9 \pm 0.9 \times 10^{-10} \text{ CM}^3/\text{S}$	SRI
$Xe(^1P_1) + Cl_2 \rightarrow XeCl^*$	$7.6 \pm 0.7 \times 10^{-10} \text{ CM}^3/\text{S}$	SRI
$Xe(5d3/2) + HCl \rightarrow XeCl^*$	$7.5 \pm 0.7 \times 10^{-10} \text{ CM}^3/\text{S}$	SRI
$Cl_2^* + Xe \rightarrow XeCl^*$	$1.1 \pm 0.1 \times 10^{-10} \text{ CM}^3/\text{S}$	SRI

RADIATION AND QUENCHING

$XeCl^*(B) \rightarrow hv(308)$	$9.0 \pm 0.2 \times 10^7/\text{S}$	KSU
$XeCl^*(C) \rightarrow hv(340)$	$7.6 \pm 0.6 \times 10^6/\text{S}$	KSU
$XeCl^*(M) \rightarrow hv$	$5.0 \pm 0.6 \times 10^7/\text{S}$	SRI, SAC
$XeCl^* + Cl_2 \rightarrow \text{QUENCH}$	$5.6 \pm 0.25 \times 10^{-10} \text{ CM}^3/\text{S}$	SRI
	$5.8 \times 10^{-10} \text{ CM}^3/\text{S}$	SAC
$XeCl^* + HCl \rightarrow \text{QUENCH}$	$7.3 \pm 0.1 \times 10^{-10} \text{ CM}^3/\text{S}$	SRI
$XeCl^* + Xe \rightarrow \text{QUENCH}$	$< 4 \times 10^{-12} \text{ CM}^3/\text{S}$	SRI, SAC
	$2.3 \times 10^{-11} \text{ CM}^3/\text{S}$	KSU
$XeCl^* + 2Xe \rightarrow Xe_2Cl^*$	$1.53 \pm 0.1 \times 10^{-30} \text{ CM}^6/\text{S}$	SRI
	$1.3 \times 10^{-30} \text{ CM}^6/\text{S}$	SAC
$XeCl^* + Xe + Ar \rightarrow Xe_2Cl^*$	$1.01 \pm 0.05 \times 10^{-30} \text{ CM}^6/\text{S}$	SRI

Xe QUENCHING

$Xe(5d3/2) + Xe \rightarrow Xe^* + Xe$	$8.1 \pm 0.8 \times 10^{-12} \text{ CM}^3/\text{S}$	SRI
$Xe(^3P_2) + HCl \rightarrow \text{PRODUCTS}$	$5.6 \times 10^{-10} \text{ CM}^3/\text{S}$	KSU
$Xe(^1P_1) + HCl \rightarrow \text{PRODUCTS}$	$(7 \times 10^{-10} \text{ CM}^3/\text{S})$	SRI
$Xe_2^* + HCl \rightarrow \text{PRODUCTS}$	$8.2 \pm 0.8 \times 10^{-10} \text{ CM}^3/\text{S}$	SRI
$Xe_2^* + Cl_2 \rightarrow \text{PRODUCTS}$	$5.0 \pm 0.6 \times 10^{-10} \text{ CM}^3/\text{S}$	SRI

$Xe_2Cl^*$  RADIATION & QUENCHING

$Xe_2Cl^* \rightarrow hv(470nm)$	$3.8 \pm 0.4 \times 10^6/\text{S}$	SRI
	$7.4 \times 10^6/\text{S}$	RICE
$Xe_2Cl^* + Cl_2 \rightarrow \text{PRODUCTS}$	$5.2 \pm 0.2 \times 10^{-10} \text{ CM}^3/\text{S}$	SRI
$Xe_2Cl^* + HCl \rightarrow \text{PRODUCTS}$	$6.1 \pm 0.2 \times 10^{-10} \text{ CM}^3/\text{S}$	SRI
$Xe_2Cl^* + Xe \rightarrow \text{PRODUCTS}$	$< 4 \times 10^{-14} \text{ CM}^3/\text{S}$	SRI

### Acknowledgments

This research was supported by the Defense Advanced Research Projects Agency through the Office of Naval Research. The experimental measurements and data analysis described here were carried out with the able assistance of R. L. Sharpless and D. L. Huestis of SRI International, K. Tang of Western Research, and M. Durrett, L. Houston, and G. K. Walters of Rice University.

### References

1. M. C. Castex, J. Chem. Phys. 66, 3854, (1977).
2. T. Moeller, B. Jordan, P. Gurtler, G. Zimmerer, D. Haaks, J. LeCalve, M. Castex; Chemical Physics, 76, 295, (1983).
3. J. H. Kolts, J. E. Velzaco and D. W. Setser, J. Chem. Phys. 71, 1247 (1979).
4. Gen Inoue, J. K. Ku, D. W. Setser J. Chem. Phys. 80, 6006, (1984).
5. R. E. Drullinger and R. N. Zare, J. Chem. Phys. 51, 5532, (1981).
6. A. Sur and J. Tellinghuisen J. Mol. Spectros. 88, 323, (1981).
7. J. LeCalve, M. C. Castex, B. Jordan, G. Zimmerer, T. Moller, and D. Haaks, private communication.
8. G Marowsky, G. P. Glass, M. Smayling, F. K. Tittel, and W. L. Wilson, J. Chem. Phys. 75, 1153 (1981).

**Appendix B**

**THE ROLE OF ELECTRONS IN EXCIMER LASERS**

**International Conference on Lasers '85  
26 December 1985, Las Vegas, NV**

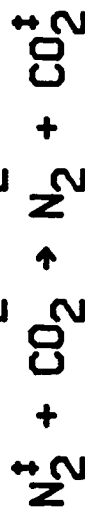
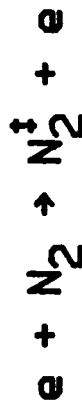
# THE ROLE OF ELECTRONS IN EXCIMER LASERS

David L. Huestis  
Chemical Physics Laboratory  
SRI International  
Menlo Park, CA 94025

## OUTLINE

ELECTRONS AS CHEMICAL SPECIES  
INDICATIONS OF OVERSIMPLIFICATION  
STATUS OF OUR UNDERSTANDING  
DEVELOPMENT OF REALISTIC ELECTRON KINETIC MODEL

## MANY GAS LASERS ARE ELECTRON-EXCITATION DOMINATED

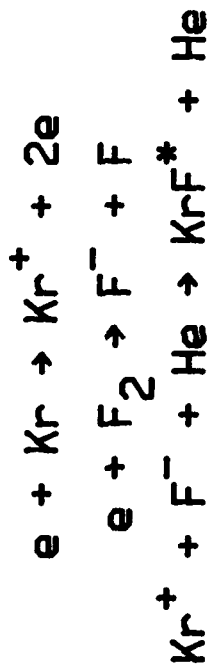
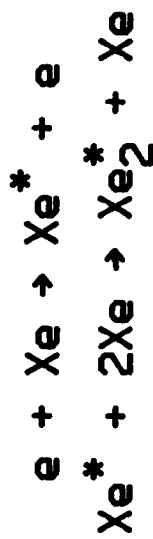


Modeling of these lasers obviously depends on a good treatment of the electron energy distribution.

But the chemistry is simple, so only a few electron cross sections are needed, and usually only for electron/ground-state collisions.

## EXCIMER LASERS ARE DOMINATED BY HIGH-PRESSURE CHEMICAL KINETICS

An excimer is an "excited dimer" with an "unstable" ground state.  
A new chemical entity must be created in a high-pressure gas:



The job of the electron is to prepare the kinetic precursors.

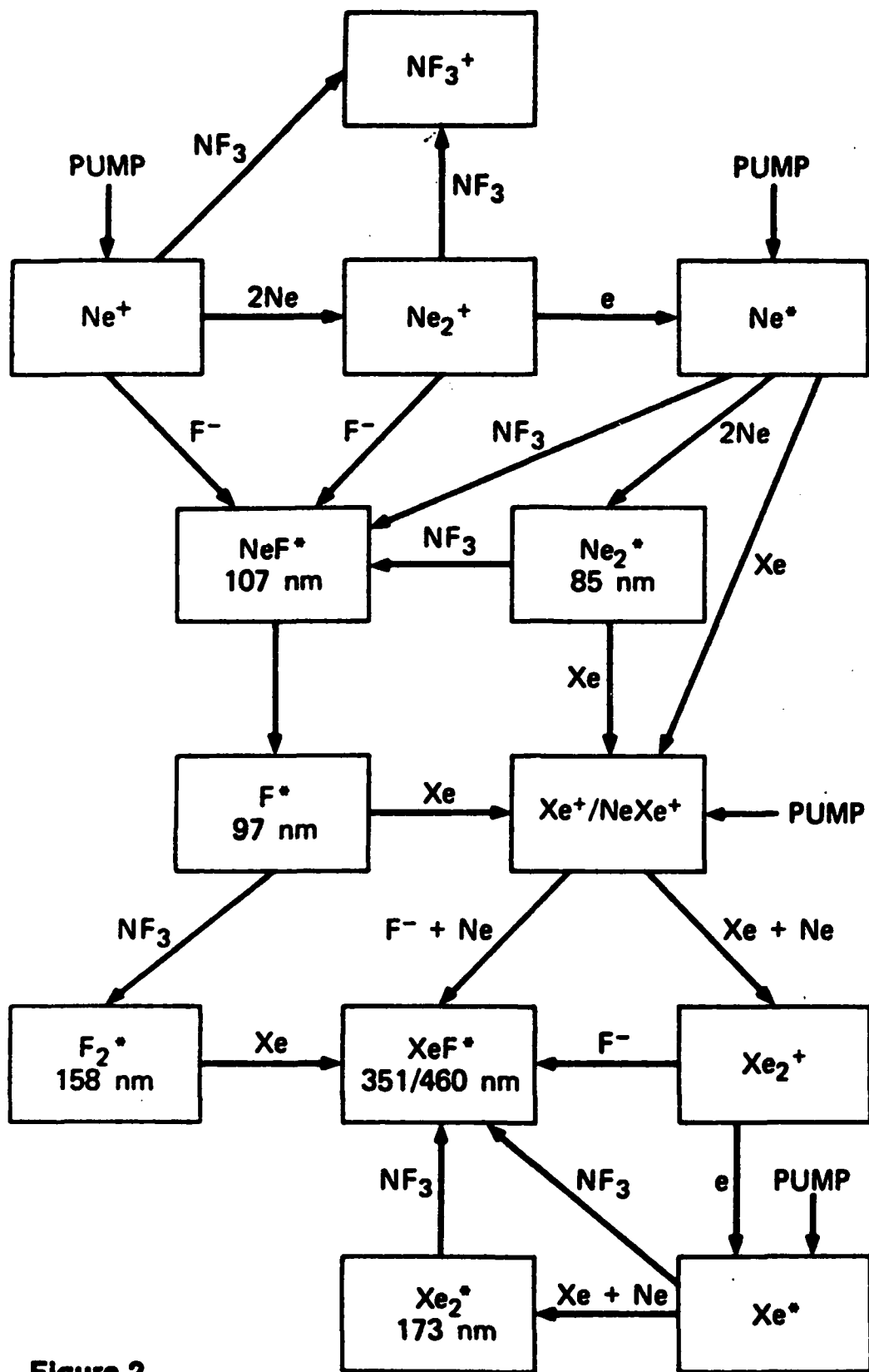


**Figure 2.**

THIS ILLUSTRATION DEPICTS THE MAJOR ENERGY FLOW PATHWAYS IN E-BEAM PUMPED Ne/Xe/NF<sub>3</sub> MIXTURES. ENERGY INPUT FROM THE ELECTRONS COMES IN ALONG THE PUMP ARROWS. THE SPECIE IN EACH BOX, PLUS THE COMPONENT ALONG THE REACTION ARROW, YIELDS THE RESULT IN THE NEXT BOX. THE WAVELENGTHS OF THE EMITTING SPECIES ARE INDICATED. THEY MAY BE SUBJECT TO QUENCHING BY NF<sub>3</sub> OR Xe (NOT SHOWN). NeF\* IS PRESUMED TO PREDISSOCIATE.

## RADIOLOGY OF THE RARE GASES

Stopping of charged particles in rare gases well studied in particle (Geiger-Müller) counters



Rg	W (eV)	Cost	Rg <sup>+</sup>	Rg <sup>*</sup>	<E <sub>ws</sub> >
He	45.2	31 eV	0.69	0.31	10.8 eV
Ne	39.3	27	0.77	0.23	9.5
Ar	26.6	20	0.77	0.23	6.9
Kr	23.0	18	0.74	0.26	6.1
Xe	20.5	15	0.69	0.31	5.3

## FLUORESCENCE AND LASER EFFICIENCIES

$$\eta_{\text{fluorescence}} \ll (h\nu/\text{quantum-cost}) \cdot \eta_{\text{kinetic}}$$

$$\eta_{\text{laser}} \ll (h\nu/\text{quantum-cost}) \cdot \eta_{\text{kinetic}} \cdot \eta_{\text{extraction}}$$

Fluorescence efficiencies of  $\text{Ar}_2^*$ ,  $\text{Kr}_2^*$ , and  $\text{Xe}_2^*$  are known to be  $\sim 50\%$  (but laser efficiencies  $\ll 1\%$ )

Rare gas halide laser efficiencies limited by absorption:

$$\eta_{\text{kinetic}} \sim 100\%$$

$$\eta_{\text{extraction}} \ll [1 - (g_0/g_a + 1)^{-1/2}]^2 \ll 50\%$$

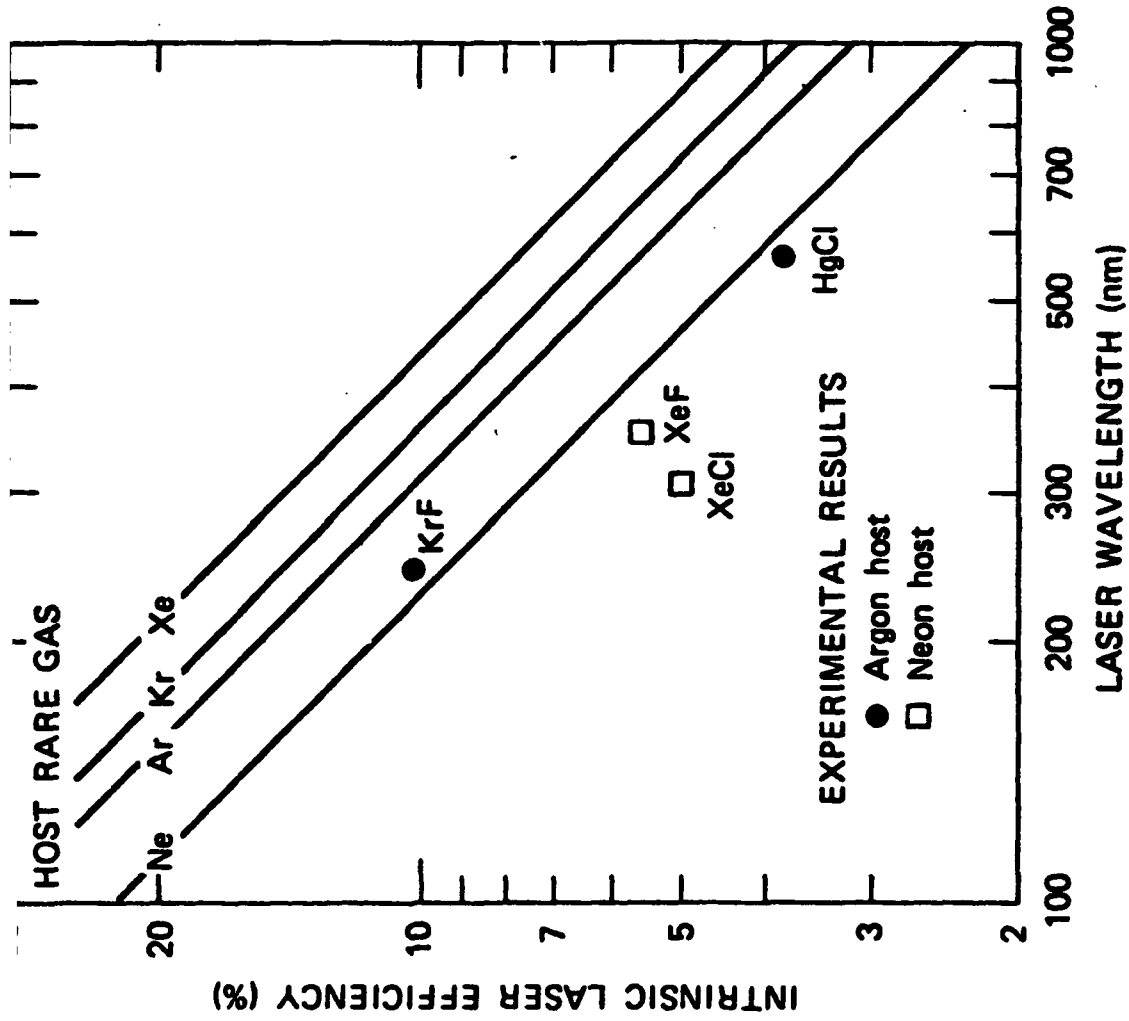


**Figure 3.**  
THE GRAPH INDICATES PREDICTED MAXIMUM INTRINSIC LASER EFFICIENCY  
UNDER ELECTRON-BEAM EXCITATION.

## **SUMMARY: ELECTRONS AS A CHEMICAL SPECIES**

- 1. Kinetic precursors created by primary electrons**
- 2. Secondary electrons rapidly cooled by elastic collisions**
- 3. Cool ~ 1 eV electrons participate in the chemistry:**



- 4. Under most conditions models based on this picture are adequate**

# INDICATIONS OF FAILURE OF THE ELECTRON CHEMISTRY MODEL

## Direct Indications:

Complete failure to explain  $\text{XeCl}^*$  formation

Time dependence of  $\text{Xe}_2^*$  fluorescence

## Indirect Indications: Apparent Electron Quenching

$\text{RgF}^* + e$        $2-4 \times 10^{-7}$  experimental  
                          $3-8 \times 10^{-8}$  theoretical

$\text{Xe}^* \cdot \text{Xe}_2^* + e$        $3-4 \times 10^{-9}$  modeling

## Xe<sup>\*</sup><sub>2</sub> FLUORESCENCE TIME HISTORY

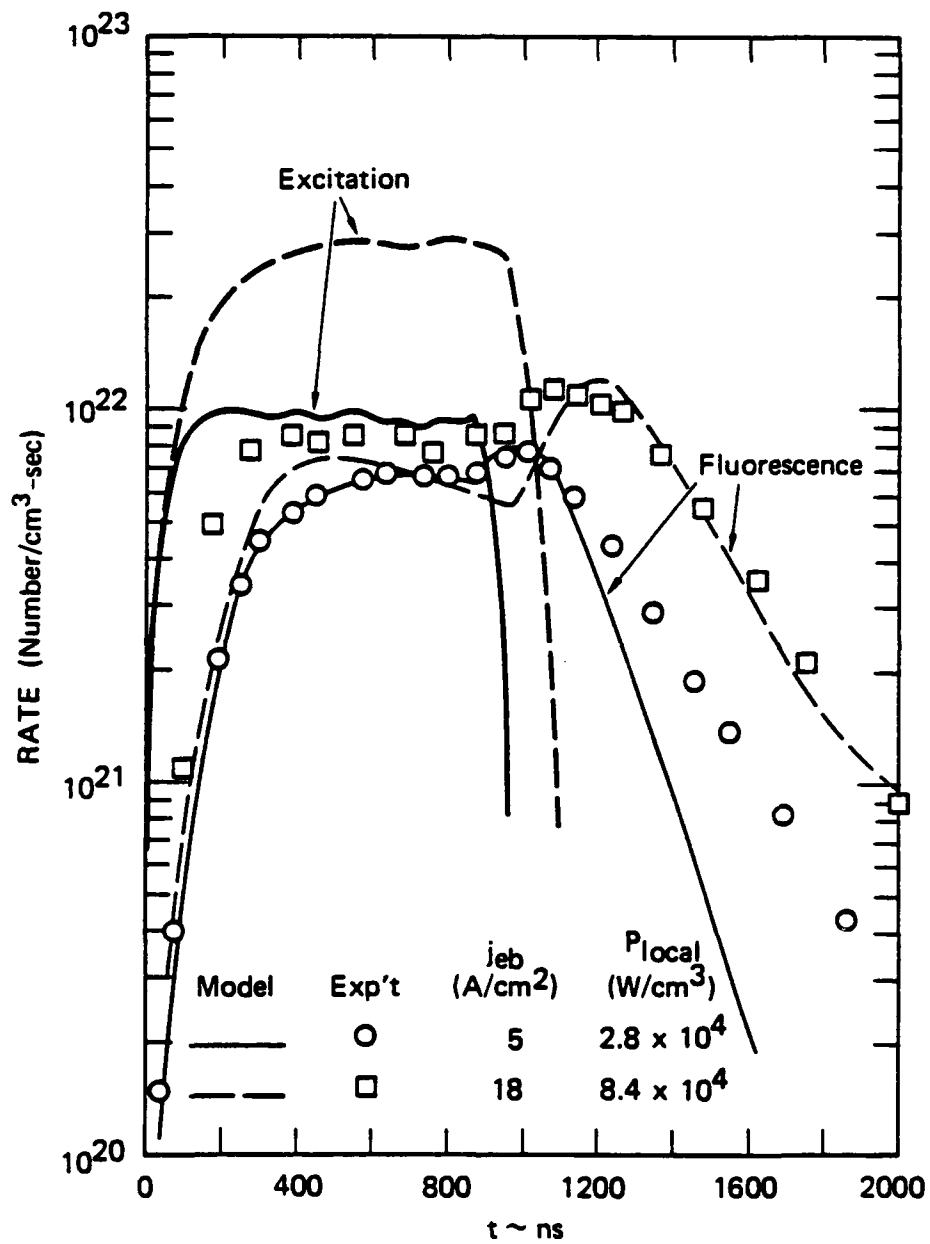
### Problems:

At all pressures decay is unexpectedly slow

At low pressures, fluorescence peaks after e-beam shuts off

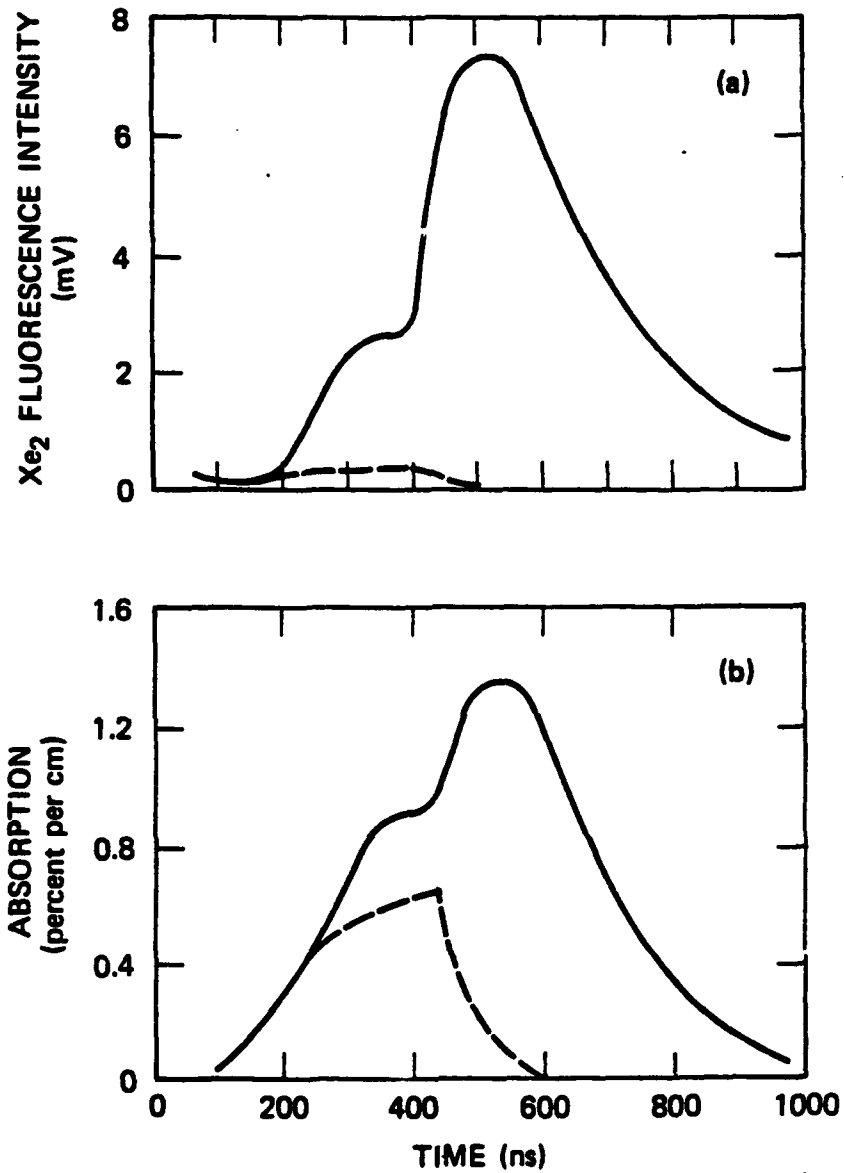
Presumed Solution: Electron impact dissociation





JA-330522-82

Figure 3



JA-1522-61A

**FIGURE 8 (a) FLUORESCENCE AT 172 nm AND (b) ABSORPTION AT 304 nm OF XENON AT 380 torr (solid lines) AND WITH ADDED NITROGEN AT 100 torr (dashed lines) UNDER ELECTRON-BEAM EXCITATION (100-400 ns)**

## **ELECTRON QUENCHING**

**Undeniably present, the question is magnitude of rate coefficient**

**Very few direct experiments on electron/excited-state collisions**

**Difficult to infer using calculated electron density**

**Insufficient data versus excitation rate**

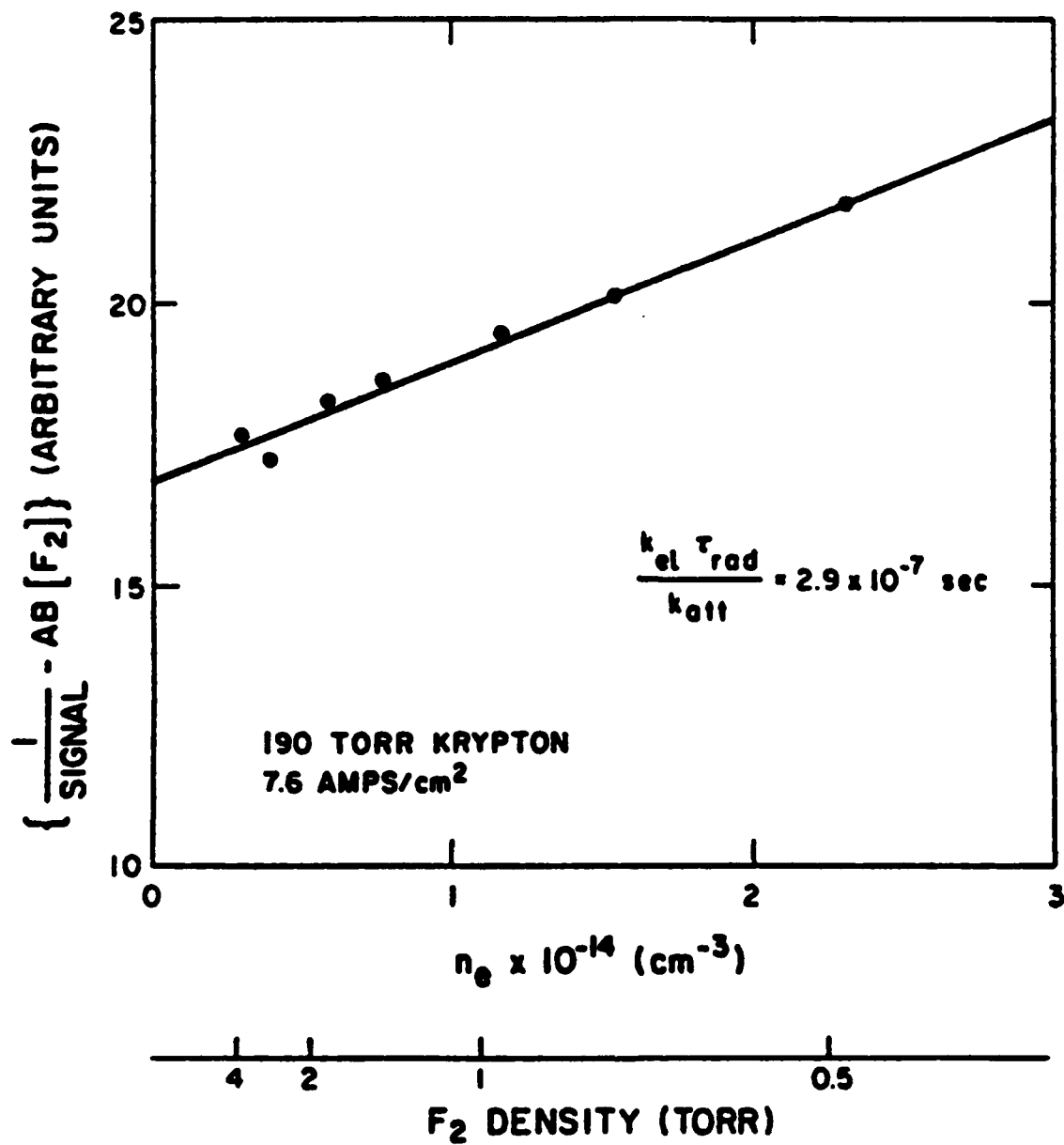


FIG. 2. Modified Stern-Vollmer plot of 1/signal (corrected for F<sub>2</sub> quenching) vs electron density (or 1/F<sub>2</sub> density).

676

Appl. Phys. Lett., Vol. 37, No. 8, 15 October 1980

## STATUS OF OUR UNDERSTANDING

The simple models still give a good picture

As the models get more complete, the oversimplifications get more difficult to remove

Few direct measurements of  $n_e$  and  $T_e$   
Models have difficulty explaining even these few

Severe shortage of reliable electron/excited-state cross sections

Measurements are needed of densities of excited-states that should be sensitive to electrons:  $\text{HCl}(v>0)$ ,  $\text{Xe}^{**}$

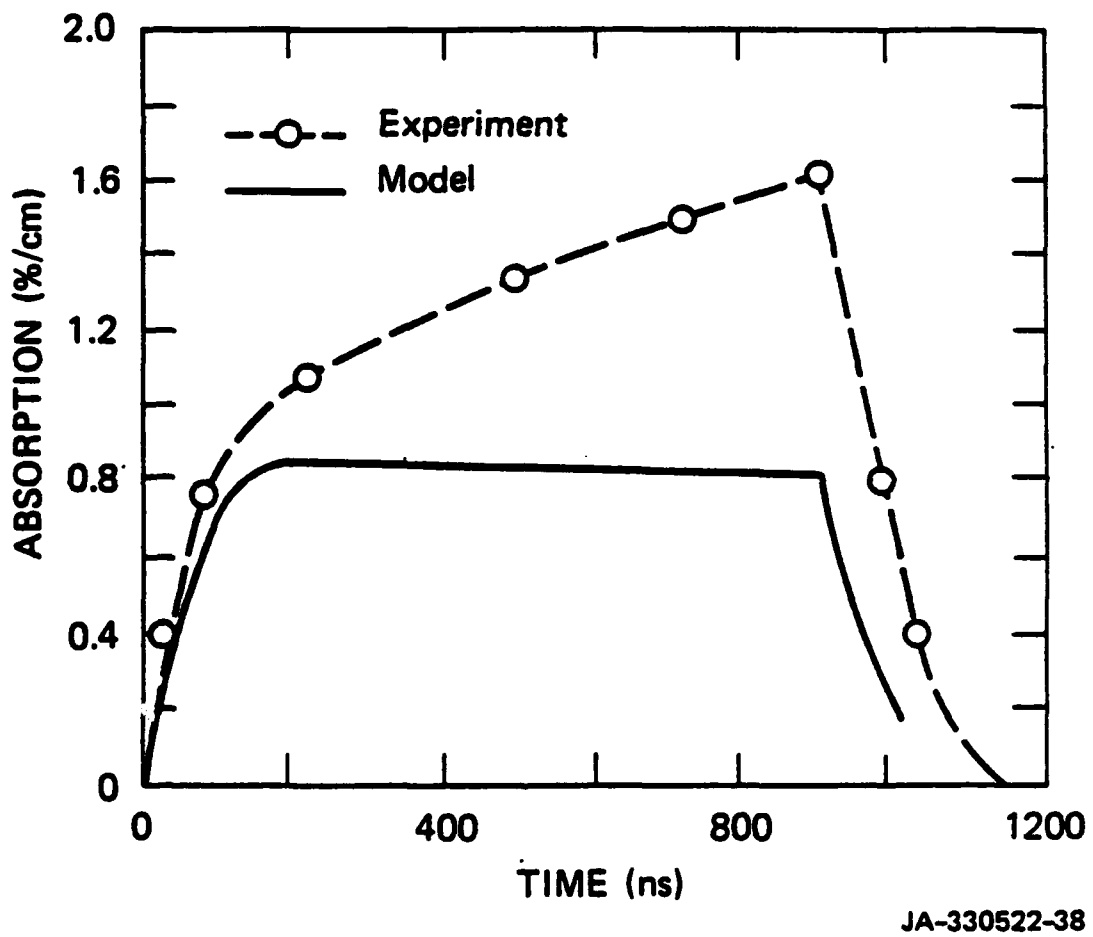


Figure 10

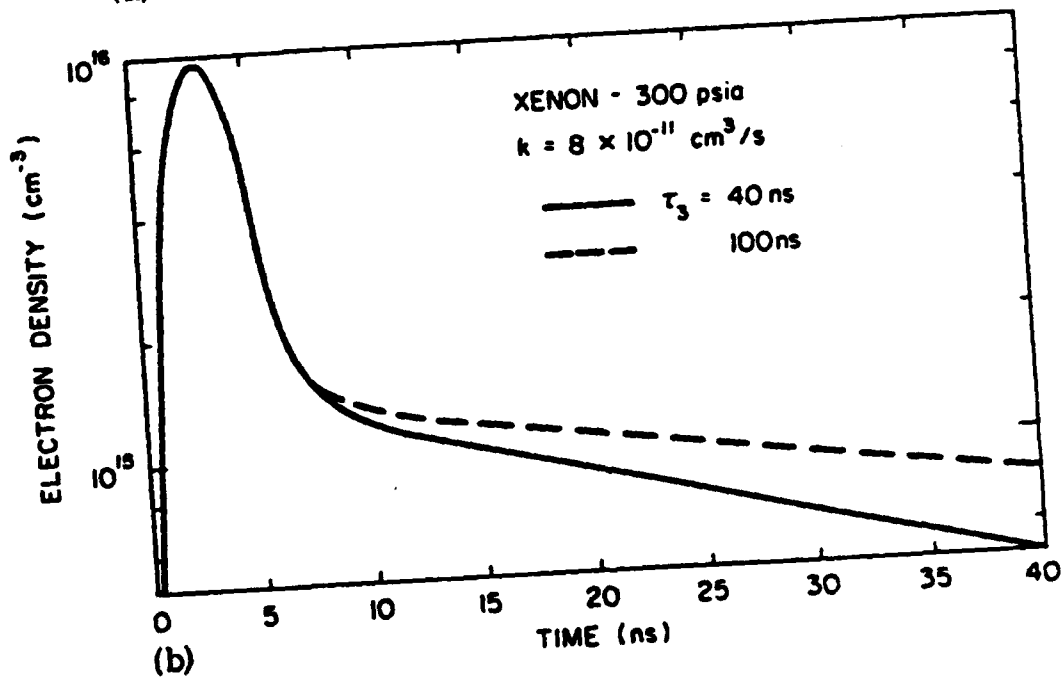
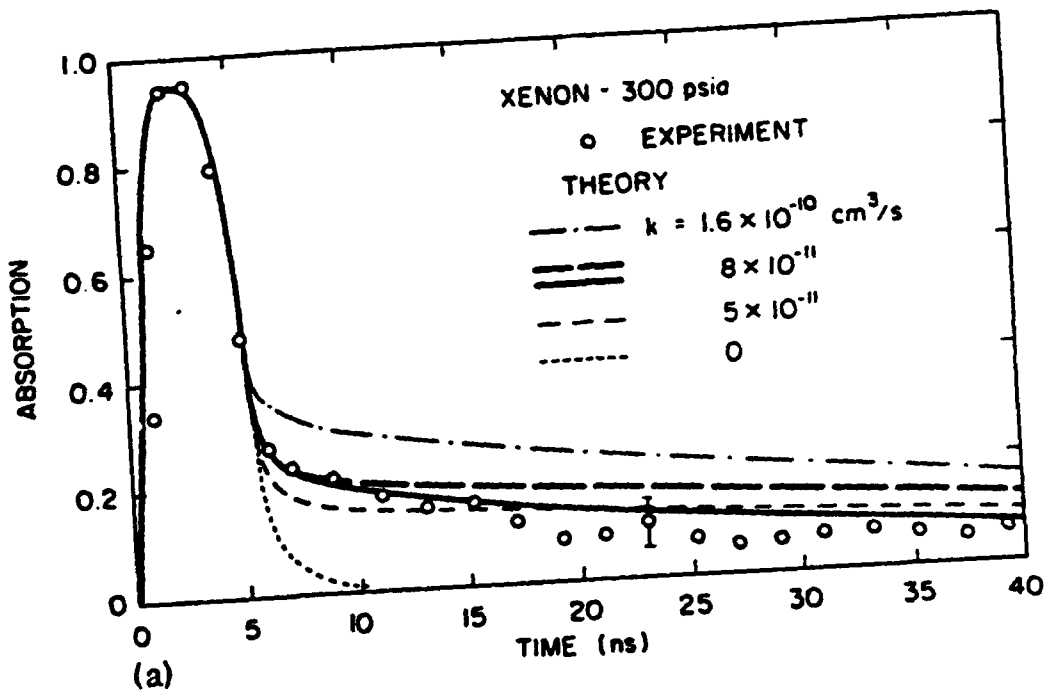


FIG. 2. (a) Comparison of experimental (open circles) and theoretical (dashed and solid lines) absorption in xenon for a Febetron charging voltage of 30 kV (0.1 cm from the foil). Each theoretical curve corresponds to a different value of the rate constant  $k$  for Eq. (2). The solid line is for a triplet lifetime of 40 nsec, whereas dashed lines are for a corresponding lifetime of 100 nsec. (b) Predicted temporal evolution of the electron density for two triplet lifetimes ( $k = 8 \times 10^{-11} \text{ cm}^3/\text{sec}$ ).

## **DEVELOPMENT OF A REALISTIC ELECTRON KINETIC MODEL**

**Good library of cross sections**

**Improvements in speed: electron-electron collisions**

**Compact model of rare gas excited states**

## OBJECTIVE OF PRESENT STUDY

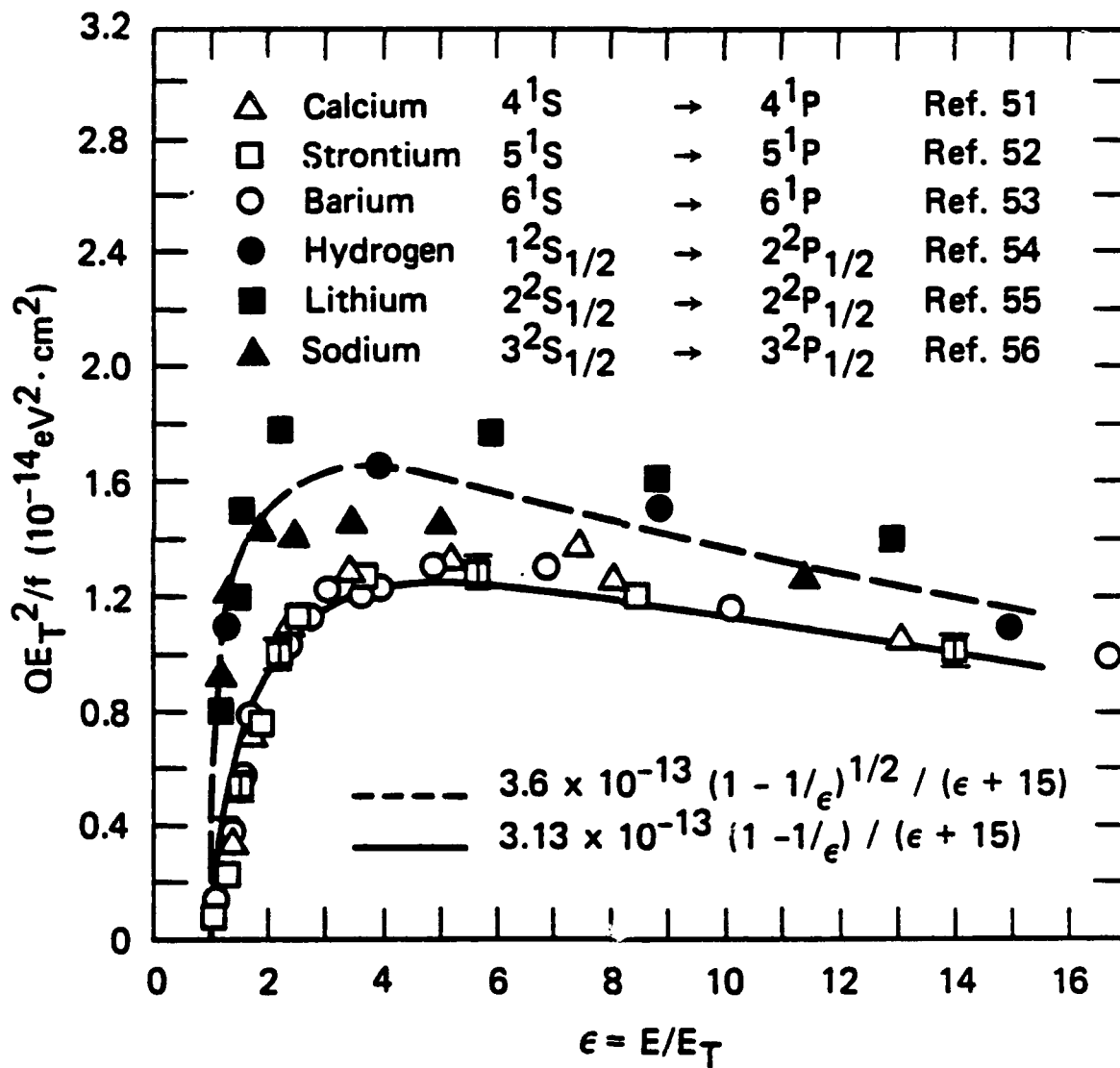
To develop a simplified picture of the rare gas excited states that can be used in laser kinetic models.

This presumably will consist of a list of "lumped" states, called  $Xe^*$ ,  $Xe^{**}$ ,  $Xe^{***}$ , etc., with average energies, rate constants, and cross sections.

## TYPICAL CONDITIONS

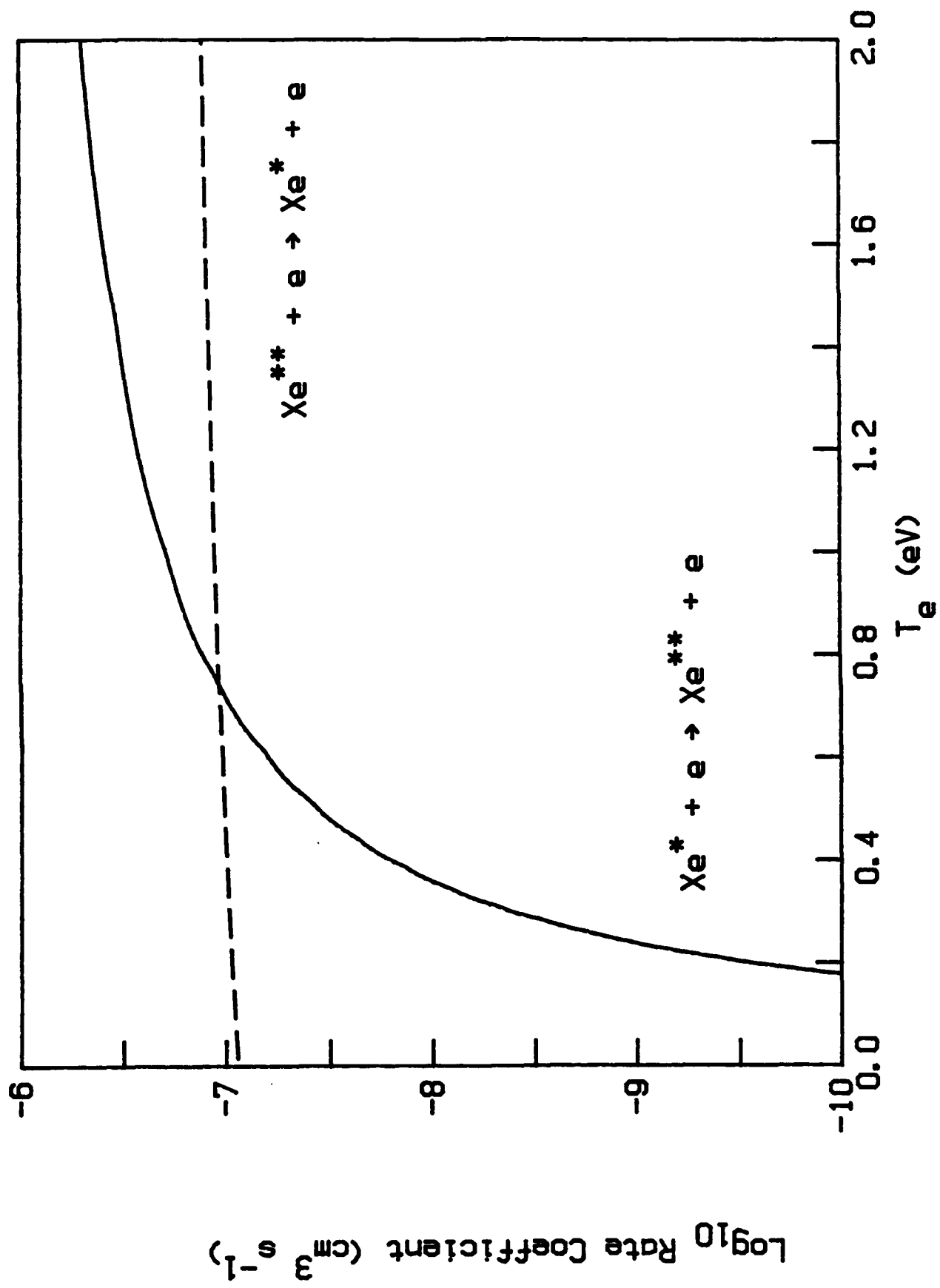
$$Xe^* \sim 10^{14}, \quad e \sim 10^{14}, \quad T_e \sim 1 \text{ eV}$$

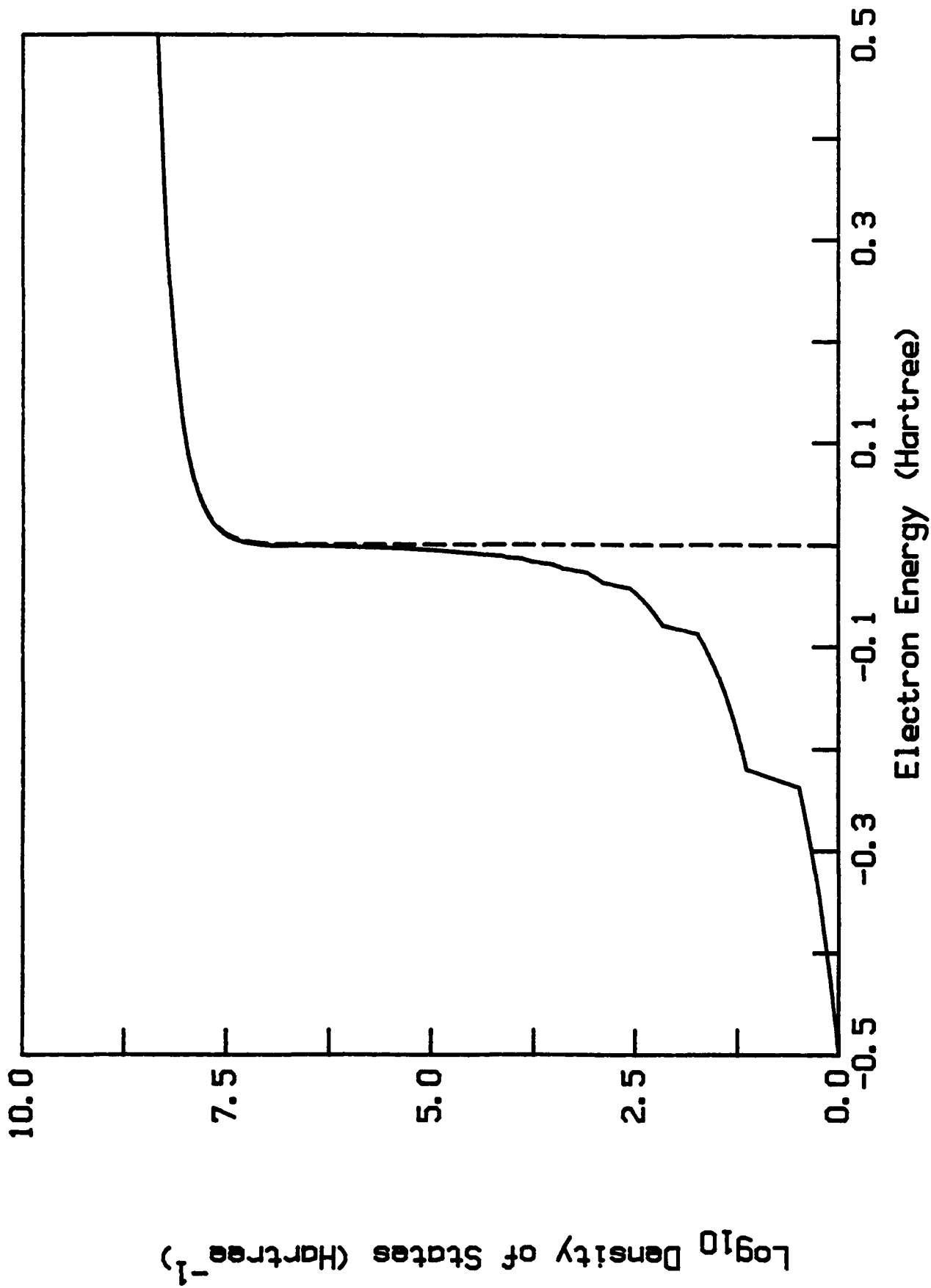
## FIRST PROBLEM IS STATISTICAL WEIGHTS OF LEVELS



JA-330522-22A

Figure 11





Box-Normalized Density of States for  $R_{\text{box}} = 1000$  bohr

## CONCLUSIONS

Completely consistent statistical mechanics requires assumption of ionization equilibrium (Saha).

Modified Boltzmann Distribution allows finite partition function, may be a useful for calculating effective statistical weights of individual levels, but needs good experimental tests.

Modified Boltzmann equation for excited state densities.

The problem of statistical weights for high levels is frequently encountered in models of discharge lamps

**Appendix C**

**RADIATIVE LIFETIMES OF THE  $0_u^-$  SUBLEVELS OF THE RARE GAS  
EXCIMERS**

39nd Annual Gaseous Electronics Conference  
7-10 October 1986, Madison, WI

[Bull. Am. Phys. Soc.32, 1160 (1987)]

**RADIATIVE LIFETIMES OF THE  $O_u^-$  SUBLEVELS  
OF THE RARE GAS EXCIMERS**

**David L. Huestis  
Chemical Physics Laboratory  
SRI International  
Menlo Park, CA 94025**

**OUTLINE**

**Introduction  
Origin of Transition Probability  
Model Hamiltonian  
Results and Conclusions**

## INTRODUCTION

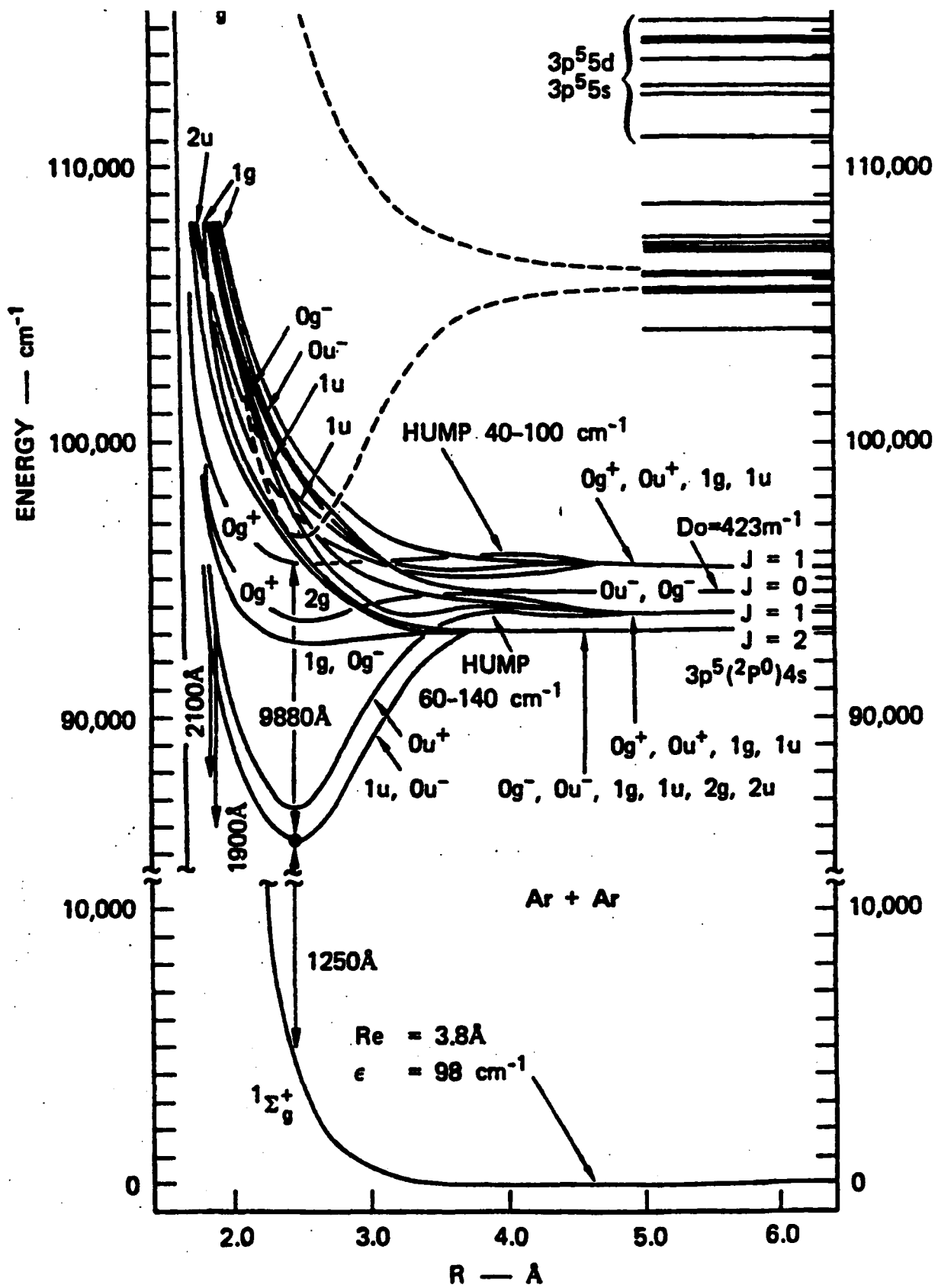
The prototype "excimer" molecules.

Still interesting as efficient light sources,  
and still incompletely understood.

The weakly bound ground state complicates  
conventional spectroscopic investigation.

In the present study we are investigating  
theoretically the fine structure of lowest of  
the excimer excited states,  ${}^3\Sigma_u^+$

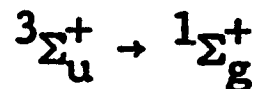
We are especially interested in the radiative  
properties of the  $0_u^-$  sublevel, which previous  
studies have supposed to be completely  
metastable.



SA-1925-1R

FIGURE 2 ARGON INTERMOLECULAR POTENTIAL CURVES

## ORIGIN OF TRANSITION PROBABILITY



$1_e \rightarrow 0_e$  weak  $P_{21}$  and  $R_{21}$  branches

$1_f \rightarrow 0_e$  weak  $Q_{31}$  branch

$0_f \rightarrow 0_e$  very weak  $Q_{11}$  branch,  $\sim J(J+1)$

$1_e$  and  $1_f$  mix with  ${}^1\Pi_1$  by spin-orbit coupling

$0_f$  mixes with  $1_f$  by Coriolis coupling

PERTURBATION TREATMENT IN HUND'S (a)

$$\lambda = E(^3\Sigma_1) - E(^3\Sigma_0) \text{ is large}$$

$$1/\tau_3 \approx 1/\tau_2 \sim |\mu_1|^2 \quad 1/\tau_1 \sim |\mu_0|^2$$

$$\mu_1 = \langle ^3\Sigma_1 | \mu | ^1\Sigma_0 \rangle \sim \langle ^3\Sigma | H_{so} | ^1\Pi \rangle \langle ^1\Pi | \mu | ^1\Sigma \rangle / ({}^1\Pi - {}^3\Sigma)$$

$$\mu_0 = \langle ^3\Sigma_0 | \mu | ^1\Sigma_0 \rangle \sim \langle ^3\Sigma_0 | H_{rot} | ^3\Sigma_1 \rangle \mu_1 / ({}^3\Sigma_1 - {}^3\Sigma_0)$$

$$\langle ^3\Sigma_0 | H_{rot} | ^3\Sigma_1 \rangle = -2B\eta [J(J+1)]^{1/2}$$

$$\eta = \langle ^3\Sigma_0 | L_- + S_- | ^3\Sigma_1 \rangle \sim \sqrt{2} ?$$

$$\tau_2/\tau_1 = 2(B\eta/\lambda)^2 J(J+1)$$

$$\langle \tau_2/\tau_1 \rangle = 2BkT\eta^2/\lambda^2 \sim 4BkT/\lambda^2$$

Table I

MOLECULAR SPIN-ORBIT MATRICES FOR sp OR p<sup>5</sup>s ATOMIC CONFIGURATIONS

O <sup>-</sup>	$3p_0^0$	$3p_2^0$	O <sup>+</sup>	$1p_1^0$	$3p_1^0$
$3p_0^0$	$\frac{W}{6} - \xi - G$	$\sqrt{\frac{2}{9}} W$	$1p_1^0$	$-\frac{W}{2} + G$	$\sqrt{\frac{1}{2}} \xi$
$3p_2^0$	$\sqrt{\frac{2}{9}} W$	$-\frac{W}{6} + \frac{\xi}{2} - G$	$3p_1^0$	$\sqrt{\frac{1}{2}} \xi$	$\frac{W}{2} - \frac{\xi}{2} - G$

1	$3p_2^1$	$3p_1^1$	$3p_1^1$	$1p_1^1$
$3p_2^1$	$\frac{\xi}{2} - G$	$-\frac{W}{2}$	$-\frac{W}{2}$	0
$3p_1^1$	$-\frac{W}{2}$	$-\frac{\xi}{2} - G$	$-\frac{\xi}{2} - G$	$\sqrt{\frac{1}{2}} \xi$
$1p_1^1$	0	$\sqrt{\frac{1}{2}} \xi$	$\sqrt{\frac{1}{2}} \xi$	$\frac{W}{2} + G$

2	$3p_2^2$
$3p_2^2$	$\frac{W}{2} + \frac{\xi}{2} - G$

$R_{G_2}^*$  CORIOLIS COUPLING IN HUND'S CASE (d)

$$\langle x_{P_j^{\Omega}} | H_{\text{rot}} | x_{P_j^{\Omega}} \rangle = B[J(J+1) + j(j+1) - 2\Omega^2]$$

$$\langle x_{P_j^{\Omega+1}} | H_{\text{rot}} | x_{P_j^{\Omega}} \rangle = -B \left\{ [J(J+1) - \Omega(\Omega+1)] [j(j+1) - \Omega(\Omega+1)] [1 + \delta_{\Omega, 0}] \right\}^{1/2}$$

5  $\langle {}^3P_2^2 | H_{\text{rot}} | {}^3P_2^1 \rangle = -2B[J(J+1) - 2]^{1/2}$

$$\langle {}^3P_2^1 | H_{\text{rot}} | {}^3P_2^0 \rangle = -2B[3J(J+1)]^{1/2}$$

$$\langle x_{P_1^1} | H_{\text{rot}} | x_{P_1^0} \rangle = -2B[J(J+1)]^{1/2}$$

CALCULATED  $R_{g_2}^*$  ENERGIES ( $\text{cm}^{-1}$ )

	$\text{Ne}_2^*$	$\text{Ar}_2^*$	$\text{Kr}_2^*$	$\text{Xe}_2^*$
$^3\Sigma_u^+$	0	0	0	0
$^1\Sigma_u^+$	930	785	765	950
$^3\Pi$	18100	15800	14200	16000
$^1\Pi$	19300	16800	16100	17400
$\zeta$	-517	-940	-3480	-6300
$B_e$	0.523	0.106	0.052	0.028
$\lambda$	0.5	1.0	12	34

$^3\Sigma_u^+$  RADIATIVE LIFETIMES ( $\mu\text{s}$ )

	$\text{Ne}_2^*$	$\text{Ar}_2^*$	$\text{Kr}_2^*$	$\text{Xe}_2^*$
$\tau_1$	26	13.7	3.1	8.5
$\tau_2$	13	6.3	0.45	0.24
$\tau_3$	26	11.6	0.53	0.24
$\langle\tau\rangle$	20	9.4	0.68	0.35
$\langle\text{expt}\rangle$	5.9	3.2	0.26	0.099
$\tau'_1$	8	4.7	1.2	2.4
$\tau'_2$	4	2.1	0.18	0.067
$\tau'_3$	8	3.9	0.21	0.067

TABLE III  
ESTIMATED LIFETIMES OF TRIPLET EXCIMERS

Excimer	$\tau_{1u} / \tau_{0u}^+$		$\tau_{1u}$ if $\tau_{0u}^+ = 4 \text{ nsec}$	Experimental Values
	$D_e = 0.5 \text{ eV}$	$D_e = 1.0$		
* $\text{Ne}_2$	1460	4800	5.8 - 19 $\mu\text{sec}$	5.1 $\mu\text{sec}$ <sup>a</sup>
* $\text{Ar}_2$	470	1500	1.9 - 6 $\mu\text{sec}$	2.8 $\mu\text{sec}$ , <sup>b</sup> 3.7 $\mu\text{sec}$ <sup>c</sup>
* $\text{Kr}_2$	48	130	0.19 - 0.52 $\mu\text{sec}$	0.3 $\mu\text{sec}$ , <sup>d</sup> 1.7 $\mu\text{sec}$ <sup>c</sup>
* $\text{Xe}_2$	24	46	96 - 184 nsec	100-160 nsec, <sup>e</sup> 500 nsec <sup>c</sup>

<sup>a</sup> P. K. Leichner, Phys. Rev. A 8, 815 (1973).

<sup>b</sup> N. Thonnard and G. S. Hurst, Phys. Rev. A 5, 1110 (1972).

<sup>c</sup> R. Boucique and P. Mortier, J. Phys. D. 3, 1905 (1970).

<sup>d</sup> P. K. Leichner and R. J. Ericson, Phys. Rev. A (in press).

<sup>e</sup> From analysis of data of Koehler, et al.<sup>6</sup> at 0.27 atm.

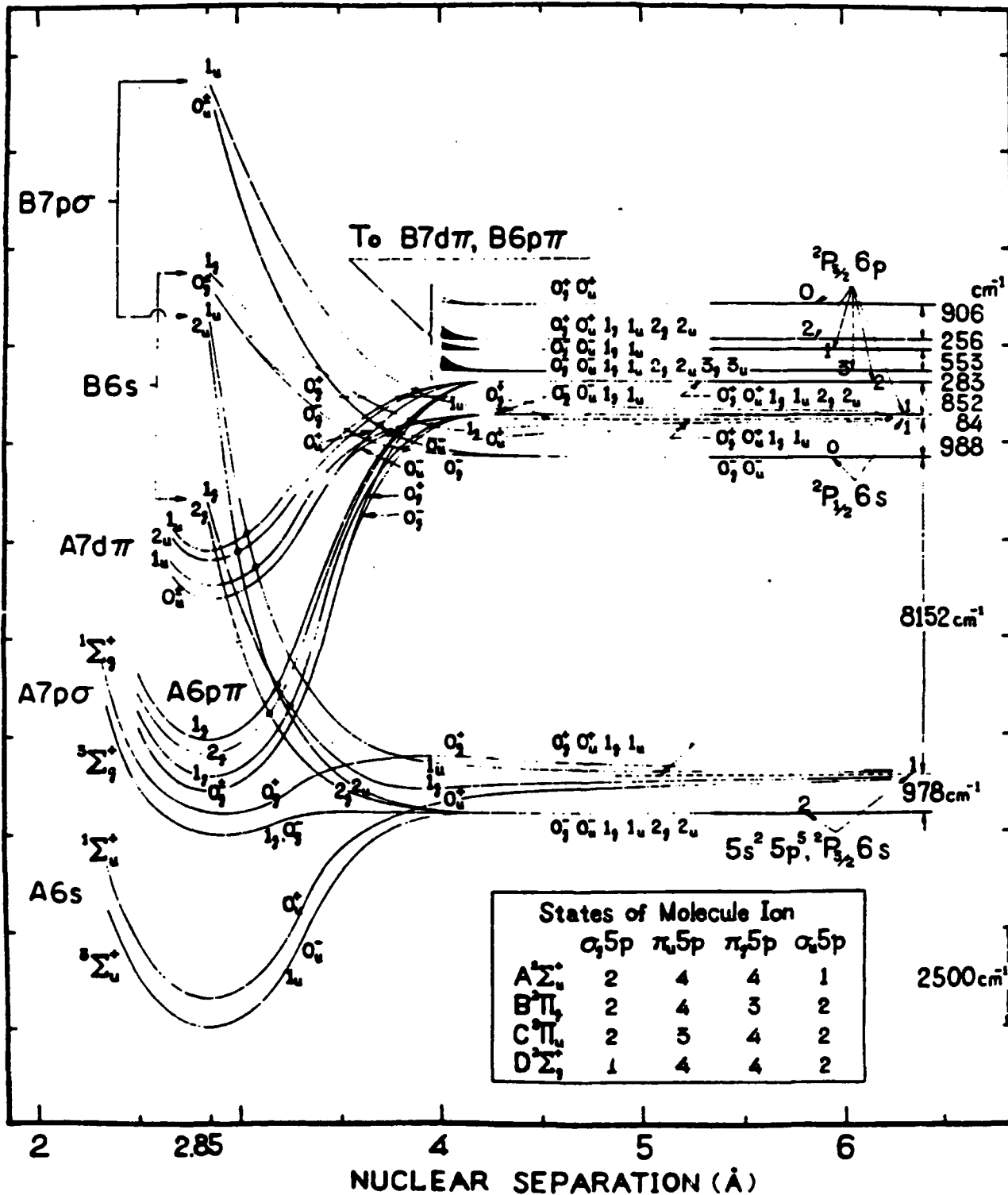


FIGURE 1 XENON INTERMOLECULAR POTENTIAL CURVES FROM THE WORK OF MULLIKAN

SA-2018-3

## CONCLUSIONS

The  $0_u^-$  sublevels of the rare gas excimers have non-negligible radiative transitions induced by rotational coupling.

In high pressure rare gases the sublevels of the  $^3\Sigma_u^+$  state should be well mixed. The observed radiative rates should be averages of the rates from the  $1_u$  and  $0_u^-$  sublevels.

There remains a factor of 2-3 disagreement between theory and experiment.

The lifetimes of the  $0_u^-$  sublevel in  $Kr_2^*$  and  $Xe_2^*$  are in a favorable range for molecular beam investigation.

**Appendix D**

**THREE-BODY REACTION OF XeCl\* TO FORM Xe<sub>2</sub>Cl**

39nd Annual Gaseous Electronics Conference  
7-10 October 1986, Madison, WI

[Bull. Am. Phys. Soc. **32**, 1170 (1987)]



# Thirty-Ninth Annual Gaseous Electronics Conference

7 - 10 October, 1986 • Madison, Wisconsin

**GECS86**

PLEASE TYPE NAME, ADDRESS  
& TELEPHONE NUMBER

D. C. Lorents

SRI International

333 Ravenswood Ave.

Menlo Park, CA 94025

(415) 859-3167

Indicate topic(s) covered in the paper by selecting a letter and a digit from the attached list. If more than one, present in order of importance.

Indicate preferred mode of presentation.

- Poster
- Lecture
- Either

Letter Digit

Letter	Digit
D	2

DO NOT WRITE IN THIS SPACE

Serial No. \_\_\_\_\_

Accepted: Yes \_\_\_\_\_ No \_\_\_\_\_

Session \_\_\_\_\_

Number \_\_\_\_\_

Date. Conf. \_\_\_\_\_

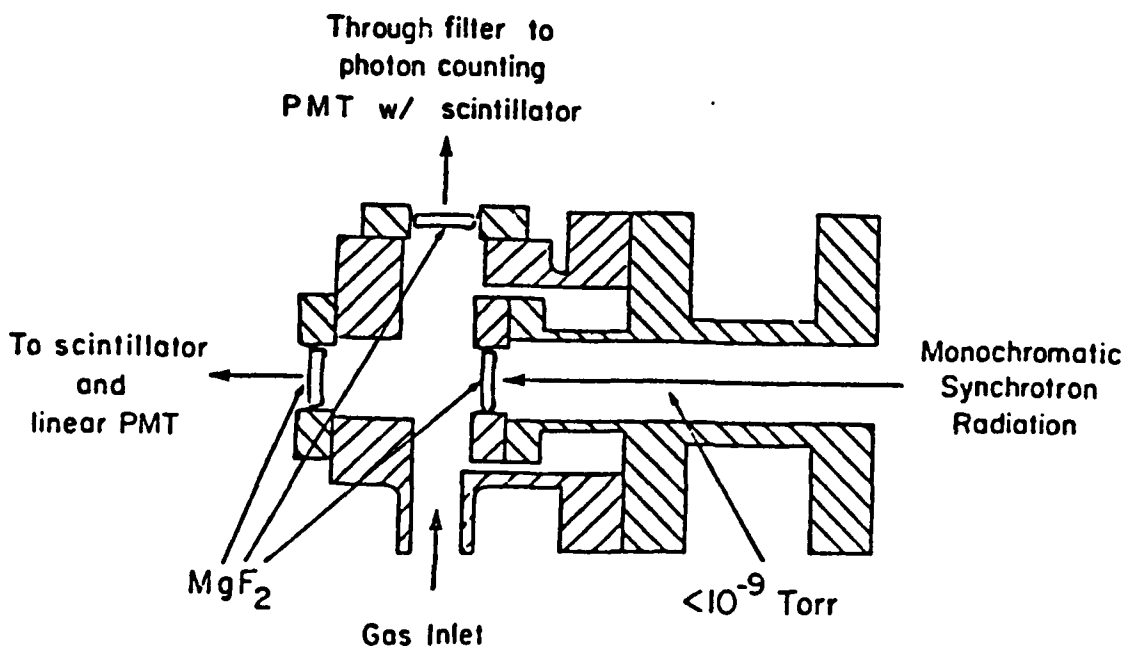
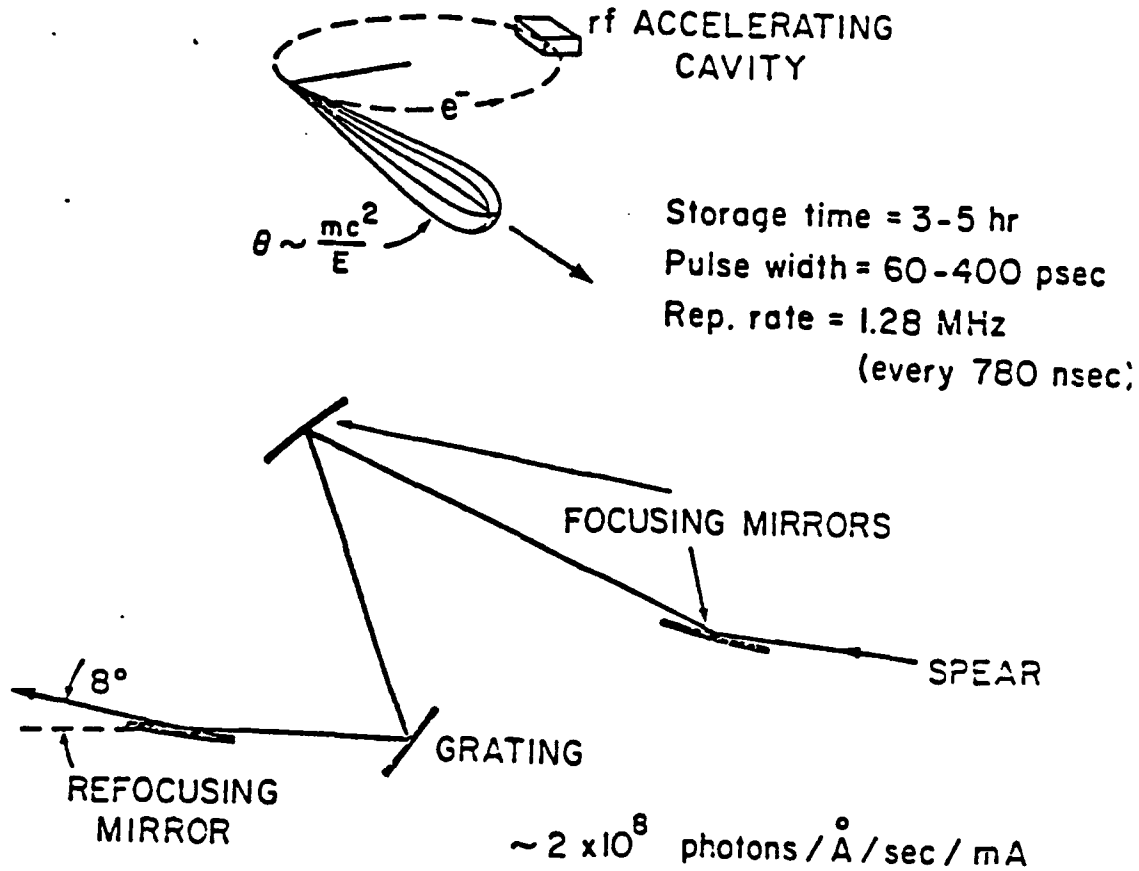
Please use this form for all papers including invited papers and papers for arranged sessions. Please indicate at the top of this form if the abstract is for an invited paper or if the abstract is intended for an arranged session.

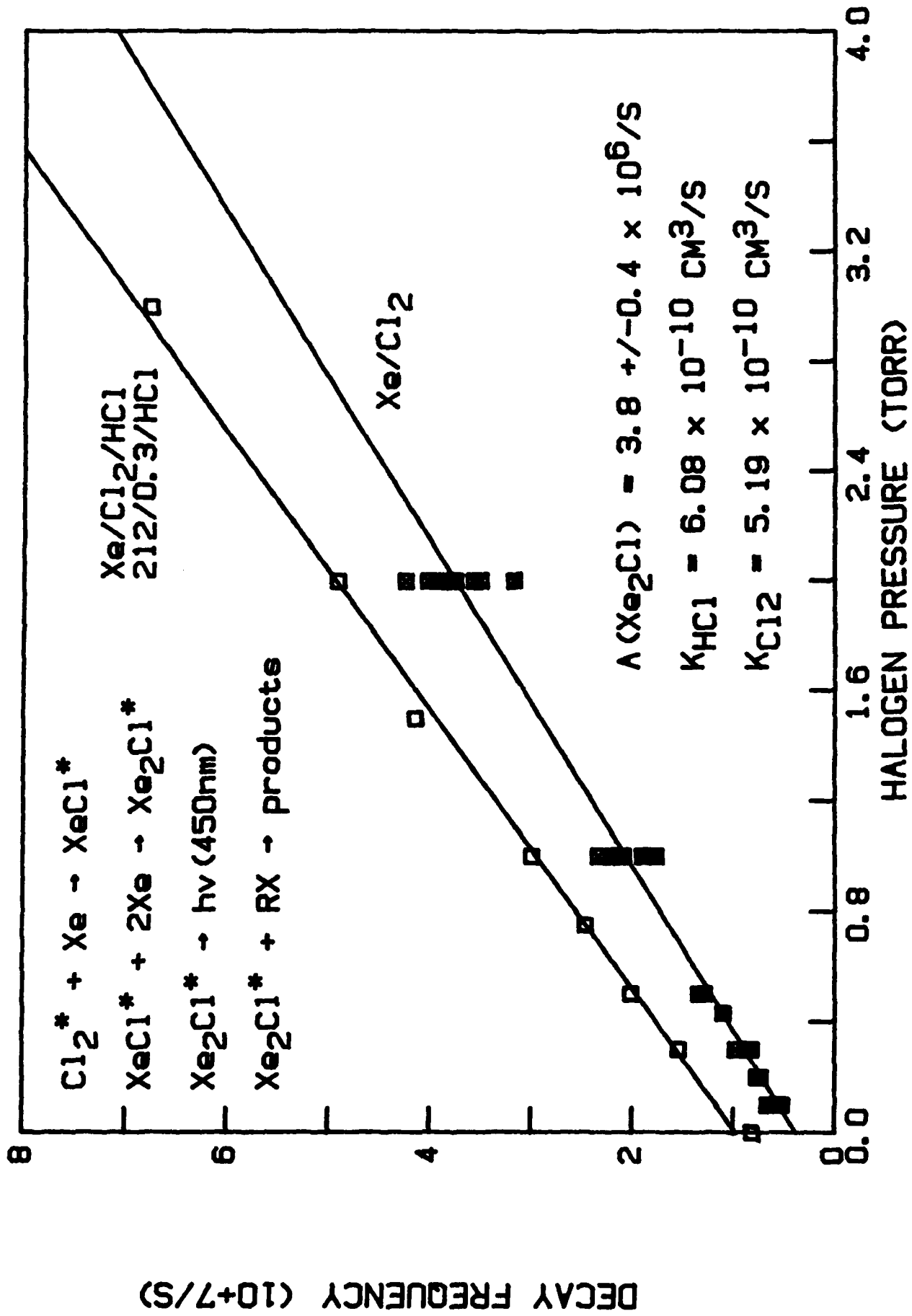
### Three-body Reaction of $XeCl^*$ to Form $Xe_2Cl$ ,<sup>#</sup>

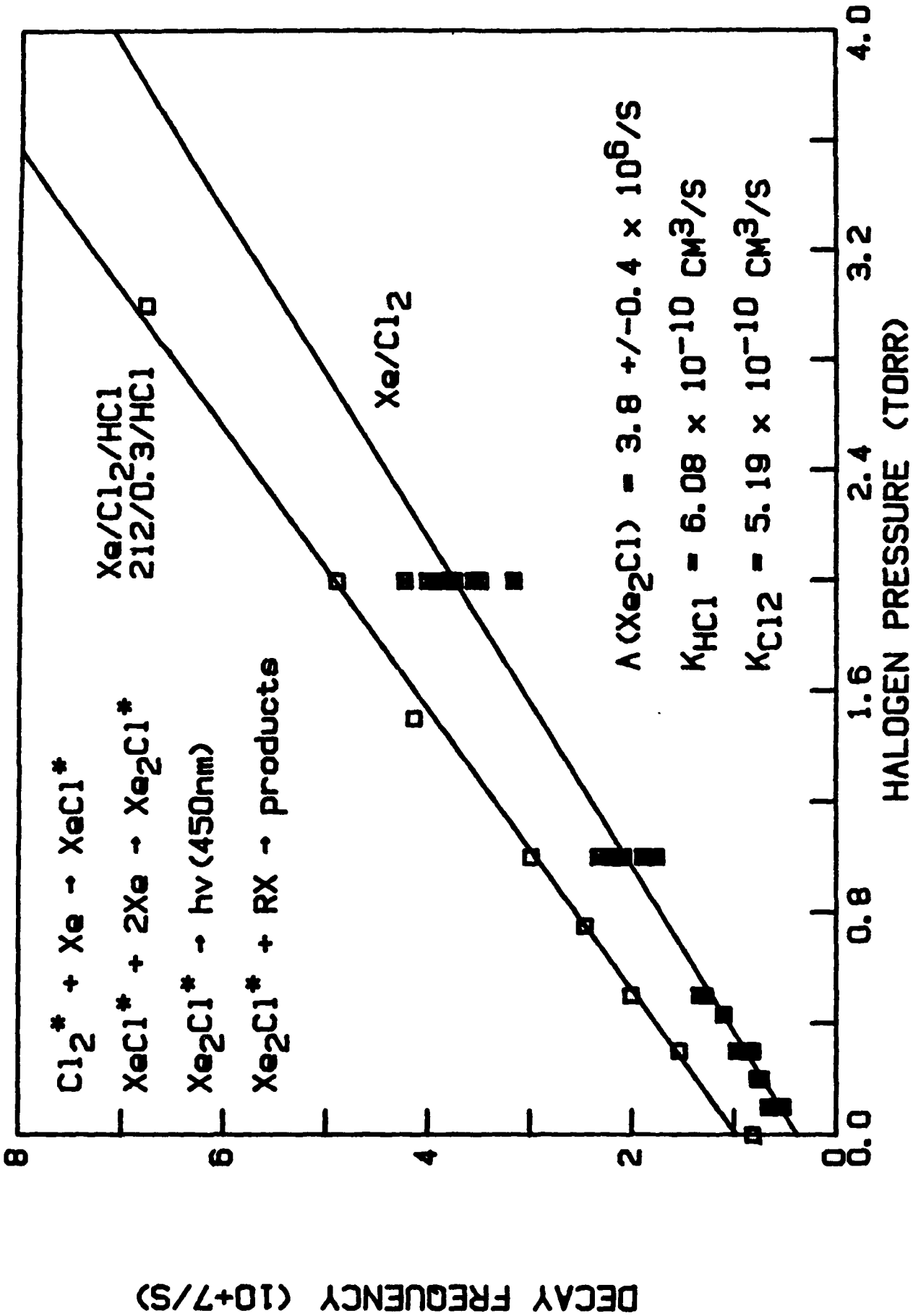
D. C. LORENTS, R. L. SHARPLESS, D. L. HUESTIS, SRI INTERNATIONAL -- Synchrotron measurements of the decay rate of  $XeCl^*$  and the formation rate of  $Xe_2Cl^*$  in Ne/Xe/ $Cl_2$  and Kr/Xe/ $Cl_2$  mixtures is composed of three components: radiation, two-body quenching and three-body reaction. The measurements at pressures up to 5000 Torr show that the reaction,  $XeCl^* + Xe + Ne \rightarrow Xe_2Cl^* + Ne$ , is not a linear function of the  $[Xe][Ne]$  product and therefore is not a simple three body reaction. Measurements at Xe pressures of 50 and 150 Torr and Ne pressures ranging from 0 to 5000 Torr can be fit with the simple pressure dependent three-body rate constant given by  $k_p = 7 \times 10^{-31} [Xe][Ne] / \{1 + 10^{-20} [Ne]\}$ . This result can be qualitatively understood in terms of the Lindemann mechanism that implies that the reaction proceeds through an intermediate complex that is relatively long-lived.

<sup>#</sup> Work supported by ONR

# Stanford Positron-Electron Accelerating Ring (SPEAR)







## RATE CONSTANTS FOR XeCl KINETICS

### FORMATION

REACTION	RATE CONSTANT	
$\text{Xe}(^3\text{P}_2) + \text{Cl}_2 \rightarrow \text{XeCl}^*$	$7.2 \times 10^{-10} \text{ CM}^3/\text{S}$	KSU
$\text{Xe}(^3\text{P}_1) + \text{Cl}_2 \rightarrow \text{XeCl}^*$	$7.9 \pm 0.9 \times 10^{-10} \text{ CM}^3/\text{S}$	SRI
$\text{Xe}(^1\text{P}_1) + \text{Cl}_2 \rightarrow \text{XeCl}^*$	$7.6 \pm 0.7 \times 10^{-10} \text{ CM}^3/\text{S}$	SRI
$\text{Xe}(5d3/2) + \text{HCl} \rightarrow \text{XeCl}^*$	$7.5 \pm 0.7 \times 10^{-10} \text{ CM}^3/\text{S}$	SRI
$\text{Cl}_2^* + \text{Xe} \rightarrow \text{XeCl}^*$	$1.1 \pm 0.1 \times 10^{-10} \text{ CM}^3/\text{S}$	SRI

### Xe QUENCHING

$\text{Xe}(5d3/2) + \text{Xe} \rightarrow \text{Xe}^* + \text{Xe}$	$8.1 \pm 0.8 \times 10^{-12} \text{CM}^3/\text{S}$	SRI
$\text{Xe}(^3\text{P}_2) + \text{HCl} \rightarrow \text{PRODUCTS}$	$5.6 \times 10^{-10} \text{CM}^3/\text{S}$	KSU
$\text{Xe}(^1\text{P}_1) + \text{HCl} \rightarrow \text{PRODUCTS}$	$(7 \times 10^{-10} \text{CM}^3/\text{S})$	SRI
$\text{Xe}_2^* + \text{HCl} \rightarrow \text{PRODUCTS}$	$8.2 \pm 0.8 \times 10^{-10} \text{CM}^3/\text{S}$	SRI
$\text{Xe}_2^* + \text{Cl}_2 \rightarrow \text{PRODUCTS}$	$5.0 \pm 0.6 \times 10^{-10} \text{CM}^3/\text{S}$	SRI

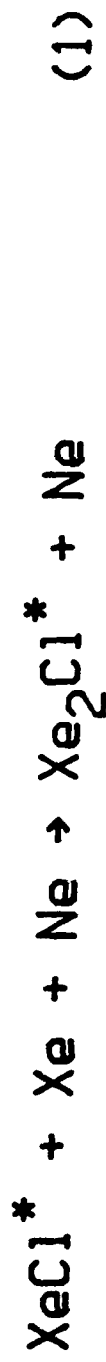
## **Xe<sub>2</sub>Cl<sup>+</sup> RADIATION & QUENCHING**

<b>Xe<sub>2</sub>Cl<sup>+</sup> → hv (470nm)</b>	<b>3.8±0.4x10<sup>6</sup>/S</b>	<b>SRI</b>
	<b>7.4 x 10<sup>6</sup>/S</b>	<b>RICE</b>
<b>Xe<sub>2</sub>Cl<sup>+</sup> + Cl<sub>2</sub> → PRODUCTS</b>	<b>5.2±0.2x10<sup>-10</sup>CM<sup>3</sup>/S</b>	<b>SRI</b>
<b>Xe<sub>2</sub>Cl<sup>+</sup> + HCl → PRODUCTS</b>	<b>6.1±0.2x10<sup>-10</sup>CM<sup>3</sup>/S</b>	<b>SRI</b>
<b>Xe<sub>2</sub>Cl<sup>+</sup> + Xe → PRODUCTS</b>	<b>&lt; 4x10<sup>-14</sup>CM<sup>3</sup>/S</b>	<b>SRI</b>

## RADIATION AND QUENCHING

$\text{XeCl}^* (\text{B}) \rightarrow \text{hv} (308)$	$9.0 \pm 0.2 \times 10^7 / \text{s}$	KSU
$\text{XeCl}^* (\text{C}) \rightarrow \text{hv} (340)$	$7.6 \pm 0.6 \times 10^6 / \text{s}$	KSU
$\text{XeCl}^* (\text{M}) \rightarrow \text{hv}$	$5.0 \pm 0.6 \times 10^7 / \text{s}$	SRI, SAC
$\text{XeCl}^* + \text{Cl}_2 \rightarrow \text{QUENCH}$	$5.6 \pm 0.25 \times 10^{-10} \text{cm}^3 / \text{s}$	SRI
	$5.8 \times 10^{-10} \text{cm}^3 / \text{s}$	SAC
$\text{XeCl}^* + \text{HCl} \rightarrow \text{QUENCH}$	$7.3 \pm 0.1 \times 10^{-10} \text{cm}^3 / \text{s}$	SRI
$\text{XeCl}^* + \text{Xe} \rightarrow \text{QUENCH}$	$< 4 \times 10^{-12} \text{cm}^3 / \text{s}$	SRI, SAC
	$2.3 \times 10^{-11} \text{cm}^3 / \text{s}$	KSU
$\text{XeCl}^* + 2\text{Xe} \rightarrow \text{Xe}_2\text{Cl}^*$	$1.53 \pm 0.1 \times 10^{-30} \text{cm}^6 / \text{s}$	SRI
	$1.3 \times 10^{-30} \text{cm}^6 / \text{s}$	SAC
$\text{XeCl}^* + \text{Xe} + \text{Ar} \rightarrow \text{Xe}_2\text{Cl}^*$	$1.01 \pm 0.05 \times 10^{-30} \text{cm}^6 / \text{s}$	SRI

### 3-BODY REACTION



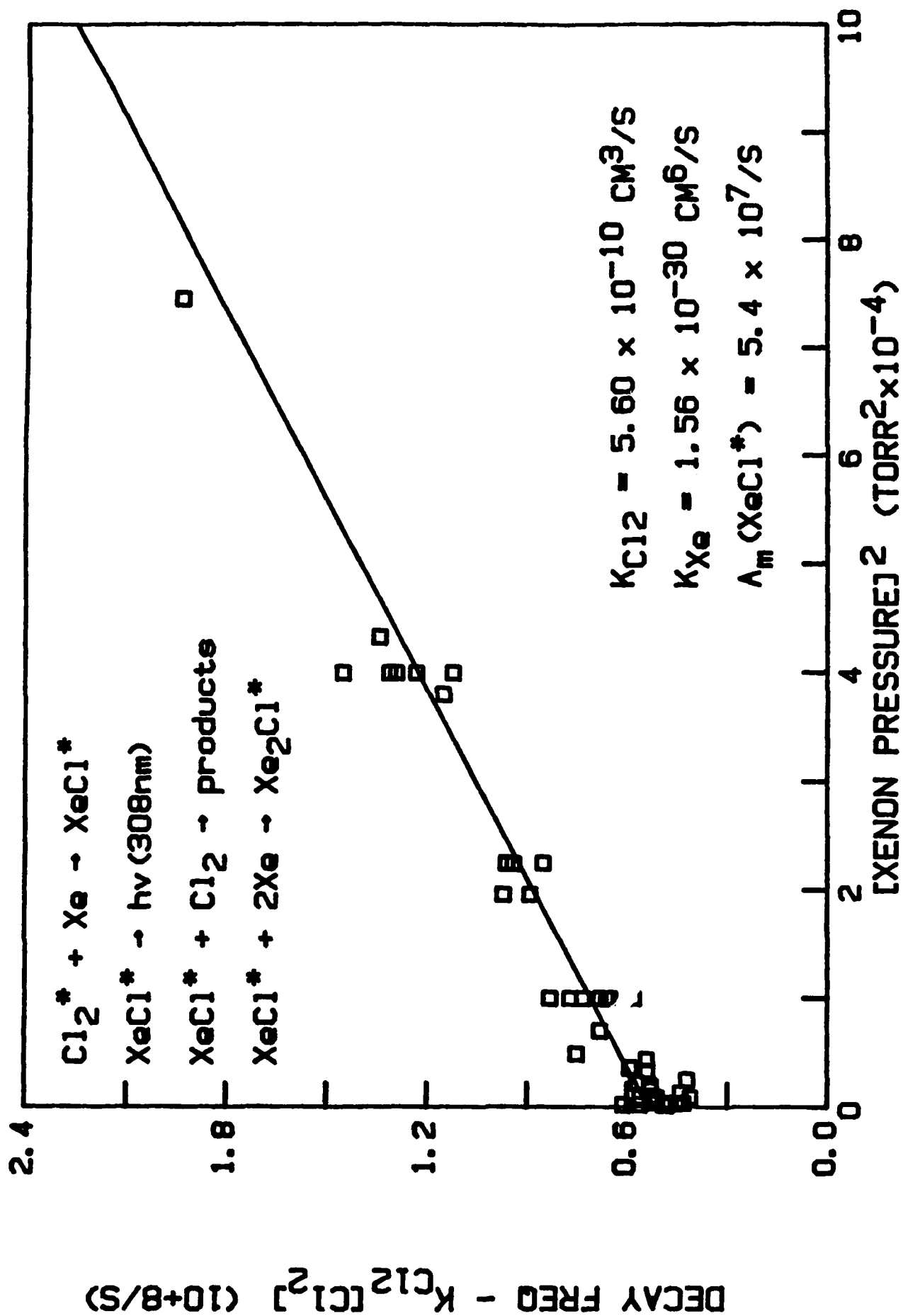
### THE LINDEMANN MECHANISM

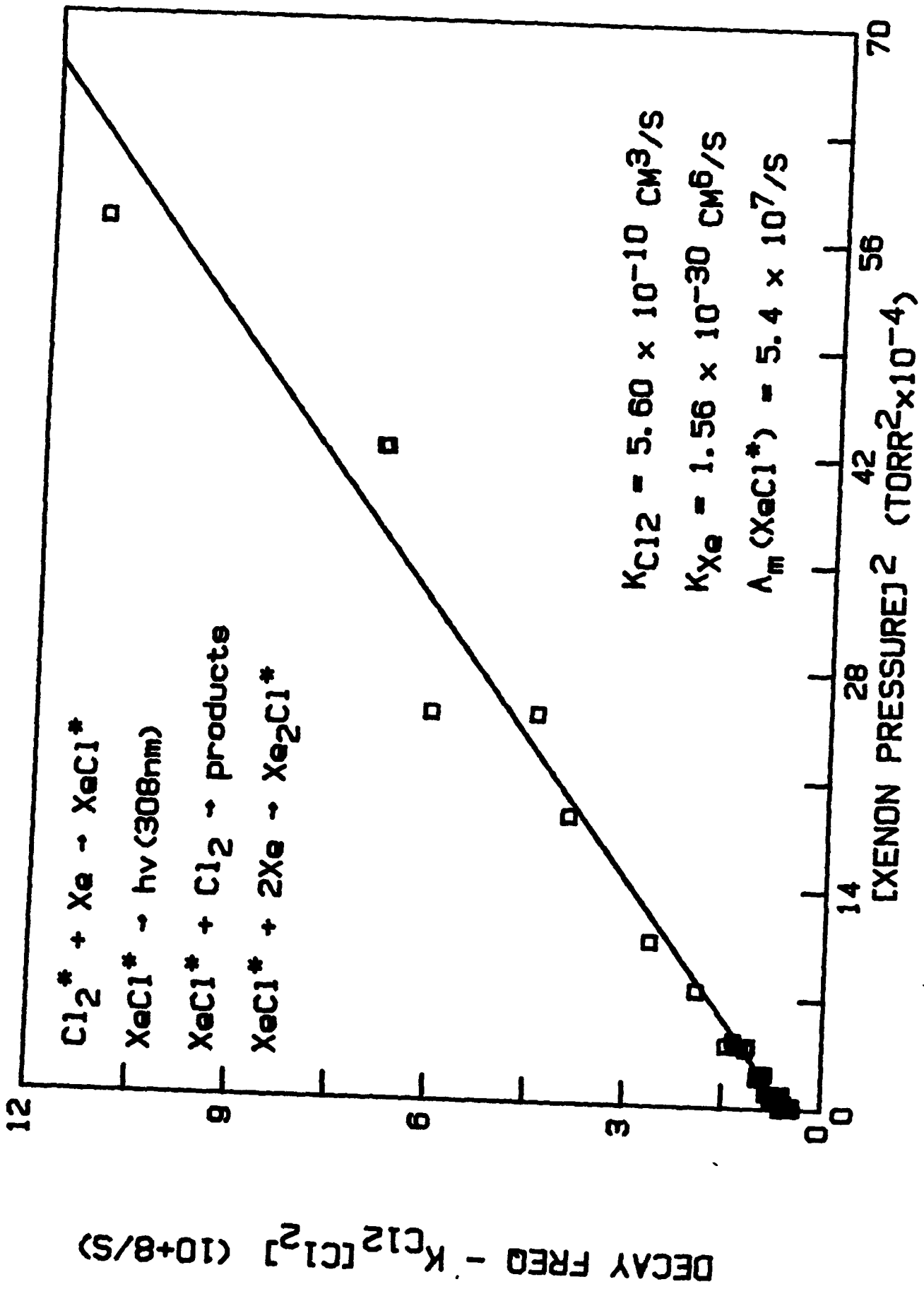


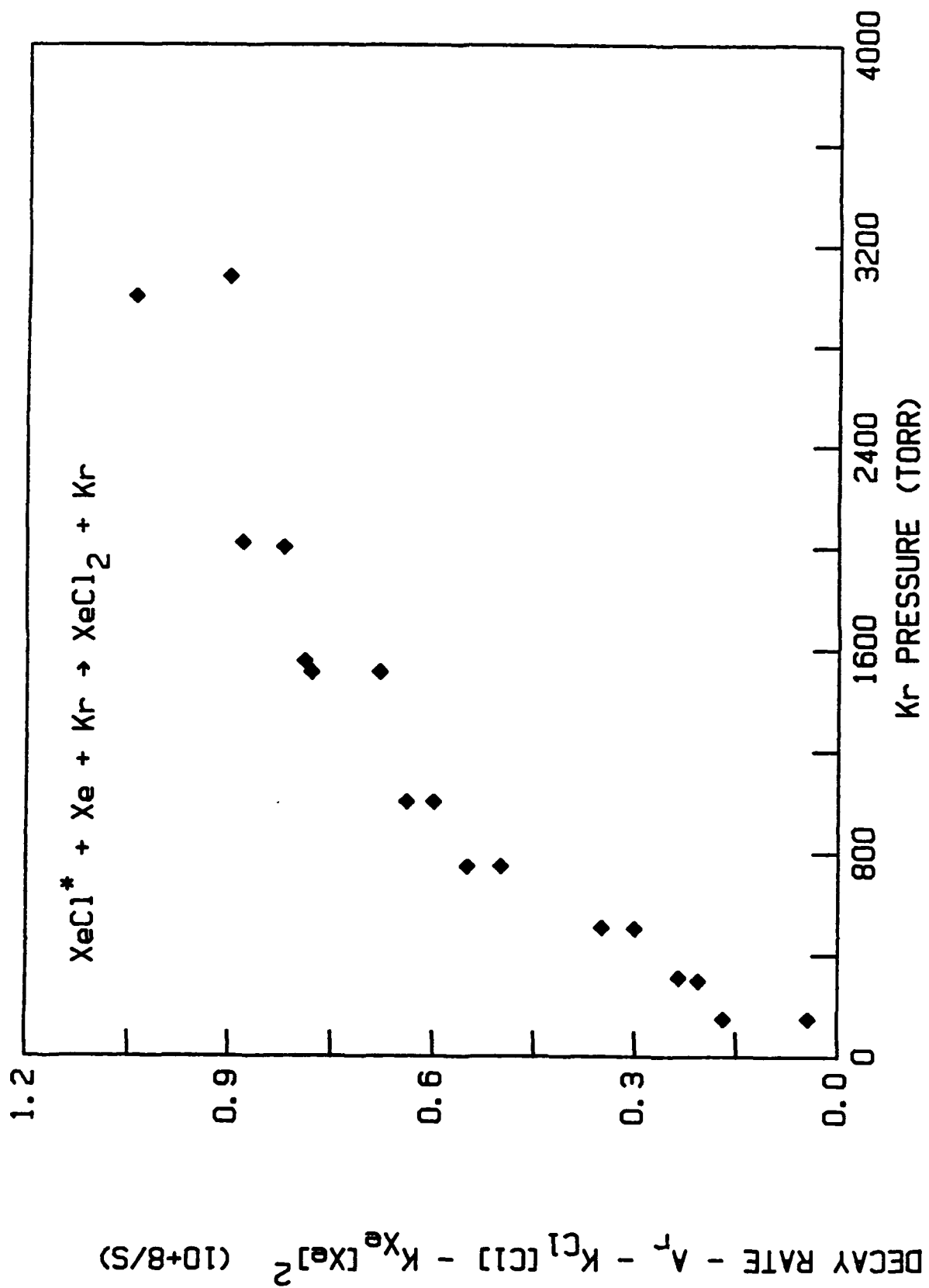
RATE OF  $\text{XeCl}^* \bullet \text{Xe}$  FORMATION =  $K_2 [\text{Xe}]$

FRACTION THAT YIELDS  $\text{Xe}_2\text{Cl}^* = K_3 [\text{Ne}] / (K_{-2} + K_3 [\text{Ne}])$

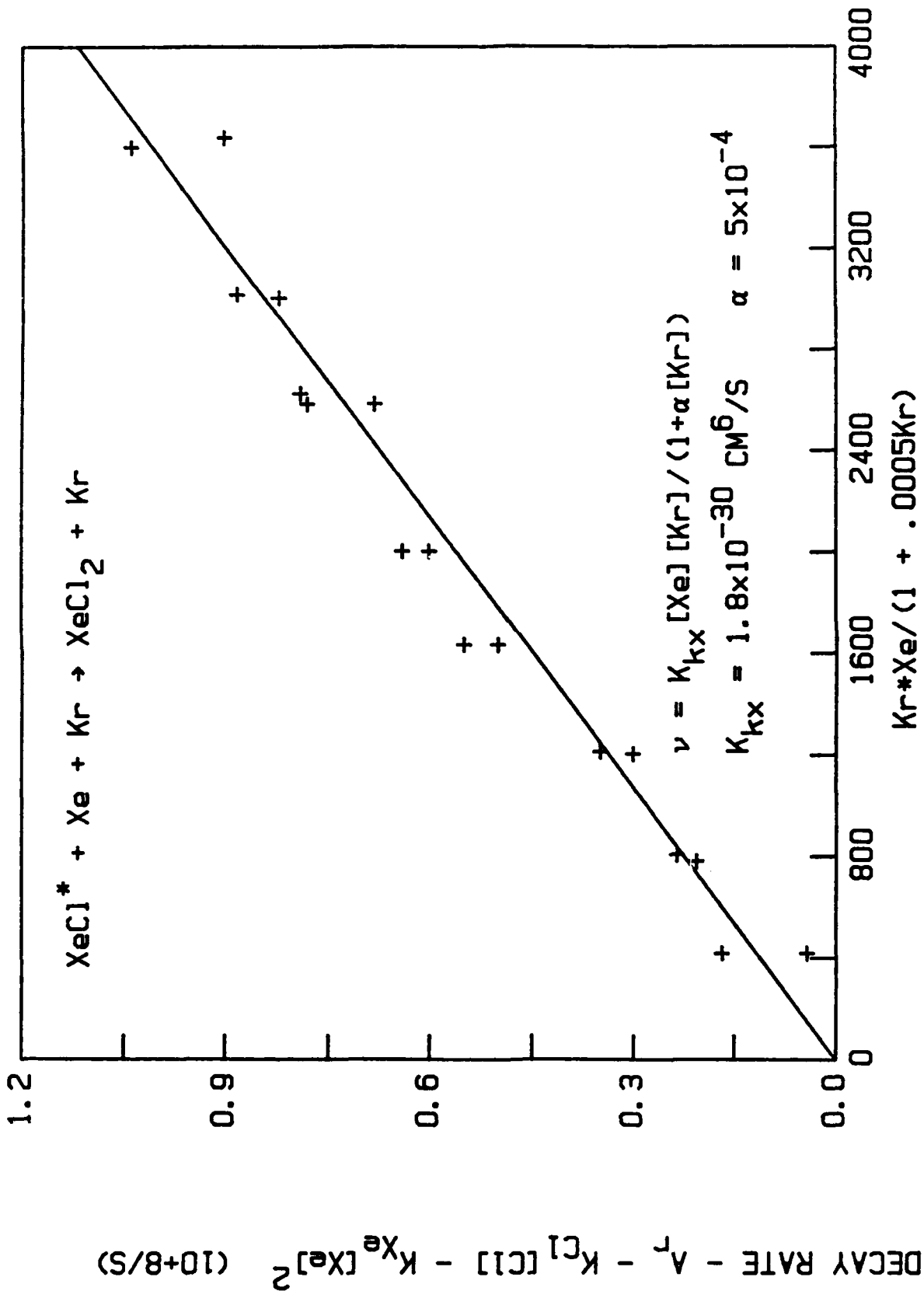
TOTAL RATE  $K_1 = K_3 K_2 [\text{Xe}] [\text{Ne}] / (K_{-2} + K_3 [\text{Ne}])$

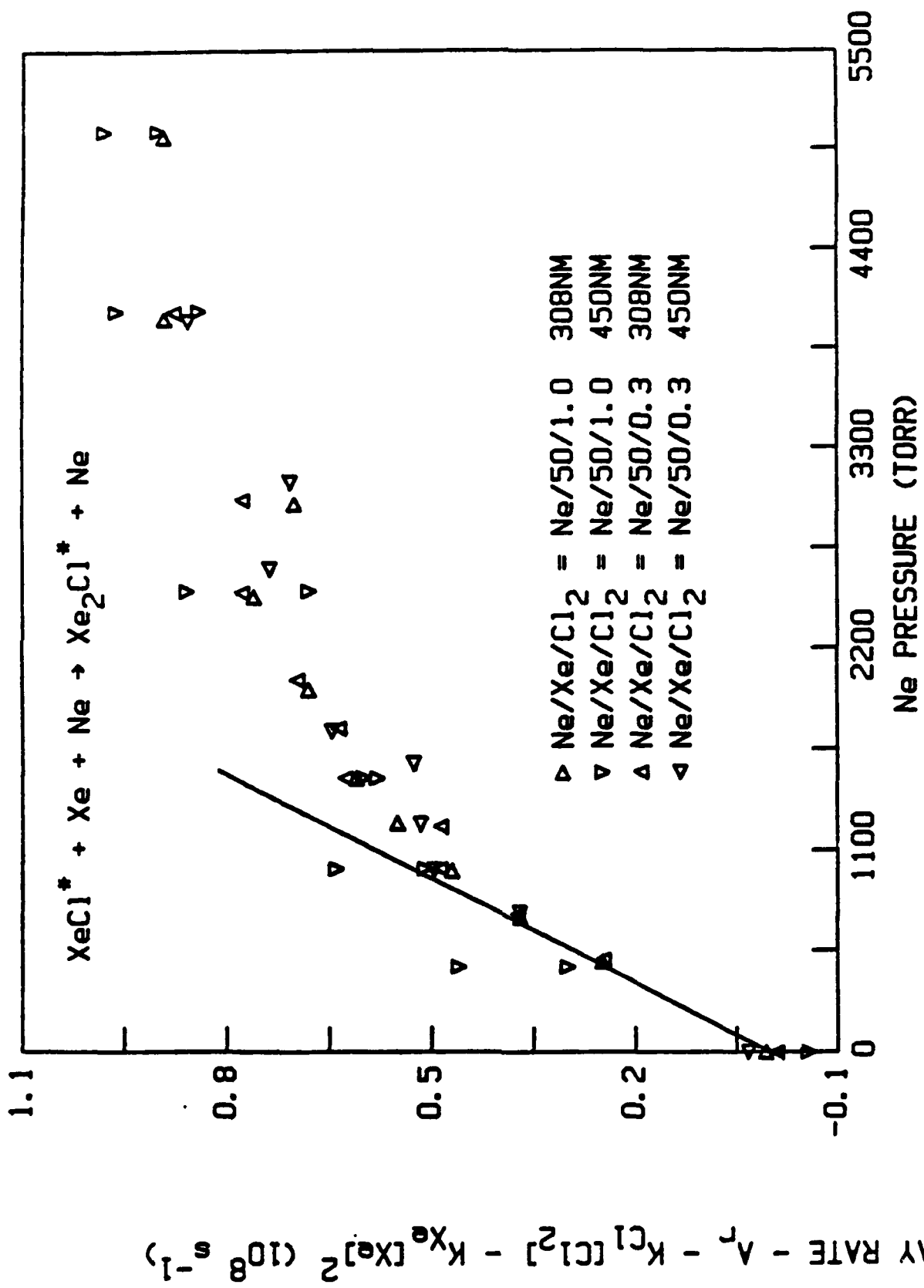




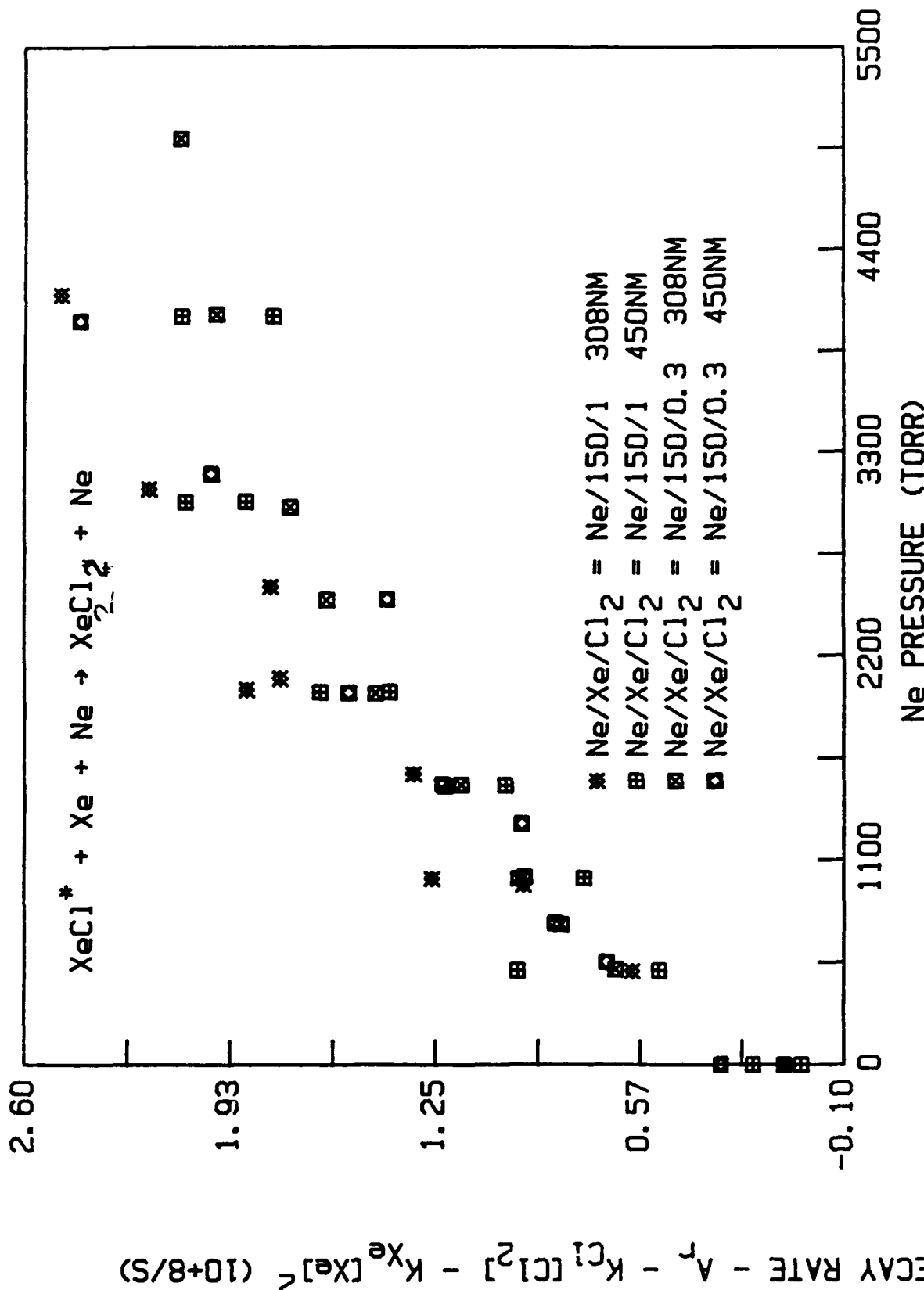


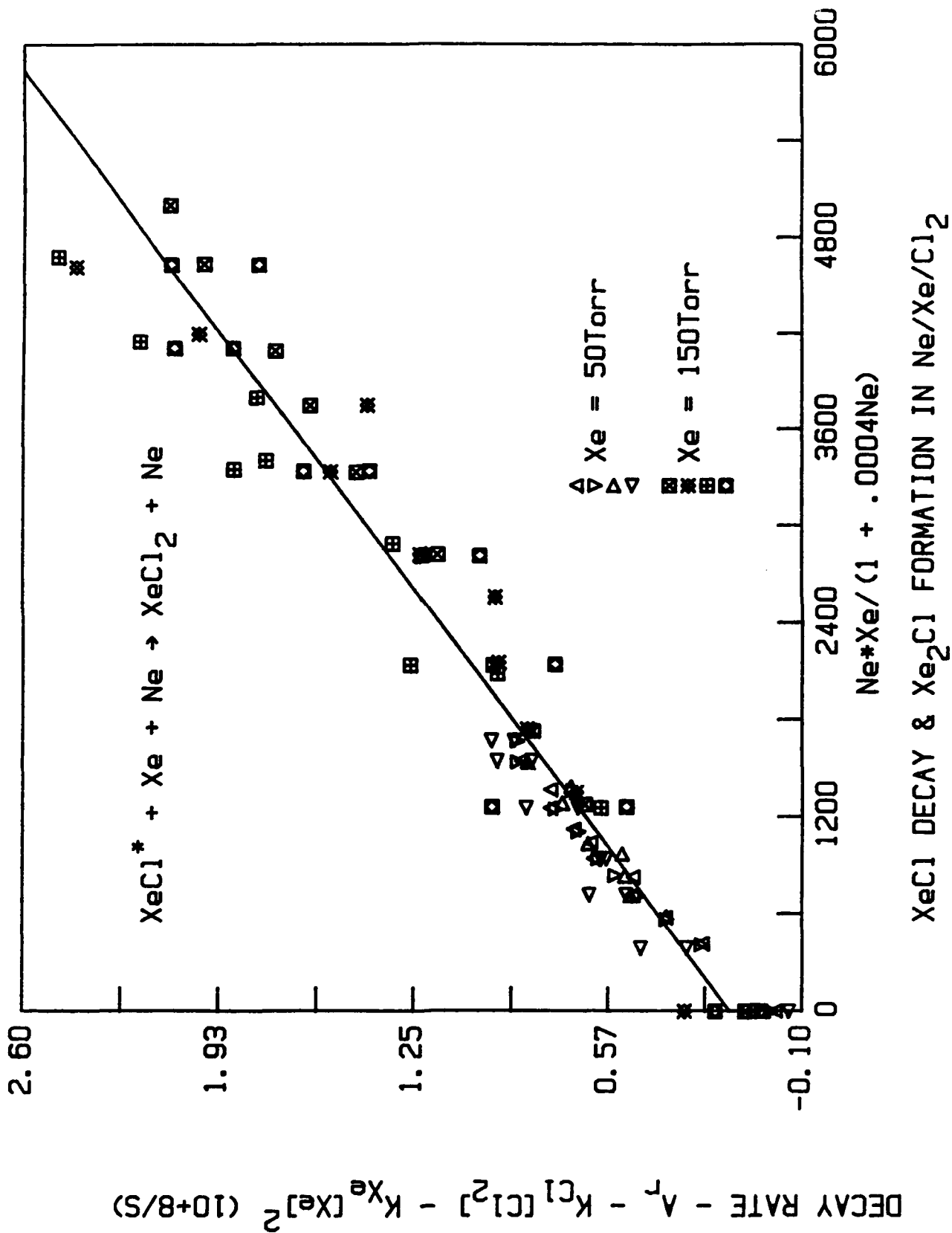
XeCl DECAY RATE In Kr/Xe/Cl<sub>2</sub> Xe = 15 Torr

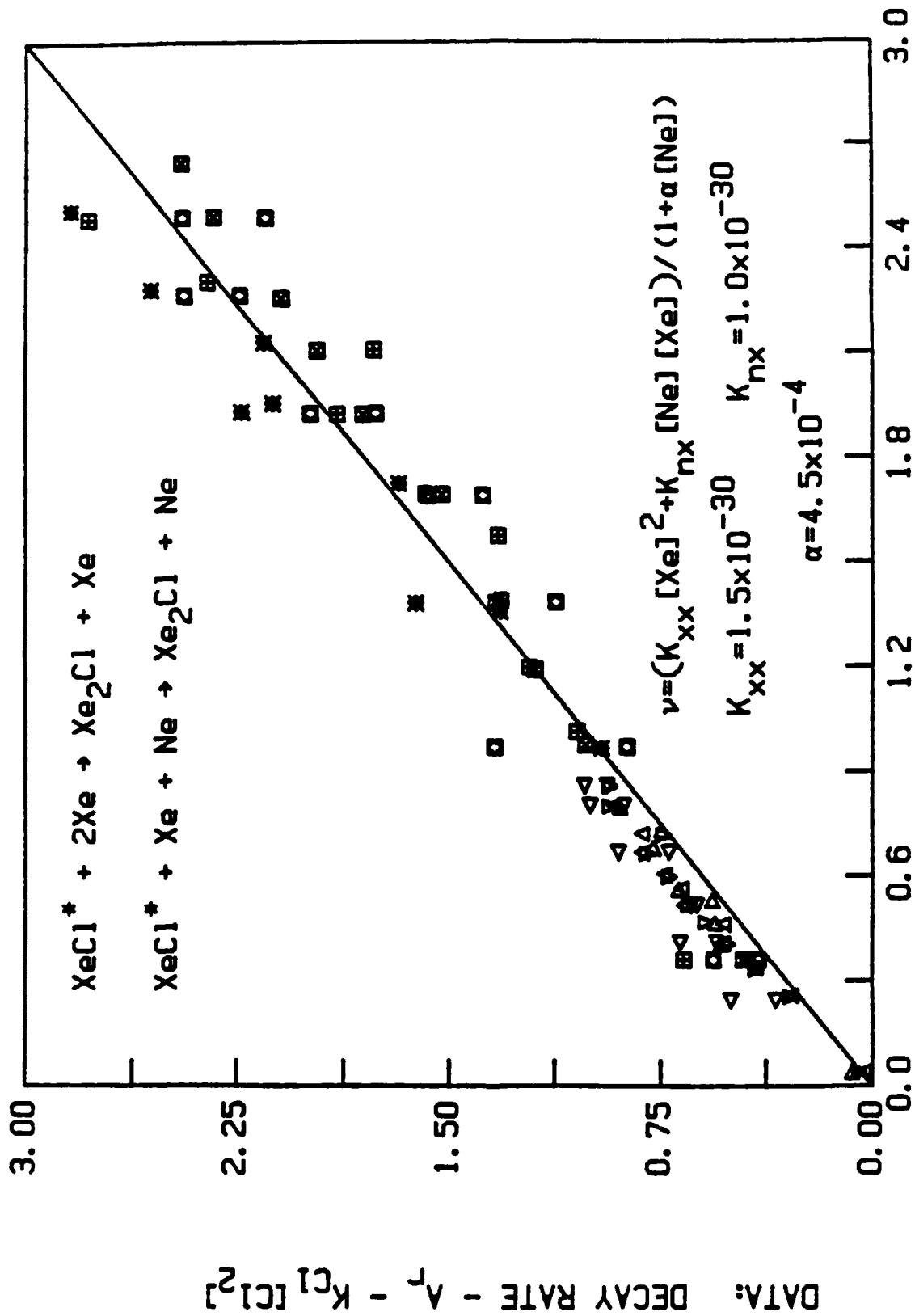




XeCl DECAY & Xe<sub>2</sub>Cl FORMATION RATE IN Ne/Xe/Cl<sub>2</sub>







$$\nu = \frac{K_{xx} [Xe]^2 + K_{nx} [Ne] [Xe]}{1 + \alpha [Ne]}$$

$$K_{xx} = 1.5 \times 10^{-30} \quad K_{nx} = 1.0 \times 10^{-30}$$

$$\alpha = 4.5 \times 10^{-4}$$

**Appendix E**

**CURRENT UNDERSTANDING OF THE XeCl LASER**

39nd Annual Gaseous Electronics Conference  
7-10 October 1986, Madison, WI

[Bull. Am. Phys. Soc.32, 1174 (1987)]

**CURRENT UNDERSTANDING OF THE XeCl LASER**

**David L. Huestis  
Chemical Physics Laboratory  
SRI International  
Menlo Park, CA 94025**

**DECEMBER 1985 WORKSHOP AT SRI**

**HISTORY**

**FUNDAMENTAL CONCEPTS**

**SPECTROSCOPY**

**ENERGY DEPOSITION**

**EXCITED STATE FORMATION**

**EXCITED STATE RELAXATION**

**ABSORPTION AND EXTRACTION**

**SUMMARY**

**WORKSHOP ON XeCl KINETICS  
19 December 1985 at SRI**

**Agenda**

- |      |   |
|------|---|
| 0815 | Introduction (Behringer & Huestis)                              |
| 0830 | Review of Laser Development and Performance (Tang)              |
| 0900 | XeCl Laser Modeling (Genoni & Palumbo)                          |
| 0930 | Electron Beams and Energy Deposition (Ewing/Moody & McAllister) |
| 1000 | Coffee  |
| 1030 | Excited State Production (Huestis & Long)                       |
| 1100 | Quenching and Relaxation (Lorents & Setser)                     |
| 1130 | Absorption and Extraction (Moody & Eden)                        |
| 1200 | Lunch   |
| 1230 | Panels  |
| 1530 | Summary of Conclusions of Panels                                |
| 1700 | Adjourn   |

## HISTORY OF THE XeCl LASER

Spectrum Observed: 1975 Velazco and Setser,

*J. Chem. Phys.* 62, 1990

E-beam Laser: 1975 Ewing and Brau,

*Appl. Phys. Lett.* 27, 350

Discharge Laser: 1977 Ishchenko et al.

*Optics Commun.* 21, 30

XeCl has received less attention than

KrF (more efficient) or XeF (longer wavelength)

XeCl is favored by long life of

Ne/Xe/HCl gas fill

## FUNDAMENTAL CONCEPTS

Spectroscopy

Choice of Excitation Technique

Electron-Beam or Discharge

Choice of Gas Mixture

First Ar/Xe/Cl<sub>2</sub> now Ne/Xe/HCl

Evaluation of Laser Performance

$$\eta_{\text{laser}} = \frac{h\nu}{(\text{quantum cost})} \bullet \eta_{\text{kinetic}} \bullet \eta_{\text{extract}}$$

Understanding and Modeling

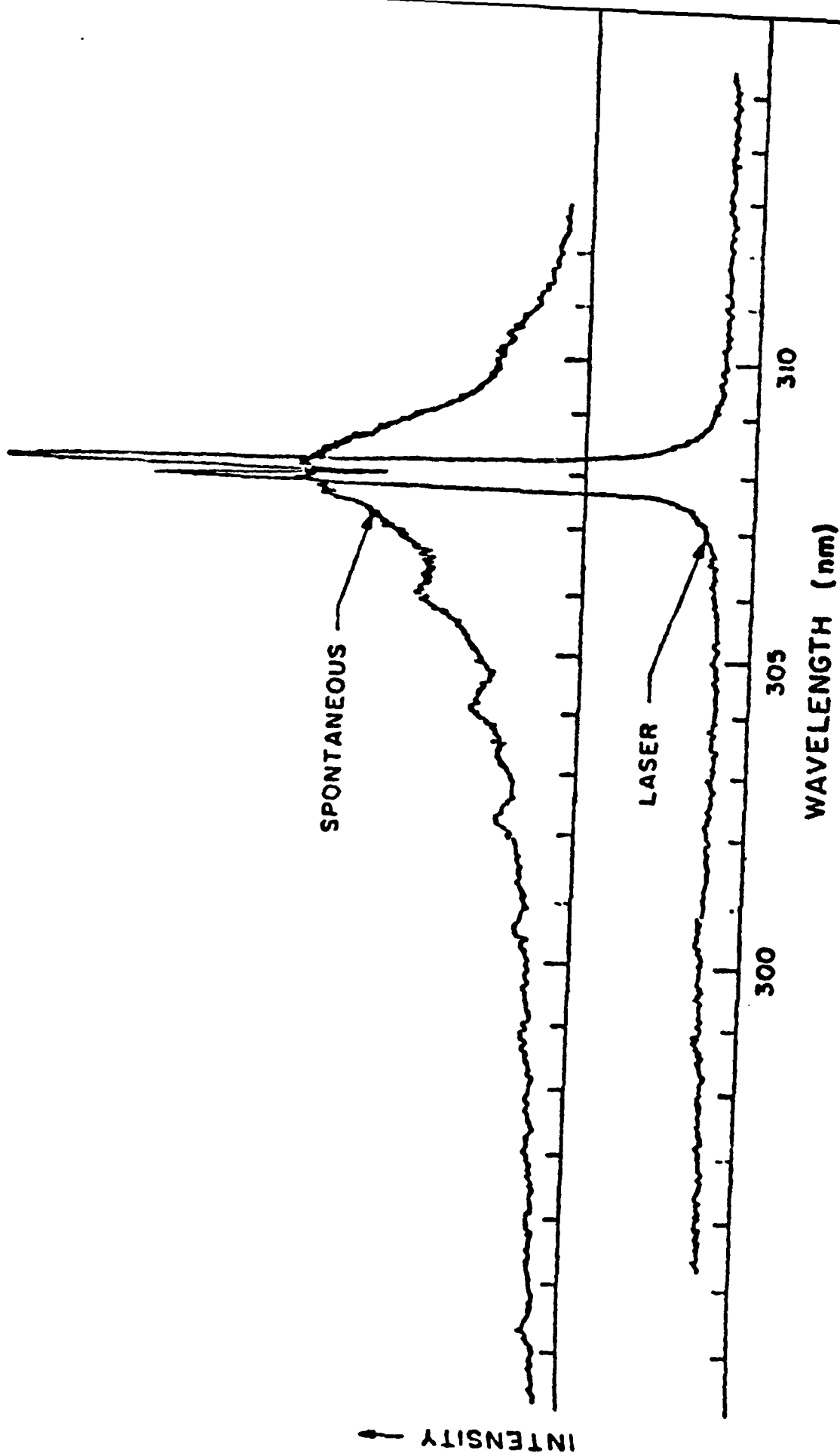
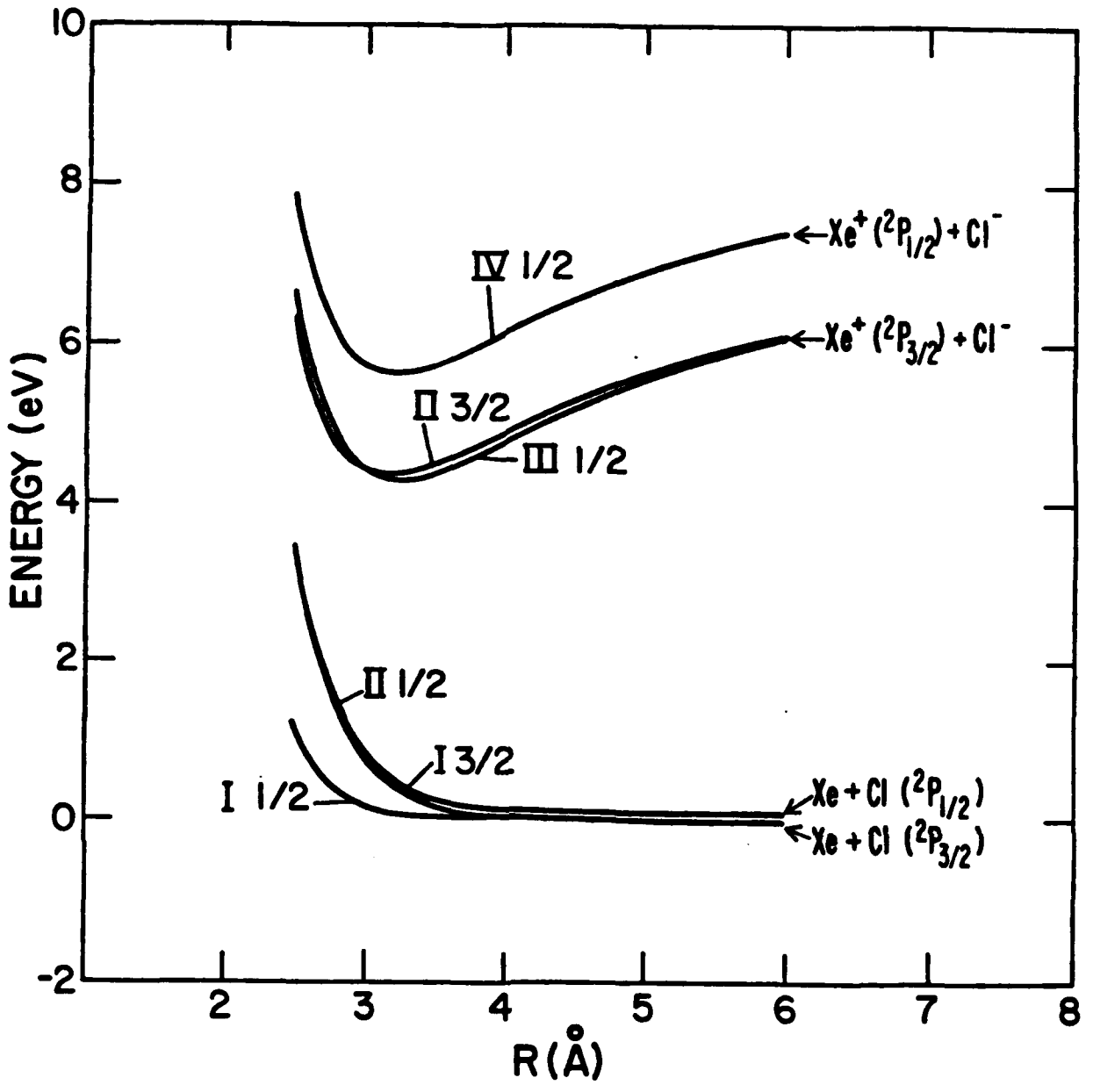


FIG. 2. Comparison of spontaneous and laser emission spectra from XeCl.



Graphical Data. A-1.10. Electronic states of XeCl including spin-orbit coupling.

## SUMMARY OF XeCl SPECTROSCOPY

General Features Understood

Upper and Lower States are Bound

Vibrational Levels Known

No Rotationally-Resolved Spectra

Location of the C(3/2) State is Uncertain

0 to 200  $\text{cm}^{-1}$  Below B(1/2)

Need to Understand Free-Bound Absorption

$\text{Xe} + \text{Cl} + h\nu \rightarrow \text{XeCl}$

## ENERGY DEPOSITION IN Ne/Xe/HCl

e (primary) + Ne  $\rightarrow$  Ne<sup>+</sup> + 2e (hot secondaries)

e (hot secondary) + Ne  $\rightarrow$  Ne\* + e (warm secondary)

e (warm secondary) Xe  $\rightarrow$  Xe<sup>+</sup> + 2e (cool secondaries)

$\rightarrow$  Xe\* + e (cool secondary)

27 eV  $\rightarrow$  0.77 Ne<sup>+</sup> + 0.23 Ne\* + 0.27 Xe<sup>+</sup> + 0.19 Xe\*

$\sim$  1.46 primary excitations

One precursor costs 18.5 eV instead of the expected 27 eV

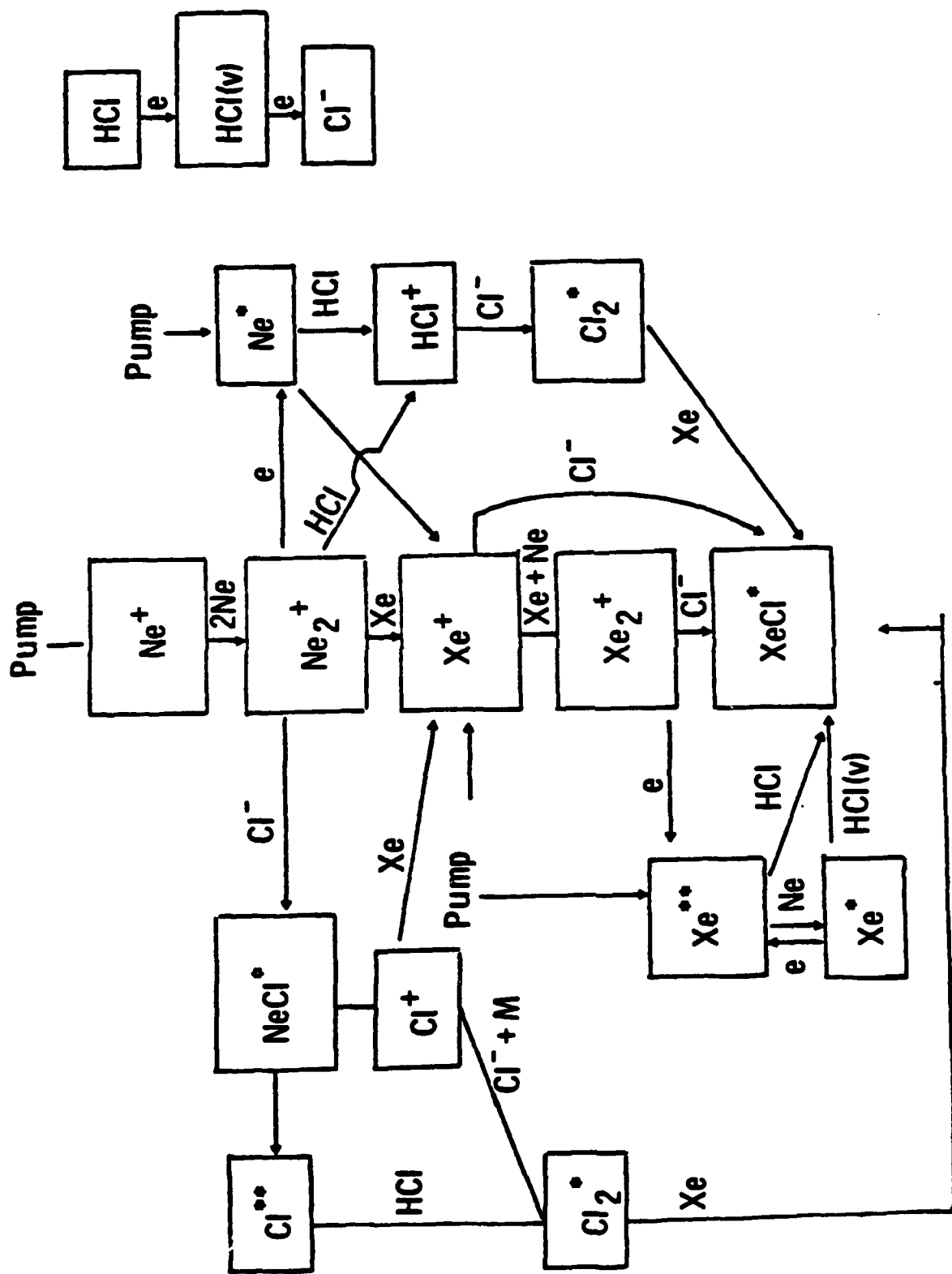


FIGURE 2 ENERGY FLOW PATHWAYS IN E-BEAM PUMPED Ne/Xe/HCl MIXTURES

## OBSERVED XeCl\* PRODUCTION YIELDS

Two experiments find high yields:

Finn et al Appl. Phys. Lett. 36, 789 (1980).

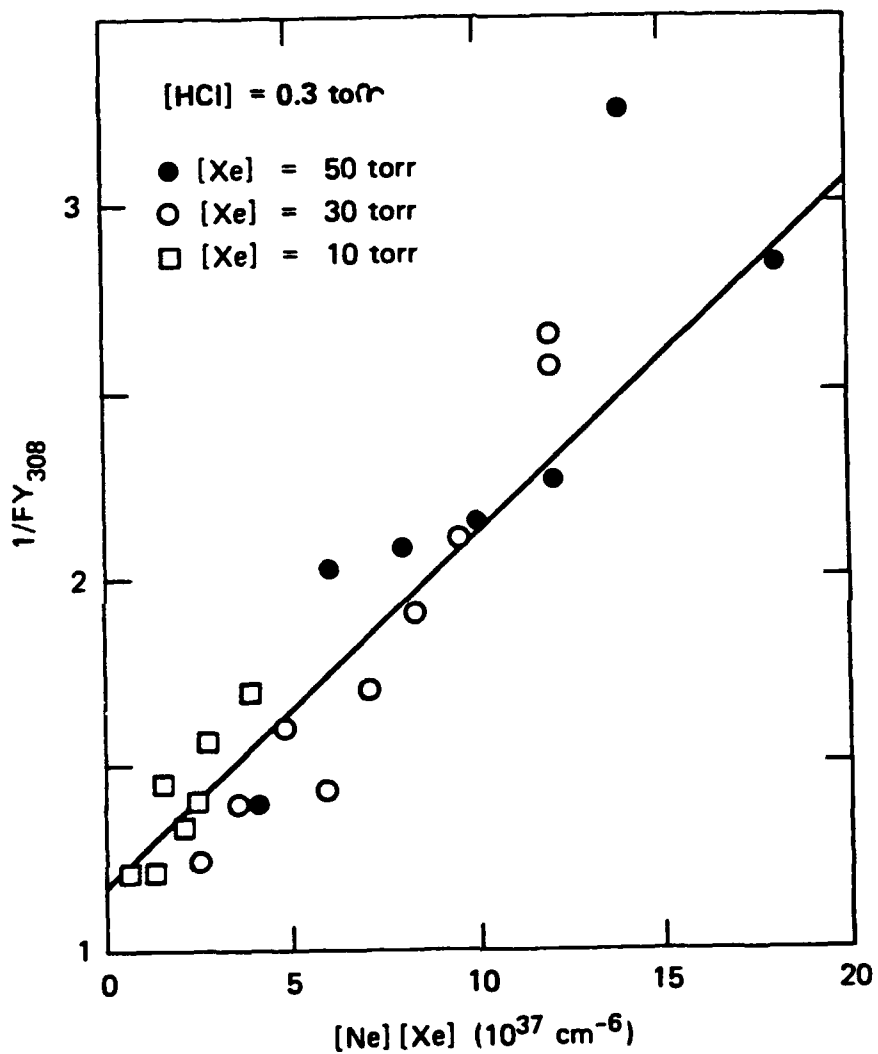
Tang et al unpublished (1981).

-----  
Yield<sup>a</sup>      Efficiency

Finn: XeCl (B) + XeCl (C)      0.8      17 %

Tang: XeCl (B)      1.0      22 %

-----  
<sup>a</sup> based on 18.5 eV per precursor



JA-1522-47

FIGURE 1 THREE BODY QUENCHING OF  $XeCl^*$

REACTIONS WITH EXCITED Xe WITH HCl

State -----  
Yield of XeCl\*

6s 0.02

6s' 0.05

6p 0.4 to 0.8

5d 0.3 to 0.7

7s 0.7

All states react rapidly:  $5-8 \times 10^{-10} \text{ cm}^3 \text{ s}^{-1}$

Based on work by Setser et al at KSU and Lorents et al at SRI

## FORMATION OF XeCl<sup>\*</sup>

**Problem:** Explain high yield of XeCl<sup>\*</sup> inspite of

$\text{Xe}^* + \text{HCl}(v=0) \text{ does not produce XeCl}^*$

$e + \text{HCl}(v=0) \rightarrow \text{H} + \text{Cl}^- \text{ is very slow}$

**Presumed Solution:** Electron excitation

$e + \text{HCl}(v=0) \rightarrow \text{HCl}(v>0) + e$

$e + \text{Xe}^* \rightarrow \text{Xe}^{**} + e$

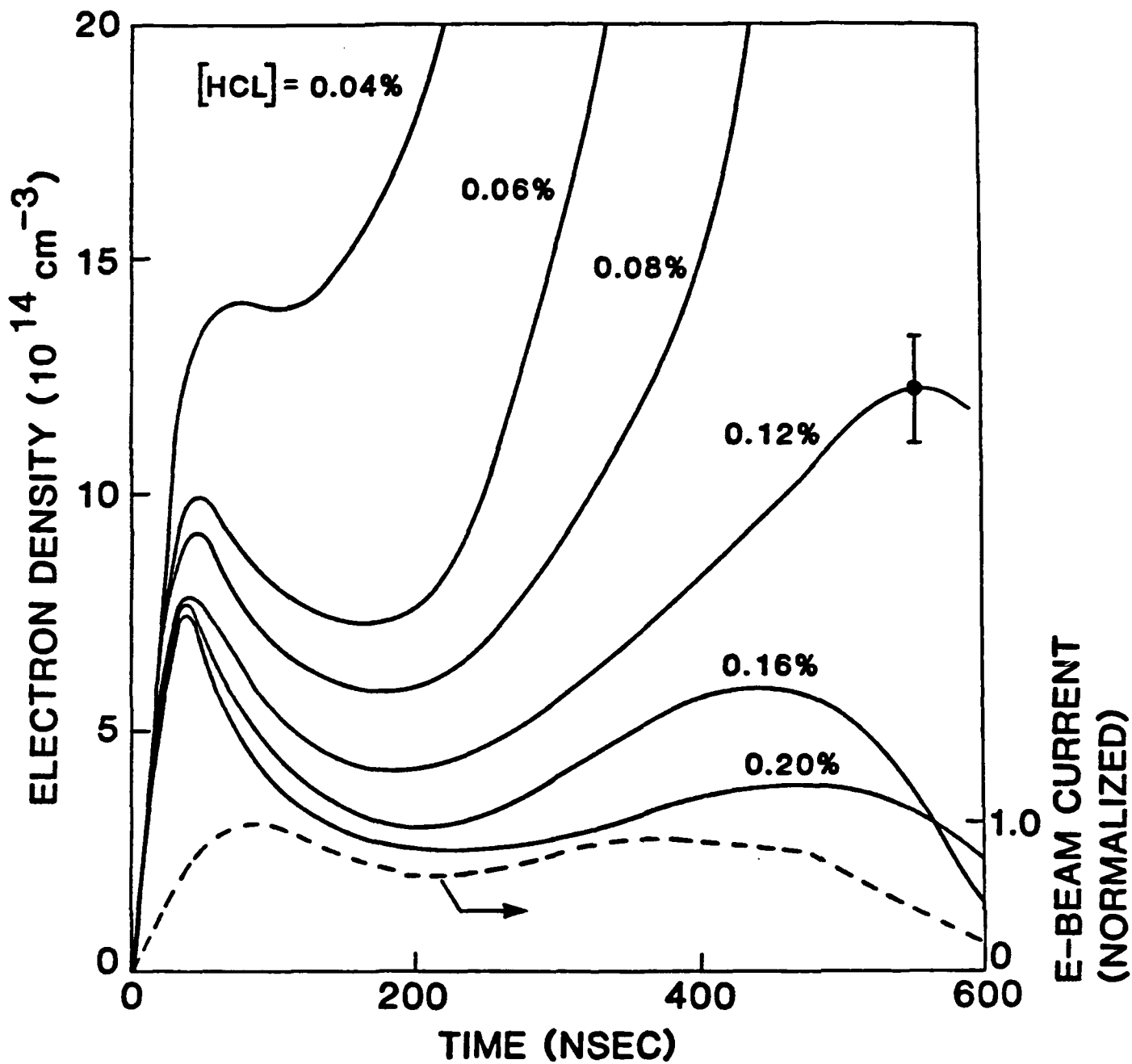
$e + \text{HCl}(v>0) \rightarrow \text{H} + \text{Cl}^-$

$\text{Xe}^{**} + \text{HCl} \rightarrow \text{XeCl}^* + \text{H}$

**Residual Problems:**

$\text{HCl}(v>0)$  density is observed to be low

$\text{Xe}^{**}$  density is also apparently low



Electron Density in E-Beam Pumped Ne/Xe/HCL  
 from Kimura et al, Spectra Technology, Inc.

## SUMMARY OF ENERGY DEPOSITION AND EXCITED STATE FORMATION

"We definitely know that we do not know how  $\text{XeCl}^*$  is formed"

The kinetic efficiency is so high that both neutral and ionic pathways must be participating effectively, in spite of apparently slow, low yield, and endothermic reactions.

We may be missing something fundamental.

How can "minor" channels,  $\text{Xe}^{**}$ , or "missing" species,  $\text{HCl}(v=1)$ , be the major precursors?

## RELAXATION PROCESSES

Quite a bit of good data exists

Major Unknowns are

Location of C State, B/C Mixing Details

Vibrational Relaxation of XeCl(B)

Understanding Two- and Three-Body Quenching

Quenching and Mixing of Xe<sup>\*</sup>, Xe<sup>\*\*</sup>, Xe<sup>\*\*\*</sup>

Serious Need for Data on Electron Collisions

## XeCl RADIATIVE RATES

$\text{XeCl}^*(\text{B}) \rightarrow h\nu(308)$	$8.9 \pm 0.2 \times 10^7 / \text{s}$	KSU
	$9.1 \times 10^7$	Theory
$\text{XeCl}^*(\text{C}) \rightarrow h\nu(340)$	$7.6 \pm 0.6 \times 10^6 / \text{s}$	KSU
	$8.3 \times 10^6$	Theory
$\text{XeCl}^*(\text{M}) \rightarrow h\nu$	$5.0 \pm 0.6 \times 10^7 / \text{s}$	SRI
	$5.1 \times 10^7 / \text{s}$	Saclay

B/C MIXING      XeCl (B) ↔ XeCl (C)



$$K_e = K_B/K_C = 1.5$$



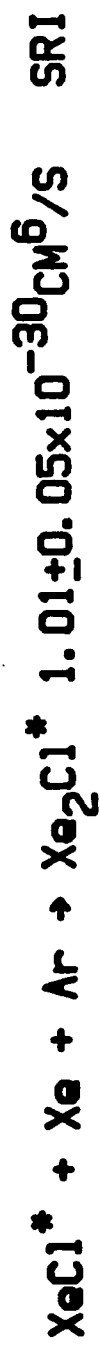
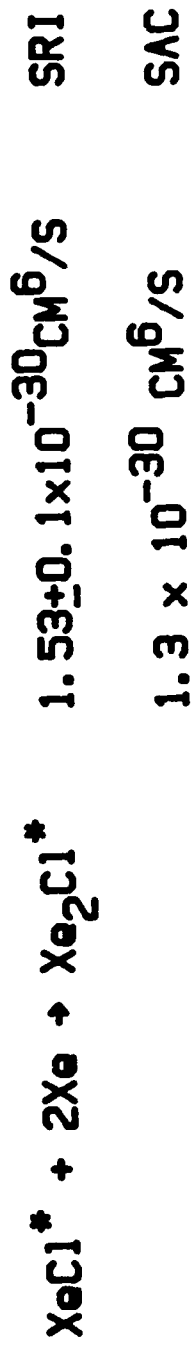
$$\Lambda_M = (\Lambda_B K_e + \Lambda_C) / (K_e + 1)$$

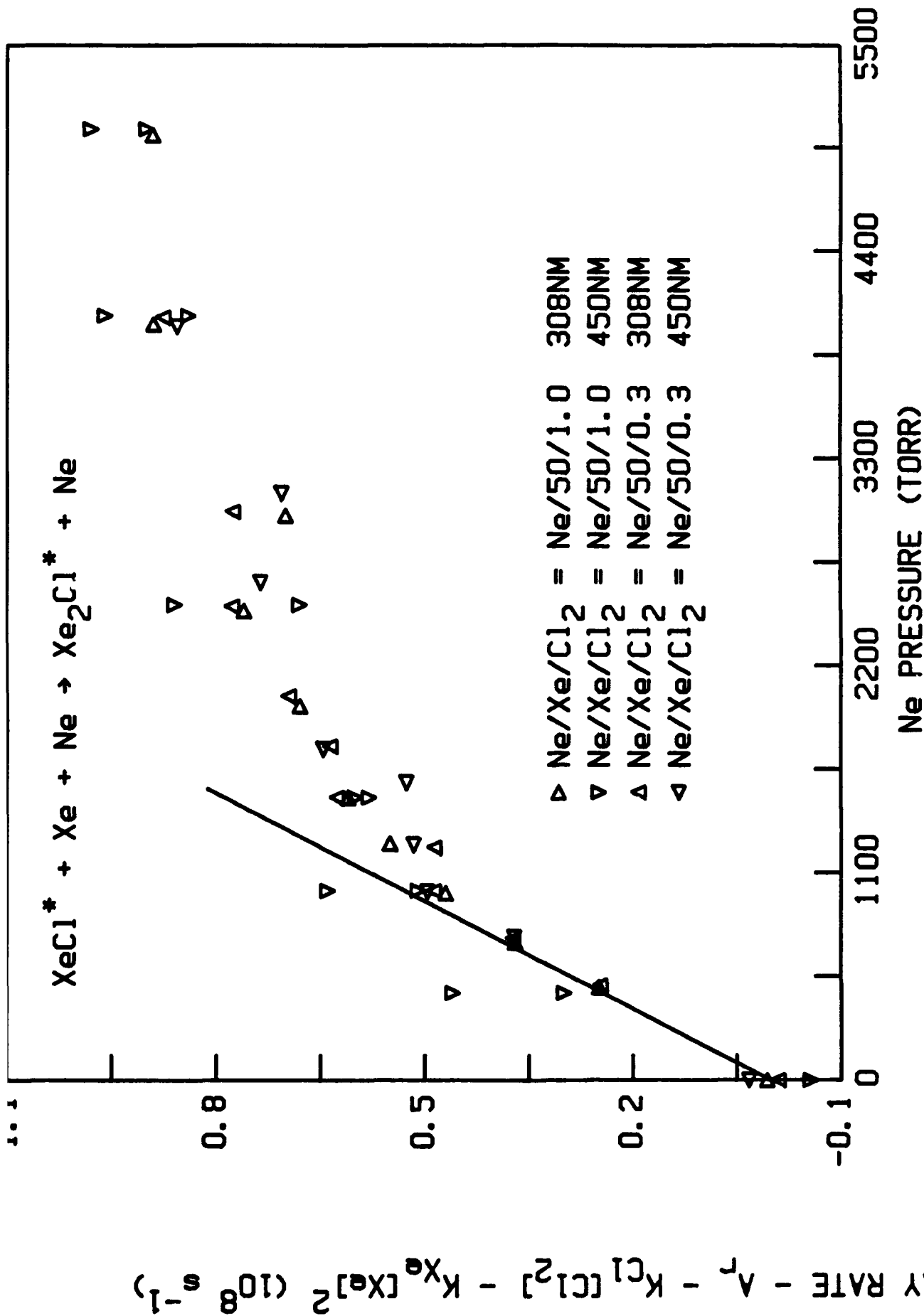
$$K_e = 1.0 \pm 0.1$$

## XeCl QUENCHING

$\text{XeCl}^* + \text{Cl}_2 \rightarrow \text{QUENCH}$	$5.6 \pm 0.25 \times 10^{-10} \text{ CM}^3/\text{S}$	SRI
	$5.8 \times 10^{-10}$	SAC
	$4.3 \times 10^{-10}$	KSU
$\text{XeCl}^* + \text{HCl} \rightarrow \text{QUENCH}$	$7.3 \pm 0.1 \times 10^{-10} \text{ CM}^3/\text{S}$	SRI
	$6.3 \times 10^{-10}$	KSU
$\text{XeCl}^* + \text{Xe} \rightarrow \text{QUENCH}$	$< 4 \times 10^{-12} \text{ CM}^3/\text{S}$	SRI
	$4 \times 10^{-12}$	Saclay
	$2.3 \times 10^{-11}$	KSU

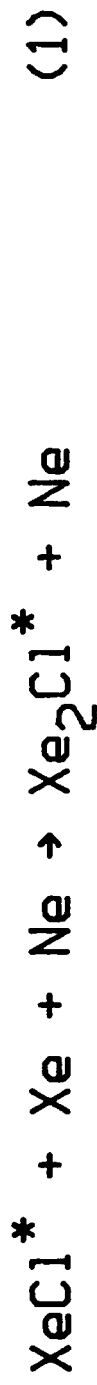
THREE BODY QUENCHING



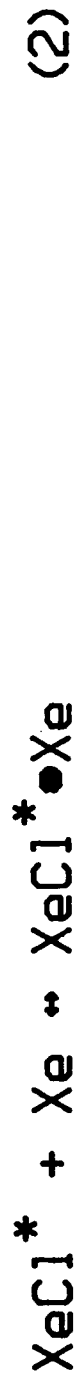


XeCl DECAY & Xe<sub>2</sub>Cl FORMATION RATE IN Ne/Xe/Cl<sub>2</sub>

### 3-BODY REACTION



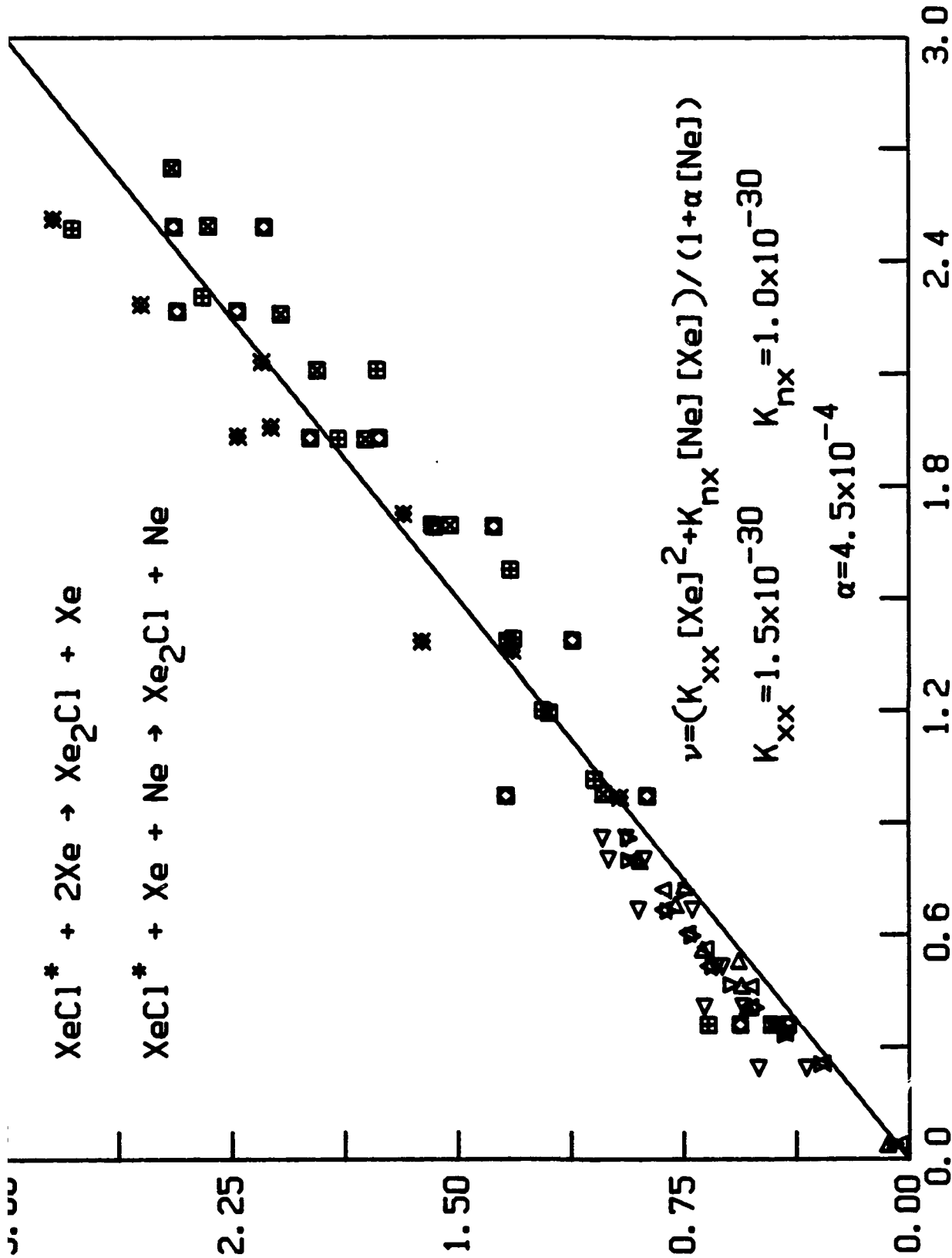
### THE LINDEMANN MECHANISM



RATE OF  $\text{XeCl}^* \bullet \text{Xe}$  FORMATION =  $K_2 [\text{Xe}]$

FRACTION THAT YIELDS  $\text{Xe}_2\text{Cl}^* = K_3 [\text{Ne}] / (K_{-2} + K_3 [\text{Ne}])$

TOTAL RATE  $K_1 = K_3 K_2 [\text{Xe}] [\text{Ne}] / (K_{-2} + K_3 [\text{Ne}])$



$$\nu = (K_{xx} [\text{Xe}]^2 + K_{nx} [\text{Ne}] [\text{Xe}]) / (1 + \alpha [\text{Ne}])$$

$$K_{xx} = 1.5 \times 10^{-30} \quad K_{nx} = 1.0 \times 10^{-30}$$

$$\alpha = 4.5 \times 10^{-4}$$

DATA: DECAY RATE -  $\nu_r - k_{Cl} [\text{Cl}]^2$

XeCl DECAY & Xe<sub>2</sub>Cl FORMATION IN Ne/Xe/Cl<sub>2</sub>

## ABSORPTION AND EXTRACTION

All Electron-Excited Rare-Gas/Halogen-Donor Mixtures Absorb Strongly at All Wavelengths Investigated

This is the Single Most Important Reduction in Laser Efficiency (~ 50%)

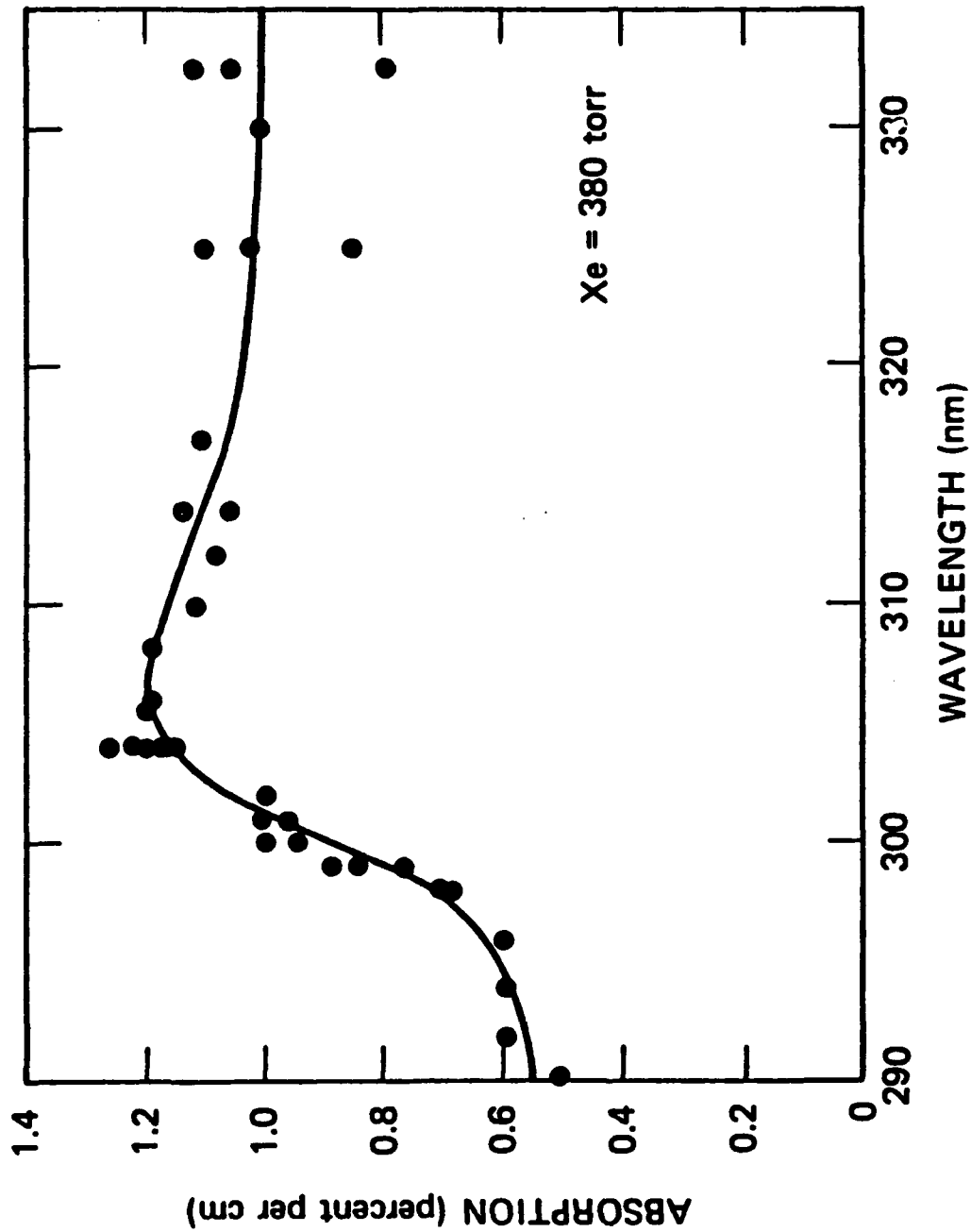
Many Species are Candidate Absorbers,  
we Know the Cross Sections for Some of them  
we have only Model Estimates of Densities

# TYPICAL XeCl ABSORPTION PREDICTIONS

---

<u>Specie</u>	<u>Absorption (%/cm)</u>
Cl <sup>-</sup>	0.14
Ne <sup>+</sup> <sub>2</sub>	0.05
Xe <sup>+</sup> <sub>2</sub>	0.03
Xe <sup>*</sup> <sub>2</sub>	0.03
Others	<u>0.01</u>
	0.26

- Assumes Fast HCl Attachment via HCl(v=1)
- No Significant Unexcited Absorbers
- Typical Gain/Loss Ratio is 12-15 at 150 kW/cc pump



JA-1522-59

FIGURE 9 PEAK AFTER-PULSE ABSORPTION SPECTRUM OF e-BEAM EXCITED XENON

# XeCI SELF-TERMINATION

---

- Evidence for Reduced Laser Efficiency at Large Input Energy/Time
  - STI (published 1981)
  - AVCO (Lasers '85)
  - Northrop (Bill Long, private communication)
- Two Possible Causes:
  - Reduced Formation Efficiency (Halogen Burnup?)
  - Increased Background Absorption
- Not Adequately Described by Existing Physics/Models

# CANDIDATE CUMULATIVE ABSORBERS

---

- **Driver Must Be:**
  - Halogen Burnup
  - Increasing Electron Density
  - Increasing Gas Temperature
  
- **Possibilities:**
  - Increasing  $\text{Cl}^-$  Density
  - Associative Absorption of  $\text{Xe}+\text{Cl}$  and/or  $\text{XeCl}(\text{X})$

# CONCLUSIONS

---

- Absorbers at Short Times Appear to be Adequately Modeled
- Temporal Evolution of Absorbers Not Understood
- Direct or Indirect Determination of Cl and Cl<sup>-</sup> Densities Indicated

## OVERALL SUMMARY

In the Absence of Knowing How Well the XeCl Laser Works, What We Know About its Kinetics Would Have Made Us Pessimistic.

We can Twist the Models into Predicting What We Have Already Observed, but Each New Experiment Forces Surprising Revisions.

What We Need are Not Just the Rates for Another Hundred Reactions, Or Merely Better Values for the Ones We Already Have.

Rather, We Need Diagnostic Experiments that Measure the Concentrations of the Minor Species that the Models Predict.

**Appendix F**

**NUMBER OF QUASIBOUND LEVELS BEHIND A ROTATIONAL BARRIER**

Phys. Rev. A37, 4971 (1988)

## Number of quasibound levels behind a rotational barrier

David L. Huestis

Chemical Physics Laboratory, SRI International, Menlo Park, California 94025

(Received 21 January 1988)

The number of quasibound or rotationally predissociating levels of diatomic molecules is investigated using a long-range approximation of the difference between the Jeffreys-Wentzel-Kramers-Brillouin estimates of the vibrational quantum numbers at the maximum of the rotational barrier and at the dissociation limit. It is found that for a fixed  $J$  the expected number of quasibound levels is approximately  $J/20$ , essentially independent of the magnitude and form of the potential and independent of the mass of the nuclei.

The effective interatomic potential for a rotating diatomic molecule,  $U_J(R)$ , is typically represented at large  $R$  by adding the rotational kinetic energy to a single-term multipole expansion, giving an expression of the form

$$U_J(R) \rightarrow \hbar^2 J(J+1)/2\mu R^2 - C_n/R^n. \quad (1)$$

Such a potential has a maximum value of

$$E_b \simeq [\hbar^2 J(J+1)/\mu]^{n/(n-2)} (nC_n)^{-2/(n-2)} (\frac{1}{2} - 1/n), \quad (2)$$

at

$$R_b \simeq \left[ \frac{n\mu C_n}{\hbar^2 J(J+1)} \right]^{1/(n-2)}, \quad (3)$$

derived from the condition  $U'_J(R_b) = 0$ . We are interested in estimating the number of quasibound vibrational levels that can exist behind this barrier. To do this we follow Stogryn and Hirschfelder<sup>1</sup> and Dickinson and Bernstein<sup>2</sup> and construct the Jeffreys-Wentzel-Kramers-Brillouin (JWKB) estimate for the vibrational quantum number  $v_b$  at the barrier maximum  $E = E_b$ , and compare it with the vibrational quantum number  $v_0$  at the dissociation limit  $E = 0$ . Suppose that  $R_1(E_b)$  and  $R_2(E_b) = R_b$  are the left- and right-hand turning points for  $E = E_b$ , as shown in Fig. 1(a); then,

$$v_b + \frac{1}{2} = \alpha \int_{R_1(E_b)}^{R_2(E_b)} [E_b - U_J(R)]^{1/2} dR, \quad (4)$$

where  $\alpha = \sqrt{(2\mu)/(\pi\hbar)}$ . Similarly, if  $R_1(0)$  and  $R_2(0) \simeq R_0$  are the left- and right-hand turning points for  $E = 0$ , we have

$$v_0 + \frac{1}{2} = \alpha \int_{R_1(0)}^{R_2(0)} [-U_J(R)]^{1/2} dR. \quad (5)$$

Thus

$$\begin{aligned} v_b - v_0 = & \alpha \int_{R_1(E_b)}^{R_1(0)} [E_b - U_J(R)]^{1/2} dR \\ & + \alpha \int_{R_1(0)}^{R_2(0)} \{ [E_b - U_J(R)]^{1/2} \\ & \quad - [-U_J(R)]^{1/2} \} dR \\ & + \alpha \int_{R_2(0)}^{R_2(E_b)} [E_b - U_J(R)]^{1/2} dR. \end{aligned} \quad (6)$$

Following the approach of LeRoy and Bernstein,<sup>3</sup> we plan to ignore the first term [supposing that  $R_1(E_b) - R_1(0)$  is small and that the repulsive wall is steep] and to replace  $U_J(R)$  by its asymptotic expansion. This gives

$$\begin{aligned} v_b - v_0 \simeq & \beta \int_0^1 \{ [1 - U_J(R)/E_b]^{1/2} \\ & \quad + [-U_J(R)/E_b]^{1/2} \}^{-1} dy \\ & + \beta \int_1^{R_b/R_0} [1 - U_J(R)/E_b]^{1/2} dy, \end{aligned} \quad (7)$$

where we have substituted  $\beta = \alpha R_0 \sqrt{E_b}$  and  $y = R/R_0$ . See Fig. 1(b) for a comparison of the exact [Eq. (6)] and long-range approximation [Eq. (7)] to the JWKB difference integrand. Deriving

$$R_0 \simeq \left[ \frac{2\mu C_n}{\hbar^2 J(J+1)} \right]^{1/(n-2)} \quad (8)$$

from the condition  $U_J(R_0) = 0$ , we are ready to perform a number of back substitutions.

The remarkable result of these substitutions is that the molecular parameters  $\mu$  and  $C_n$  disappear entirely, and

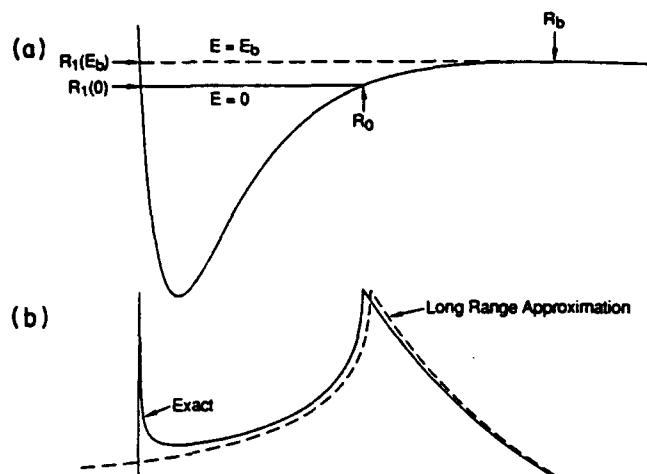


FIG. 1. (a) Upper curve: Effective potential  $U_J(R)$  based on a Leonard-Jones (12,6) form. (b) Lower curves: JWKB difference integrands for the exact potential and for the long-range approximation.

only the dependencies on  $n$  and  $J$  remain. We first note that  $R_b/R_0 = (n/2)^{1/(n-2)} \equiv \rho_n$ , then we evaluate  $\beta = [J(J+1)/\gamma_n]^{1/2}/\pi$ , where

$$\gamma_n = \frac{(n/2)^{n/(n-2)}}{(n/2-1)}, \quad (9)$$

and further observe that  $-U_J(R)/E_b = \gamma_n(y^{-n} - y^{-2})$ . Thus we have

$$v_b - v_0 \approx [J(J+1)]^{1/2} I_n, \quad (10)$$

where

$$I_n = \frac{1}{\pi\sqrt{\gamma_n}} \left[ \int_0^1 \{ [1 + \gamma_n(y^{-n} - y^{-2})]^{1/2} + [\gamma_n(y^{-n} - y^{-2})]^{1/2} \}^{-1} dy + \int_1^{\rho_n} [1 + \gamma_n(y^{-n} - y^{-2})]^{1/2} dy \right]. \quad (11)$$

We have just shown that the number of quasibound levels does not depend on  $\mu$  and  $C_n$ .

An even more surprising result is obtained when we evaluate the integral  $I_n$ . Integrating numerically we find the results given in Table I, and we conclude that the number of quasibound vibrational levels is effectively independent of  $n$  as well. Also included in Table I are the numbers derived by Dickinson and Bernstein<sup>2</sup> for  $n=4, 6, 8$ . They considered potentials for which the JWKB integrals for  $v_b$  and  $v_0$  could be evaluated explicitly in terms of elliptic integrals and extracted the leading term in  $J$  of the difference between them. They noticed the near independence on  $n$ , but their formulation did not make clear that the expected number of quasibound levels for low  $J$ ,

TABLE I. Numerical values for the integral  $I_n$ .

$n$	Present	Ref. 2
3	0.0451	
4	0.0498	0.0498
5	0.0498	
6	0.0482	0.0482
7	0.0462	
8	0.0441	0.044
9	0.0420	
10	0.0401	

$$N_{QB}(J) = v_b - v_0 = 0.048 \pm 0.02 [J(J+1)]^{1/2} \approx J/20, \quad (12)$$

is entirely independent of the molecule under consideration.

To assess the applicability of the expressions derived above, we have examined the published compilations of quasibound levels in which it is claimed that all the quasibound levels have been calculated. The formula for  $N_{QB}(J)$  above indicates the average number of quasibound levels expected. For any specific  $J$ , we expect to find at least  $J/20 - 1$  and at most  $J/20 + 1$  levels. To evaluate whether the number of levels found matches our expectation we count all the levels expected for angular momenta up to the specific value of  $J$ ,

$$T_{QB}(J) = \sum_{L=0}^J N_{QB}(L) \approx J(J+2)/40. \quad (13)$$

Figure 2 shows a graphical comparison of the numbers

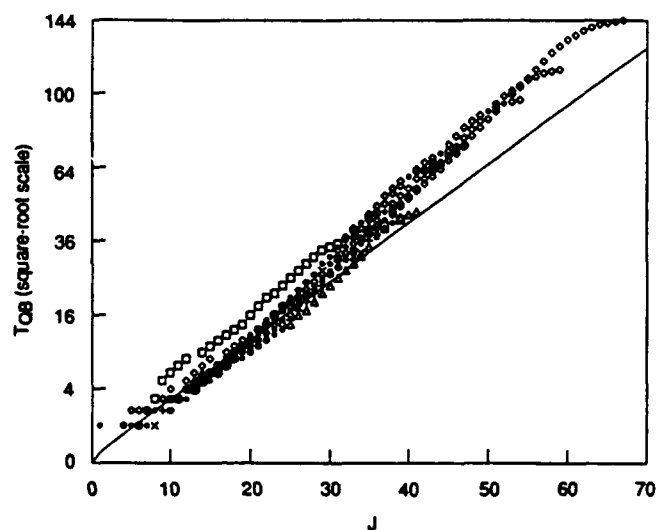


FIG. 2. Graphical comparison of expected number of quasibound levels with the numbers found in exact calculations.  $\times$ 's,  $\text{HeH}^+$  (Ref. 4);  $+$ 's,  $\text{CH}^+$  (Ref. 5); diamonds,  $\text{H}_2$ ,  $\text{HD}$ ,  $\text{D}_2$  (Ref. 6) and  $\text{HT}$ ,  $\text{DT}$ ,  $\text{T}_2$  (Ref. 7); squares,  $\text{HgH}$  (Refs. 8 and 9); triangles,  $\text{H}_2^+$  (Refs. 10 and 11); filled circles, more than one superimposed symbol.

TABLE II. Numbers of quasibound levels in ranges of  $J$ .

$J_{\max}$	$T_{\text{QB}}$ obs	$T_{\text{QB}}$ calc	$N_{\text{QB}}$ in ranges of $J$ 's, $T_{\text{QB}}(J) - T_{\text{QB}}(J - 10)$								
			0-9	10-19	20-29	30-39	40-49	50-59	60-69		
$^3\text{He}^1\text{H}^{+a}$	26	20	19	2	8	10					
$^4\text{He}^1\text{H}^{+a}$	27	21	20	2	7	14					
$^3\text{He}^1\text{H}^{+a}$	34	32	31	1	8	14	7				
$\text{CH}^{+b}$	36	37	34	2	6	15	14				
$^4\text{He}^2\text{H}^{+a}$	36	39	34	2	8	17	12				
$\text{H}_2^c$	38	47	38	2	8	19	18				
$\text{HgH}^d$	39	43	40	5	9	10	10				
$\text{H}_2^{+e}$	41	46	44	2	6	12	23	2			
$\text{HD}^c$	44	65	51	3	8	18	19	7			
$\text{HT}^f$	47	73	58	2	8	16	30	17			
$\text{D}_2^c$	54	96	76	2	7	15	17	36	8		
$\text{DT}^f$	59	113	90	1	8	15	25	36	28		
$\text{T}_2^f$	67	144	116	1	7	16	24	34	45	17	
Eq. (13)				2.5	7.5	12.5	17.5	22.5	27.5	32.5	

<sup>a</sup> Reference 4.<sup>b</sup> Reference 5.<sup>c</sup> Reference 6.<sup>d</sup> References 8 and 9.<sup>e</sup> References 10 and 11.<sup>f</sup> Reference 7.

of quasibound levels found in exact calculations from the literature with the above simple formula (we have used a square-root scale on the  $y$  axis to make the low  $J$  values more discernible). For low  $J$  (say  $< 30$ ), the present theory is clearly consistent with the exact results. The only exceptional case is  $\text{HgH}$ , for which the potential is known to have an abrupt change of form at  $R \approx 4 \text{ \AA}$  (Ref. 12) and thus cannot be represented by a single long-range multipole term. For higher values of  $J$ , the present theory consistently underestimates the number of quasibound levels, because of the increasing contribution of the left-hand turning points to the JWKB difference in-

tegral; however, the exact calculations continue to exhibit a common dependence on  $J$ .

Table II shows numerical summaries of these same comparisons. The levels have been grouped in ranges of ten values of  $J$ . Again, we see that essentially perfect agreement for low  $J$  and rather good agreement even for the total number of quasibound levels up to the highest  $J$  for which quasibound levels are supported by the potential.

This work was supported by the U.S. Office of Naval Research.

<sup>1</sup>D. E. Stogryn and J. O. Hirschfelder, *J. Chem. Phys.* **31**, 1531 (1959).<sup>2</sup>A. S. Dickinson and R. B. Bernstein, *Mol. Phys.* **18**, 305 (1970).<sup>3</sup>R. J. LeRoy and R. B. Bernstein, *J. Chem. Phys.* **52**, 3869 (1970).<sup>4</sup>R. I. Price, *Chem. Phys.* **31**, 309 (1978).<sup>5</sup>H. Helm, P. C. Cosby, M. M. Graff, and J. T. Moseley, *Phys. Rev. A* **25**, 304 (1982).<sup>6</sup>R. J. LeRoy, *J. Chem. Phys.* **54**, 5433 (1971); University of Wisconsin Theoretical Chemistry Institute Report No. WIS-TCI-387, 1971 (unpublished).<sup>7</sup>C. Schwartz and R. J. LeRoy, *J. Mol. Spec.* **121**, 420 (1987); R.

J. LeRoy and C. Schwartz, University of Waterloo Chemical Physics Research Report No. CP-301R (revised 2nd printing, 1987) (unpublished).

<sup>8</sup>W. C. Stwalley, A. Niehaus, and D. R. Herschbach, *J. Chem. Phys.* **63**, 3081 (1975).<sup>9</sup>M. Hehenberger, P. Froelich, and E. Brändas, *J. Chem. Phys.* **65**, 4571 (1976).<sup>10</sup>M. Kuriyan and H. O. Pritchard, *Can. J. Phys.* **55**, 3420 (1977).<sup>11</sup>J. P. Davis and W. R. Thorson, *Can. J. Phys.* **56**, 996 (1978).<sup>12</sup>W. C. Stwalley, *J. Chem. Phys.* **63**, 3062 (1975).

**Appendix G**

**COLLISIONAL PROCESSES IN XeF(X)**

## COLLISIONAL PROCESSES IN XeF(X)

G. Black, L. E. Jusinski, and D. L. Huestis  
Molecular Physics Laboratory  
SRI International  
Menlo Park, CA 94025

### ABSTRACT

Collision-induced dissociation of XeF(X) has been studied with He, Ne, Ar, Kr, Xe, N<sub>2</sub>, SF<sub>6</sub>, and XeF<sub>2</sub> as collision partners, giving dissociation rate constants of 0.58, 0.62, 0.76, 0.68, 0.75, 1.13, 1.05, and  $7.3 (\pm 10\%) \times 10^{-12} \text{ cm}^3 \text{ molec}^{-1} \text{ s}^{-1}$  respectively. The values for He and Ne are in reasonable agreement with those found previously [Fulghum *et al.* Appl. Phys. Lett. **35**, 247 (1979)]. Except for XeF<sub>2</sub>, there is only slight dependence on the nature of the collision partner. By following the approach to association/dissociation equilibrium in Xe, we are able to determine that the yields of bound XeF(X) from photodissociation of XeF<sub>2</sub> at 193 and 248 nm are only 0.4% and 0.08% respectively, with fragmentation to give three atoms the dominant pathway. Vibrational relaxation is observed and studied in detail for collisions with XeF<sub>2</sub>, with which it is found to be very fast.

## INTRODUCTION

The XeF(B-X) laser operates in the near ultraviolet on a number of bound-bound transitions, as listed in Table I and illustrated in Figure 1, terminating on various vibrational levels of the ground  $X^2\Sigma^+$  state. The ground state of XeF is weakly bound ( $D_e \approx 1175 \text{ cm}^{-1}$ ), supporting a total of  $15 \pm 2$  closely spaced vibrational levels ( $\omega_e = 226 \text{ cm}^{-1}$ ). [2,3] In the absence of collisional processes depleting these levels, the ground-state population would accumulate and eventually exceed that in the upper laser level, resulting in termination of laser action. Vibrational relaxation in the lower levels is insufficient to adequately deplete the population, since the small vibrational spacing leads to estimates that 9.6% and 4.4% of the ground state molecules will be in  $v'' = 2$  and  $v'' = 3$ , respectively, in equilibrium at room temperature [4]. On the other hand, the binding energy of the ground state of XeF is sufficiently weak that the lower level population can be depleted by collision-induced dissociation, which removes the ground state entirely (rather than simply changing its vibrational distribution).

Determination of the rates of collision-induced dissociation is a complicated task with an extensive literature (e.g., see Dove *et al.* [5]). Experimental measurements exist on a number of systems, usually from shock tube studies. These have been modeled by master equation treatments using semiempirical microscopic rate coefficients. In a number of cases, *ab initio* collision dynamics studies helped supply these rate coefficients. For XeF(X), the previous work consists of (1) modeling studies [8,9,10], (2) inferences from laser gain and fluorescence measurements [4,6,7], and (3) direct measurements of vibrationally resolved collision-induced dissociation by He and Ne [11,12,13]. In addition to these gases, collision-induced dissociation has been studied with Ar, Kr, Xe, N<sub>2</sub>, SF<sub>6</sub>, and XeF<sub>2</sub> in the work described here. We also report some measurements of vibrational relaxation in XeF(X) by XeF<sub>2</sub>.

## EXPERIMENTAL

The source of the XeF(X) for these experiments was photodissociation of XeF<sub>2</sub>. Photodissociation was carried out at both 193 nm (ArF) and 248 nm (KrF) using an excimer laser (Lambda Physik EMG 102 in the unstable resonator configuration). A schematic of the apparatus is shown in Figure 2. A similar approach has been used previously in our laboratory [14,15] and elsewhere [12,13]. At 193 nm, the absorption cross section of XeF<sub>2</sub> is  $6 \times 10^{-19} \text{ cm}^2$  and at 248 nm, a factor of 3-4 smaller [16,17]. The apertured excimer beam (6-mm diameter) irradiated the sample with typically 10 mJ at KrF and 2 mJ at ArF in a 10-ns pulse, dissociating  $\leq 1\%$  of the XeF<sub>2</sub>. The path length through the cell was  $\approx 30 \text{ cm}$  and the cell volume  $\approx 300 \text{ cm}^3$ . Gas mixtures were made up in a stainless steel mixing tank ( $\approx 4 \text{ liter}$  volume) and then slowly flowed through the cell to avoid buildup of photolysis products.

The XeF(X) ground state was detected by LIF on the B  $\leftarrow$  X transition. Observations were made on  $v'' = 0-5$ , in all cases pumping up to the  $v' = 0$  level and monitoring either (0,2) or (0,3) emission. The pumping source was a Quanta-Ray Nd:Yag-dye laser system that, after doubling provided  $\approx 5 \text{ mJ}$  in the cell in the 340 - 360-nm region of the B-X (0,0-5) transitions in a pulse of  $\approx 5\text{-ns}$  duration with a linewidth of  $\approx 0.5 \text{ cm}^{-1}$ . For these measurements, the lasers were operated at 10 Hz and were adjusted to overlap spatially along the length of the cell. The time delay between the photodissociation and probe lasers was set by a digital delay generator programmed in a nonlinear ramp from a VAX 11/750 computer in another room. [DID WE CALIBRATE THE TIME BASE?]

The detection system, situated perpendicular to the laser beams, consisted of a 0.35-m monochromator equipped with an RCA C31034A photomultiplier. For most measurements, the monochromator slits were set at 200  $\mu\text{m}$  providing a spectral bandwidth of 0.4 nm. The photomultiplier output passed to a boxcar averager (Stanford Research Systems Model SR250) and

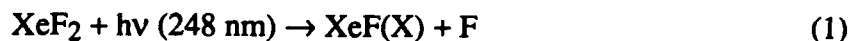
then to the computer for storage and subsequent analysis. [WHAT WAS THE SETTING ON THE BOXCAR? WINDOW POSITION AND WIDTH?]

Most measurements were made with the dye laser wavelengths close to the band origins, in which case a number of rotational lines overlapped the dye output and the largest signal was obtained. Because this approach favors low values of  $J''$ , many measurements were made with the dye pump wavelength shifted several Å to the red of the band origin, where higher  $J''$  levels would be excited. Since no significant difference could be found in the results, rotational energy apparently was rapidly equilibrated within each vibrational level (i.e. faster than vibrational relaxation or collision-induced dissociation). Because the dye laser power is sufficient to saturate the  $B \leftarrow X$  transitions within its  $\approx 0.5 \text{ cm}^{-1}$  bandwidth, the intensity of the LIF signal had only very slight dependence on dye laser energy. Hence, the signal intensity is relatively independent of the absorption cross section for the pumped transition and effectively proportional to the ground-state population.

## RESULTS AND DISCUSSION

### COLLISION-INDUCED DISSOCIATION

Figure 3 shows the temporal behavior of the  $\text{XeF}(v''=0)$  level when  $\text{XeF}_2$  at a pressure of 0.5 torr is photodissociated at 248 nm. The solid line is a two-exponential least-squares fit. The monochromator is set to observe the (0,3)  $\text{B}\leftarrow\text{X}$  emission, and the spike at the origin originates from the production of this emission feature by the KrF laser alone. This interfering emission was observed to exhibit a squared dependence on the KrF intensity, as expected, since direct production of  $\text{XeF}(\text{B})$  is not energetically possible at 248-nm. In previous work in this laboratory [15] the production of  $\text{B}\rightarrow\text{X}$  emission in 248 nm photodissociation of  $\text{XeF}_2$  was attributed to the sequence of reactions



It was also shown previously [14] that photodissociation of  $\text{XeF}_2$  by the KrF laser leads to a strongly nonthermal vibrational distribution in  $\text{XeF}(\text{X})$ . The behavior shown in Figure 3, in which little  $v'' = 0$  is produced directly but builds up rapidly by vibrational cascade from higher levels followed by a slower removal by collision-induced dissociation, supports this conclusion.

Figure 4 shows a similar experiment using 193 nm to photodissociate the  $\text{XeF}_2$ . Interference from the ArF laser is also apparent. In this case, the  $\text{B}\rightarrow\text{X}$  (0,3) emission produced by the 193-nm radiation exhibited a first-power dependence on excimer energy, since direct production of  $\text{XeF}(\text{B})$  is possible at this wavelength. Figure 4 shows that, in this case, any rise of

XeF( $v''=0$ ) due to vibrational relaxation was small compared to the direct production by photodissociation at 193 nm. This finding conflicts with earlier work [12] on this same system. As with 248 nm, the subsequent slow decay reflects collision-induced dissociation.

Confirmation of this view was obtained from observations of the other  $v''$  levels. Figure 5 shows temporal profiles of  $v'' = 0-3$  using KrF photodissociation. Up to  $v'' = 3$ , effectively the same slow final decay could be seen, confirming collision-induced dissociation from a relaxed or steady-state distribution of vibrational levels. For  $v'' = 4$  and 5, only the much faster initial disappearance could be detected. Thus, we interpret the fast initial decays of  $v'' > 1$  and build up of  $v'' = 0$  in terms of vibrational relaxation, (see below). The steady-state vibrational distribution is expected to be Boltzmann-like for low values of  $v$ , with the higher levels (within  $kT$  of the dissociation limit) suppressed owing to more rapid collision-induced dissociation [18]. The experimentally observed rate of collision-induced dissociation is then an average of the state-specific rates weighted by the steady-state vibrational populations.

Figure 6 shows the rate of collision-induced dissociation as a function of XeF<sub>2</sub> pressure for experiments with both 248- and 193-nm photodissociation using observation on only the  $v'' = 0$  level. With 248-nm photodissociation, where both the rise and fall of the XeF(X) <sub>$v''=0$</sub>  signal could be observed, the addition of other gases was observed to increase both the rate of  $v'' = 0$  production by vibrational relaxation and its rate of removal by collision-induced dissociation. The effect of He on the rate of collision-induced dissociation (after correcting for the effect of XeF<sub>2</sub>) is shown in Figure 7. The other gases studied gave similar effects, and the resulting rate coefficients are shown in Table II.

As can be seen from the results in Table II, except for XeF<sub>2</sub>, there is very little dependence of the rate coefficients on the nature of the collision partner. This finding agrees with theoretical expectations [4]. Clearly, specific chemical effects are associated with the much higher rates for XeF<sub>2</sub>. Within the respective error bars, the value for He is in agreement with the value of  $(0.44 \pm 0.10) \times 10^{-12} \text{ cm}^3 \text{ molec}^{-1} \text{ s}^{-1}$  determined by Fulghum *et al.* [12], but it is a factor of 2 larger than

their subsequent value of  $0.31 \times 10^{-12}$ . The intercept value in Figure 2 of this earlier work [12], which should be due to collision-induced dissociation by  $\text{XeF}_2$ , gives a very large rate coefficient,  $\approx 2 \times 10^{-11} \text{ cm}^3 \text{ molec}^{-1} \text{ s}^{-1}$  when interpreted in this way. Perhaps the accumulation of photolysis products, resulting from the lack of a flow system in this earlier work is the source of the disagreement (despite the use of very low photolysis intensities to minimize the extent of photodecomposition). Our rate coefficient for Ne is somewhat larger than the  $0.33 \text{ } 0.2 \times 10^{-12}$  found by Fughum *et al.* and more than three times the value of  $0.18 \times 10^{-12}$  inferred independently by Tang *et al.* [8,10] and Rokni *et al.* [9] from laser gain and from sidelight-fluorescence suppression measurements, respectively.

## XENON EXPERIMENTS

With xenon as the added gas, the observations were somewhat different, as Figure 8 shows. A rise is seen to a steady-state intensity lasting several milliscads. The steady-state signal arises from the steady-state concentration of  $\text{XeF}(X)_{v''=0}$  established in the equilibrium



and the rate of approach to this steady state will reflect the rate of collision-induced dissociation (if vibrational relaxation is the faster process, as found in the other systems). On this basis, the value for Xe shown in Table II was obtained. The Xe dependence of the rise frequency is shown in Figure 9. The steady-state signal, whose magnitude is roughly proportional to the Xe density as expected [at high density, Xe quenches  $\text{XeF}(B)$ ], eventually decays as F atoms and XeF molecules diffuse out from the common volume illuminated by the two laser beams.

It is interesting to compare our results to those of Appelman and Clyne [19], who studied the disappearance of F atoms in a mixture of Xe and Ar buffer gases. They attributed this loss to three-body formation of XeF in the reaction



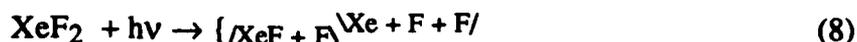
with subsequent loss of XeF resulting in formation of XeF<sub>2</sub>. They performed these measurements under a single set of conditions, [Xe] = 3 × 10<sup>16</sup> cm<sup>-3</sup> and [Ar] = 5 × 10<sup>16</sup> cm<sup>-3</sup>, and observed a decay frequency of 5.6·s<sup>-1</sup>. Our results suggest that under these conditions the three-body formation of XeF will reach equilibrium with collision-induced dissociation on a much faster time scale (6 × 10<sup>4</sup>·s<sup>-1</sup>). Thus, the net loss of F atoms Appleman and Clyne observed must be controlled by other reactions. Possible candidates are



and



Our Xe studies also allow us to estimate the branching ratio for the process



We can use steady-state concentration of XeF at long time to calibrate the XeF produced directly by the photolysis laser. Figure 10 shows temporal profiles of XeF(X)<sub>v''=0</sub> resulting from 193-nm photolysis at two relatively low Xe pressures (25 and 50 torr). In both cases, the amount of XeF(X) produced by the laser is comparable to that in the eventual steady state. For pressures ≥ 50 torr, the signal rises to the steady-state value, whereas for [Xe] ≤ 25 torr, the signal falls. A similar relationship holds for the higher vibrational levels, v'' = 1-4, confirming that vibrational relaxation is much faster than collision-induced dissociation. [COULD THIS JUST MEAN THAT THE INITIAL DISTRIBUTION IS SIMILAR TO THE STEAD-STATE DISTRIBUTION?]

Thus, we conclude that for 193-nm photolysis at Xe pressure of about 35 torr,

$$[\text{XeF(X)}]_{\text{initial}} \approx [\text{XeF(X)}]_{\text{equilibrium}} \quad (9)$$

when summed over the first five vibrational levels. Our previous calculation of the equilibrium constant [4] allows us to infer that at 35 torr

$$\sum_{v''=0}^4 [\text{XeF(X)}]_{\text{equilibrium}} \approx 0.002 [\text{F}]_{\text{equilibrium}} \quad (10)$$

Hence, we can conclude that the production of XeF(X) is a minor product of XeF<sub>2</sub> photolysis at 193 nm, with a quantum yield of 0.4-0.1% (note that two F atoms are produced for each dissociation). Furthermore, the direct yield of XeF(B) at 193 nm must be very small (<0.01%).

A similar investigation with 248-nm photodissociation gave an even smaller yield of the v'' = 0-4 bound levels (quantum yield ≈ 0.08%). Within the experimental errors, the bound levels above v'' = 4 can be neglected, and the above numbers represent the total yield of bound levels.

## VIBRATIONAL RELAXATION

As mentioned above and illustrated in Figure 5, with XeF<sub>2</sub> alone and with the KrF laser, the v'' = 0 rise time and the initial decays of v'' = 2-5 were sufficiently slow that they could be measured despite interference from excimer-produced fluorescence. Figure 11 shows the results as functions of XeF<sub>2</sub> density, and Table III lists the slopes. The rate of formation of v'' = 0 should correspond to an "effective" rate coefficient for vibrational relaxation from all the higher levels. Because of the suggestive pattern exhibited by the effective rate coefficients listed in Table III, it is tempting to infer that vibrational relaxation occurs in Δv'' = 1 steps, for which the numbers listed in Table III would then be the state-to-state rate coefficients (the rise of v'' = 0 being the relaxation of v''=1). This inference poses two problems. First, the rates observed are very high, and could result from a "chemical" rather than "physical" relaxation mechanism. A possibility is F atom exchange,



which might be expected to accomplish energy scrambling. Second, in each case, the separation between the neighboring vibrational levels is less than  $kT$ , so that in addition to cascade filling from above, any given vibrational level is also significantly repopulated by vibrational excitation from the next lower level. The net result is that multiple-exponential decays should always be observed and the rate coefficients derived from fitting the data should depend on the initial conditions, on the rate of decay of the resulting equilibrium distribution, and on the signal-to-noise ratio.

In an attempt to quantify these arguments, we tried to simulate the data shown in Figure 5 using a model similar to that developed previously [4,7] (The vibration and dissociation parameters,  $Q$  and  $C$ , respectively, were increased by a factor of 17, and a constant,  $4.4 \times 10^{-12}$ , was added to each state-specific dissociation rate coefficient). The result, assuming the population is initially in  $v'' = 3$  is shown in Figure 12. Table III lists the model rate coefficients for single-step vibrational relaxation and excitation, along with the total-removal rate coefficient, for each level. We are encouraged in our interpretation of the experiments by the agreement between the observed effective rate coefficients and the  $\Delta v'' = 1$  values from the model, despite the fact that the model predicts that the total rates of removal from each level are a factor of 2 to 3 larger.

## ACKNOWLEDGMENTS

We are pleased to acknowledge the assistance of Dr. M. R. Taherian in preparing the apparatus and computer interface for these experiments. The VAX 11/750 computer used in these experiments was purchased under Grant No. PHY-8114611 from the National Science Foundation. The research reported here was supported by the Office of Naval Research.

## REFERENCES

1. J. Tellinghuisen, P. C. Tellinghuisen, G. C. Tisone, J. M. Hoffman, and A. K. Hays, J. Chem. Phys. **68**, 5177 (1978).
2. P. C. Tellinghuisen, J. Tellinghuisen, J. A. Coxon, J. E. Velazco, and D. W. Setser, J. Chem. Phys. **68**, 5187 (1978).
3. P. C. Tellinghuisen and J. Tellinghuisen, Appl. Phys. Lett. **43**, 898 (1983).
4. D. L. Huestis, R. M. Hill, D. J. Eckstrom, M. V. McCusker, D. C. Lorents, H. H. Nakano, B. E. Perry, J. A. Margevicius, and N. E. Schlotter, "New Electronic Transition Laser Systems," Report No. MP 78-07, SRI International, Menlo Park, CA (May 1978).
5. J. E. Dove, M. E. Mandy, N. Sathyamurthy, and T. Joseph, Chem. Phys. Lett. **127**, 1 (1986).
6. C. Duzy and V. H. Shui, "Theoretical Study of XeF Vibrational Excitation and Dissociation," presented at the 31st Annual Gaseous Electronics Conference, 17-20 October 1978, Buffalo, NY.
7. D. L. Huestis, D. J. Eckstrom, B. E. Perry, R. M. Hill, W. K. Bischel, K. Y. Tang, and D. C. Lorents, "Electronic Transition Laser Systems," Report No. MP 81-004, SRI International, Menlo Park, CA (March 1981).
8. K. Y. Tang, R. O. Hunter, Jr., and D. L. Huestis, "Lower level removal in XeF," presented at the 31st Annual Gaseous Electronics Conference, 17-20 October 1978, Buffalo, NY.
9. M. Rokni, J. H. Jacob, J. C. Hsia, and D. W. Trainor, Appl. Phys. Lett. **36**, 243 (1980).

10. K. Y. Tang, R. O. Hunter, Jr., and D. L. Huestis, "Lower level removal in XeF," Appendix D in Reference [7].
11. S. F. Fulghum, I. P. Herman, M. S. Feld, and A. Javan, *Appl. Phys. Lett.* **33**, 926 (1978).
12. S. F. Fulghum, M. S. Feld, and A. Javan, *Appl. Phys. Lett.* **35**, 247 (1979).
13. S. F. Fulghum, M. S. Feld, and A. Javan, *IEEE J. Quantum Electron.* **QE-16**, 815 (1980).
14. H. Helm, D. L. Huestis, M. J. Dyer, and D. C. Lorents, *J. Chem. Phys.* **79**, 3220 (1983).
15. H. Helm, L. E. Jusinski, D. C. Lorents, and D. L. Huestis, *J. Chem. Phys.* **80**, 1796 (1984).
16. G. Black, R. L. Sharpless, D. C. Lorents, D. L. Huestis, R. A. Gutcheck, T. D. Bonifield, D. A. Helms, and G. K. Walters, *J. Chem. Phys.* **75**, 4840 (1981).
17. N. K. Bibinov, I. P. Vinogradov, L. D. Mikheev, and D. B. Stavrovskii, *Kvanovaya Electron. (Moscow)* **8**, 1945 (1981) [*Sov. J. Quantum Electron.* **11**, 1178 (1981)].
18. C. A. Brau, J. C. Keck, and G. F. Carrier, *Phys. Fluids* **9**, 1885 (1966).
19. E. H. Appleman and M.A.A. Clyne, *J. Chem. Soc., Faraday Trans. I*, **71**, 2072 (1975).

**Table 1**  
**XeF LASER TRANSITIONS [1]**

348.8 nm	$v' = 2 \rightarrow v'' = 5$
351.1 nm	$v' = 1 \rightarrow v'' = 4$
-351.3 nm	$v' = 0 \rightarrow v'' = 2$
353.2 nm	$v' = 0 \rightarrow v'' = 3$
353.2 nm	$v' = 1 \rightarrow v'' = 6$

**Table 2**  
**Rate Coefficients for Collision-Induced  
Dissociation of XeF(X) at 300 K**

Gas	Rate Coefficients ( $10^{-12} \text{ cm}^3 \text{ molec}^{-1} \text{ s}^{-1}$ )		
	Present Work	Previous Work	
He	$.58 \pm 0.06$	$0.44 \pm 0.1^a$	$0.31^b$
Ne	$.62 \pm 0.06$	$0.33 \pm 0.2^a$	$0.18^c$
Ar	$.76 \pm 0.08$		
Kr	$.68 \pm 0.07$		
Xe	$.75 \pm 0.08$		
N <sub>2</sub>	$1.13 \pm 0.11$		
SF <sub>6</sub>	$1.05 \pm 0.15$		
XeF <sub>2</sub>	$7.3 \pm 0.8$	$\sim 20^d$	

<sup>a</sup> Reference [12]

<sup>b</sup> Reference [13]

<sup>c</sup> References [8,9,10]

<sup>d</sup> Estimated from intercept in Figure 2 from Reference [12]

**Table 3**  
**Effective Rate Coefficients for Vibrational Relaxation**  
**of XeF(X) by XeF<sub>2</sub> at 300 K**

Process	Observed Rate <sup>a</sup>	v''	Rate Coefficients from Model <sup>a</sup>		Total
			$\Delta v'' = 1$	$\Delta v'' = +1$	
		0		0.4	0.5
Rise of v''=0	0.78	1	1.1	0.6	1.8
Decay of v''=2	1.2	2	1.4	0.9	2.5
Decay of v''=3	1.7	3	1.9	1.4	3.7
Decay of v''=4	2.8	4	2.6	2.1	5.8
Decay of v''=5	3.4	5	3.6	3.3	10.2

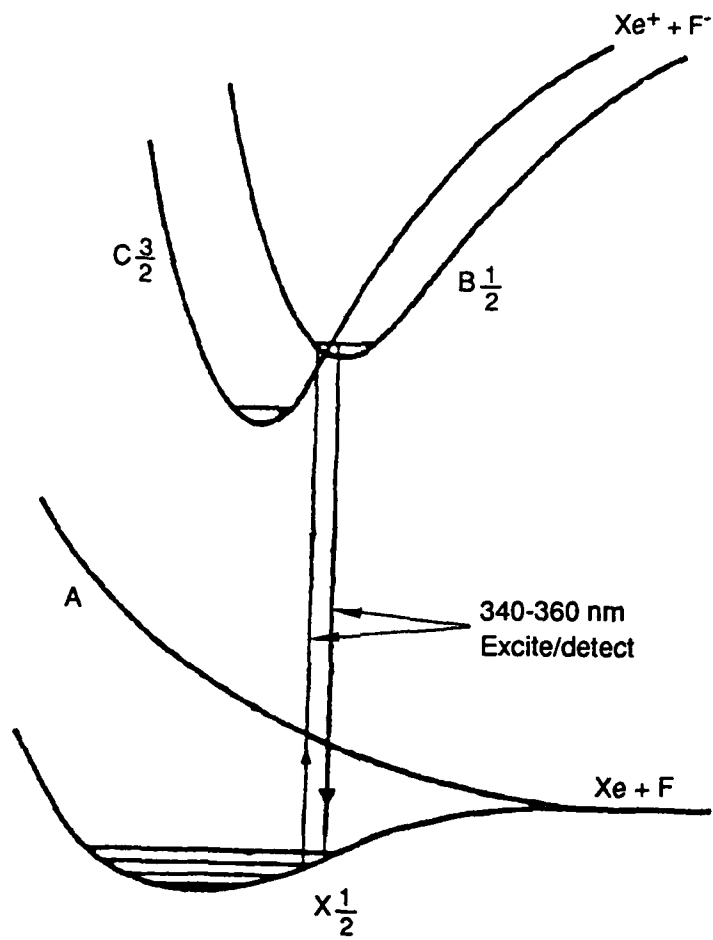
---

<sup>a</sup> In units of  $10^{-10} \text{ cm}^3 \text{ molec}^{-1} \text{ s}^{-1}$

## FIGURE CAPTIONS

1. Schematic XeF energy level diagram.
2. Schematic of the experimental apparatus for XeF production by photodissociation of XeF<sub>2</sub> and for monitoring its decay by LIF.
3. XeF(X)<sub>v</sub>" = 0 production by 248-nm photodissociation of XeF<sub>2</sub> at 0.51 torr and its subsequent disappearance by collision-induced dissociation.
4. XeF(X)<sub>v</sub>" = 0 production by 193-nm photodissociation of XeF<sub>2</sub> at 0.42 torr and its subsequent disappearance by collision-induced dissociation.
5. Comparison of time histories of XeF(X)<sub>v</sub>"=0,1,2,3 populations following KrF laser photolysis of 0.66 torr of XeF<sub>2</sub>.
6. XeF(X)<sub>v</sub>"=0 decay rate by collision-induced dissociation versus concentration of XeF<sub>2</sub>.
7. XeF(X)<sub>v</sub>"=0 decay rate by collision-induced dissociation versus concentration of He.
8. Temporal profile of XeF(X)<sub>v</sub>"=0 in the 248-nm photodissociation of XeF<sub>2</sub> at 1.0 torr in the presence of 50 torr of Xe.
9. Rate of collision-induced dissociation of XeF(X) by Xe, derived from the rate of rise of XeF(X)<sub>v</sub>"=0.
10. Temporal profile of XeF(X)<sub>v</sub>"=0 in the 193-nm photodissociation of XeF<sub>2</sub> at 0.33 torr in the presence of 50 torr of Xe (upper curve) and at 0.50 torr in the presence of 25 torr of Xe (lower curve).

11. Fast decay rates of  $\text{XeF}(X)_{v''=2-5}$  and vibrational relaxation rate into  $\text{XeF}(X)_{v''=0}$  versus concentration of  $\text{XeF}_2$ .
12. Comparison of model calculations with observed  $\text{XeF}(X)_{v''=0,1,2,3}$  populations following KrF laser photolysis of 0.66 torr of  $\text{XeF}_2$ .



RAM-7123-1

Figure 1. Schematic XeF energy level diagram.

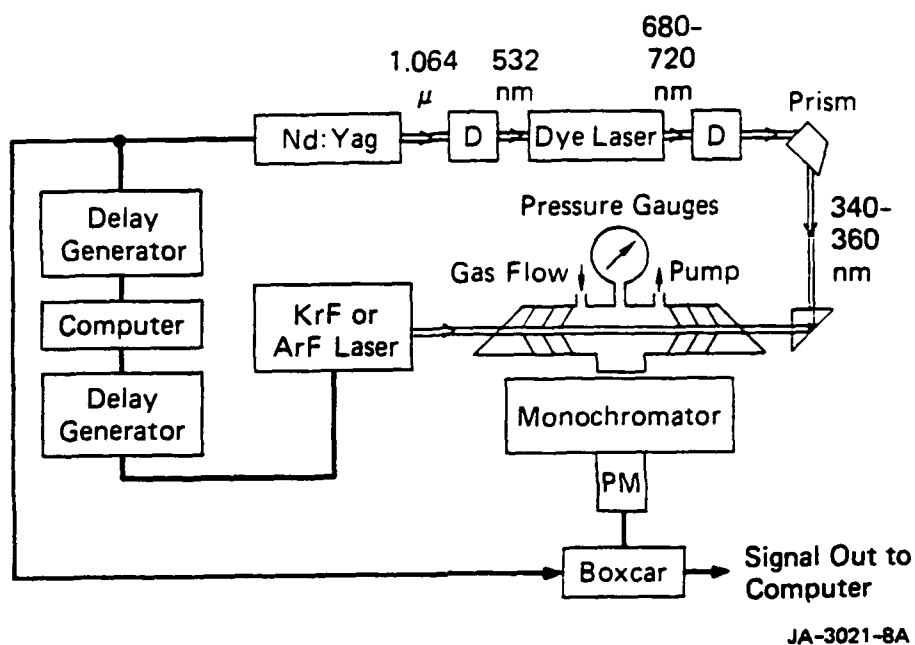
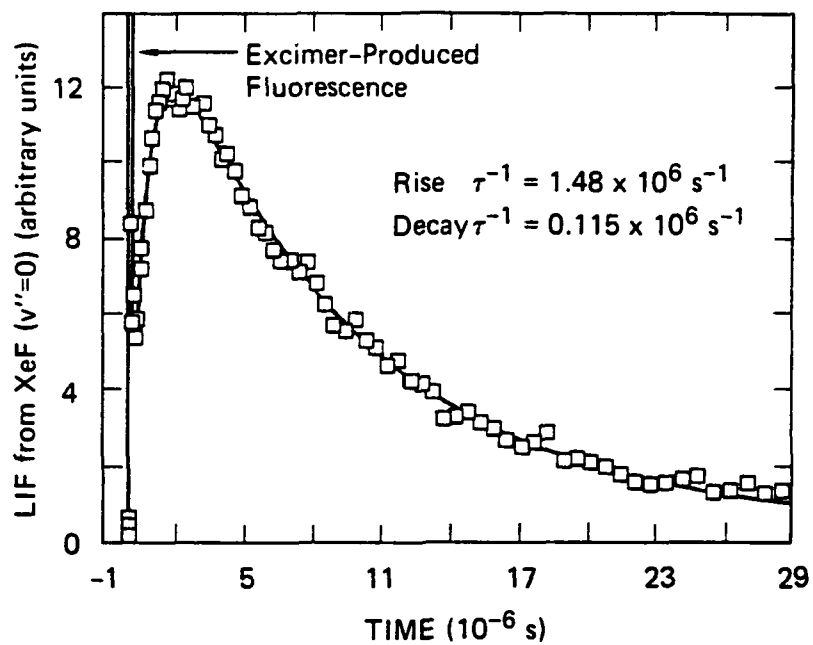
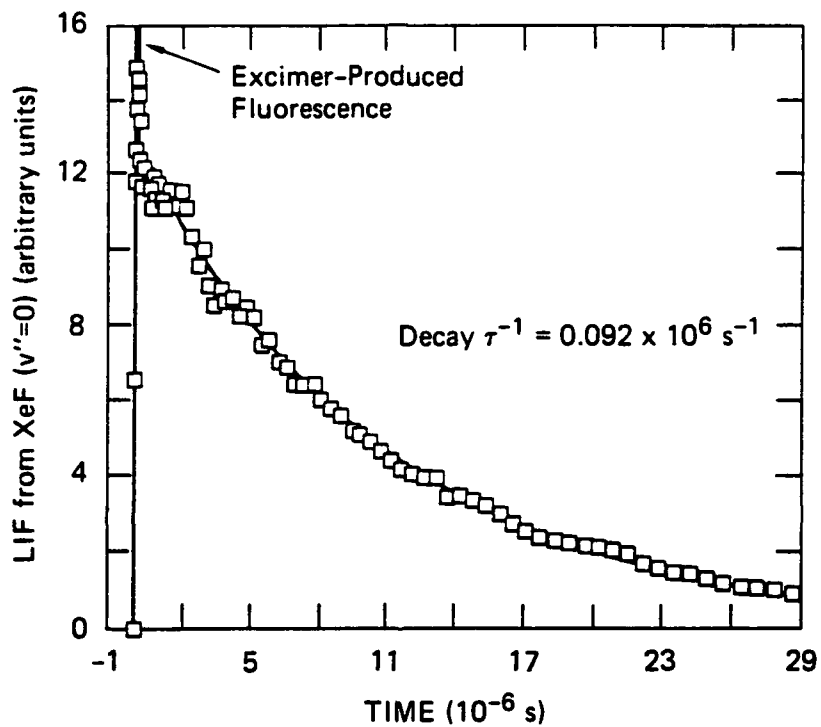


Figure 2. Schematic of the experimental apparatus for XeF production by photodissociation of XeF<sub>2</sub> and for monitoring its decay by LIF.



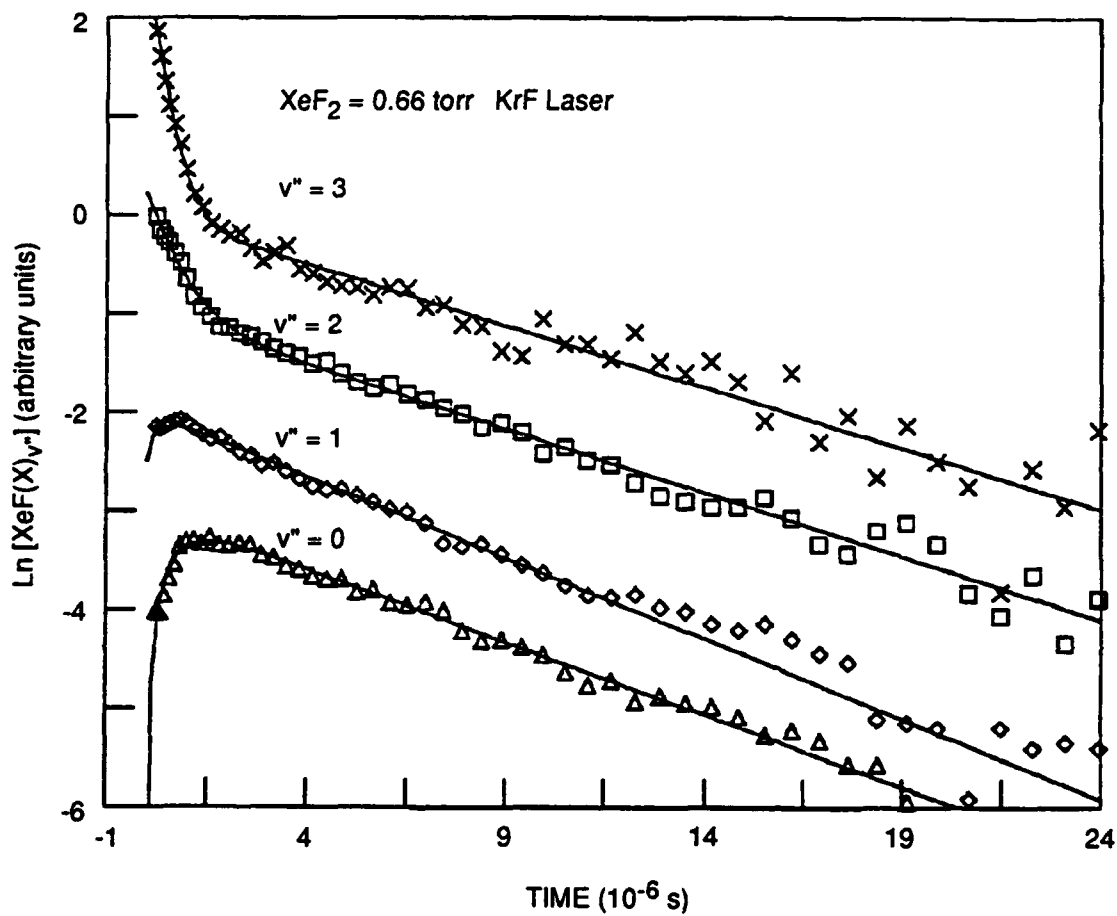
JA-8041-12

Figure 3.  $\text{XeF}(X)v''=0$  production by 248-nm photodissociation of  $\text{XeF}_2$  at 0.51 torr and its subsequent disappearance by collision-induced dissociation.



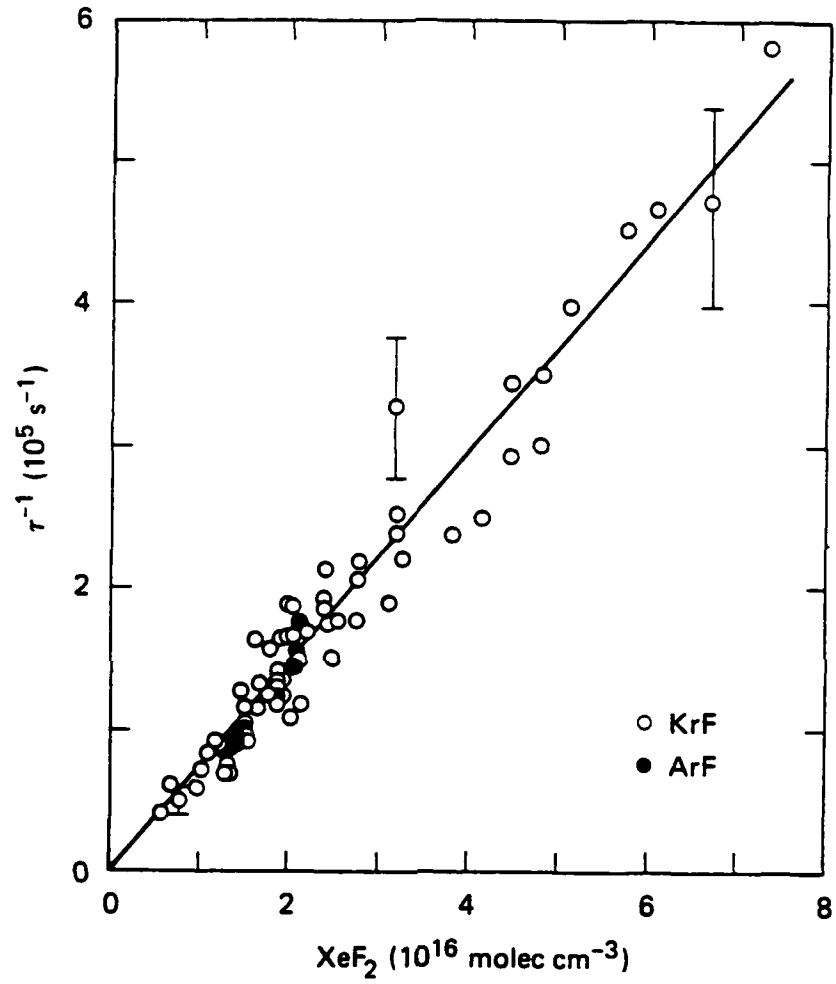
JA-8041-13

Figure 4.  $\text{XeF}(X)v''_0$  production by 193-nm photodissociation of  $\text{XeF}_2$  at 0.42 torr and its subsequent disappearance by collision-induced dissociation.



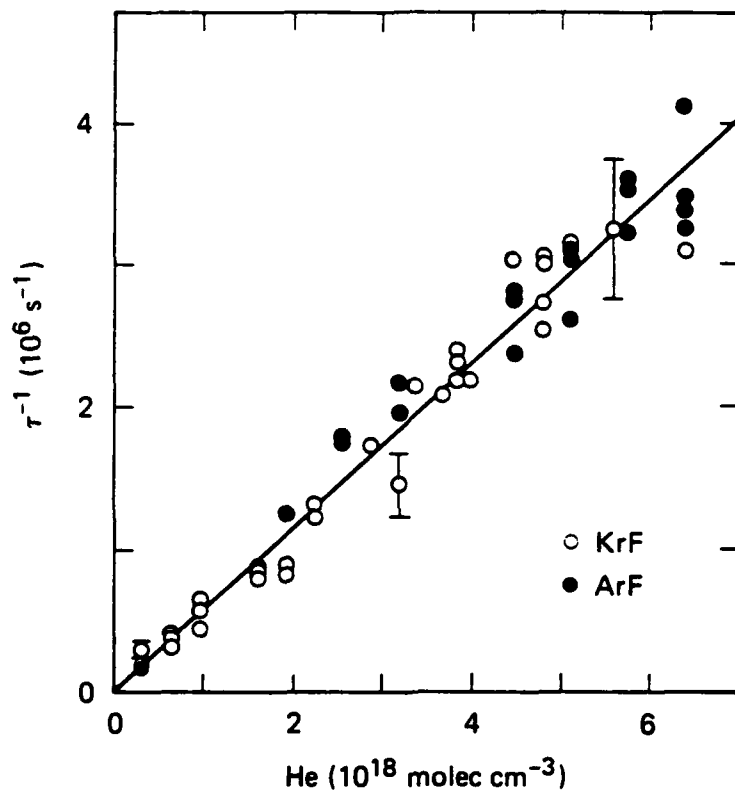
RAM-7123-2

Figure 5. Comparison of time histories of XeF(X)<sub>v''=0, 1, 2, 3</sub> populations following KrF laser photolysis of 0.66 torr of XeF<sub>2</sub>.



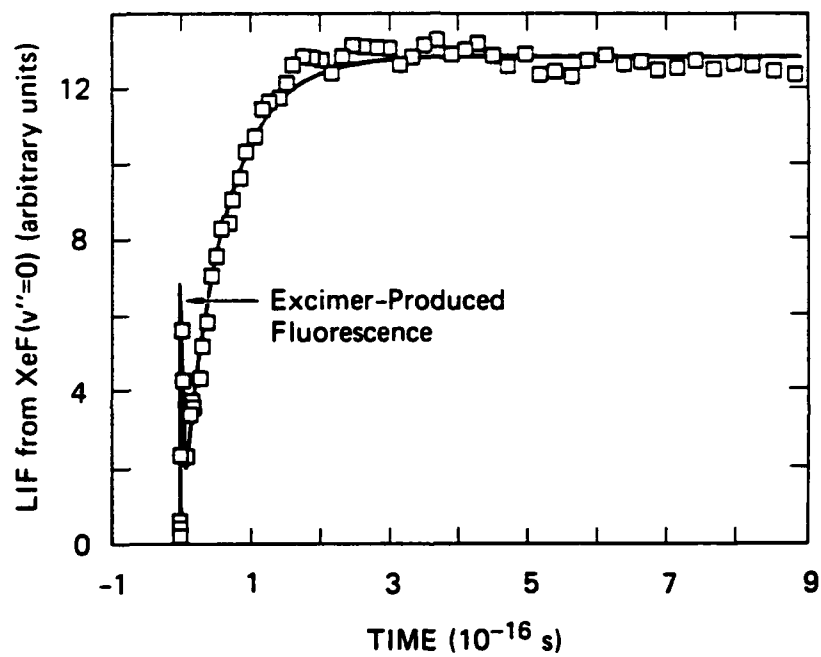
JA-8041-14

Figure 6.  $\text{XeF}(X)_{v=0}$  decay rate by collision-induced dissociation versus concentration of  $\text{XeF}_2$ .



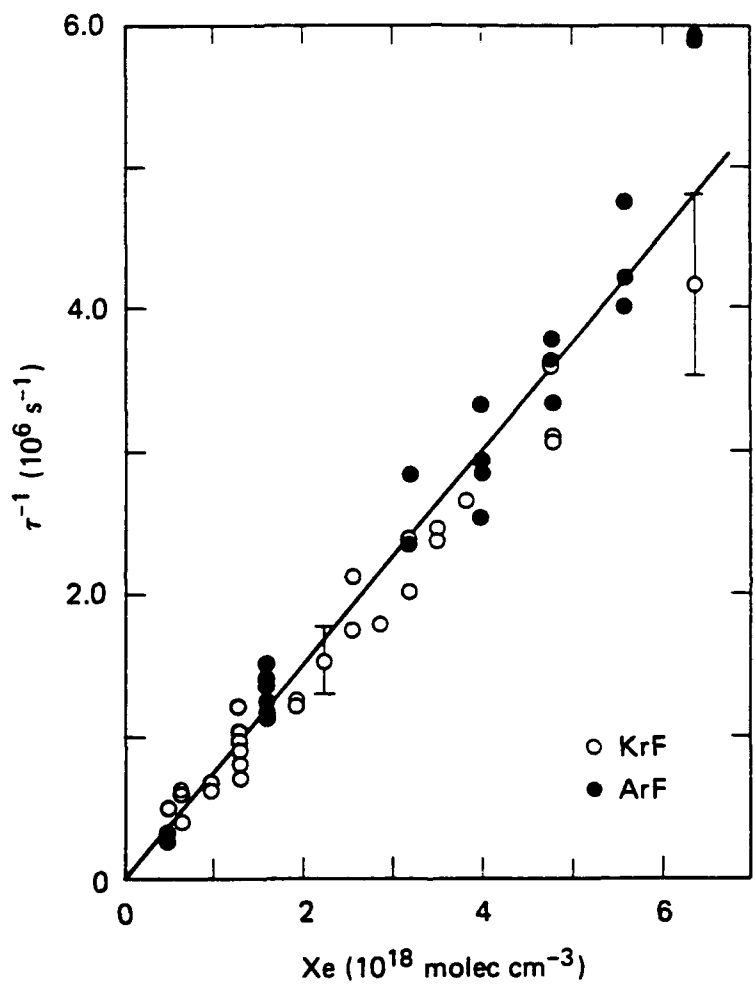
JA-8041-15

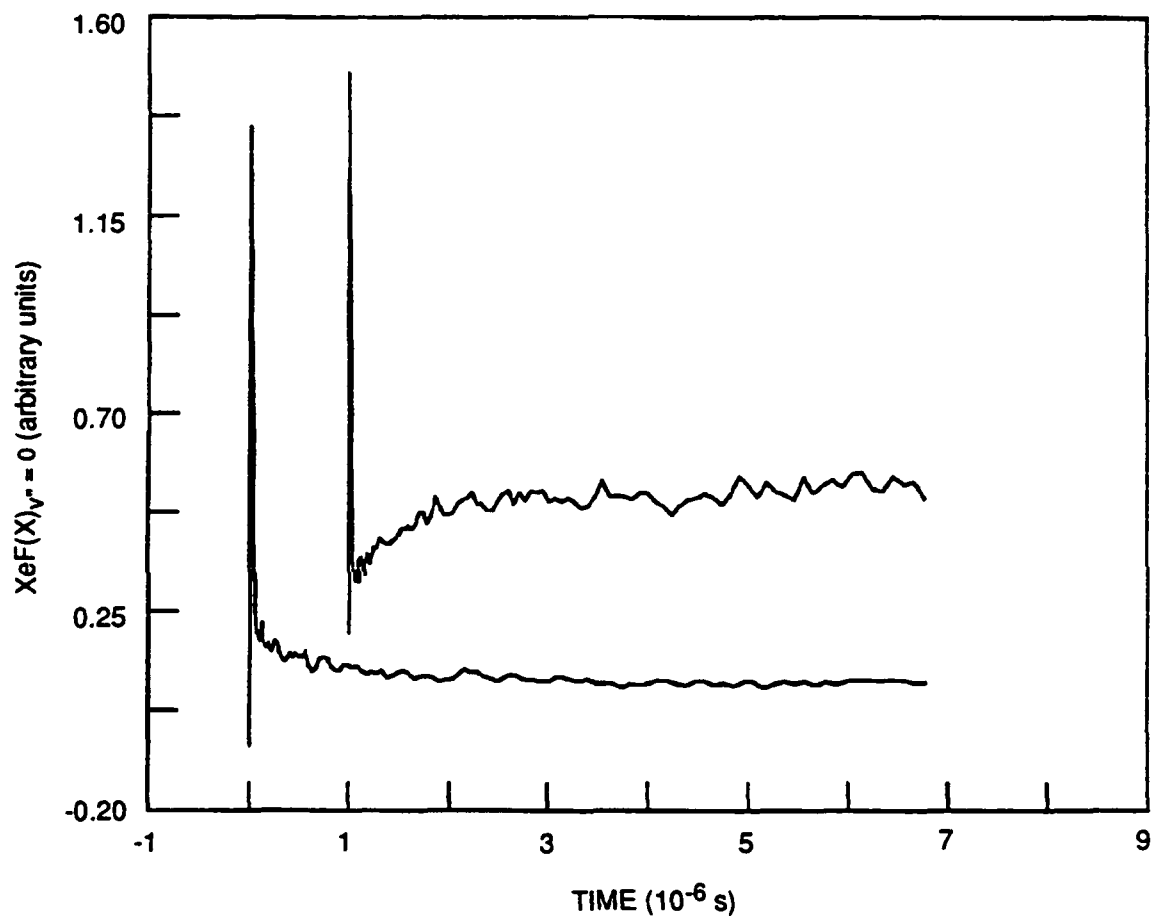
Figure 7.  $\text{XeF}(X)_{v=0}$  decay rate by collision-induced dissociation versus concentration of He.



JA-8041-16

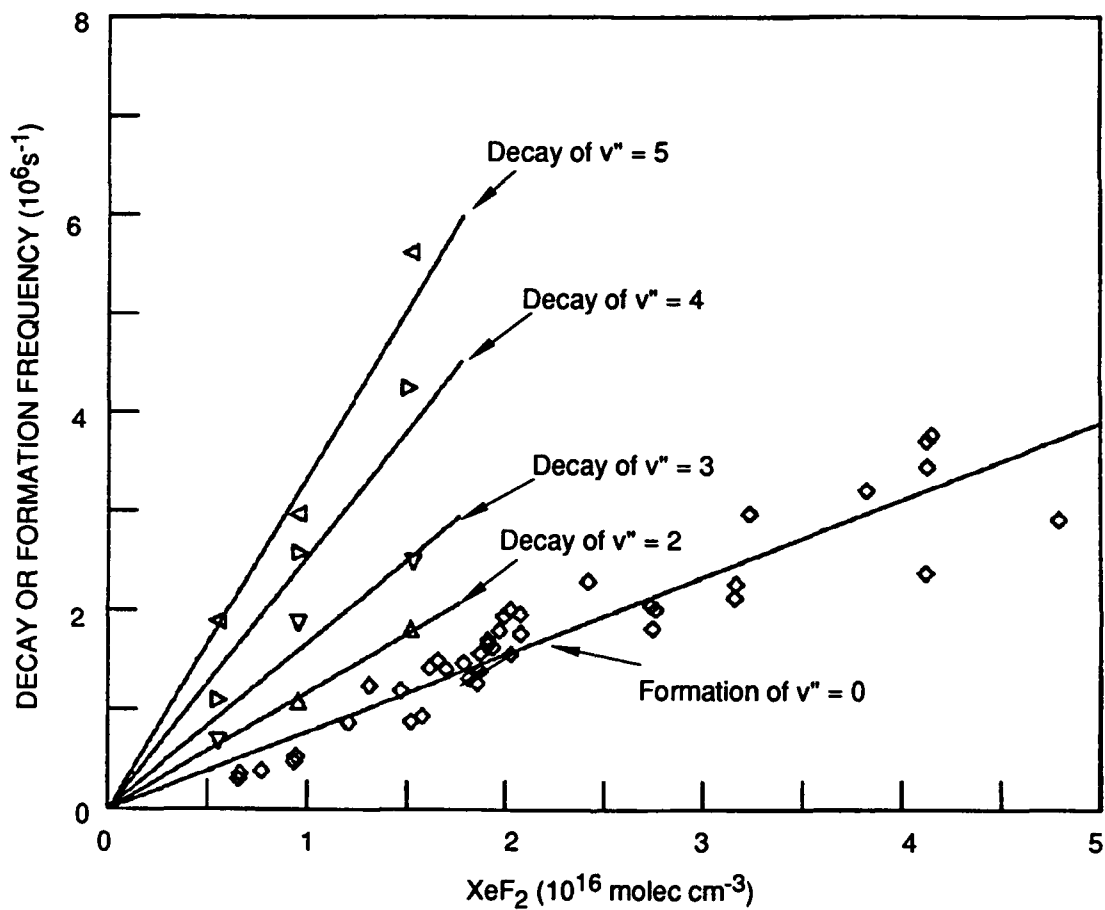
Figure 8. Temporal profile of XeF(X)<sub>v''=0</sub> in the 248-nm photodissociation of XeF<sub>2</sub> at 1.0 torr in the presence of 50 torr of Xe.





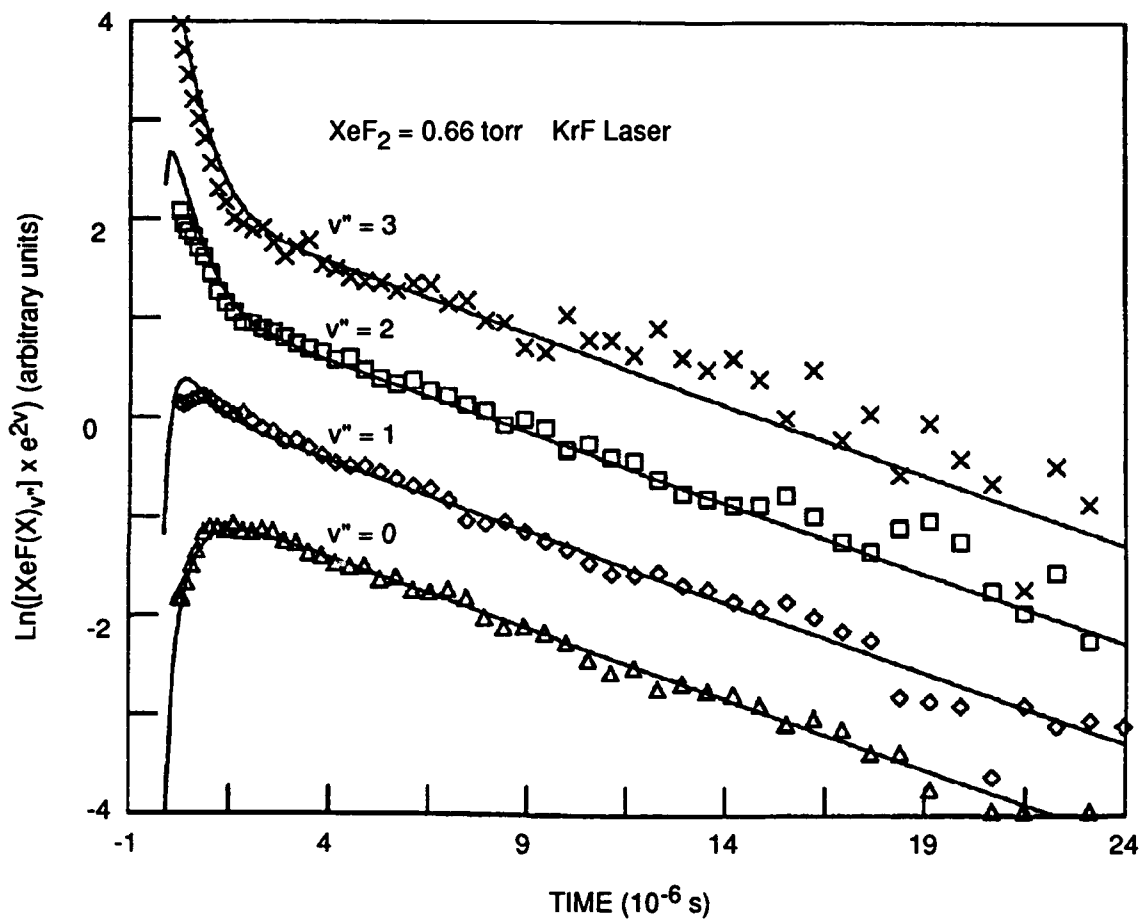
RAM-7123-3

Figure 10. Temporal profile of  $\text{XeF}(X)_{v=0}$  in the 193-nm photodissociation of  $\text{XeF}_2$  at 0.33 torr in the presence of 50 torr of Xe (upper curve) and at 0.50 torr in the presence of 25 torr of Xe (lower curve).



RAM-7123-4

Figure 11. Fast decay rates of  $\text{XeF}(X)_{v''=2-5}$  and vibrational relaxation rate into  $\text{XeF}(X)_{v''=0}$  versus concentration of  $\text{XeF}_2$ .



RAM-7123-5

Figure 12. Comparison of model calculations with observed XeF(X)  $v'' = 0, 1, 2, 3$  populations following KrF laser photolysis of 0.66 torr of XeF<sub>2</sub>.

**Appendix H**

**ANGULAR DEPENDENCE OF THE VIBRATIONAL RAMAN LINEWIDTHS  
FOR STIMULATED RAMAN SCATTERING IN H<sub>2</sub>**

International Laser Science Conference  
19-24 October 1986, Seattle, WA

Presented at: International Laser Science Conference, Seattle, WA,  
October 19-24, 1986, paper III-WE10.

## ANGULAR DEPENDENCE OF THE VIBRATIONAL RAMAN LINEWIDTHS FOR STIMULATED RAMAN SCATTERING IN H<sub>2</sub>

G. C. Herring, Mark J. Dyer, and William K. Bischel  
Chemical Physics Laboratory, SRI International  
Menlo Park, CA 94025

### ABSTRACT

We have measured the angular and density dependence of the Dicke narrowed vibrational line shapes for stimulated Raman scattering in H<sub>2</sub>. Measurements were made on the Q(1) transition for angles of 0-165 deg and for densities of 1-25 amagat. We have found an empirical formula that agrees with the results of these linewidth measurements to within 5%. This empirical formula will be useful for modeling the Raman gain coefficient as a function of angle for Raman beam clean-up and aperture combining.

### INTRODUCTION

Raman beam clean-up and aperture combining is currently a topic of intense research within the laser community. This technique improves the spatial mode of coherent light sources by using stimulated Raman scattering in H<sub>2</sub> to amplify a high quality Stokes beam. Energy is simultaneously transferred from several high intensity, poor quality pump beams to the high quality Stokes seed beam by crossing the pump beams at small angles to the Stokes beam. Thus the angular dependence of the Raman gain needs to be well characterized before this type of beam clean-up process can be accurately modeled. For pump and Stokes beams that are linearly polarized in the same directions, the angular dependence of the gain comes only from the angular dependence of the linewidth (the peak value of the steady-state gain coefficient is inversely proportional to linewidth). Previous experimental work reports linewidth measurements for only the forward and backward directions.<sup>1</sup> This work presents experimental results for the angular dependence of the vibrational Raman linewidth in gas phase H<sub>2</sub>.

### EXPERIMENTAL DETAILS

Using a standard quasi-cw stimulated Raman spectrometer,<sup>2</sup> we have measured the linewidth of the Q(1) line for angles of 0-165 degrees and densities of 1-25 amagat. Both the cw probe (683 nm) and the pulsed pump (532 nm) are single mode lasers, with the 10 ns pulsed laser limiting the spectral resolution to about 100 MHz. This laser linewidth was determined from the excess linewidth not accounted for by pressure or Doppler broadening in a copropagating

geometry, where the lineshape is well known, and from assuming that the laser line shape is Gaussian. For small angles (less than 30 deg) and small densities (less than 10 amagat), this laser linewidth was accounted for by fitting the data to Voigt line shapes. For large angles or large densities the 100 MHz width of the laser is negligible. These data were fit to pure Lorentzian line shapes.

#### EMPIRICAL MODEL

The density dependence of these measured linewidths was compared to an empirical model given by

$$\Delta\nu = \frac{A}{\left[\rho^n + \left(\frac{A}{\delta\nu_D}\right)^n\right]^{\frac{1}{n}}} + B\rho \quad (1)$$

and to the diffusion model<sup>3</sup> given by

$$\Delta\nu = \frac{A}{\rho} + B\rho \quad (2)$$

where  $\delta\nu_D$  is the Doppler broadened linewidth, B is the density broadening coefficient,  $\rho$  is the density. The quantity A is given by

$$A = \frac{D}{\pi} \left[ 2k_p k_s (1 - \cos\theta) + k_R^2 \right] \quad (3)$$

where  $\theta$  is the crossing angle, D is the self-diffusion coefficient, and  $k_p$ ,  $k_s$ , and  $k_R$  are the pump, stokes (probe), and Raman shift wave numbers respectively.

We find that Eq. 1, with  $n = 1.5$ , gives the best fit to our data and predicts the linewidths to within 5% of our measurements for all angles and densities. At densities below 1 amagat, the differences between the data and the model become larger. Because Eq. 1 is empirical, no physical significance should be attached to the value of 1.5 for n. The experimental data and the empirical fit of Eq. 1 for four different crossing angles is illustrated in Fig. 1.

Although useful for modeling purposes, the empirical Eq. 1 does little to help the understanding of the physics of the collisional contribution to the line shape. However, line shape measurements with uncertainties of less than 1% are necessary to compare with more physically meaningful models such as the Galatry and related line shapes.<sup>4</sup> We plan to make improved measurements (modifying our pulsed pump laser with a single mode seed laser) to make this comparison.

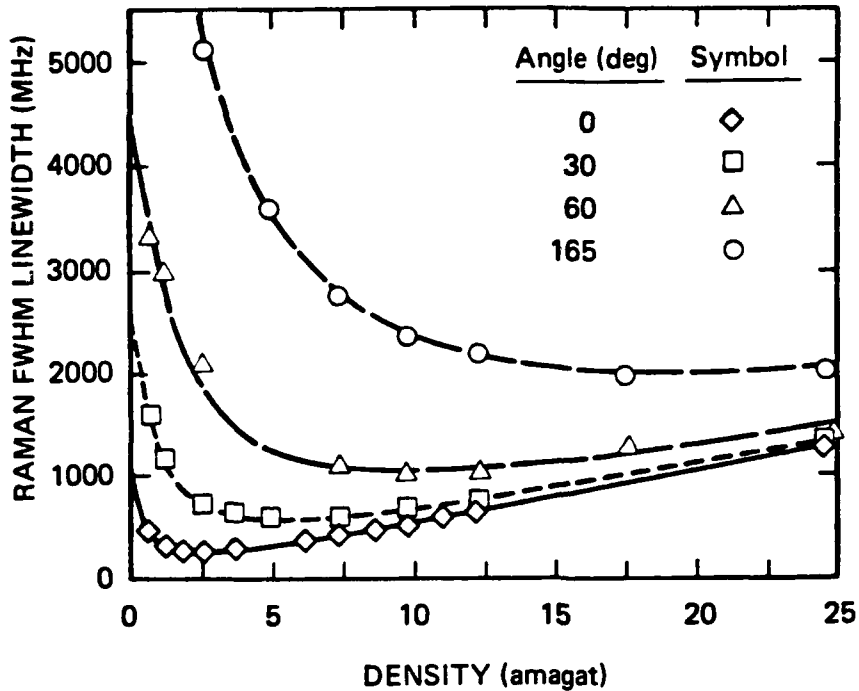


Figure 1. Comparison of the experimental data (symbols) and the empirical model (solid and dashed lines) of Eq. 1, with  $n = 1.5$ .

#### ACKNOWLEDGEMENT

This work was supported by the Defense Advanced Research Agency under Contract N0014-84-C-0256, through the Office of Naval Research.

#### REFERENCES

1. J. R. Murray and A. Javan, *J. Mol. Spectrosc.* **42**, 1 (1972).
2. P. Esherick and A. Owyong, "High-Resolution Stimulated Raman Spectroscopy," in *Advances in Infrared and Raman Spectroscopy*, R.J.H. Clark and R. E. Hestor, eds. (Heydon, London, 1983), pp. 130-187.
3. W. K. Bischel and M. J. Dyer, *Phys. Rev. A* **33**, 3113 (1986).
4. P. L. Varghese and R. K. Hanson, *Appl. Opt.* **23**, 2376 (1984).

## INTRODUCTION

Goal: Measure the angular dependence of the stimulated Raman gain coefficient for the vibrational Q branch lines in H<sub>2</sub>

Motivation: (1) Application to aperture combining and beam clean-up

(2) Aid in the understanding of the lineshape when collisional broadening and narrowing are both appreciable

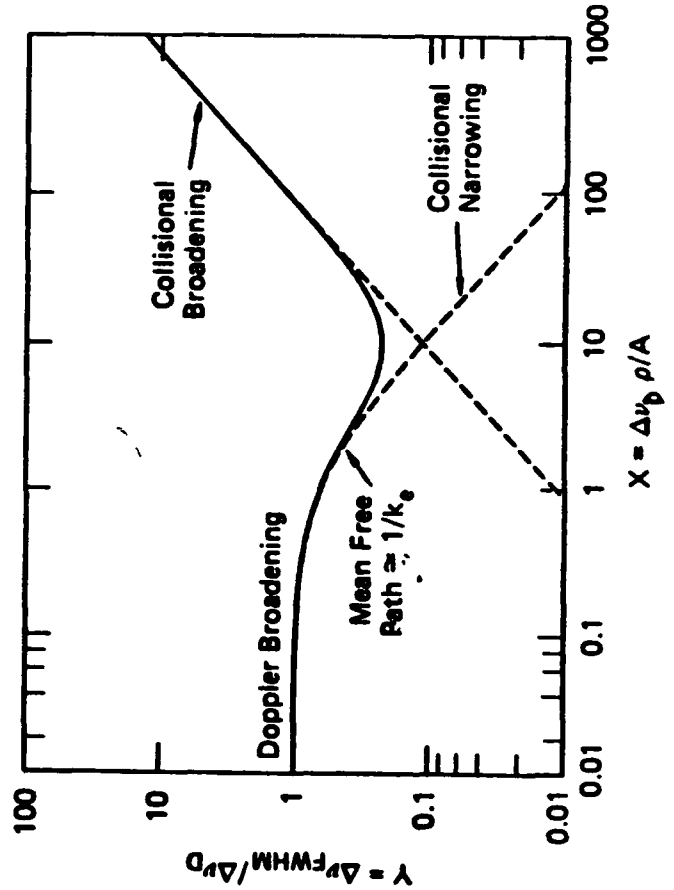
# Raman Linewidth Contributions in Dicke Narrowing Region

Broadening:  $\Delta\nu \propto \rho$

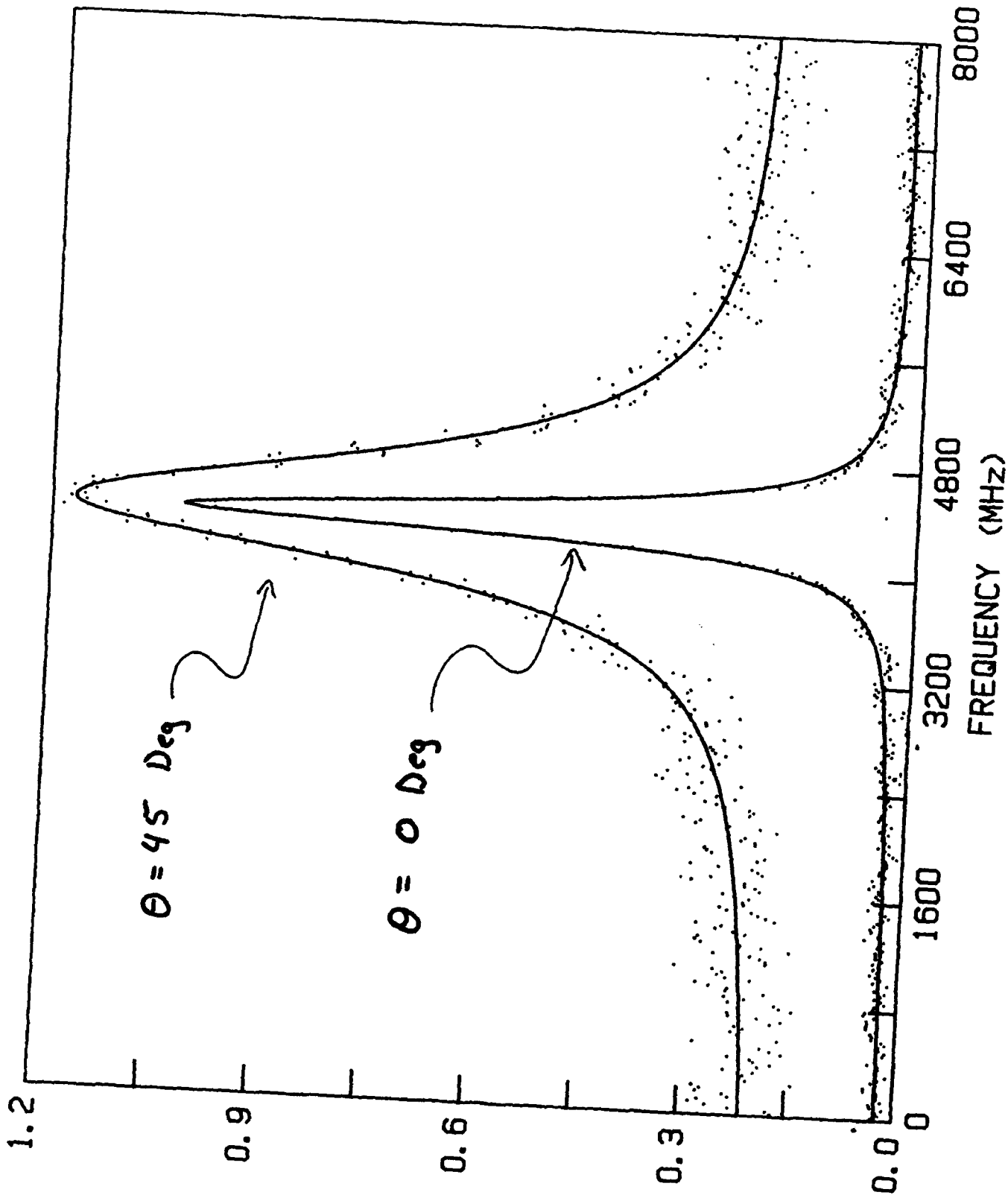
Narrowing:  $\Delta\nu = \frac{A}{\rho} \propto \frac{k_e^2}{\rho}$

Doppler:  $\Delta\nu_D \propto k_e$

$$k_e = \sqrt{2 k_p k_s (1 - \cos \theta) + k_r^2}$$



Net Result:



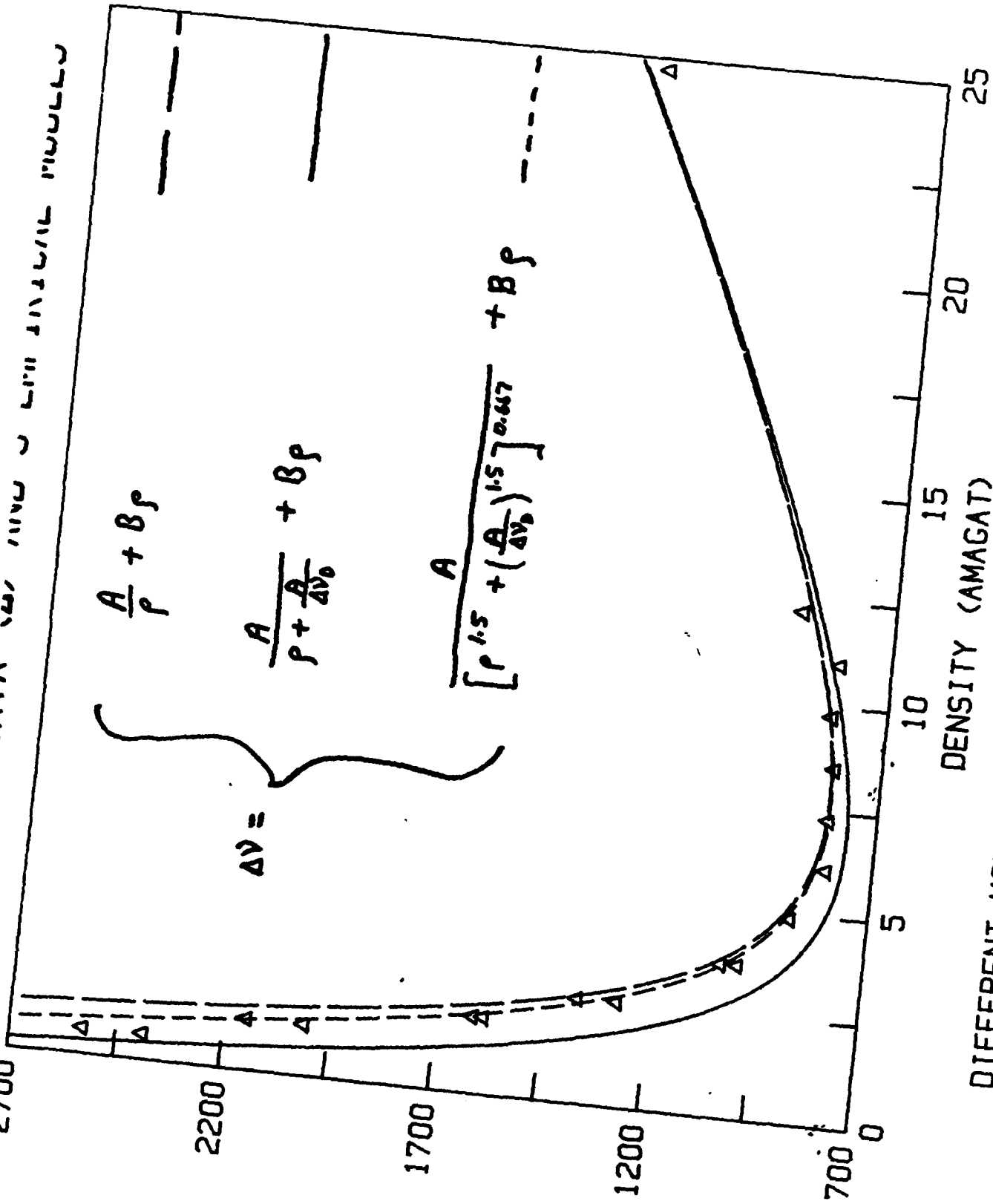
H<sub>2</sub> Q(1) LINE PROFILES AT 3000 TORR AND 295 K (3.7 AMAGAT)

RELATIVE SIGNAL

FWHM LINEWIDTH (MHZ)

H-7

DIFFERENT MODELS OF H<sub>2</sub> Q(1) LINEWIDTH AT 45 DEG

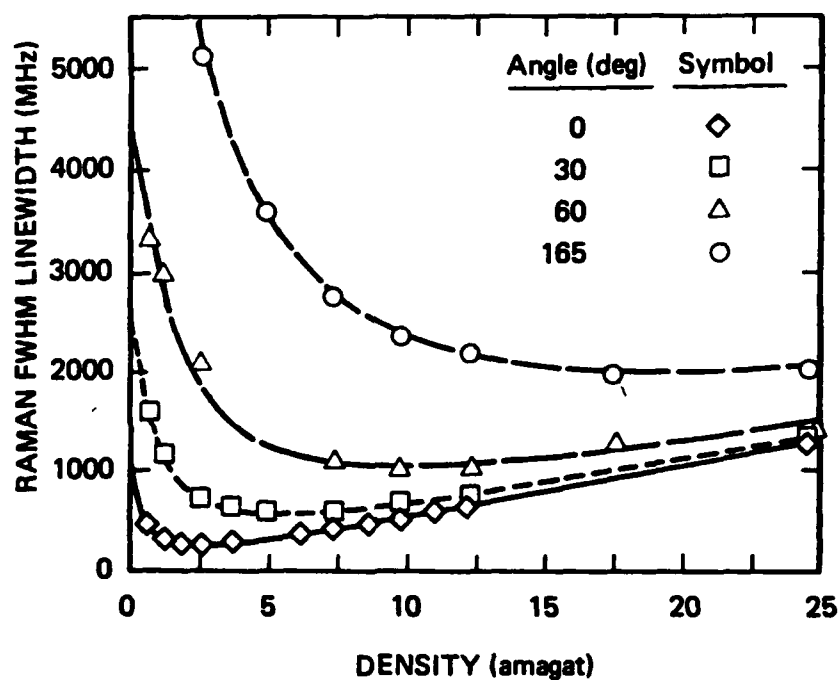


Eq. 1

Eq. 2

Eq. 3

## Comparison Between Data and Empirical Fit



$$\Delta\nu = \frac{A}{\left[ \rho^{1.5} + \left( \frac{A}{\Delta\nu_0} \right)^{1.5} \right]^{0.667}} + B\rho$$

$$A = \frac{D}{\pi} \left[ 2 K_p K_s (1 - \cos\theta) + K_r^2 \right]$$

## SUMMARY

- 1) Measured Raman lineshapes for Q(1) vibrations in H<sub>2</sub> vs. density (1-25 amagat) and vs. angle (0-165 deg).
- 2) Developed an empirical model that predicts the linewidths to within 5% of our measurements.

## Future Work

Higher signal-to-noise measurements will allow comparison to Galatry and other related lineshapes

**Appendix I**

**VIBRATIONAL RAMAN CROSS SECTIONS OF THE FUNDAMENTAL AND  
OVERTONE TRANSITIONS IN H<sub>2</sub>, D<sub>2</sub>, AND N<sub>2</sub>**

# VIBRATIONAL RAMAN CROSS SECTIONS OF THE FUNDAMENTAL AND OVERTONE TRANSITIONS IN H<sub>2</sub>, D<sub>2</sub>, and N<sub>2</sub>

G. C. Herring,<sup>†</sup> and William K. Bischel<sup>††</sup>  
Molecular Physics Laboratory  
SRI International, Menlo Park, CA 94025

and

Winifred M. Huo  
NASA Ames Research Center  
Moffett Field, CA 94035

## ABSTRACT

Theoretical and experimental results are presented for Raman scattering cross sections of the vibrational fundamental overtone transitions in gas phase H<sub>2</sub>, D<sub>2</sub>, and N<sub>2</sub>. Cross sections for the first overtones of H<sub>2</sub>, D<sub>2</sub>, and N<sub>2</sub> have been measured at 488 nm, while cross sections for the fundamental and first two overtones of H<sub>2</sub> and D<sub>2</sub> have been calculated as a function of wavelength from *ab initio* theory. For H<sub>2</sub>, the first overtone experimental result of  $5.1 \pm 1.5 \times 10^{-33} \text{ cm}^2 \text{ sr}^{-1}$ , is in reasonable agreement with the theoretical value of  $4.0 \times 10^{-33}$ . The measured value for N<sub>2</sub> of  $1.3 \pm 0.5 \times 10^{-33}$  is to be compared with the theoretical value of  $0.64 \times 10^{-33}$  of Langhoff et al. The role of nonadiabatic effects, arising from the breakdown of the Born-Oppenheimer approximation, is discussed for the overtone transitions.

---

<sup>†</sup> Current Address: NASA Langley Research Center, Hampton, VA 23665-5225

<sup>††</sup> Current Address: Coherent, Inc. 3210 Porter Drive, Palo Alto, CA 94304

## INTRODUCTION

In the vibrational Raman spectroscopy of diatomic gases, rigorous selection rules governing the change of vibrational quantum numbers do not exist. However, most of the past studies have been restricted to the O, Q, and S branches of the fundamental transition.<sup>1-3</sup> This limitation is mainly due to the fact that the overtone transitions are orders of magnitude weaker, making quantitative measurements difficult. Although the Raman overtone frequencies do not provide any new information about the vibrational constants of diatomic molecules, they can furnish an independent check of the constants derived from previous quadrupole experiments.<sup>4</sup> More importantly, experimental overtone cross sections can be used to verify or improve the approximations employed in the calculation of Raman transition probabilities. Since overtone transitions are related to the second and higher derivatives of the dynamic polarizability, they generally provide a more stringent test of the quality of the calculation than the fundamental transition. Overtone cross sections will also be useful for experiments<sup>5</sup> that require populating the higher lying vibrational levels of molecules.

The first overtone ( $\Delta v = 2$ ) has been measured<sup>6</sup> in solid  $H_2$ , and theoretical work for the first overtone of gas phase  $H_2^+$  has also been published,<sup>7</sup> but very little work has been reported on overtones of neutral diatomic molecules in the gas phase. In this paper, measurements of Raman scattering cross sections for the first vibrational overtone of  $H_2$ ,  $D_2$ , and  $N_2$  gases are reported. Theoretical calculations of the transition polarizabilities of  $H_2$  and  $D_2$  based on a sum-over-states method, are also presented for transitions from the ground state ( $v = 0 \rightarrow v' = 0, 1, 2, 3$ ) and the first vibration state ( $v = 1 \rightarrow v' = 1, 2, 3, 4$ ). These results are compared with the experiment for  $\Delta v = 1, 2$ . For  $N_2$ , an overtone cross section is determined from the dependence of theoretical static polarizabilities<sup>8</sup> on the internuclear separation. The present experimental results are compared with Knippers et al.<sup>9</sup> and Veirs,<sup>10</sup> who have also observed Raman overtones in diatomic gases. No

previous calculations of Raman overtones of H<sub>2</sub> and N<sub>2</sub> have been reported, even though accurate calculations of the dynamic polarizability<sup>11-15</sup> and Raman fundamental cross sections<sup>12-15</sup> have been reported for H<sub>2</sub>. A number of theoretical calculations on N<sub>2</sub> have also appeared in the literature. Good agreements with experimental data are found in the recent calculation of Langhoff et al.<sup>8</sup> on the static polarizability and polarizability derivatives of N<sub>2</sub>.

## EXPERIMENTAL DETAILS

The experimental apparatus used for the overtone measurements is similar to those used routinely in spontaneous Raman spectroscopy.<sup>1</sup> An Ar ion laser provided from one to five watts of linearly polarized light at wavelengths of 458 nm, 488 nm, or 515 nm. This beam was focussed into a cell containing H<sub>2</sub> at 295 K and 760 torr or into the room air for the N<sub>2</sub> experiments. In both cases, a 25-cm focal length lens was used to produce a beam diameter of 50  $\mu$ m at the focal plane. The Raman-scattered light was collected over a solid angle of 1 steradian at right angles to both the propagation direction and the electric field direction of the pump beam. This light was then directed through a polarization scrambler and into a 0.75-m Spex 1402 double monochromator (f/7). Slit widths were set at 800  $\mu$ m, giving the monochromator a resolution of 5  $\text{\AA}$  at visible wavelengths. The Raman signal was detected with a RCA 31034A photomultiplier tube which was cooled to -30° C and biased at 1300 volts. Output pulses from the photomultiplier tube were amplified by a factor of 250 and a pulse height discriminator was set to reject pulses smaller than 200 mv. Under these conditions, the dark count was typically 75 counts/s, while the Raman overtone signals were about 5 and 20 counts/s for N<sub>2</sub> and H<sub>2</sub> respectively. Time constants were 2 s and 40 s for the fundamental and overtone scans, respectively. The combined relative efficiency of the monochromator and photomultiplier tube was calibrated with an Optronics 220C spectral standard which is traceable to the NBS.

Overtone cross sections were experimentally determined by measuring the ratio of the overtone signal to the fundamental signal and using this ratio with the previously measured fundamental cross sections.<sup>2</sup> The Raman signal ratio of the overtone to the fundamental was measured by sequentially tuning the monochromator over these two transitions and comparing the integrated areas of the two transitions. Corrections in all of these ratios were made for changes in laser power, monochromator transmission and dispersion, and photomultiplier tube sensitivity. In N<sub>2</sub>, all of the individual rotational

transitions of the Q branch are so closely spaced that only a single spectral line was observed under the experimental conditions described above. Thus the nitrogen cross section measured here is the integrated cross section over the entire Q branch. In H<sub>2</sub>, the rotational transitions were resolved in the overtone, but were not resolved in the fundamental transition. Because of the long time constants used in the overtone scans, only the Q(0) and Q(1) transitions were typically recorded, while the entire integrated Q branch was recorded for the fundamental scans. Thus an additional correction (ratio of Q(0) plus Q(1) to the integrated Q branch) was made for the measured ratio in H<sub>2</sub> to obtain the total integrated Q branch ratio.

Results of the present measurements of the Raman overtone cross sections in H<sub>2</sub> and N<sub>2</sub> are shown in Table I, where the reported values are the average of five separate measurements. Uncertainties for each individual measurement were estimated to be  $\pm 20\%$  and  $40\%$  for H<sub>2</sub> and N<sub>2</sub> respectively. The uncertainties shown in Table I for this work are one standard deviation of the average for the five different measurements. Previous measurements of the fundamental cross sections and present theoretical results are also shown in Table I.

Our current overtone measurements have varying degrees of agreement with two previous overtone measurements. Our H<sub>2</sub> result is about 30% larger than the result of Veirs. However, this difference is well within the error bars of both experiments. In contrast, our N<sub>2</sub> and D<sub>2</sub> results are a factor of 3 greater than the results of Knippers et al.<sup>9</sup> Since we have carefully calibrated the wavelength response of our Raman spectrometer, and our results are consistent with those of Veirs,<sup>10</sup> we believe our determination of the cross section is the most accurate.

An attempt to observe the second overtone ( $\Delta v=3$ ) in both H<sub>2</sub> and N<sub>2</sub> was made using the 364 nm line of the Ar<sup>+</sup> ion laser. No signal was found in either case. This was

not surprising since calculations show that the signal exacted for a 2:1 signal-to-noise ratio was 40 times smaller than the detection limit.

## THEORETICAL CALCULATIONS

In the case of a linearly polarized pump beam, with the scattering angle  $90^\circ$  to both the polarization vector and the direction of incidence (without polarization analyzer), the Raman cross section for a Q(J) branch transition of a diatomic molecule in the  $^1\Sigma$  state is given by<sup>1</sup>

$$\frac{\partial \sigma_{vJ,v'J}}{\partial \Omega} = (2\pi)^4 (v_P - v_R)^4 (2J + 1) \times \left[ \begin{pmatrix} JJ0 \\ 000 \end{pmatrix}^2 \alpha_{vJ,v'J}^2 + \frac{7}{45} \begin{pmatrix} JJ2 \\ 000 \end{pmatrix}^2 \gamma_{vJ,v'J}^2 \right] \quad (1)$$

where  $v$  and  $v'$  are the vibrational quantum numbers of the initial and final states,  $J$  is the rotational quantum number,  $v_P$  is the frequency (in  $\text{cm}^{-1}$ ) of the incident beam and  $v_R$  is the Raman transition frequency. Also,  $\alpha_{vJ,v'J}$  and  $\gamma_{vJ,v'J}$  are the isotropic and anisotropic components of the transition polarizability. For  $v=v'$ , they reduce to the standard definition of the isotropic and anisotropic components of the polarizability of a molecule in the  $(v,J)$  state. Since this paper deals with Q branch transition only, the simpler notation  $\alpha_{vv'}$  and  $\gamma_{vv'}$  will be used and their  $J$  dependence will be implicitly assumed.

The quantities  $\alpha_{vv'}$  and  $\gamma_{vv'}$  are related to the parallel and perpendicular components of the transition polarizabilities,  $\alpha_{\parallel, vv'}$  and  $\alpha_{\perp, vv'}$ .

$$\alpha_{vv'} = \frac{1}{3} \left( \alpha_{\parallel, vv'} + 2\alpha_{\perp, vv'} \right). \quad (2)$$

$$\gamma_{vv'} = \alpha_{\parallel, vv'} - \alpha_{\perp, vv'}. \quad (3)$$

Using the Kramers-Heisenberg formula,  $\alpha_{\parallel, \nu\nu'}$  can be expressed as

$$\alpha_{\parallel, \nu\nu'} = \sum_i \sum_{v_i} \langle \Psi_{0v_i J_i} | \mu_{\parallel} | \Psi_{iv_i J_i} \rangle \langle \Psi_{iv_i J_i} | \mu_{\parallel} | \Psi_{0v J} \rangle \times \left( \frac{1}{E_{iv_i J_i} - E_{0v J} - \nu_p} + \frac{1}{E_{iv_i J_i} - E_{0v J} + \nu_s} \right) \quad (4)$$

where  $\mu_{\parallel}$  denotes the parallel component of the dipole operator,  $\psi$  is the rovibronic wavefunction of the molecule,  $o$  denotes the initial (=final) electronic state, and  $\nu_s$  is the frequency of the scattered beam. The index  $i$  sums over all electronic states,  $v_i$  the vibrational levels of  $i$ , and  $J_i$  its rotational quantum number. The summations over  $i$  and  $v_i$  include integration over the continuum portion of the electronic and vibrational manifold. The summation over  $J_i$ , ( $J_i = J, J \pm 1$ ), has been carried out implicitly in the derivation of the 3-j symbols in Eq. (1), with the assumption that the dipole matrix elements of the three possible  $J_i$  are the same. Notice that Eq. (4) is applicable to a molecule without a permanent dipole moment.

In Eq. (4,) nuclear motions are included explicitly in the summation. On the other hand, in the Born-Oppenheimer approximation, the electronic polarizability is first calculated in the fixed-nuclei approximation and then integrated over the initial and final rovibronic states:

$$\alpha_{\parallel}(\nu_p, R) = \sum_i \langle \Phi_0(r, R) | \mu_{\parallel} | \Phi_i(r, R) \rangle_{\mathbf{r}} \langle \Phi_i(r, R) | \mu_{\parallel} | \Phi_0(r, R) \rangle_{\mathbf{r}} \times \left( \frac{1}{E_i(R) - E_0(R) - \nu_p} + \frac{1}{E_i(R) - E_0(R) + \nu_s} \right), \quad (5)$$

and

$$\alpha_{||, v v'} = \langle \chi_v'(R) | \alpha_{||}(v_p R) | \chi_v(R) \rangle. \quad (6)$$

In Eq. (5),  $r$  and  $R$  denote the electronic and nuclear coordinates, and the subscript  $r$  attached to the bracket denotes integration over electronic coordinates alone. Also,  $\Phi$  is the fixed-nuclei electronic wavefunction and  $\chi$  is the vibrational wavefunction of the electronic state  $o$ . The difference between Born-Oppenheimer and nonadiabatic treatments have been discussed in detail by Bishop and Cheung.<sup>11</sup> In their calculation on  $H_2$ , they recast the ro-vibronic problem into a secular equation problem. Their results are considered intermediate between the fixed-nuclei and nonadiabatic treatments. The calculations of Rychlewski,<sup>12</sup> Huo and Jaffe,<sup>14</sup> Ford and Browne,<sup>15</sup> and Langhoff et al,<sup>8</sup> are all based on the Born-Oppenheimer approximation, even though different methods are used in the treatment of the electronic part of the problem.

In the present calculation on  $H_2$ , a method which is a combination of Eq. (4) and (5) was employed.<sup>16</sup> From a previous sum-over-state calculation,<sup>14</sup> it was found that approximately 75% of  $\alpha_{00}$  and 90% of  $\alpha_{01}$  come from the contributions of  $B^1\Sigma_u^+$  and  $C^1\Pi_u$  states, the two lowest excited singlet states of  $H_2$ . Thus, in this study, the nonadiabatic effects from these two states were accounted for by carrying out explicit summation over their ro-vibrational levels, as given in Eq. (4). The contributions from the remainder of the electronic states were calculated using the Born-Oppenheimer approximation, as in Eq. (5). In this manner, a major portion of the nonadiabatic effects has been included. The electronic wavefunctions used are configuration-interaction (CI) wavefunctions constructed to satisfy the Dalgarno-Epstein condition,<sup>17</sup> which enables us to replace the infinite sum over electronic states by a finite sum. The details of the electronic calculations have been described previously.<sup>14</sup> The vibrational wavefunctions were the numerical solutions of the one-dimensional Schrödinger equation of vibrational motion,

obtained using the Numerov-Cooley technique. The potential functions for the X, B, and C state vibrations were taken from the work of Kolos and Wolniewicz.<sup>18-20</sup>

A summary of the H<sub>2</sub> Rayleigh and Raman cross sections from the present calculation is given in Tables II and III. Average polarizabilities and polarizability anisotropies are also given for each transition. Table II contains results for transitions originating in  $v = 0$ , while Table III contains results for transitions originating in  $v = 1$ . The numbers given in Table II are used in Fig. 1 to show the relative wavelength dependence of the square of the polarizabilities (proportional to the scattering cross section  $\frac{\partial\sigma}{\partial\Omega}$ ) for the different scattering processes in H<sub>2</sub>. In addition to illustrating the difference in the wavelength dependence of the different processes, Fig. 1 also shows the preresonance enhancement for the fundamental with the  $2p\sigma^1\Sigma_u^+$  state at  $90,000\text{ cm}^{-1}$ . All cross sections given in Tables II and III are averaged over the thermal distribution of initial rotational levels. One of the interesting results of these calculations is that the polarizability anisotropy for the first overtone crosses zero between 250 and 300 nm. Thus the cross sections for the S branch of the  $v = 0 \rightarrow 2$  transition will vanish for pump lasers in this wavelength region.

Theoretical cross sections at 488 nm are compared to experimental cross sections in Table I. For H<sub>2</sub>, the theoretical overtone values of Table I are taken directly from Table II. The corresponding quantity for N<sub>2</sub>, calculated from the theoretical static polarizability of Langhoff et al. using Eq. (6), is also presented. An RKR potential is used for the N<sub>2</sub> vibration.<sup>21</sup> For comparison purposes, previous calculations of the fundamental cross sections are also listed. Since Rychlewski, and Ford and Browne, did not include 488 nm in their calculation of H<sub>2</sub> fundamental, the tabulated cross sections are obtained by spline fitting the frequency dependence of their published  $\alpha_{01}$  and  $\gamma_{01}$ .

## DISCUSSION

It is illustrative to compare the experimental cross section of the fundamental transition with theory first. Overall, good agreement between theory and experiment is obtained for both molecules. In particular, the three calculations on H<sub>2</sub> using the adiabatic approximation are in excellent agreement with each other. Among the three, the wavefunction employed by Rychlewski is of the highest quality. The nonadiabatic result, from an unpublished calculation of Huo,<sup>16</sup> is  $\approx 10\%$  smaller, and is in somewhat closer agreement with experiment. The electronic wavefunctions used in the nonadiabatic calculation are determined in a manner similar to those used in Ref. 14. The difference between the results in Ref. 14 and 16 is partially due to the difference in the basis sets, and partially due to nonadiabatic effects. The calculation of Cheung et. al.<sup>13</sup> also includes nonadiabatic effects. Their cross section is not included in Table I because their  $\alpha_{01}$  is not tabulated in Ref. 13. There is no reported nonadiabatic calculations in the literature for N<sub>2</sub>. However, N<sub>2</sub> is a heavier molecule. It is possible that, at least for the fundamental, the nonadiabatic effect in N<sub>2</sub> is smaller than in H<sub>2</sub>. Indeed the theoretical cross section of the N<sub>2</sub> fundamental agrees well with experiment. It should be noted that the N<sub>2</sub> cross section is deduced from a static field calculation. However,  $\alpha_{01}$  and  $\gamma_{01}$  of N<sub>2</sub> are weakly dependent on  $\nu_p$  at 488 nm, and only a small error is expected to result from the neglect of frequency dependence in these two quantities.

For the overtone transitions, the calculated cross section of H<sub>2</sub> is approximately 20% smaller than the experimental value, but lies inside the experimental error limit. For N<sub>2</sub>, the theoretical value is also smaller than our experiment by a factor of two. There are two possible sources for the discrepancies: the quality of the electronic wavefunctions

used, and incomplete treatment of nonadiabatic effects. In the simple harmonic oscillator approximation,  $\alpha_{v'v}$  and  $\gamma_{v'v}$  for the first overtone transition are expressed in terms of the second derivatives of the dynamic polarizabilities  $\alpha(v_p, R)$  and  $\gamma(v_p, R)$ . Thus, a calculation of these quantities generally requires wavefunctions of higher quality than the fundamental transition. Even though exact vibrational wavefunctions are used in our calculation, the stringent demand of high-quality wavefunctions probably still holds. Certainly it is one possible source of the observed deviation.

Nonadiabatic effects is another possible source of error in the theoretical treatment of the  $N_2$  overtone cross section. To understand the importance of vibronic coupling in overtone transitions, it is worthwhile to analyze the two nonadiabatic calculations of  $H_2$ . For the fundamental, 91% of  $\alpha_{01}$  and 112% of  $\gamma_{01}$  comes from the contributions of B and C states. (For  $\gamma_{01}$ , the contribution from the remainder of the electronic states are opposite in sign from the B and C contribution, resulting in a final value smaller than the B and C contribution alone.) It is reasonable to assume that most of the nonadiabatic effects are accounted for if Eq. (4) is used for those two states. On the other hand, only 72% of  $\alpha_{02}$  and 34% of  $\gamma_{02}$  come from the B and C contribution. Thus, nonadiabatic treatment of those two states alone is probably insufficient. It is even more illustrative to compare the contributions from the bound and continuum vibrational levels of those two states. For  $\alpha_{01}$  the contribution from the continuum portion of B state vibrational manifold is 4.1% of the bound level contribution, and it is 14.5% for the C state. In the case of  $\alpha_{02}$ , the ratios are 77.4% and 74.2%, respectively. The heavy participation of the B and C continuum in the overtone is a reflection of the vastly different spatial extent of the  $v=0$  and  $v=2$  vibrational wavefunctions of the ground state, much more so than the case between  $v=0$  and 1. This finding strongly suggests that contributions from other electronic states should also be calculated using Eq. (4) instead of Eq. (5).

For N<sub>2</sub>, nonadiabatic studies have not been reported in the literature. However, a comparison of the adiabatic cross section with experiment indicates that nonadiabatic effects, assumed to be unimportant for the fundamental, may well play a more important role in the overtone transition. Another possible source of error, resulting from the use of static-field  $\alpha_{02}$  and  $\gamma_{02}$ , is estimated to be 1-2%, based on the corresponding frequency dependence found in H<sub>2</sub>.

Finally, we can compare the theoretical results for the  $v=1$  polarizability  $\alpha_{11}$  to measurements<sup>22,23</sup> of the change in the index of refraction between the ground and first vibrational state at 693 nm. The index of refraction for the  $v=1$  level is particularly important for calculating phase perturbations (and hence the beam quality) that occur in large scale Raman amplifiers.<sup>24</sup> From Tables II and III, we obtain the value for  $\Delta\alpha = \alpha_{11} - \alpha_{00} = 7.08 \times 10^{-26} \text{ cm}^3$ . The theory predicts that the index of refraction of the  $v = 1$  vibrational level is 8.6% larger than that of the  $v = 0$  level. This can be compared with the previously measured value<sup>23</sup> of  $\Delta\alpha = 1.53 \pm 0.22 \times 10^{-25} \text{ cm}^3$  (19% larger than the  $v = 0$  level) and a semi-empirical calculation<sup>25</sup> of  $1.40 \times 10^{-25} \text{ cm}^3$ . The discrepancy is larger by more than the estimated error of < 5% in the present theoretical calculation. Since the present theory predicts  $\alpha_{00}$  of  $v = 0$  to within the error bars of the index of refraction data<sup>16</sup> (<1%),  $\alpha_{01}$  for the  $v=0 \rightarrow 1$  transition to within the error bars of Raman scattering data,<sup>2</sup> (<5%), and  $\alpha_{02}$  for the  $v=0 \rightarrow 2$  transition to within the experimental error bar (20%), it is hard to rationalize such a large discrepancy between the experiment and our theory. We therefore conclude that additional experimental and theoretical research is required to resolve the differences.

10. K. Veirs, "A Raman Spectroscopic Investigation of Molecular Hydrogen," Materials and Research Division, Lawrence Berkeley Laboratory, University of California, Report LBL 20565, UC 34A, December 1985.
11. D. M. Bishop and L. M. Cheung, *J. Chem. Phys.* **72**, 5125 (1980).
12. J. Rychlewski, *J. Chem. Phys.* **78**, 7252 (1983).
13. L. M. Cheung, D. M. Bishop, D. L. Drapcho, and G. M. Rosenblatt, *Chem. Phys. Letters* **80**, 445 (1981).
14. W. M. Huo and R. L. Jaffe, *Phys. Rev. Letters*, **47**, 30 (1981).
15. A. L. Ford and J. C. Browne, *Phys. Rev. A* **7**, 418 (1973).
16. W. M. Huo, unpublished, 1985.
17. A. Dalgarno and S. T. Epstein, *J. Chem. Phys.* **50**, 2837 (1969).
18. W. Kolos and L. Wolniewicz, *J. Chem. Phys.* **43**, 2429 (1965).
19. W. Kolos and L. Wolniewicz, *J. Chem. Phys.* **45**, 509 (1966).
20. W. Kolos and L. Wolniewicz, *J. Chem. Phys.* **48**, 3672 (1968).
21. A. Lofthus and P. H. Krupenie, *J. Phys. and Chem. Reference Data* **6**, 113 (1977); 2429 (1965).
22. U. S. Butylkin, G. V. Venkin, L. L. Kulyuk, D. I. Maleev, V. P. Protasov, and Yu. G. Khronopulo, *ZhETF Pis. Red.* **19**, 474 (1974) [*JETP Lett.* **19**, 253 (1974)].

23. M. I. Baklushina, B. Ya. Zel'dovich, N. A. Mel'nikov, N. F. Pilipetskii, Yu. P. Raizer, A. N. Sudarkin, and V. V. Shkunov, *Zh. Eksp. Teor. Fiz.* **73**, 831 (1977) [*Sov. Phys. JETP* **46**, 436 (1977)].
24. A. Flusberg and D. Korff, "Effect of Beam Quality on Transient Refractive-Index Changes in Stimulated Raman Scattering," *Conference on Lasers and Electro-Optics*, San Francisco (9-13 June 1986).
25. B. Wilhelmi and E. Heunamn, *Zh. Prikl. Spektrosk.* **19**, 3 (1973).

## CONCLUSION

In summary, experimental and theoretical results are presented for the fundamental and overtone Raman cross sections in  $H_2$ ,  $D_2$ , and  $N_2$ . The  $H_2$  fundamental measurement is in better agreement with the partially nonadiabatic calculation than with the completely adiabatic calculation. In addition, the  $H_2$  overtone measurement is in satisfactory agreement with the partial nonadiabatic calculation. For  $N_2$ , although the fundamental adiabatic result is in good agreement with experiment, the overtone adiabatic result is a factor of 2 smaller than the experiment. These results suggest that the partially nonadiabatic treatment describes the Raman process in gas phase diatomic molecules better than a purely adiabatic treatment. To further test this conclusion, purely nonadiabatic calculations and more accurate experimental measurements would both be helpful.

## ACKNOWLEDGMENT

G.C.H. and W.K.B acknowledge support from the Defense Advanced Research Projects Agency under Contract N00014-8884-C-0256 through the Office of Naval Research. W.M.H. gratefully acknowledges the use of unpublished data from S. Langhoff in the calculation of the N<sub>2</sub> overtone polarizability.

## REFERENCES

1. H. W. Schrötter and H. W. Klöckner, in *Raman et al. Spectroscopy of Gases and Liquids*, edited by A. Weber (Springer, et al. Berlin, 1979).
2. W. K. Bischel and G. Black, in AIP Conference Proceedings, No. et al. 100, Subseries on Optical Science and Engineering, No. 3, Excimer Lasers 1983, edited by C. K. Rhodes, H. Esser, and H. Pummer (AIP, New York, 1983).
3. D. G. Fouche and C. K. Chang, *Appl. Phys. Lett.* **20**, 256 (1972).
4. U. Fink, T. A. Wiggins, and D. H. Rank, *J. Mol. Spectry.* **18**, 384 (1965).
5. T. Kreutz, J. Gelfand, and R. B. Miles, "Overtone Stimulated Raman Pumping of H<sub>2</sub> from  $v=0$  to  $v=2$ , and Subsequent Time Domain Photoacoustic Detection of Vibrational Relaxation," Ohio State University Molecular Spectroscopy Symposium, Columbus, OH, June, 1985.
6. W. C. Prior and E. J. Ellin, *Can. J. Phys.* **50**, 1471 (1972); N. H. Rich and W.R.C. Prior, *Raman News Letter* **36**, (1971).
7. A. I. Sherstyuk and N. S. Yakovleva, *Opt. Spectrosc.* **45**, 23 (1978)
8. S. R. Langhoff, C. W. Bauschlicher, Jr., and D. P. Chong, *J. Chem. Phys.* **78**, 5287 (1983).
9. W. Knippers, K. Van Helvoort and S. Stolte, *Chem. Phys. Lett.* **121**, 279 (1985).

Table 1. Vibrational Raman cross section  $\frac{\partial\sigma}{\partial\Omega}$  for the fundamental and first two overtone Q-branch transitions ( $\lambda_p = 488$  nm).

	Fundamental ( $v=0 \rightarrow 1$ ) $\times 10^{-30} \text{ cm}^2 \text{ sr}^{-1}$		1st Overtone ( $v=0 \rightarrow 2$ ) $\times 10^{-32} \text{ cm}^2 \text{ sr}^{-1}$		2nd Overtone ( $v=0 \rightarrow 3$ ) $\times 10^{-34} \text{ cm}^2 \text{ sr}^{-1}$	
	D <sub>2</sub>	H <sub>2</sub>	D <sub>2</sub>	H <sub>2</sub>	N <sub>2</sub>	H <sub>2</sub>
<b>Experiment</b>						
Present Work						
Ref. 9			0.44±0.1	0.51±0.15	0.13±0.05	≤3
Ref. 10					0.38	
Ref. 1	1.2	1.3	0.55±0.01	0.13±0.5		0.047±0.16
Ref. 2	1.1±0.11	1.4±0.14	0.57±0.06			
Ref. 3		1.3±0.5	0.56±0.22			
<b>Theory, Nonadiabatic Present Work</b>						
Ref. 16	1.42				0.4	0.32
<b>Theory, Adiabatic</b>						
Ref. 12	1.57					
Ref. 14	1.64					
Ref. 15	1.53					
Ref. 8		0.53				0.064

\* Uncertainty estimated at a factor of 2-3.

Table 2. Nonadiabatic calculation of the wavelength dependence of the average polarizability  $\alpha$ , polarizability anisotropy  $\gamma$  (in atomic units\*) an differential scattering cross section  $\frac{\partial\sigma}{\partial\Omega}$  of Rayleigh and vibrational Raman transitions for the ground state ( $v=0$ ) in  $H_2$ . The  $\Delta\nu$  frequencies are for the Q(0) transition  $\frac{\partial\sigma}{\partial\Omega}$  is calculated from Eq. 1 for the entire Q branch at 298 K.

$\lambda(\text{nm})$	Rayleigh			Vibrational Raman								
	$\alpha_{00}$	$\gamma_{00}$	$\frac{\partial\sigma}{\partial\Omega}$	$\alpha_{01}$	$\gamma_{01}$	$\frac{\partial\sigma}{\partial\Omega}$	$\alpha_{02}$	$\gamma_{02}$	$\frac{\partial\sigma}{\partial\Omega}$	$\alpha_{03}$	$\gamma_{03}$	$\frac{\partial\sigma}{\partial\Omega}$
	a.u.	a.u.	$10^{-28} \text{ cm}^2/\text{sr}$	a.u.	a.u.	$10^{-30} \text{ cm}^2/\text{sr}$	a.u.	a.u.	$10^{-32} \text{ cm}^2/\text{sr}$	a.u.	a.u.	$10^{-33} \text{ cm}^2/\text{sr}$
$\infty$	5.469	2.013	0.0	.694	.581	0.0	-.0692	-.0139	0.0	.0127	-.0002	0.0
600	5.584	2.085	0.828	.733	.625	0.468	-.0701	-.0103	0.092	.0126	-.0011	0.0032
550	5.607	2.099	1.19	.738	.631	0.750	-.0701	-.0097	0.176	.0126	-.0012	0.0093
500	5.637	2.118	1.75	.745	.638	1.25	-.0701	-.0093	0.342	.0126	-.0012	0.0252
450	5.678	2.144	2.71	.755	.649	2.16	-.0701	-.0070	1.38	.0125	-.0014	0.0651
400	5.736	2.181	4.44	.770	.665	3.98	-.0701	-.0070	1.38	.0125	-.0015	0.166
350	5.824	2.238	7.78	.791	.689	7.92	-.070	-.0048	2.97	.0125	-.0017	0.427
300	5.965	2.331	15.2	.828	.729	17.7	-.070	-.0008	6.76	.0124	-.0021	1.135
250	6.218	2.501	34.2	.896	.806	47.2	-.068	.0078	16.6	.0121	-.0028	3.198
200	6.757	2.881	98.6	1.05	.986	174.0	-.062	.0323	41.4	.0115	-.0039	9.702

\* 1 a.u. =  $1.481845 \times 10^{-25} \text{ cm}^3$

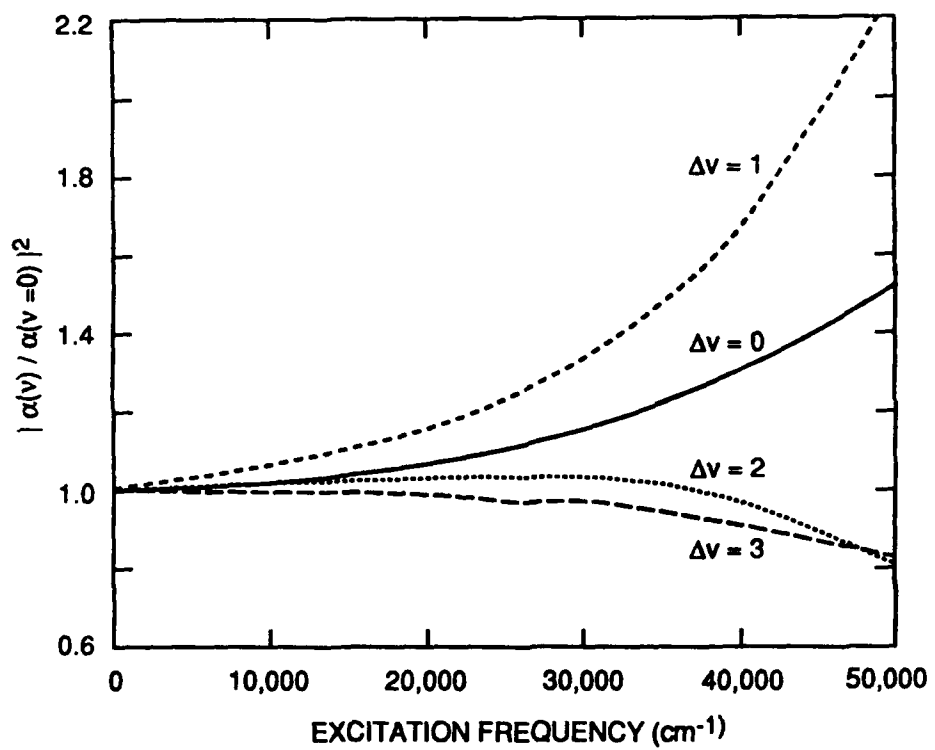
Table 3. Nonadiabatic calculation of the wavelength dependence of the average polarizability  $\alpha$ , polarizability anisotropy  $\gamma$  (in atomic units\*) an differential scattering cross section  $\frac{\partial\sigma}{\partial\Omega}$  of Rayleigh and vibrational Raman transitions for the excited state ( $v=1$ ) in  $H_2$ . The  $\Delta\nu$  frequencies are for the Q(0) transition  $\frac{\partial\sigma}{\partial\Omega}$  is calculated from Eq. 1 for the entire Q branch at 298 K.

$\lambda(\text{nm})$	Rayleigh			Vibrational Raman								
	$\alpha_{11}$	$\gamma_{11}$	$\frac{\partial\sigma}{\partial\Omega}$	$\alpha_{12}$	$\gamma_{12}$	$\frac{\partial\sigma}{\partial\Omega}$	$\alpha_{13}$	$\gamma_{13}$	$\frac{\partial\sigma}{\partial\Omega}$	$\alpha_{14}$	$\gamma_{14}$	$\frac{\partial\sigma}{\partial\Omega}$
	a.u.	a.u.	$10^{-28} \text{ cm}^2/\text{sr}$	a.u.	a.u.	$10^{-30} \text{ cm}^2/\text{sr}$	a.u.	a.u.	$10^{-32} \text{ cm}^2/\text{sr}$	a.u.	a.u.	$10^{-33} \text{ cm}^2/\text{sr}$
$\infty$	5.923	2.473	0.0	1.01	.901	0.0	-.135	-.052	0.0	.0252	-.0003	0.0
600	6.062	2.576	0.985	1.07	.974	1.09	-.138	-.047	0.444	.0248	-.0026	0.0208
550	6.089	2.596	1.40	1.08	.984	1.73	-.138	-.047	0.825	.0247	-.0027	0.0539
500	6.125	2.623	2.08	1.09	.997	2.85	-.138	-.046	1.56	.0247	-.0030	0.133
450	6.175	2.661	3.22	1.11	1.02	4.93	-.138	-.0044	3.02	.0256	-.0033	0.322
400	6.249	2.716	5.27	1.13	1.04	9.04	-.139	-.042	6.08	.0245	-.0038	0.774
350	6.354	2.799	9.29	1.17	1.09	18.0	-.139	-.038	12.9	.0242	-.0045	1.89
300	6.529	2.936	18.2	1.23	1.16	40.03	-.139	-.031	29.1	.0238	-.0057	4.78
250	6.845	3.193	41.6	1.34	1.30	109.0	-.138	-.016	71.4	.0229	-.0080	12.6
200	7.536	3.789	123.0	1.60	1.63	415.0	-.124	.032	169.0	.0206	-.0125	34.1

\* 1 a.u. =  $1.481845 \times 10^{-25} \text{ cm}^3$

## FIGURE CAPTIONS

Figure 1. Relative frequency dependence of the square of the average polarizabilities,  $|\alpha(\nu)/\alpha(\nu = 0)|^2$ , for Rayleigh scattering with  $\Delta\nu = 0$  (solid), fundamental Raman with  $\Delta\nu = 1$  (medium dash), 1st overtone Raman with  $\Delta\nu = 2$  (short dash), and 2nd overtone Raman  $\Delta\nu = 3$  (long dash).



CM-330511-8A

**Appendix J**

**OPTICAL STARK SHIFT SPECTROSCOPY:  
MEASUREMENT OF THE  $v = 1$  POLARIZABILITY OF  $H_2$**

Phys. Rev. A44, 3138 (1991)

Optical Stark shift spectroscopy: Measurement of the  $\nu = 1$  polarizability in  $H_2$ 

Mark J. Dyer and William K. Bischel\*

Molecular Physics Laboratory, SRI International, Menlo Park, California 94025

(Received 12 November 1990)

We report a quantitative determination of the  $\nu = 1$  polarizability in  $H_2$  by measuring the optical Stark shift and splitting of the  $Q(0)$  and  $Q(1)$  vibrational Raman transitions. For the  $Q(1)$  transition, the  $M_J = \pm 1, 0$  components are resolved, thereby allowing a determination of the polarizability anisotropy for the  $\nu = 1$  state. The measured optical Stark shift of the  $Q(0)$  transition at 1060 nm is 23  $\text{MHz GW}^{-1} \text{cm}^2$ , giving a polarizability difference between the  $\nu = 1$  and 0 states of  $\Delta\alpha = 0.49 \pm 0.03$  a.u., in good agreement with *ab initio* theory.

## INTRODUCTION

The optical Stark effect will cause the rotational-vibrational energy levels in small molecules to shift and split due to the presence of a high-intensity nonresonant laser field. This effect has recently been observed for both vibrational [1] and rotational [2] Raman transitions in high-resolution Raman gain experiments using an optically applied Stark field. Because shifting of the energy levels effectively broadens the observed linewidths, it is one of the important mechanisms that limit the spectral resolution of coherent Raman experiments. Hence, the optical Stark effect has recently been included in the theory [3] of saturation processes in coherent anti-Stokes Raman spectroscopy (CARS). In other experiments, the broadening and shift of the anti-Stokes radiation generated by multiwave Raman mixing has been interpreted to be due to the optical Stark effect [4,5]. While all these experiments have tried to interpret their results based on order-of-magnitude estimates of the optical Stark effect, there have been no quantitative experiments that have used the nonresonant optical Stark effect to derive fundamental constants for the excited vibrational states of small molecules.

We report an experiment to use optical Stark spectroscopy for quantitative measurement of the polarizability and the polarizability anisotropy of the  $\nu = 1$  vibrational state in  $H_2$ . Hydrogen is a particularly interesting first molecule to study for a number of reasons. First, there are accurate *ab initio* calculations [6] of polarizabilities in  $H_2$  that can be used to make a quantitative comparison between theory and experiment.

Second, accurate knowledge of the optical Stark shift in  $H_2$  is of great practical importance in the design of Raman amplifiers and beam combining techniques [7] since  $H_2$  is the gas most often used for stimulated Raman frequency conversion applications. For this application, it is quite important to know the polarizability of the  $\nu = 1$  in  $H_2$  since the change in the polarizability between the  $\nu = 0$  and the  $\nu = 1$  vibrational states ( $\Delta\alpha$ ) will determine the phase perturbations (and hence the beam quality) that occur across the spatial aperture of a large scale Raman amplifier [7]. The exact value of  $\Delta\alpha$  has been an issue for a number of years due to the fact that there is a factor-

of-2 discrepancy between current measurements [8] and *ab initio* theory [6]. An accurate measurement of the optical Stark effect for the vibrational Raman transition in  $H_2$  would resolve this controversy.

The goal of our experiments was to measure the optical Stark effect for the  $Q(0)$  and  $Q(1)$  vibrational Raman transitions in  $H_2$  and compare the measurements to *ab initio* theory. The energy levels and splittings in an optical field for the  $Q(1)$  transition are illustrated in Fig. 1, where the magnitude of the shifts in units of  $\text{MHz}/(\text{GW cm}^{-2})$  are calculated from the data presented in this paper and Ref. [6]. Without the high-intensity nonresonant optical field, the zero-pressure Raman frequency shift for the  $Q(1)$  transition is  $4155.247 \pm 0.007 \text{ cm}^{-1}$  as measured by Fourier-transform Raman spectroscopy [9]. When the nonresonant field is applied, there is a shift of the  $\nu = 0$  and 1 vibrational levels from their zero field values, and

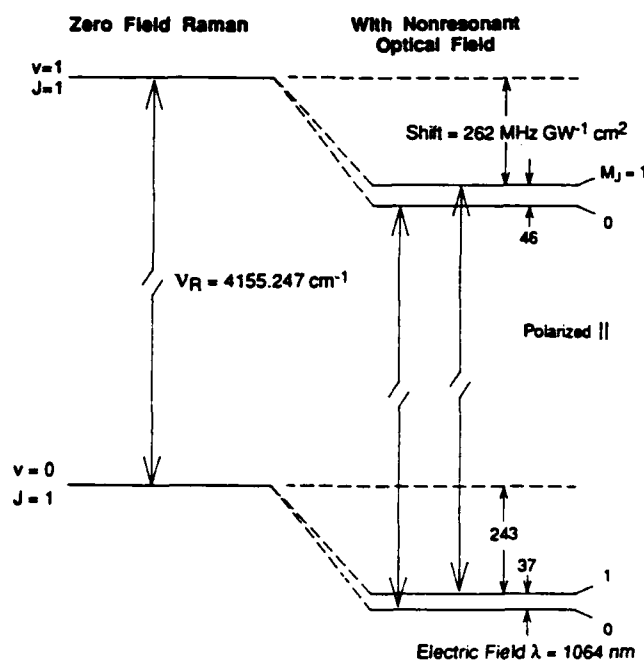


FIG. 1. Schematic illustrating level shifts of the  $Q(1)$  branch in  $H_2$  under the influence of a strong electric field.

the  $M_J$  degeneracy of the  $J=1$  rotational level is split. (The  $J=0$  levels will only show a shift since they are non-degenerate.) As illustrated in Fig. 1, the magnitude of shift in the vibrational levels (which is proportional to the average polarizability; see theory section) is approximately six times larger than the magnitude of the  $M_J$  splitting (which is proportional to the polarizability anisotropy). We can indirectly observe these energy-level shifts by carefully measuring the shift of the Raman transition frequency (illustrated by the arrows in Fig. 1) with and without the nonresonant field. The shift of the Raman frequency is due to the difference in the optical Stark shifts of the  $v=0$  and 1 levels, and hence the Raman frequency would not change if the polarizabilities for these levels were the same (i.e., if  $\Delta\alpha=0$ ).

In our experiments we use linear polarization for both the Raman pump-probe field and the nonresonant field. Therefore we have a selection rule of  $\Delta M=0$  for the Raman transitions. As illustrated in Fig. 1, we expect to observe two Raman transitions for  $M_J=0$  and  $\pm 1$ . The splitting between the  $M_J=0$  and  $\pm 1$  Raman transitions is only  $\sim 9$  MHz/GW cm<sup>-2</sup> making these splittings extremely difficult to observe experimentally.

### EXPERIMENT

The experimental apparatus is illustrated in Fig. 2 and consisted of a quasi-cw Raman gain spectrometer [10] using a Moletron MY-34 Nd:YAG (where YAG represents yttrium aluminum garnet) laser, modified and injection-locked to a Lightwave Electronics S-100 injection seeding system [11] as the pulsed pump laser source, and an argon-ion pumped Coherent CR699-29 Ring Dye Laser as the continuous tunable narrow-band probe laser. The Nd:YAG laser typically produces several hundred

millijoules of transform-limited light at 1.06  $\mu\text{m}$  in a 20-ns FWHM (full width at half maximum) duration, which when doubled to 532 nm yields a 14-ns pulse with a bandwidth of 22 MHz. The dye laser was operated at 683 nm to probe both the  $Q(0)$  and  $Q(1)$  transitions in  $\text{H}_2$  with a few hundred milliwatts and a time-averaged bandwidth of roughly 8 MHz.

As shown in Fig. 2, both pump and probe beams were spatially filtered immediately after their sources, expanded and collimated with telescopes, then combined on a 683-nm dichroic mirror before being focused together by a 40-cm focal length lens into a cell containing hydrogen gas. The cell was constructed from stainless steel and designed for high pressure. Both ends of the cylindrical cell were sealed by fused silica windows with triple "V" antireflection coatings at the three wavelengths used here. The spot diameters at the input lens of the Raman cell were 1.6 and 2.1 cm for pump and probe, respectively, producing FWHM beam waists, which were scanned in profile by a 1- $\mu\text{m}$  pinhole, of 25  $\mu\text{m}$  in the center of the cell. Assuming a shift coefficient of 25 MHz GW<sup>-1</sup> cm<sup>2</sup>, this relatively tight focusing of the pump-probe beams meant that the energy of the 532-nm pump had to be held below 120  $\mu\text{J}$  for a 14-ns FWHM pulsewidth (an intensity of 1 GW/cm<sup>2</sup>) in order to avoid more than a 5% shift or broadening contribution on a 500-MHz Raman linewidth by the 532-nm pump. Intensities at or below this level, however, provided adequate Raman gain signals at the hydrogen densities investigated, and the small Rayleigh ranges of the pump and probe allowed selection of a tight confocal parameter for the ir beam that would push the intensity of the applied optical field beyond 100 GW/cm<sup>2</sup>, well above the intensity expected to resolve the shifted from unshifted line shapes.

The high-intensity nonresonant optical field was sup

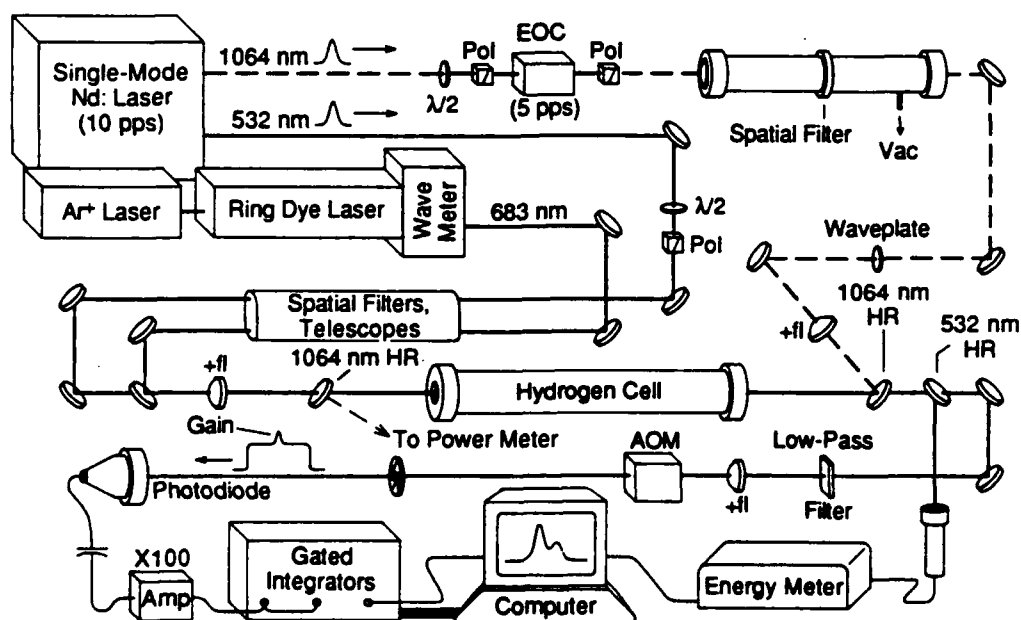


FIG. 2. Experimental layout for the measurement of the optical Stark effect in  $\text{H}_2$ .

plied by the residual ir fundamental of the Nd:YAG laser. The beam was first passed through a Laser Metrics Electro-Optic Chopper (EOC), then into a vacuum spatial filter, and collimated for delivery to the Raman cell. The chopper served dual purposes as a switch and a polarizer for the ir beam. The spatial filter under vacuum cleaned up the transverse mode quality of the beam and significantly reduced power fluctuations of the ir due to air particulates and pinhole breakdown. This ultimately proved vital in reducing broadening effects on the shifted line shape associated with ir field variations. The collimated ir beam was then passed through a 50-cm lens and counterpropagated against the pump-probe beams after being directed into the Raman cell by an ir high reflector (HR) transparent to the pump-probe combination. The waist of the beam, measured to be  $75 \mu\text{m}$  in diameter at FWHM, was carefully positioned to overlap

the waists of the pump and probe beams; the optical paths between laser source and cell center for the 1064- and 532-nm beams were made equal so that the peaks of both would overlap in time as well. Figure 3(a) shows the spatial profiles and Fig. 3(b) shows the temporal overlap achieved in the experiment. Upon exiting the cell, the ir beam was picked off by an identical ir dichroic reflector and sent into a power meter.

After passage through the Raman cell, the 532-nm pump was separated from the probe by a dichroic, measured and integrated by a pyroelectric energy detector and boxcar averager, and recorded by computer for normalization. The transmitted probe was down-collimated, filtered to remove residual pump light, mildly focused through an acousto-optic modulator (AOM) operating in first order, and sent into an EG&G FND 100 photodiode having a 1-ns rise-time response. The resulting gain signal detected by the photodiode exhibited the form of the 14-ns pump pulse shape superimposed atop the 200- $\mu\text{s}$ -wide chopped CW probe background. This signal was enhanced through a 5–500-MHz bandpass, 20-dB gain AvanteK amplifier, where the CW probe offset was filtered out, and sent into two SRS boxcar integrators operating with 2-ns gate widths and toggled at 5 Hz, half the trigger rate of the pump laser.

An example of the Raman gain signal is given in Fig. 3(b). The single-shot trace was acquired as the ring laser swept in frequency over the transition. The result of the optically induced Stark shift of the transition away from the probe frequency is manifested here as a dip in the gain signal at peak ir intensity. All boxcar channels were triggered off the Q-switched Nd:YAG laser oscillator cavity emission in order to reduce boxcar gate jitter on the signals to below 0.2 ns. The averaged output of the integrators were then recorded by computer. This entire arrangement made possible the controlled application of the ir field to the Raman interaction region on altering pulses of the pump laser as the frequency of the probe laser was tuned through the vibrational Raman transition, thus facilitating collection of shifted and unshifted spectral data on the same scan.

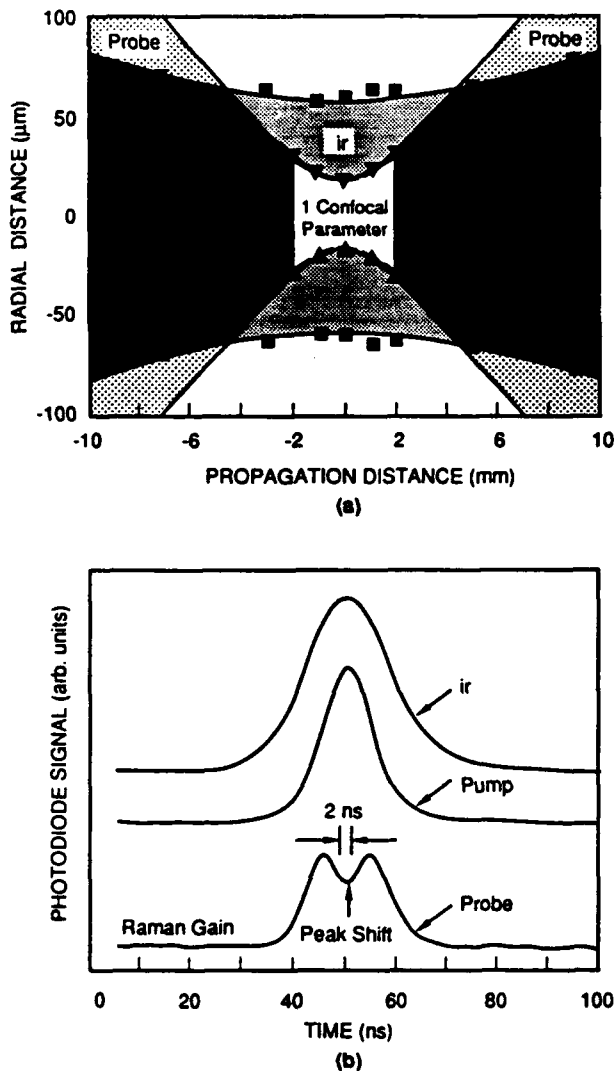


FIG. 3. Spatial and temporal overlap for optical Stark-shift measurements. (a)  $1/e^2$  intensity data points for spatial cross sections of the ir and probe. The theoretical curves for the  $1/e^2$  intensity plots for the ir probe and pump (dashed) beams are shown. Digitized oscilloscope traces (b) depict the time evolution of the ir, pump, and the Raman gain signal.

#### LINE-SHAPE ANALYSIS

Analysis of the data was performed on a DEC VAX 11/750 using a routine designed to remove the Gaussian laser linewidth contribution and then generate a fit to the experimental data. The line shapes used to fit the unshifted data were the theoretically predicted Lorentzian profiles, and the optical Stark-shifted data should, under conditions of a homogeneous, steady-state field, remain Lorentzian with a shift in frequency being the only distinction from the optical field-free data. The ir Stark field applied in our experiment, however, had Gaussian temporal and spatial mode distributions, so its slightly varied temporal and spatial behavior over the regions sampled in time and space contributed to a broadening of the ideal line shape. As a rule, our fits were started using the unshifted linewidth and allowing the peak position to be the

only adjustable parameter; then width and height parameters were freed to obtain the best fit to the side of the Lorentzian furthest from the unshifted line position. This method of analysis was based on the fact that the peak position is theoretically predicted to shift linearly with peak field intensity, and the part of the Lorentzian shifted the furthest corresponds to gain in the region subjected to the most intense part of the ir field; hence, if there are intensity gradients away from the peak intruding upon the Raman gain region, the line shape will broaden in a direction favoring the lower intensities or smaller shifts. As an alternative, assuming nothing about the temporal and spatial distributions of the ir field, the data were also fit in entirety by floating all parameters, and although the differences in the fitting techniques were observable, shift results agreed to within the experimental error of the measurements.

### RESULTS

Typical data are given in Fig. 4 at a density of 1.81 amagat of  $H_2$  and a laser intensity of nearly 100  $GW/cm^2$ . The observed shifts were density independent for both transitions in the absence of four-wave mixing for counterpropagating ir and pump-probe geometries. Polarizations of the pump and probe were identical for all measurements, and the ir polarization was initially fixed parallel to the pump-probe beams. Measurements involving different combinations of ir polarization and propagation direction were also made but the data will not be presented in this paper. Figures 4 and 5 show the raw data and fit as a function of frequency for an ir laser intensity of 100  $GW/cm^2$  and Fig. 6 graphs the dependence

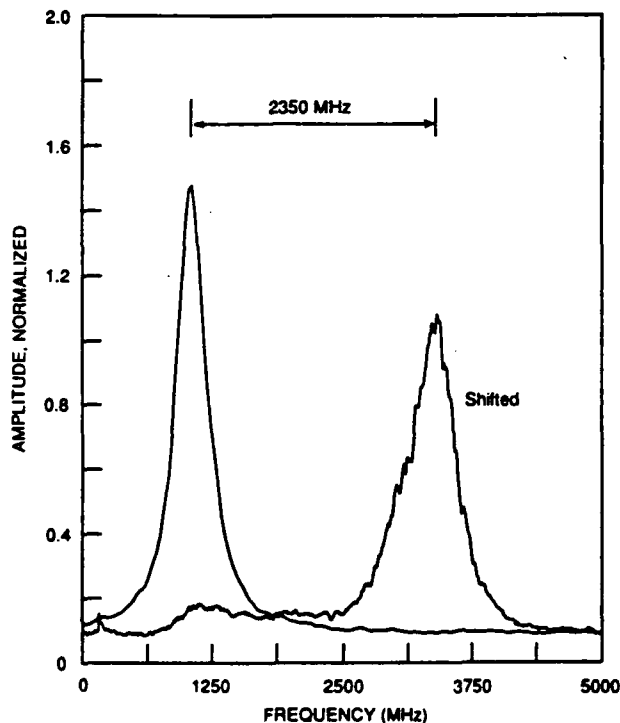


FIG. 4. Raman gain of the unshifted and shifted  $Q(0)$  branch of  $H_2$  at 1.81 amagat and 300 K.

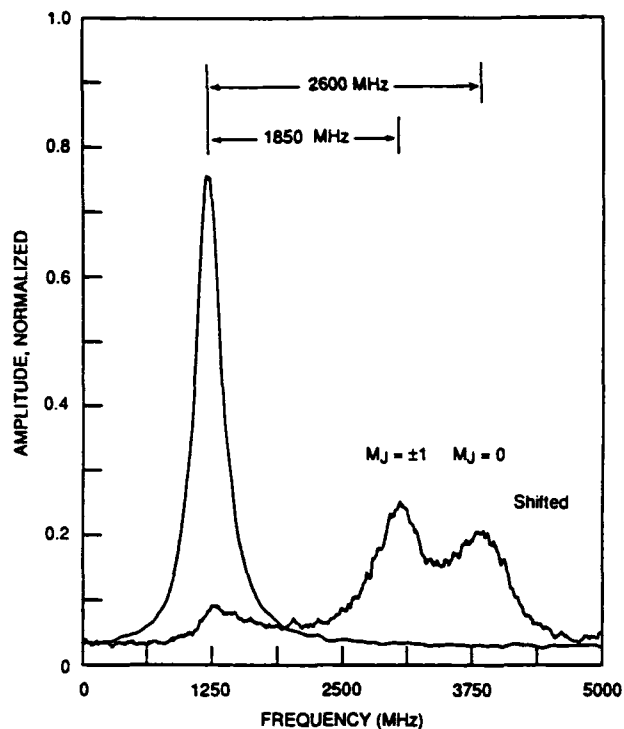


FIG. 5. Unshifted and shifted line shapes from Raman gain on the  $Q(1)$  branch of  $H_2$  at 1.81 amagat and 300 K.

of the optical Stark shift versus ir field intensity for the  $Q(0)$  and  $Q(1)$  transitions, along with a linear least-squares fit to each of the  $M_J$  levels undergoing the shift. For the  $Q(0)$  transition (Fig. 6), the line shifts scaled with ir field intensity and the data yielded a shift coefficient of 23  $MHz GW^{-1} cm^2$ . Shifting of the  $Q(1)$  transition (Fig. 5) was measured to be 27  $MHz GW^{-1} cm^2$  for  $M_J = 0$  and 19  $MHz GW^{-1} cm^2$  for  $M_J = \pm 1$ . The  $M_J$  splittings of a rovibrational level have been resolved, thus allowing the determination of the polarization anisotropy of the excited state.

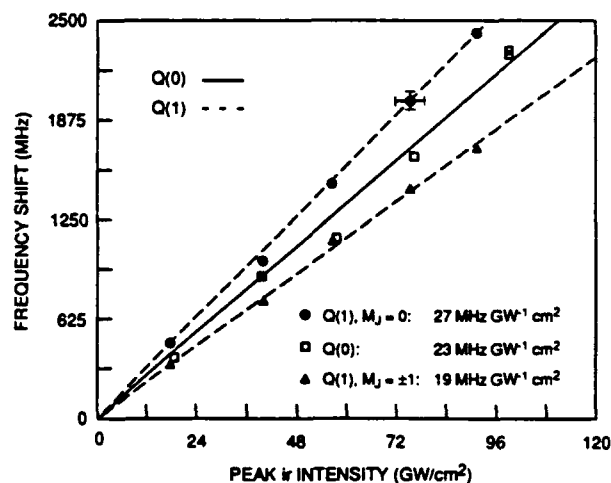


FIG. 6. Plot of the optical Stark shifts of  $Q(0)$  and  $Q(1)$  in  $H_2$  vs peak ir intensity, and linear least-squares fits to individual  $M_J$  levels.

TABLE I. Wavelength dependence of the optical Stark shift for the  $Q(0)$  and  $Q(1)$  vibrational Raman transitions in  $H_2$ . 1 atomic unit (a.u.) =  $1.481845 \times 10^{-25} \text{ cm}^3$ .

Wavelength $\lambda$ (nm)	Polarizabilities (a.u.)						Optical Stark shift $\Delta\nu_S$ (MHz $\text{GW}^{-1} \text{ cm}^2$ )		
	$\alpha_{00}$	$\gamma_{00}$	$\alpha_{11}$	$\gamma_{11}$	$\Delta\alpha$	$\Delta\gamma$	$Q(0)$	$Q(1)$	$Q(1)$
							$M_J=0$	$M_J=\pm 1$	
$\infty$	5.469	2.013	5.923	2.473	0.454	0.460	21	27	18
600	5.584	2.085	6.062	2.576	0.478	0.491	22	29	19
500	5.637	2.118	6.125	2.623	0.488	0.505	23	29	20
400	5.736	2.181	6.249	2.716	0.513	0.525	24	31	21
300	5.965	2.331	6.529	2.936	0.564	0.605	27	34	23
250	6.218	2.501	6.845	3.193	0.627	0.692	29	38	25
200	6.757	2.881	7.536	3.789	0.780	0.910	37	48	31

Uncertainties in the final fits were relatively small compared to the experimental uncertainty, which we conservatively estimate to be less than 10%, arising primarily from beam overlap and peak intensity measurement errors.

### THEORY AND DISCUSSION

The optical Stark shift of a molecular rotational-vibrational level with quantum numbers  $\nu, J, M$  can be calculated from the following expression [2,12]:

$$\Delta E_{\nu, J, M} = -\frac{1}{4}[\alpha_{\nu} + C(J, M)\gamma_{\nu}](|E_0|^2), \quad (1)$$

where  $\alpha$  is the isotropic part of the polarizability [ $\alpha_{\nu} = \frac{1}{3}(\alpha_{\parallel} + 2\alpha_{\perp})$ ] and  $\gamma$  is the anisotropic part of the polarizability ( $\gamma = \alpha_{\parallel} - \alpha_{\perp}$ ),  $E_0$  is the ir laser field, and

$$C(J, M) = \frac{2J(J+1) - 3M^2}{3(2J+3)(2J-1)}. \quad (2)$$

Using the definition for the intensity  $|E_0|^2 = 8\pi I/c$ , where  $I$  is the peak ir laser intensity, we then calculate the optical Stark shift  $\Delta\nu_S$  for a  $Q$  branch transition to be the difference in shifts between the upper and lower states,

$$\Delta\nu_S (\text{MHz}) = 46.8I \left[ \frac{\text{GW}}{\text{cm}^2} \right] [\Delta\alpha + C(J, M)\Delta\gamma], \quad (3)$$

where we have introduced the notation  $\Delta\alpha = \alpha_{11} - \alpha_{00}$  to denote the difference between the  $\nu=1$  and the  $\nu=0$  polarizabilities (similarly for  $\Delta\gamma$ ). In Eq. (3),  $\Delta\nu_S$  is in units of MHz, the polarizabilities are in atomic units (1 a.u. =  $1.481845 \times 10^{-25} \text{ cm}^3$ ), and  $I$  is in units of  $\text{GW}/\text{cm}^2$ . The calculated optical Stark shifts as a function of wavelength are listed in Table I, where the wavelength-dependent polarizabilities are taken from Ref. [6]. We see from Table I that the optical Stark shift around  $\lambda=1060 \text{ nm}$  ranges from 19 to 29  $\text{MHz GW}^{-1} \text{ cm}^2$  for the different  $M_J$  components with an average value of 23 MHz.

The *ab initio* theoretical values from Table I are compared to the experimental measurements in Table II,

where the agreement is surprisingly good for an experiment where the laser intensity had to be measured. Analysis of the  $Q(1)$  shifts gives  $\Delta\alpha = 0.462 \pm 0.02$  and  $\Delta\gamma = 0.450 \pm 0.02$ . No significant differences for  $\Delta\alpha$  of  $J=1$  and 0 were found. These results indicate that the  $\nu=1$  excited-state polarizabilities can be accurately calculated for the simplest diatomic molecule ( $H_2$ ), and provide a favorable basis to judge the accuracy of the calculations of the  $\nu=1$  polarizability at other wavelengths as well as that of higher-order polarizabilities [6]. We can also compare our results to those of a previous experiment [13] that reported a shift of approximately  $-0.02 \text{ cm}^{-1}$  for the  $Q(1)$  transition under a field of about  $30 \text{ GW}/\text{cm}^2$ , which gives a shift coefficient of  $\sim 20 \text{ MHz GW}^{-1} \text{ cm}^2$ .

The difference in the index of refraction between  $\nu=1$  and 0 (proportional only to  $\Delta\alpha$ ) is also given in Table II to be 8.4%. This is compared with the only other experiments [8] that have measured this quantity to be 19%. We conclude that the previous experiments published a  $\Delta n$  that was too large by over a factor of 2. The practical

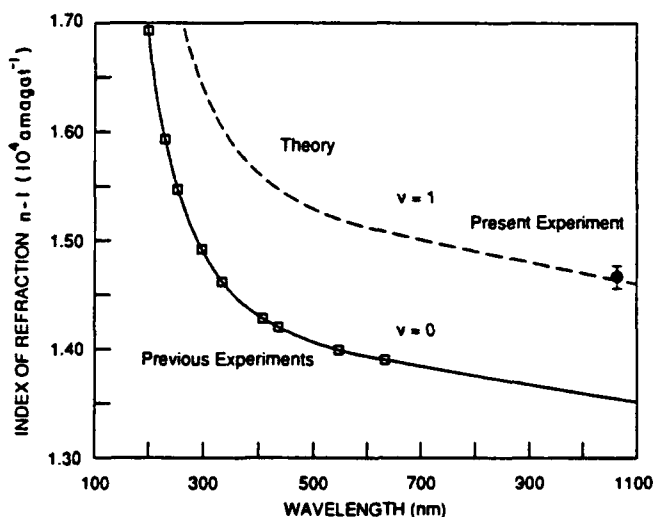


FIG. 7. Index of refraction of  $H_2$  ( $\nu=0$ ) and ( $\nu=1$ ) vs wavelength. Experimental data for  $\nu=0$  taken from Ref. [14].

TABLE II. Index of refraction measurement of  $H_2$  ( $\nu=1$ ) at  $\lambda=1060$  nm using the Stark effect. Error bars are one standard deviation for the fit illustrated in Fig. 6.

Transition	$\Delta\nu$ (MHz/GW cm <sup>-2</sup> )		$\Delta(n-1)_{av}$ (%)		
	Expt.	Theory	Expt.	Theory	Ref. [8]
$Q(0)$	23.0±1.2	22			
$Q(1) M_J=0$	27.0±0.7	28	8.4±0.3	8.4	19
$Q(1) M_J=\pm 1$	19.0±0.6	19			

consequence of this measurement is that the beam uniformity of the pump laser required for large scale Raman amplifiers [7] can be significantly relaxed from previously used values, thus reducing the overall cost of the device.

Finally, we illustrate in Fig. 7 the comparison between theory [6] and experiment for the absolute index of refraction for the  $\nu=0$  state (where the data have been taken from Ref. [14]) and the  $\nu=1$  state (data from the present experiment). Once again we see that the ground-state polarizabilities are well known and can be used to determine the absolute polarizability of the  $\nu=1$  excited state.

### CONCLUSION

We report a quantitative measurement of the average polarizability and the polarizability anisotropy of the

$\nu=1$  excited state in  $H_2$  from a measurement of the non-resonant optical Stark shift for the  $Q(0)$  and  $Q(1)$  Raman transitions. In these experiments the  $M_J$  splitting of the  $Q(1)$  line has been observed, thus allowing the determination of the polarizability anisotropy. The results are in good agreement with *ab initio* theory, thus giving confidence in the ability of theory to predict higher-order polarizabilities in  $H_2$ .

### ACKNOWLEDGMENT

We acknowledge support for this work from the Defense Advanced Research Projects Agency under Contract No. N000 14-8884-C-0256 through the Office of Naval Research.

\*Present address: Coherent Inc., 3210 Porter Drive, Palo Alto, CA 94304.

- [1] L. A. Rahn, R. L. Farrow, M. L. Koszykowski, and P. L. Mattern, *Phys. Rev. Lett.* **45**, 620 (1980).
- [2] R. L. Farrow and L. A. Rahn, *Phys. Rev. Lett.* **48**, 395 (1982).
- [3] M. Pealat, M. Lefebvre, J.-P. E. Taran, and P. L. Kelley, *Phys. Rev. A* **38**, 1948 (1988).
- [4] William K. Bischel, Douglas J. Bamford, and Mark J. Dyer, *Proc. SPIE* **912**, 191 (1988).
- [5] Wallace L. Glab and Jan P. Hessler, *Appl. Opt.* **27**, 5123 (1988).
- [6] Winifred M. Huo, G. C. Herring, and William K. Bischel (unpublished).
- [7] A. Flusberg and D. Korff, *J. Opt. Soc. Am. B* **3**, 1338 (1986).
- [8] V.S. Butylkin, G. V. Venkin, L. L. Kulyuk, D. I. Maleev, V. P. Protasov, and Yu. G. Khronopulo, *Pis'ma Zh. Eksp. Teor. Fiz.* **7**, 474 (1974) [*JETP Lett.* **19**, 253 (1974)]; M. I. Baklushina, B. Ya. Zel'dovich, N. A. Mel'nikov, N. F. Pilipetskii, Yu. P. Raizer, A. N. Sudarkin, and V. V. Shkunov, *Zh. Eksp. Teor. Fiz.* **73**, 831 (1977) [*Sov. Phys.—JETP* **46**, 436 (1977)]; B. Wilhelmi and E. von Heumann, *Zh. Prikl. Spectrosk.* **19**, 550 (1973).
- [9] D. A. Jennings, A. Weber, and J. W. Brault, *Appl. Opt.* **25**, 284 (1986).
- [10] P. Esherick and A. Owyong, *High Resolution Stimulated Raman Spectroscopy*, in *Advances in Infrared and Raman Spectroscopy*, edited by R. J. H. Clark and R. E. Hestor (Heydon and Son, Ltd., London, 1983).
- [11] Mark J. Dyer, William K. Bischel, and David G. Scerbak, *Proc. SPIE* **912**, 32 (1988).
- [12] W. H. Flygare, *Molecular Structure and Dynamics* (Prentice-Hall, Englewood Cliffs, NJ, 1978) p. 193.
- [13] R. Farrow and L. Rahn, in *Raman Spectroscopy: Linear and Nonlinear* (Wiley, London, 1982), pp. 159 and 160.
- [14] G.A. Victor and A. Dalgarno, *J. Chem. Phys.* **50**, 2535 (1969).

**Appendix K**

**TEMPERATURE AND DENSITY DEPENDENCE OF THE LINEWIDTHS AND  
LINE SHIFTS OF THE ROTATIONAL RAMAN LINES IN N<sub>2</sub> AND H<sub>2</sub>**

Phys. Rev. A34, 1944 (1986)

# Temperature and density dependence of the linewidths and line shifts of the rotational Raman lines in N<sub>2</sub> and H<sub>2</sub>

G. C. Herring, Mark J. Dyer, and William K. Bischel

*Chemical Physics Laboratory, SRI International, Menlo Park, California 94025*

(Received 10 February 1986)

The temperature and density dependence of the rotational Raman linewidths and line shifts for the diatomic molecules N<sub>2</sub> and H<sub>2</sub> has been measured using stimulated Raman gain spectroscopy. Room-temperature results for the density-broadening coefficients,  $B$ , in N<sub>2</sub> are compared with *ab initio* calculations, while the low-temperature (80 and 195 K) results are the first to be reported, to our knowledge. Values of  $\gamma$  in the relation,  $B \propto T^\gamma$ , were determined from fits to the data for self-broadening in N<sub>2</sub> yielding  $0.25 < \gamma < 0.39$ . Foreign-gas (O<sub>2</sub>) broadening coefficients for the N<sub>2</sub> transitions were also measured and found to be 10–15% smaller than the self-broadening coefficients. Our linewidth and line-shift results for H<sub>2</sub> are in general agreement with previous measurements.

## I. INTRODUCTION

Modeling the rotational Raman gain in N<sub>2</sub> is of interest since stimulated Raman scattering will alter the mode quality of a high-intensity beam propagating through air.<sup>1</sup> Accurate knowledge of the Raman linewidths is necessary<sup>2</sup> for any useful model because the steady-state Raman gain is inversely proportional to the linewidth. Results of previous studies<sup>3–7</sup> of the room-temperature rotational Raman linewidths in N<sub>2</sub> typically differ by 30%, while results at other temperatures have not been reported. The main purpose of this work is to measure the temperature dependence of the linewidths and line shifts for the rotational Raman transitions (*S* branch) in N<sub>2</sub>.

This work differs from previous measurements of rotational Raman linewidths<sup>3–7</sup> in three aspects. First, we have measured the temperature dependence of the line broadening over the range 80–300 K. Previous work in N<sub>2</sub> has been only for room temperature. Second, the densities, used in this work (0.01–2.0 amagat) are 2 orders of magnitude lower than those (1.0–100 amagat) used in previous measurements. Complications due to overlapping of adjacent lines are eliminated by working at lower densities where the Raman lines are typically separated by 100 linewidths. Finally, all previous measurements have used spontaneous Raman scattering, whereas we have used stimulated Raman scattering, which has a frequency resolution several orders of magnitude higher than its spontaneous counterpart.

This paper reports experimental results for line-broadening and line-shift coefficients for Stokes rotational Raman transitions in N<sub>2</sub> and H<sub>2</sub>. Results are presented for the even-*J* transitions, *S*(2) through *S*(16), at temperatures of 80, 195, and 295 K in N<sub>2</sub> and for *S*(0) and *S*(1) at temperatures of 80 and 295 K in H<sub>2</sub>. The foreign-gas (O<sub>2</sub>) broadening and shifts of the four strongest N<sub>2</sub> transitions have also been measured at 195 and 295 K. The room-temperature broadening coefficients in N<sub>2</sub> are compared with *ab initio* calculations, whereas the low-temperature N<sub>2</sub> self-broadening and the O<sub>2</sub> foreign-gas results are the first to be reported to our knowledge. The present tem-

perature dependence of N<sub>2</sub> is compared to that found in studies of CO and CO<sub>2</sub>. Finally the present H<sub>2</sub> results are compared with previous measurements.

## II. EXPERIMENTAL PROCEDURE

### A. Apparatus

An overview of the experimental setup is shown in Fig. 1. This quasi-cw stimulated Raman spectrometer is similar to that developed by Esherick and Owyong<sup>8</sup> and consists of a cw probe laser, a tunable, pulsed pump laser, a pair of gas (sample and reference) cells, and fast photodiodes to detect the induced Raman gain on the probe beams.

The probe laser is a Kr<sup>+</sup>-ion laser, operating at 568 nm and forced into single-mode operation with the insertion of a temperature-stabilized etalon into the cavity. This laser has a time-averaged linewidth less than 30 MHz. The probe beam was split into two equal intensity beams so that Raman signals could be simultaneously obtained from two separate gas samples. After passing through their respective sample cells, both of the cw probe beams were chopped at 10 Hz with a mechanical chopper (not shown in Fig. 1). This resulted in 170- $\mu$ sec square-wave pulses that were incident on the photodiodes. Chopping of the probe increases the saturation intensity for the photodiodes. The average power of the probe beams was 150 mW in both the sample and reference cells.

The pump laser was a tunable, single-mode (1-MHz linewidth) cw dye laser that was pulse amplified using a Quanta-Ray PDA-1. The cw dye laser input to the PDA-1 was typically 400 mW. The PDA-1 was pumped with the 532-nm output (130 mJ per pulse) from a frequency-doubled YAG laser (where YAG denotes yttrium aluminum garnet). At 565 nm, the tunable output of the PDA-1 consisted of 2-mJ, 10-nsec [full width at half maximum (FWHM)] pulses at 10 Hz. The linewidth of the pump laser was 100 MHz, about a factor of 2 larger than the Fourier transform for a 10-nsec pulse. Peak pump intensities at the focal planes were estimated to be 5

GW/cm<sup>2</sup> in the sample cell and 70% of that in the reference cell.

The pump probe beams were mode-matched and then were focused and crossed in the gas cells using 40-cm focal length lenses. The crossing angle was 1.0° in both of the cells. A series of diaphragms placed around the probe beams was used to eliminate scattered pump light. Both probe beams were monitored with reverse-biased photodiodes that had rise times of less than 1.0 nsec, and were terminated with 50-Ω resistors. The total probe power incident on the photodiodes during the 170-μsec probe-laser pulses was 10 mW. Capacitors (300 pF) were used to block the 170-μsec pulses and to pass the 10-nsec Raman signals. These signals were amplified by a factor of 100 and then averaged with gated integrators. Output time constants for the integrators and total scan times were usually 0.5 sec and 4 min, respectively. Occasionally, for weak transitions, time constants and scan times were increased to 2.5 sec and 10 min, respectively. After the pump beam exited the reference cell, it was also monitored with a third photodiode. This signal was used to normalize the two Raman signals for slow-pump power variations during the scans.

The sample cell was constructed by attaching a pair of 3.0-cm-diam Brewster window extensions to a drilled-out 10 cm<sup>3</sup> cube of aluminum. One face of the aluminum cube is in contact with a second reservoir that can be filled with either liquid N<sub>2</sub> or an acetone dry-ice bath. The cooled sample cell was insulated with a vacuum, and the temperature was monitored with a thermocouple that was imbedded in the aluminum cube. The reference gas cell was kept at room temperature and a pressure of 10 Torr for N<sub>2</sub> scans and 200 Torr for most of the H<sub>2</sub> scans.

The temperature dependence of the linewidths and line shifts was measured by taking measurements at three temperatures: 80, 195, and 295 K. At each temperature the line shape was recorded for several densities over the range 0.01–2.0 amagat. For the low-temperature runs, there was a time period ranging from a few to 15 minutes between scans with different densities, so that any gas added between scans always had sufficient time to come to thermal equilibrium with the cell. For each set of runs at constant temperature, the density was randomly changed rather than constantly adding or eliminating gas from the sample cell for each succeeding run.

The pressure in the experimental cells was measured using a 10000-Torr MKS Baratron gauge, and the temperature was measured using a Chromel-Alumel thermocouple gauged referenced to 273 K. The density for both N<sub>2</sub> and H<sub>2</sub> was calculated using the perfect gas law since the density calculated using the second virial coefficient<sup>9</sup> deviates from this calculation by less than 1% at the densities and temperatures used in these experiments.

### B. Data analysis

All of the experimental line shapes were fit to either Voigt or Lorentzian profiles rather than the more accurate Galatry profile,<sup>10</sup> which accounts for Dicke narrowing. Using the Voigt profile is a good approximation for the N<sub>2</sub> rotational transitions studied here since the

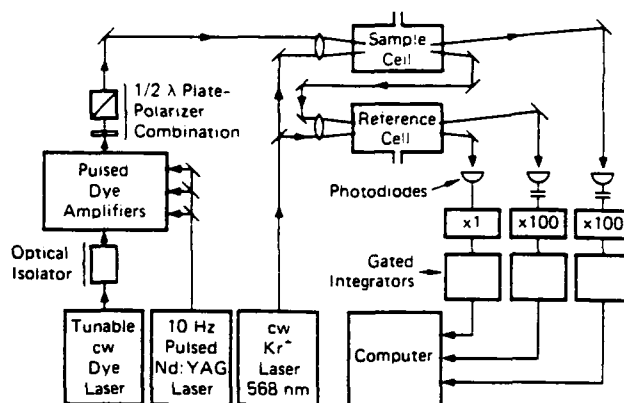


FIG. 1. Schematic of experimental apparatus for quasi-cw stimulated Raman spectroscopy.

Doppler broadening (5 MHz), and hence the Dicke narrowing, is negligible. This is also a good approximation for the H<sub>2</sub> transitions, since the instrumental width typically accounts for one-half the total linewidth and uncertainties in the instrumental linewidth will mask the small difference between the Voigt and Galatry profiles. Thus we have used Voigt profiles to fit our data using the procedure described here.

Since the laser linewidth was comparable to the low-density Raman linewidth, it was important to account for this instrumental width in the data analysis. Although the pump-laser frequency profile was not directly measured, it was indirectly determined by scanning the laser over a narrow Raman line [e.g., S(0) in H<sub>2</sub> at 5 Torr]. This transition has negligible (1 MHz) collisional broadening compared to 100 MHz of Doppler broadening. The profile for this transition was found to fit extremely well to a pure Gaussian. Since the convolution of two Gaussians results in another Gaussian, we concluded that the pump-laser profile could be approximated as a Gaussian. Fitting Voigt profiles to low-density, narrow N<sub>2</sub> line profiles with known Doppler and Lorentzian contributions confirmed this conclusion. The probe-laser linewidth was assumed to be negligible when convolved with the pump linewidth; thus all the data presented here were analyzed

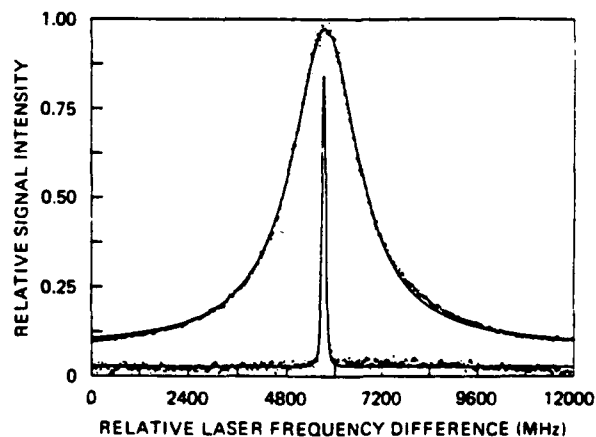


FIG. 2. Example of S(10) line shape in N<sub>2</sub> at 295 K and 10 Torr (narrower profile) and at 195 K and 400 Torr (wider profile). Individual dots are data and the solid lines are Voigt fits.

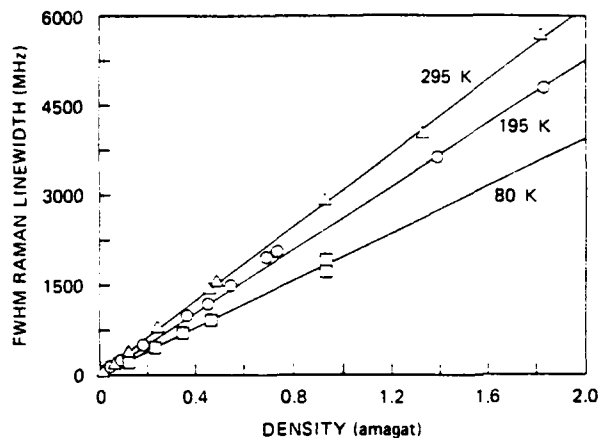


FIG. 3.  $S(10)$  linewidths in  $N_2$  at temperatures of 80 K ( $\square$ ), 195 K ( $\circ$ ), and 295 K ( $\triangle$ ). Solid lines are linear least-squares fits to the data.

assuming a Gaussian profile for the instrumental width.

The fitting procedure used to determine the Lorentzian portion of the line shapes was different for the  $N_2$  and  $H_2$  data. We first describe the fitting procedure for the  $N_2$  transition. For high densities in  $N_2$ , Doppler broadening (5 MHz) and the laser linewidth (100 MHz) can be neglected. This fact is confirmed with the following result: Fitting Voigt profiles with freely varying Lorentzian and Gaussian parameters to our higher density (greater than 0.1 amagat) data gave negligible Gaussian components. Thus sample cell line shapes for high densities were first fitted to pure Lorentzians to get a first approximation to the Lorentzian width. The low-density reference cell data were then fitted to Voigt line shapes with a fixed Lorentzian (determined from the high-density fits) and variable Gaussian components. This Gaussian component, representing the pump-laser profile for that particular scan, was then used in a final Voigt fit to the sample cell profile. Any fluctuations in the pump-laser linewidth from scan to scan were accounted for with this procedure. These Gaussian components were typically within  $\pm 20$  MHz of an approximate average value of 100 MHz. The change in Lorentzian linewidth determined from the first Lorentzian fit and the final Voigt fit was

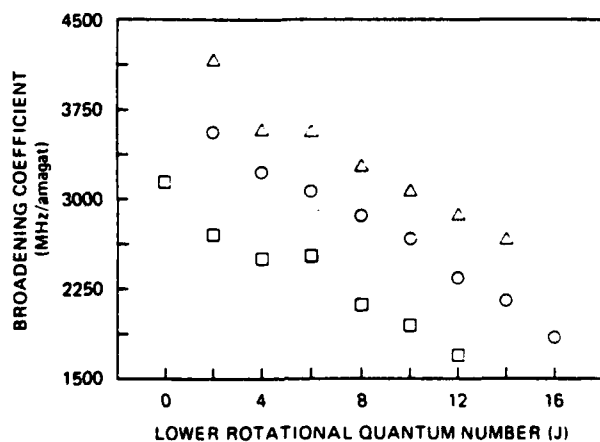


FIG. 4.  $J$  dependence of the  $N_2$  rotational Raman broadening coefficients for 80 K ( $\square$ ), 195 K ( $\circ$ ), and 295 K ( $\triangle$ ).

TABLE I. Temperature dependence of the self-broadening coefficients for the rotational Raman lines of  $N_2$ .

$S(J)$	$B$ (MHz/amagat)		
	295 K	195 K	80 K
0		$4730 \pm 700$	$3140 \pm 470$
2	$4160 \pm 400$	$3560 \pm 350$	$2700 \pm 270$
4	$3580 \pm 60$	$3230 \pm 320$	$2490 \pm 250$
6	$3560 \pm 30$	$3070 \pm 30$	$2520 \pm 40$
8	$3270 \pm 60$	$2860 \pm 30$	$2120 \pm 60$
10	$3060 \pm 60$	$2660 \pm 30$	$1940 \pm 40$
12	$2870 \pm 50$	$2340 \pm 260$	$1690 \pm 100$
14	$2660 \pm 270$	$2150 \pm 215$	
16		$1840 \pm 185$	

typically a few percent and further iterations were not necessary.

For the  $H_2$  transitions studied, experimental constraints did not allow the density in the cell to be larger than 3 amagat. Therefore the approximate density-broadening coefficient could not be determined from the high-density data. Hence, the above procedure was not applicable. Instead, all of the  $H_2$  line shapes were fitted to Voigt profiles with freely adjustable Lorentzian and Gaussian components.

### III. RESULTS

#### A. Line broadening in $N_2$

An example of the  $S(10)$  Raman profile in  $N_2$  is shown in Fig. 2. The narrower profile was taken at 10 Torr and 295 K and the wider profile was taken at 400 Torr and 195 K. Individual dots represent the data, and the solid line represents the fit for a Voigt line shape, which is dominated by its Lorentzian component for the 400-Torr data. A slight asymmetry is observable in the data of Fig. 2 and was characteristic of most of the  $N_2$  data obtained. An asymmetry of this magnitude will not have an appreciable effect on the linewidth determinations, but could produce significant systematic errors in the line-shift determinations because the line shifts are so small. This asymmetry is discussed later in Sec. III C.

For densities larger than 0.004 amagat ( $\sim 3$  Torr at 298 K), the rotational Raman lines of  $N_2$  are collision broadened giving a Lorentzian line-shape function. Hence, the linewidth will be a linear function of density. We have therefore taken the Lorentzian component resulting from the data-fitting procedure described in Sec. II B

TABLE II. Comparison of different measurements of the room-temperature self-broadening in  $N_2$ .

$S(J)$	$B$ (MHz/amagat)			
	Present work	Ref. 3	Ref. 6	Ref. 7
2	$4160 \pm 400$	3370		
4	$3580 \pm 60$	3050	2590	$3280 \pm 300$
6	$3570 \pm 30$	3050		
8	$3270 \pm 60$	2660	2300	$3150 \pm 300$
10	$3070 \pm 60$	2590		
12	$2870 \pm 50$	2400	1980	$2820 \pm 300$
14	$2660 \pm 270$	2205		
16		2080		

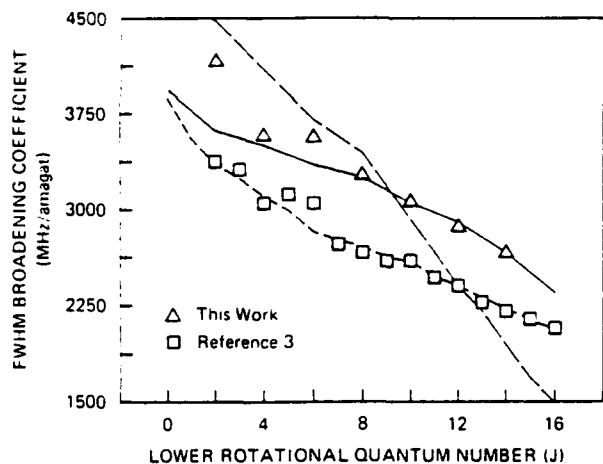


FIG. 5. Comparison of theoretical calculations with experimental data for collisional broadening of the rotational Raman lines in  $N_2$  at room temperature. The calculations are from Ref. 11 (long dash), Ref. 12 (short dash), and Ref. 13 (solid line). The experimental data are from Ref. 3 ( $\square$ ) and this work ( $\triangle$ ).

and determined the density-broadening coefficients  $B$  for each temperature studied by fitting the linewidths to a straight line. The data and the linear fit (solid line) for the  $S(10)$  transition are given in Fig. 3 for temperatures of 298, 195, and 80 K. Individual points indicate the data, and the solid lines represent the least-squares fits. The statistical uncertainties (one standard deviation) for the broadening coefficients determined from the fits in Fig. 3 are 1–2%. Systematic errors, due to uncertainty in the dye-laser scan width, are about 1% or less.

Table I summarizes all of the  $N_2$  self-broadening coefficients measured in this study. These values are graphically illustrated in Fig. 4 as a function of rotational quantum number. Odd- $J$  transitions in  $N_2$  were not studied. For  $S(4)$  through  $S(12)$ , the specified uncertainties are one standard deviation for the least-squares fit. For  $S(0)$ ,  $S(2)$ ,  $S(14)$ , and  $S(16)$ , data were obtained at only one density, and the uncertainties shown for these transitions represent the error in the linewidth determination of a single-line profile.

Earlier room-temperature measurements by different authors<sup>3,6,7</sup> have shown considerable disagreement (30%). Table II compares these earlier results with our present results. It can be seen that the three earlier studies show significant differences, while our current measurement is consistent with that of Ref. 7. The results of the three previous studies that are shown in Table II were obtained at densities where adjacent lines appreciably overlapped with one another, whereas the present results were obtained at densities where there was no overlapping. We postulate that the differences in the experimental results of the previous studies given in Table II are due to systematic errors arising from the overlapping of adjacent lines.

Theoretical calculations of the collision-broadened Raman linewidth have been performed by Grey and Van Kranendonk,<sup>11</sup> Srivastava and Zaidi,<sup>12</sup> and Robert and Bonamy.<sup>13</sup> The difference in these three approaches is in the treatment of the short-range intermolecular interactions. The results of these different approaches are

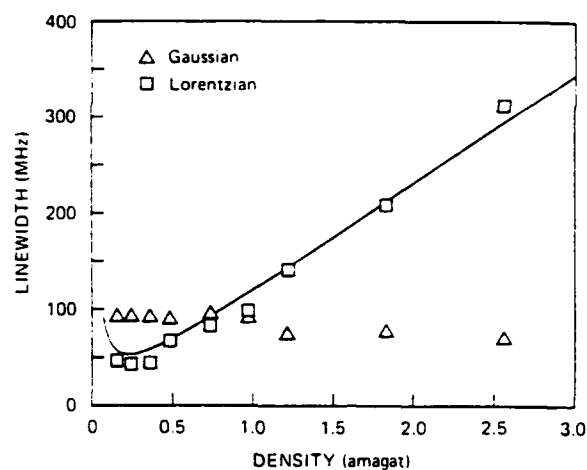


FIG. 6. Lorentzian ( $\square$ ) and Gaussian ( $\triangle$ ) components from Voigt fits to data as a function of density for  $S(1)$  in  $H_2$ . Solid line is a linear one-parameter fit to Eq. (1).

compared with our measurements in Fig. 5, where the room-temperature broadening coefficients are shown as a function of rotational quantum number  $J$ . We also show the experimental values of Jammu *et al.*<sup>3</sup> for comparison. It should be noted that Srivastava and Zaidi<sup>12</sup> have used an adjustable parameter to obtain their fit to the data of Jammu *et al.*,<sup>3</sup> whereas the calculations of Grey and Van Kranendonk<sup>11</sup> and Robert and Bonamy<sup>13</sup> do not use any adjustable parameters. Figure 5 shows the *ab initio* calculations of Robert and Bonamy<sup>13</sup> to be in the best agreement with our measurements.

To compare the pure rotational linewidths to the pure vibrational linewidths, we first note that the present rotational broadening coefficients are 10–15% larger than previously measured<sup>14–16</sup>  $Q$ -branch vibrational broadening coefficients for low densities (0.1 amagat). Because negligible Doppler broadening of the rotational transitions means that Dicke narrowing is also negligible, the rotational line shapes are accurately described by Voigt profiles, while the vibrational transitions (with 20 times more Doppler broadening) require Galatry profiles for the most accurate fits. Also, because the vibrational transitions (0.3  $cm^{-1}$ ) are more closely spaced than the rotational (8  $cm^{-1}$ ) transitions, coherent line-mixing effects must be included to precisely describe the vibrational line shapes at densities of 1 amagat or larger.

Previous to this work, only atomic foreign-gas (He and Ar) broadening of the  $N_2$  rotational transitions had been investigated.<sup>3</sup> We have also measured diatomic foreign-gas ( $O_2$ ) broadening coefficients at 195 and 295 K for the four strongest  $N_2$  transitions. Our  $O_2$  results in Table III

TABLE III. Temperature dependence of the foreign-gas ( $O_2$ ) broadening coefficients of  $N_2$  rotational Raman lines.

$S(J)$	$B$ (MHz/amagat)	
	295 K	195 K
6	$2970 \pm 130$	$2690 \pm 120$
8	$2770 \pm 80$	$2600 \pm 100$
10	$2750 \pm 50$	$2410 \pm 100$
12	$2450 \pm 70$	$1980 \pm 100$

TABLE IV. H<sub>2</sub> rotational Raman parameters for an ortho:para ratio of 3:1.

<i>T</i> (K)	<i>S</i> ( <i>J</i> )	$\nu_R$ (cm <sup>-1</sup> )	$\Delta\nu_D$ (MHz)	$D_0^a$ (cm <sup>2</sup> amagat sec <sup>-1</sup> )	<i>A</i> (MHz amagat)	$\rho_c$ (amagat)
80	0	354	48	0.871	1.37	0.095
	1	587	80	0.493	2.10	0.088
295	0	354	92	1.19	1.87	0.068
	1	587	153	1.42	6.15	0.134

<sup>a</sup>Reference 18.

show that the foreign-gas broadening by O<sub>2</sub> is typically 85–90% of the self-broadening at both temperatures. Thus the foreign-gas broadening by O<sub>2</sub> is approximately 30% larger than the foreign-gas broadening by the atomic gases.<sup>3</sup>

### B. Line broadening in H<sub>2</sub>

The Raman linewidth for H<sub>2</sub> has a much more complex density dependence than that for N<sub>2</sub>. This results mainly from the fact that the H<sub>2</sub> density-broadening coefficient is approximately a factor of 30 smaller than the N<sub>2</sub> broadening coefficient, and thus Dicke<sup>17</sup> or collisional narrowing of the Raman linewidth can be observed<sup>18,19</sup> in the low-density regime if the resolution is high enough. A summary of the relevant collisional processes that contribute to the linewidth at various densities is given in Ref. 18.

For densities above a certain cutoff density ( $\rho_c$  defined below), the Raman line-shape function is Lorentzian with a FWHM linewidth  $\Delta\nu$  that can be expressed as

$$\Delta\nu = A/\rho + B\rho, \quad (1)$$

where *A* (MHz amagat) is a coefficient proportional to the self-diffusion coefficient  $D_0$  (cm<sup>2</sup> amagat sec<sup>-1</sup>). For forward scattering,<sup>18</sup> *A* is equal to

$$A = 4\pi^2\nu_R^2 D_0 \quad (2)$$

where  $\nu_R$  is the Raman transition frequency in cm<sup>-1</sup>.

This model is known as the diffusion model of the Raman linewidth and it diverges as the density approaches zero. There is a cutoff density,  $\rho_c$ , at which this model predicts a linewidth that is 10% larger than that predicted by the "hard collision" line-shape theory.<sup>18</sup> We have previously determined that

$$\rho_c = 3.33A/\Delta\nu_D, \quad (3)$$

where  $\Delta\nu_D$  (MHz) is the FWHM Doppler width of the Raman transition given by (forward scattering)

$$\Delta\nu_D = 7.15 \times 10^{-7} \nu_R (T/m)^{1/2}, \quad (4)$$

where  $\nu_R$  is in MHz, *T* is the temperature in K, and *m* is the mass in amu. For densities larger than  $\rho_c$ , the line shape is Lorentzian and the widths can be effectively modeled using Eq. (1).

For example, the experimental data set for the *S*(1) transition at 298 K is given in Fig. 6. From the Voigt fit, we determine both the Lorentzian and Gaussian contributions to the experimental linewidth. Since the Raman line shape is Lorentzian for all densities shown in Fig. 6, the Gaussian contribution is due to the spectral width of the pulsed dye laser. The Lorentzian and Gaussian contributions to the linewidth are plotted in Fig. 6, where we see that the Gaussian contribution is approximately constant while the Lorentzian contribution varies approximately linear in density.

Unfortunately, the 100-MHz resolution of our current laser system does not allow the Dicke narrowing of the H<sub>2</sub> rotational Raman linewidth to be resolved with any precision. We have therefore chosen a fitting procedure that uses  $D_0$  determined from our previous study<sup>18</sup> to calculate *A* from Eq. (2). The Lorentzian component of the experimental linewidth for densities larger than  $\rho_c$  is then fitted to Eq. (1) with one free parameter *B*. The parameters used in this fitting procedure are given in Table IV.

The density-broadening coefficients *B* determined using this procedure are given in Table V, where the uncertainties shown are one standard deviation for the one-parameter linear least-squares fit. This fit is illustrated by the solid line in Fig. 6 for the *S*(1) transition. The maximum correction to the linewidth due to including the collisional narrowing term in Eq. (1) is on the order of 5–10%.

We have also included in Table V data from the previous work of Van Den Hout *et al.*<sup>20</sup> and Cooper, May, and Gupta.<sup>21</sup> There are small discrepancies with the results of Refs. 20 and 21. Some of these differences could be due to small errors in our estimate of *A* for these rotational transitions. We emphasize that the N<sub>2</sub> results of Sec. IIIA are free of this problem since Dicke narrowing is negligible.

TABLE V. Self-broadening coefficients for the rotational Raman lines of H<sub>2</sub>.

<i>S</i> ( <i>J</i> )	<i>B</i> (MHz/amagat)				
	295 K			80 K	
	This work	Ref. 20	Ref. 21	This work	Ref. 20
0	77±2	84±2	84±2	67±2	63±1
1	114±5	104±2	105±4	110±3	99±1

### C. Line shifts in N<sub>2</sub> and H<sub>2</sub>

In all of the above cases for which density-broadening measurements were reported, we have also made density line-shift measurements. In all cases the line shifts were only a few percent of the linewidth, and hence any asymmetries in the line shapes need to be carefully analyzed.

The asymmetry in Fig. 2 is typical of that observed in our data for the higher-density N<sub>2</sub> data. The lower-density N<sub>2</sub> data contained an asymmetry that occurred only further out in the wing of the spectral profiles. About 80% of the total number of line profiles at all densities and temperatures exhibited this small asymmetry, where the data were slightly larger than the symmetric fit on the high-frequency side of the line. Roughly 20% of the line profiles were symmetric and only rarely did the asymmetry appear such that the data were smaller than the fit on the high-frequency side. It was determined that this asymmetry was not due to the saturation of the detection system by either the probe beam or the Raman signal. By scanning the dye laser backwards, it was determined that the asymmetry always remains such that the data are larger than the fit on the high-frequency side of the line, where the high-frequency side corresponds to a larger Raman shift. For densities above 0.5 amagat and for the pump-laser intensities used here, this asymmetry is not consistent with the measured magnitudes of Stark effects in N<sub>2</sub>.<sup>22</sup> At this time we are unable to determine the cause of these asymmetries.

In N<sub>2</sub>, both the self-density shifts and the O<sub>2</sub> foreign-gas density shifts were found to lie in the range 50–150 MHz/amagat for the transitions and temperatures discussed above. There was no uniform dependence with either temperature or quantum number *J*. More importantly, there were inconsistencies observed in both the data acquired during the course of a single day and in the data collected from day to day. These inconsistencies have forced us to conclude that the line-shift measurements in N<sub>2</sub> are substantially disturbed by the asymmetric line shapes. The data can, however, be used to establish an upper limit to the magnitude of the line shifts. For all transitions and temperatures indicated for N<sub>2</sub> in Tables I and III, the density line shifts are less than 150 MHz/amagat. Future elimination of the asymmetry would enable us to detect line shifts as small as 10 MHz/amagat with our current experimental apparatus.

The density shifts observed in H<sub>2</sub>, unlike those in N<sub>2</sub>, were free of the inconsistencies mentioned above. Data for *S*(1) in H<sub>2</sub> at 295 K are illustrated in Fig. 7, where the density shift is defined as

$$\delta\nu = \nu_R(\rho) - \nu_R(0), \quad (5)$$

where  $\nu_R(\rho)$  is the Raman transition frequency at the density  $\rho$ . Hence a negative shift results in a smaller Raman frequency. Density shifts were plotted as a function of density difference between the sample and reference cells rather than density because data were collected for reference cell pressures of 50, 100, and 200 Torr. The temperature is 295 K for the data of Fig. 7. A summary of our H<sub>2</sub> density-shift results is given in Table VI, along with the results from Refs. 20 and 21. The agreement be-

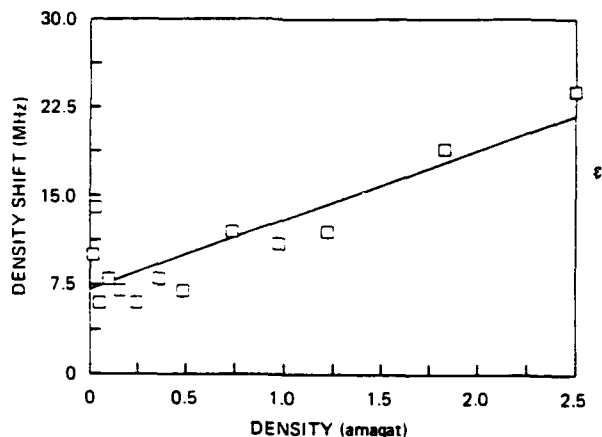


FIG. 7. Example of data for line-shift determination for *S*(1) in H<sub>2</sub> at 295 K. The solid line is the least-squares fit.

tween our results and those of Ref. 21 is consistent with the combined uncertainties for the two experiments.

It should be noted that the density shift for the rotational Raman line in H<sub>2</sub> is substantially different from that observed for the vibrational Raman lines.<sup>18</sup> For example, at 80 K, the shift of the *Q*(1) vibrational transition is 13 times larger than the *S*(1) rotational Raman line. This difference results from the perturbation of the vibrational frequency of the H<sub>2</sub> molecule during an elastic collision, an effect not present for the rotational transition.

## IV. DISCUSSION

A simple qualitative understanding of this temperature dependence for the N<sub>2</sub> rotational Raman broadening data given in Table I can be obtained from a consideration of Anderson's impact theory of the collisional broadening.<sup>23</sup> The linewidth can be expressed as

$$\Delta\nu = n \langle \nu \sigma(v) \rangle \approx n \langle \nu \rangle \langle \sigma(v) \rangle, \quad (6)$$

where  $n$  is the molecular number density (cm<sup>-3</sup>),  $v$  is the relative velocity of the collision partners,  $\sigma$  is the collisional-broadening cross section, and the angular brackets denote an average over the velocity distribution of the gas. As can be seen from Eq. (6), the temperature dependence of the density-broadening coefficient is implicit in the velocity dependence of the collisional cross section. For example, if we assume a "hard-sphere" model for the cross section (velocity independent), the density-broadening coefficient ( $\Delta\nu/n$ ) measured in our experiment would be proportional to  $T^{0.5}$ .

The broadening cross section is composed of contributions from several different types of collisions. Both elastic phase-perturbing collisions, and rotationally inelastic

TABLE VI. Temperature dependence of the density line shifts for H<sub>2</sub> rotational Raman lines.

<i>S</i> ( <i>J</i> )	$\delta\nu = \nu_R(\rho) - \nu_R(0)$ (MHz/amagat)			
	295 K		80 K	
	This work	Ref. 21	This work	Ref. 20
0	6.5 ± 3	3.1 ± 1.5	-22.3 ± 0.6	-22.3
1	5.9 ± 1	4.0 ± 1.5	-23.0 ± 0.6	-17.8

collisions contribute to the linewidth. However, there are several cases where the contribution from elastic collisions is small. For example, the linewidth for isotropic vibrational  $Q$ -branch Raman scattering have no contribution from elastic collisions<sup>24</sup> if collisions perturb the ground and final vibrational level the same amount. This appears to be a good approximation for all cases except for hydrogen.<sup>18</sup>

Rotational Raman linewidths, on the other hand, have contributions from phase-perturbing elastic collisions. This is the primary reason why rotational Raman transitions usually have larger linewidths than vibrational Raman transitions. However, for the case of  $N_2$ ,  $CO$ , and  $CO_2$ , it has been calculated<sup>11</sup> that elastic collisions contribute no more than 15% of the cross section. The present  $N_2$  rotational linewidth measurements are 15% larger than the previous  $N_2$  vibrational measurements,<sup>14-16</sup> in good agreement with the conclusion that elastic collisions account for 15% of the rotational linewidths. Therefore, in most cases, the primary problem is to calculate the velocity dependence of the cross section for rotationally inelastic collisions.

The calculation of the collisional cross section has been the subject of considerable research. A good review of the various approaches to this calculation for Raman transitions has been given by Srivastava and Zaidi.<sup>25</sup> One approach to this calculation is to expand the long-range part of the intermolecular potential in a multipole expansion,<sup>11,23,25</sup> and then calculate the contribution to the cross section of each term in this expansion. Using this approach, Gray and Van Kranendonk<sup>11</sup> have shown that for molecules such as  $N_2$ ,  $CO$ , and  $CO_2$ , the most important terms in this expansion for self-broadening are the quadrupole-quadrupole (QQ) potential and the dispersion potential.

It can be shown<sup>23</sup> in general that the velocity dependence of these contributions to the cross section scales as

$$\langle \sigma \rangle \propto \langle v^{-2/(n-1)} \rangle, \quad (7)$$

where  $n$  is the exponent of the radial dependence of the long-range part of the potential in the form  $V(r) \sim r^{-n}$ . For the QQ potential,  $n=5$ , while for the dispersion potential  $n=6$ . Substituting Eq. (7) into Eq. (6) and remembering that  $v \propto T^{0.5}$ , we find that the density-broadening coefficient should scale with temperature as

$$(\Delta\nu/n) \propto T^{(n-3)/(2(n-1))}. \quad (8)$$

From this simple argument, we would expect our density-broadening coefficients to scale as  $T^{0.25-0.3}$ , depending on the relative contribution to the cross section of the QQ and dispersion forces.

To test this simple model of the temperature dependence, we have fitted our data in Table I to the equation

$$B = B_0(T/295)^\gamma, \quad (9)$$

where  $B_0$  is the density-broadening coefficient at 295 K. The results are given in Table VII as a function of initial rotational state. We find that  $0.26 < \gamma < 0.39$ , in reasonable agreement with this simple picture. We believe that most of the scatter in  $\gamma$  as a function of  $J$  is due to the

TABLE VII. Fit parameters for temperature dependence of density self-broadening coefficients in  $N_2$ .

$S(J)$	$B_0$ (MHz amagat <sup>-1</sup> )	$\gamma$	$C_0$ (MHz amagat <sup>-1</sup> K <sup>-1</sup> )
2	4160	0.33±0.02	6.8±0.4
4	3580	0.28±0.01	5.1±0.7
6	3560	0.26±0.04	4.8±0.1
8	3270	0.33±0.004	5.4±0.7
10	3060	0.35±0.002	5.2±0.6
12	2870	0.39±0.03	5.4±0.1

fact that a much larger temperature range needs to be investigated to accurately determine this small temperature dependence.

However, the scaling given in Eq. (9) may not be valid over a wide temperature range. By theoretically examining temperature dependence of the rotational Raman linewidth over a wide range, Pack<sup>26</sup> proposes a quadratic temperature scaling law for density-broadening coefficients that can be written as

$$B = B_0 + C_0(T - 295) + D_0(T - 295)^2, \quad (10)$$

where  $B_0$  is the broadening coefficient at 298 K [same as in Eq. (9)], and  $C_0$  and  $D_0$  are fitting coefficients. We have previously used this temperature scaling formula in modeling Raman linewidths in  $H_2$ .<sup>18</sup> The data from Table I have been fitted to Eq. (10) assuming  $D_0=0$ , and the results are also given in Table VII. We find that this expression is just as useful as Eq. (9) in modeling the dependence of the density-broadening coefficient over the limited temperature range investigated in our experiment. Both Eqs. (9) and (10) can be used to predict  $B$  to better than 3% over the range of 80–300 K. Recent studies show that the temperature dependence for vibrational  $N_2$  line shape is accurately described by a modified exponential gap scaling law<sup>27</sup> or a polynomial inverse energy-gap law.<sup>28</sup> Thus, although Eqs. (9) and (10) are useful for predicting low-temperature rotational Raman linewidths for  $N_2$ , additional data (more data points covering a larger temperature region) are necessary to unambiguously determine the temperature dependence.

There are few molecular systems for which the rotational Raman linewidths have been determined as a function of temperature, and no other studies in  $N_2$ . However, there have been extensive studies of the temperature dependence of absorption linewidths in  $CO$  (Ref. 29) and  $CO_2$ .<sup>30</sup> The absolute magnitude of the linewidths determined from absorption will be different from those determined from Raman scattering. This is due to the fact that different states are involved in the calculation of the collision cross section. However, the temperature dependence will be similar if the same terms in the multipole potential are responsible for the broadening. This is the case<sup>11</sup> for both  $CO$  and  $CO_2$  where the most important terms in the potential are the same as for  $N_2$ .

Most of the data for linewidths in the literature are given in terms of pressure-broadening coefficients. We can compare results by noting that  $\gamma$  in Eq. (9) is related to  $\eta$  by  $\gamma = 1 - \eta$ , where  $\eta$  is the exponent of the tempera-

ture for pressure-broadening coefficients. The  $\eta$  values for the  $N_2$  rotational Raman linewidths of this study cover a similar range of values as observed for the  $N_2$  vibrational Raman linewidths<sup>28</sup> and the absorption linewidths in CO (Ref. 29) and  $CO_2$ .<sup>30</sup>

The details of the exact theoretical temperature dependence of the rotational Raman linewidths requires an *ab initio* calculation of the velocity-dependent collisional cross section, and is beyond the scope of this study. However, the precision of the data presented here should allow a detailed comparison with linewidths calculated from the various theoretical approaches thus allowing new theoretical advances to be made.

## V. CONCLUSIONS

The density self-broadening coefficients have been measured at temperatures of 80, 195, and 295 K for the even- $J$  rotational Raman transitions in  $N_2$ . The temperature dependence of these coefficients was found to fit both linear and  $T^\gamma$  models to within 3%, however, additional temperature-dependent data are necessary to accurately determine the temperature dependence of these rotational

linewidths. The room-temperature results of this work are in agreement (less than 5% differences for  $J > 2$ ) with the most recent *ab initio* calculations. Foreign-gas broadening of these  $N_2$  transitions, due to  $O_2$ , was also measured and found to be 10–15% smaller than the self-broadening coefficients. We have also determined that the density self-shifts and  $O_2$  foreign-gas shifts for these same  $N_2$  lines are no larger than 150 MHz/amagat. In a previous paper,<sup>2</sup> we have used the above results in the modeling of the temperature dependence of the steady-state Raman gain coefficient in  $N_2$ .

The rotational Raman density broadening and shifts in  $H_2$  were measured at 80 and 295 K. Our results were in general agreement with previous experimental work. This agreement of our  $H_2$  data with other independent measurements provides confidence in the new temperature-dependent  $N_2$  results presented above.

## ACKNOWLEDGMENT

This work was supported by the Defense Advanced Research Projects Agency under Contract No. N00014-84-C-0256 through the U.S. Office of Naval Research.

- <sup>1</sup>M. Henesian, C. Swift, and J. R. Murray, *Opt. Lett.* **10**, 565 (1985).
- <sup>2</sup>G. C. Herring, Mark J. Dyer, and William K. Bischel, *Opt. Lett.* **11**, 348 (1986).
- <sup>3</sup>K. S. Jammu, G. E. St. John, and H. L. Welsh, *Can. J. Phys.* **44**, 797 (1966).
- <sup>4</sup>G. V. Milahailov, *Zh. Eksp. Teor. Fiz.* **36**, 1368 (1959) [*Sov. Phys.—JETP* **9**, 974 (1959)].
- <sup>5</sup>Yu A. Lazarev, *Opt. Spectrosc.* **13**, 373 (1962).
- <sup>6</sup>F. Pinter, *Opt. Spectrosc.* **17**, 428 (1964).
- <sup>7</sup>H. G. M. Edwards, D. A. Long, and S. W. Webb, *Self- and Foreign-Gas Broadening of the Pure Rotational Raman Lines of Oxygen and Nitrogen*, Proceedings of the 9th International Conference on Raman Spectroscopy, 1984 (unpublished) p. 760.
- <sup>8</sup>P. Esherick and A. Owyong, in *Advances in Infrared and Raman Spectroscopy*, edited by R. J. Clark and R. E. Hester (Heyden, London, 1983), Vol. 9.
- <sup>9</sup>Joseph O. Herschfelder, Charles F. Cartiss, and R. Byron Bird, *Molecular Theory of Gases and Liquids* (Wiley, New York, 1954).
- <sup>10</sup>Philip L. Varghese and Ronald K. Hanson, *Appl. Opt.* **23**, 2376 (1984).
- <sup>11</sup>C. G. Grey and J. Van Kranendonk, *Can. J. Phys.* **44**, 2411 (1966).
- <sup>12</sup>R. P. Shrivastava and H. R. Zaidi, *Can. J. Phys.* **55**, 542 (1977).
- <sup>13</sup>D. Robert and J. Bonamy, *J. Phys. (Paris)* **40**, 923 (1979).
- <sup>14</sup>G. J. Rosasco, W. Lempert, W. S. Hurst, and A. Fien, *Chem. Phys. Lett.* **97**, 435 (1983).
- <sup>15</sup>M. L. Koszykowski, L. A. Rahn, and R. E. Palmer, *J. Chem. Phys.* (to be published).
- <sup>16</sup>G. Millot, B. Lavorel, R. Saint-Loup, and H. Berger, *J. Phys. (Paris)* **46**, 1925 (1985).
- <sup>17</sup>R. H. Dicke, *Phys. Rev.* **89**, 472 (1953).
- <sup>18</sup>William K. Bischel and Mark J. Dyer, *Phys. Rev. A* **33**, 3113 (1986).
- <sup>19</sup>B. K. Gupta and A. D. May, *Can. J. Phys.* **50**, 1747 (1972).
- <sup>20</sup>K. D. Van Den Hout, P. W. Hermans, E. Mazur, and H. F. P. Knapp, *Physica (Utrecht)* **104A**, 509 (1980).
- <sup>21</sup>V. G. Cooper, A. D. May, and B. K. Gupta, *Can. J. Phys.* **48**, 725 (1970).
- <sup>22</sup>R. L. Farrow, and L. A. Rahn, *Phys. Rev. Lett.* **48**, 395 (1982).
- <sup>23</sup>C. H. Townes, and A. L. Schawlow, *Microwave Spectroscopy* (Dover, New York, 1975), pp. 368 and 369.
- <sup>24</sup>R. P. Srivastava and H. R. Zaidi, in *Raman Spectroscopy of Gases and Liquids*, edited by A. Weber (Springer, Berlin, 1979).
- <sup>25</sup>R. P. Srivastava and H. R. Zaidi, in *Raman Spectroscopy of Gases and Liquids*, edited by A. Weber (Springer, Berlin, 1979), pp. 167–198.
- <sup>26</sup>Russell T. Pack, *J. Chem. Phys.* **70**, 3424 (1979).
- <sup>27</sup>L. A. Rahn and R. E. Palmer, *J. Opt. Soc. Am. B* (to be published).
- <sup>28</sup>B. Lavorel, G. Millot, R. Saint-Loup, C. Wenger, H. Berger, J. P. Sala, J. Bonamy, and D. Robert, *J. Phys. (Paris)* **47**, 417 (1986).
- <sup>29</sup>Jeffrey N-P. Sun and Peter R. Griffiths, *Appl. Opt.* **20**, 1691 (1981); Prasad Varanasi and Sunil Sarangi, *J. Quant. Spectrosc. Radiat. Transfer* **15**, 473 (1975).
- <sup>30</sup>W. G. Planet and G. L. Tetteimer, *J. Quant. Spectrosc. Radiat. Transfer* **22**, 345 (1979); Lloyd D. Tubbs and Dudley Williams, *J. Opt. Soc. Am.* **62**, 284 (1972); R. Ely and T. K. McCubbin, Jr., *Appl. Opt.* **9**, 1230 (1970).

**Appendix L**

**TEMPERATURE AND WAVELENGTH DEPENDENCE  
OF THE ROTATIONAL RAMAN GAIN COEFFICIENT IN N<sub>2</sub>**

Optics Lett. **11**, 348 (1986)

# Temperature and wavelength dependence of the rotational Raman gain coefficient in N<sub>2</sub>

G. C. Herring, Mark J. Dyer, and William K. Bischel

Chemical Physics Laboratory, SRI International, Menlo Park, California 94025

Received August 12, 1985; accepted March 6, 1986

The temperature, wavelength, and  $J$  dependence of the rotational Raman gain coefficient has been determined for the S-branch transitions in N<sub>2</sub>. First, the temperature dependence (80–300 K) of the density-broadening coefficients was measured using stimulated Raman spectroscopy. Second, the wavelength dependence (250–600 nm) of the polarizability anisotropy was empirically determined by fitting to the most recent experimental data. These two results were then used to calculate the rotational Raman gain coefficients with accuracies estimated at 5%. At room temperature, the high-density limit of the steady-state gain coefficient of the strongest line, S(10), is  $4.8 \times 10^{-12}$  cm/W for a Stokes wavelength of 568 nm.

There are many applications, such as laser fusion, that require the propagation of high-intensity lasers through the atmosphere. Recently there has been renewed interest in the nonlinear optical processes that limit the maximum transmitted laser intensity for a given propagation distance. Several different nonlinear effects may be important, and some of these were summarized by Zuev<sup>1</sup> in 1982. However, it has only recently been suggested that rotational stimulated Raman scattering (RSRS) in N<sub>2</sub> may ultimately limit the maximum intensity that can be propagated through air if the frequency and divergence of the laser are to remain unchanged. This suggestion is supported by recent experiments<sup>2</sup> at Lawrence Livermore National Laboratory, where RSRS in N<sub>2</sub> was observed when the NOVA fusion laser was propagated through 100 m of air at intensities in the range of a few gigawatts per square centimeter.

This observation has reinforced the need for accurate modeling of stimulated Raman scattering in air. Unfortunately, the existing uncertainties<sup>2,3</sup> in the steady-state gain coefficient in N<sub>2</sub> limit the usefulness of any potential model. In particular, no data exist for the temperature dependence of the gain coefficient, an important consideration in any model. In this Letter we present new experimental results for the temperature dependence of the Raman gain coefficient for the most important S-branch rotational transitions in N<sub>2</sub>.

Direct measurement of the gain coefficient requires an accurate measurement of the laser intensity in the interaction region. For low-gain Raman systems such as N<sub>2</sub>, this is extremely difficult since a focused geometry is usually required if adequate signal strengths are to be obtained. Alternatively, it was recently experimentally demonstrated<sup>4</sup> that the gain coefficient can be accurately calculated if the line-shape function for the Raman transition and the polarizability anisotropy are known precisely. We have chosen this alternative method for determining the rotational Raman gain coefficients in N<sub>2</sub>. Using stimulated Raman gain spectroscopy,<sup>5</sup> we have measured the density and temperature dependence of the Raman linewidths for the

Stokes-branch rotational transitions in N<sub>2</sub>. In addition, the relative scattering cross sections were measured for these same rotational lines. Using the results of these measurements and previously published values<sup>6–9</sup> of the polarizability anisotropy, we have calculated the high-density Raman gain in the temperature region 80–300 K for four of these rotational transitions.

For a Lorentzian line-shape function, the peak plane-wave, steady-state Raman gain coefficient is<sup>10</sup>

$$g = \frac{2\lambda_s^2 \Delta N}{h\nu_s \pi \Delta\nu} \frac{\partial\sigma}{\partial\Omega}, \quad (1)$$

where  $\nu_s$  is the Stokes frequency in hertz,  $\lambda_s$  is the Stokes wavelength in the medium,  $\Delta N$  is the linewidth (FWHM) in hertz, and  $\Delta N$  is the population difference, which is equal to  $N(J) - [N(J')(2J+1)/(2J'+1)]$ .  $N(J)$  is the Boltzmann statistical population density in a state with rotational quantum number  $J$ . The rotational Raman scattering cross section for incident and scattered waves linearly polarized in the same direction is given by<sup>11</sup>

$$\frac{\partial\sigma}{\partial\Omega} = \frac{2}{15} \left( \frac{2\pi\nu_s}{c} \right)^4 \frac{(J+1)(J+2)}{(2J+1)(2J+3)} \gamma^2, \quad (2)$$

where  $\gamma$  is the polarizability anisotropy. The linewidth in Eq. (1) varies with  $J$ , density, and temperature, while  $\gamma$  varies with pump-laser frequency. Thus it is necessary to know this parametric dependence in order to calculate the Raman gain accurately.

The experimental setup is a quasi-cw stimulated Raman spectrometer similar to that in Ref. 5. The cw probe laser, which provides 150 mW of power in the interaction region, is a single-mode Kr<sup>+</sup>-ion laser operating at 568 nm. The pump laser is a Coherent 699-29 single-mode cw ring dye laser that is pulse amplified using a Quanta-Ray PDA-1 amplifier. At 565 nm, the tunable output of the pump laser consists of 3-mJ, 10-nsec (FWHM) pulses at 10 Hz. The frequency resolution of this system, limited by the linewidth of the pulsed laser, is approximately 100 MHz. A 250- $\mu$ m-

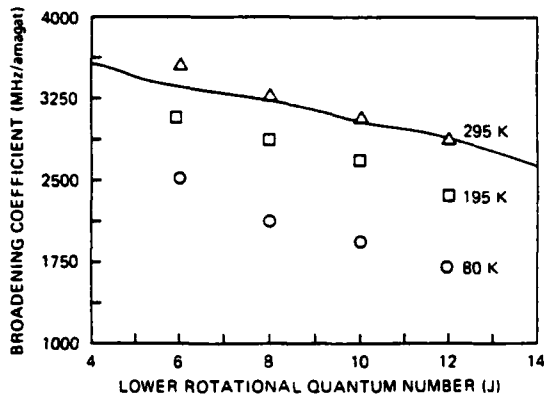


Fig. 1. Measured temperature dependence of the density-broadening coefficient for Stokes-branch rotational Raman transitions in  $N_2$ . The solid line indicates the most recent room-temperature *ab initio* calculations given in Ref. 12.

diameter pinhole is used to improve the spatial mode of the pump beam and to verify that the beam does not move when the dye laser is tuned over wavelength intervals of 10 nm. The pump and probe beams were focused and crossed (angle of 1 deg) at the center of a gas sample cell using a 40-cm focal-length lens. After the cell, stray pump light was isolated from the probe beam with a second pinhole while an ac-coupled photodiode was used to monitor the probe intensity. The Raman gain signal, which appears as a 10-nsec pulse on the probe-laser intensity, is averaged with a gated integrator and stored on a disk for later analysis.

Density-broadening coefficients were determined for the  $S(6)$ ,  $S(8)$ ,  $S(10)$ , and  $S(12)$  rotational transitions in  $N_2$ . The data were taken at three temperatures (295, 195, and 80 K) for densities spanning the range 0.01–2 amagats. The results of these measurements are shown in Fig. 1 and listed in Table 1. The values for the density-broadening coefficient at room temperature are in agreement with *ab initio* theory<sup>12</sup> (solid line in Fig. 1) and are in good agreement with recent linewidth measurements<sup>13</sup> made using spontaneous scattering. Simultaneous recording of the Raman signals at two different pressures also permitted the observation of density shifts of the Raman transition frequency. We have determined that the density shifts are less than 150 MHz/amagat for all rotational lines and temperatures studied. These broadening and shift measurements will be described in greater detail in a future publication.<sup>14</sup>

The ground-state polarizability anisotropy is defined as  $\gamma = \alpha_{\parallel} - \alpha_{\perp}$ , where ( $\perp$ ,  $\parallel$ ) indicate the perpendicular and parallel components, respectively, of the polarizability  $\alpha$ . We can model the wavelength dependence of  $\gamma$  by using an empirical formula<sup>6</sup>

$$\gamma(\nu) = \alpha_{s\parallel} \left( \frac{\nu_{i\parallel}^2}{\nu_{i\parallel}^2 - \nu^2} \right) - \alpha_{s\perp} \left( \frac{\nu_{i\perp}^2}{\nu_{i\perp}^2 - \nu^2} \right), \quad (3)$$

where  $\nu$  is the pump-laser frequency,  $\alpha_{s\perp, \parallel}$  is the static or dc polarizability, and  $\nu_{i\perp, \parallel}$  is an effective intermediate state. The  $\nu_{i\perp, \parallel}$  were determined first by fitting Eq. (3) to the results of recent *ab initio* calculations<sup>7</sup> for  $\alpha_{\parallel}$  and  $\alpha_{\perp}$ . The  $\alpha_{s\parallel}$  and  $\alpha_{s\perp}$  were then obtained by

fitting Eq. (3), with  $\nu_{i\perp, \parallel}$  fixed, to recent experimental determinations<sup>6,8,9</sup> of  $\alpha_{\parallel}$  and  $\alpha_{\perp}$  to obtain  $\alpha_{s\parallel}$  and  $\alpha_{s\perp}$ . The  $N_2$  parameters derived using this procedure are  $\nu_{i\parallel} = 1.260 \times 10^5 \text{ cm}^{-1}$ ,  $\nu_{i\perp} = 1.323 \times 10^5 \text{ cm}^{-1}$ ,  $\alpha_{s\parallel} = 2.200 \times 10^{-24} \text{ cm}^3$ , and  $\alpha_{s\perp} = 1.507 \times 10^{-24} \text{ cm}^3$ .

In Fig. 2, the wavelength dependence of  $\gamma(\nu)$ , from Eq. (3), is shown along with several experimental values. We have used data from Refs. 6, 8, and 9 only to determine the  $\alpha_{s\perp, \parallel}$  because these measurements have substantially smaller uncertainties than those of the other references cited in Fig. 2. Equations (2) and (3) yield cross sections that are in agreement with direct measurements.<sup>15,16</sup>

In  $N_2$ , the  $J$  dependence of the polarizability anisotropy,  $\gamma$ , is negligible<sup>17,18</sup> for  $J \lesssim 20$ . We have verified this conclusion by determining the relative cross sections from our stimulated Raman line-shape measurements. Thus we have used Eq. (3) to determine the polarizability anisotropy for all transitions studied in this Letter.

The reliability of Eq. (3) can be checked by using the parameters  $\alpha_{s\perp, \parallel}$  and  $\nu_{i\perp, \parallel}$  to calculate the index of refraction  $n$ ; the result can then be compared with experimental data. The expression for  $n - 1$  is

$$\frac{2}{3}(n - 1) \simeq \frac{n^2 - 1}{n^2 + 2} = \frac{4\pi N}{9} \times \left[ \alpha_{s\perp} \left( \frac{2\nu_{i\perp}^2}{\nu_{i\perp}^2 - \nu^2} \right) + \alpha_{s\parallel} \left( \frac{\nu_{i\parallel}^2}{\nu_{i\parallel}^2 - \nu^2} \right) \right], \quad (4)$$

where  $N$  is the density. Over the wavelength range 250–600 nm, expression (4) agrees with experimental data<sup>19</sup> to better than 0.5%, verifying a high accuracy for  $\gamma(\nu)$  of Eq. (3).

We have used Eqs. (1)–(3) and our linewidth data to calculate the Raman gain coefficient for the rotational transitions as a function of temperature in the limit where density broadening is the dominant contributor to the linewidth. For  $N_2$ , this high-density limit cor-

Table 1. Temperature Dependence of Rotational Raman Linewidths, Fractional Population Differences, and Gain Coefficients for  $S$  Branch in  $N_2^a$

S-Branch Transition $S(J)$	Fractional Population Difference	Broadening Coefficient (MHz/amagat)	Gain Coefficient ( $10^{-12} \text{ cm}^2/\text{W}$ )
$T = 295 \text{ K}$			
6	0.0282	3570	3.6
8	0.0337	3280	4.6
10	0.0335	3070	4.8
12	0.0289	2870	4.3
$T = 195 \text{ K}$			
6	0.0485	3070	7.2
8	0.0491	2860	7.6
10	0.0399	2660	6.5
12	0.0271	2340	4.9
$T = 80 \text{ K}$			
6	0.0897	2530	16.1
8	0.0452	2120	9.3
10	0.0156	1950	3.4
12	0.00378	1690	0.91

<sup>a</sup> ( $\lambda_s = 568 \text{ nm}$ ).

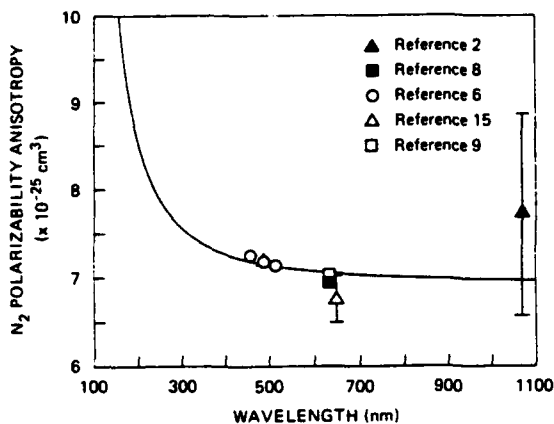


Fig. 2. Wavelength dependence of the  $N_2$  polarizability anisotropy. Solid line is given by Eq. (3), which was derived with a fit to the data of Refs. 6, 8, and 9. Data of Refs. 2 and 15 were not used in the fit but are shown for comparison.

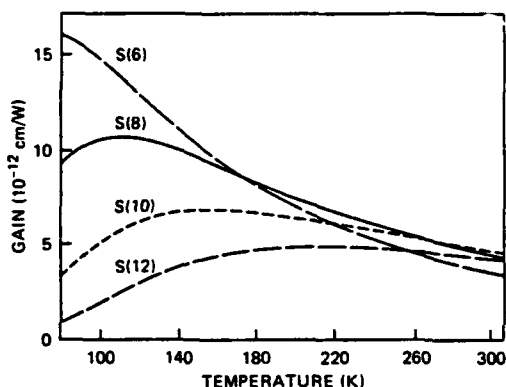


Fig. 3. Temperature dependence of the plane-wave, steady-state Raman gain in  $N_2$  calculated from Eq. (1) for the high-density limit ( $\rho > 0.01$  amagat). The pump and Stokes polarizations are linear and parallel.

responds to densities greater than 0.01 amagat. The results are summarized in Table 1, while the temperature dependence is illustrated in Fig. 3. These results were obtained by assuming that the rotational linewidths are linear with temperature and the polarizability anisotropy is constant with  $J$ .

The accuracy of the gain coefficients reported here is limited by the uncertainties in the linewidths and the polarizability anisotropy. Our linewidth measurements have uncertainties of 2% (one standard deviation) as given by the linear fits used to determine the broadening coefficients.<sup>14</sup> The uncertainty in the polarizability anisotropy was estimated to be 1.5% from the differences in the results of different investigators. Thus the accuracy of the gain coefficients reported here is approximately 5%.

We can compare the pure  $N_2$  gain coefficients reported here with the air coefficients reported by Henesian *et al.*,<sup>2</sup> since we have also measured<sup>14</sup> the foreign gas broadening coefficients of  $O_2$ . After correcting for  $N_2$  and  $O_2$  densities,  $\lambda_s$ , and the wavelength dependence of the polarizability anisotropy [Eq. (3)], we obtain a  $N_2$  gain coefficient of  $2.0 \times 10^{-12}$  cm/W for 1

atm (80/20% mixture of  $N_2/O_2$ ) at  $\lambda_s = 1.07 \mu\text{m}$ . This is 25% smaller than the value of Henesian *et al.*<sup>2</sup> but consistent with their error bar of a few tens of percents.

In conclusion, we have made linewidth and cross-section measurements that will facilitate the modeling of stimulated rotational Raman scattering in  $N_2$ . Linewidths are linear with density for densities from 0.01 to 2.0 amagats and are also linear with temperature for temperatures from 80 to 300 K. Within the accuracy ( $\pm 5\%$ ) of our relative measurements, the polarizability anisotropy was found to be independent of  $J$  for  $S(2)$  through  $S(16)$ . The new linewidth data presented here can now be used to predict accurately ( $\pm 5\%$ ) the rotational Raman gain over a wide range of temperatures and densities in  $N_2$ .

This research was supported by the Defense Advanced Research Projects Agency under contract N00014-84-C-0256 through the U.S. Office of Naval Research.

## References

1. V. E. Zuev, *Laser Beams in the Atmosphere* (Consultants Bureau, New York, 1982), pp. 243-314.
2. M. Henesian, C. Swift, and J. R. Murray, *Opt. Lett.* **10**, 565 (1985).
3. V. S. Averbakh, A. I. Makarov, and V. I. Talanov, *Sov. J. Quantum Electron.* **8**, 472 (1978).
4. W. K. Bischel and M. J. Dyer, *J. Opt. Soc. Am. B* **3**, 677 (1986).
5. P. Esherick and A. Owyong, in *Advances in Infrared and Raman Spectroscopy*, R. J. H. Clark and R. E. Hestor, eds. (Heyden, London, 1983), pp. 130-187.
6. G. R. Alms, A. K. Burnham, and W. H. Flygare, *J. Chem. Phys.* **63**, 3321 (1975).
7. P. W. Langhoff, *J. Chem. Phys.* **57**, 2604 (1972).
8. M. P. Bogaard, A. D. Buckingham, R. K. Pierens, and A. H. White, *J. Chem. Soc. Faraday Trans. 1* **74**, 3008 (1978).
9. N. J. Bridge and A. D. Buckingham, *Proc. R. Soc. London Ser. A* **295**, 334 (1966).
10. J. R. Murray, J. Goldhar, D. Eimerl, and A. Szoke, *IEEE J. Quantum Electron.* **QE-15**, 342 (1979).
11. D. A. Long, *Raman Spectroscopy* (McGraw-Hill, London, 1977).
12. D. Robert and J. Bony, *J. Phys. (Paris)* **40**, 923 (1978).
13. H. G. M. Edwards, D. A. Long, and S. W. Webb, "Self- and foreign-gas broadening of the pure rotational Raman line of oxygen and nitrogen," presented at the IXth International Conference on Raman Spectroscopy, Tokyo, August 27-September 1, 1984.
14. G. C. Herring, M. J. Dyer, and W. K. Bischel, "Temperature and density dependence of the linewidths and line-shifts of the rotational Raman lines in  $N_2$  and  $H_2$ " (submitted to *Phys. Rev. A*).
15. C. M. Penny, R. L. St. Peters, and M. Lapp, *J. Opt. Soc. Am.* **64**, 712 (1974).
16. W. R. Fenner, H. A. Hyatt, J. M. Kellam, and S. P. S. Porto, *J. Opt. Soc. Am.* **63**, 73, 1604 (1973).
17. C. Asawaroengchai and G. M. Rosenblatt, *J. Chem. Phys.* **72**, 2664 (1979).
18. H. Hamaguchi, A. D. Buckingham, and W. J. Jones, *Mol. Phys.* **43**, 1311 (1981).
19. Landolt-Börnstein, *Zahlenwerte und Funktionen*. II Band, 8 Teil, *Optische Konstanten* (Springer-Verlag, Berlin, 1962).

**Appendix M**

**MODEL OF THE ROTATIONAL RAMAN GAIN COEFFICIENTS FOR N<sub>2</sub> IN  
THE ATMOSPHERE**

Appl. Optics **26**, 2988 (1987)

# Model of the rotational Raman gain coefficients for $N_2$ in the atmosphere

G. C. Herring and William K. Bischel

A model for stimulated Raman scattering in the atmosphere is described for the pure rotational transitions in  $N_2$ . This model accounts for the wavelength dependence of the  $N_2$  polarizability anisotropy, altitude and seasonal temperature variations in the atmosphere, and the  $O_2$  foreign-gas density broadening. This information is used to calculate the steady-state plane-wave Raman gain profile over the lower 100 km of the atmosphere. Over altitudes of 0–40 km, temperature variations produce 30% changes in the gain coefficients of  $1 \text{ km}^{-1} \text{ cm}^2 \text{ MW}^{-1}$  for the strongest lines at Stokes wavelengths of 350 nm.

## I. Introduction

Several nonlinear effects, summarized by Zuev,<sup>1</sup> are possible when a high intensity laser beam propagates through the atmosphere. Recent work<sup>2–4</sup> has focused on the possibility that stimulated rotational Raman scattering in  $N_2$  may have the lowest threshold intensity. Stimulated Raman scattering then limits the maximum laser intensity that can be transmitted through the atmosphere if the divergence of the beam is required to remain unchanged. To establish this maximum intensity, it is necessary to obtain an accurate description of the steady-state Raman gain coefficient in the atmosphere.

This paper describes a model of the Raman gain coefficient for the  $N_2$  S-branch rotational transitions in the atmosphere. This model is based on our recent study<sup>3</sup> of the temperature dependence of the rotational Raman gain. In the present atmospheric work, we use the same temperature dependence as described in Ref. 3, although we also include the effect of foreign-gas ( $O_2$ ) broadening on the  $N_2$  Raman lines. This temperature-dependent Raman gain coefficient is used with a published atmospheric model<sup>5</sup> to calculate the atmospheric  $N_2$  Raman gain coefficient. The important new contribution of this paper is a temperature-dependent description of the rotational  $N_2$  Ra-

man gain coefficient as a function of altitude (0–100 km) in the atmosphere.

The modeling of the propagation of a high intensity laser pulse through a Raman medium, such as the atmosphere, requires a propagation code that includes transient effects, off-axis propagation for the generated beams, the inclusion of all possible Stokes and anti-Stokes orders that can be generated, and the provision for a variable pump laser bandwidth. Codes including some of these effects are currently being developed in several laboratories including our own.<sup>6</sup> The model of the steady-state gain coefficient presented here is an important input to these codes.

## II. Model Description

### A. Atmospheric Model

In our atmospheric gain model, the Raman gain calculation uses the altitude-dependent temperature,  $N_2$  density, and  $O_2$  density as input data. We have taken these data from actual atmospheric measurements at Wallops Island, VA (38°N), as published by Banks and Kockarts.<sup>5</sup> Slightly different results are expected if the standard atmospheric model<sup>7</sup> is used. Temperatures and densities for  $N_2$  and  $O_2$  were taken from Table 3.1 of Ref. 5. Densities were extrapolated for the first 15 km (omitted from Table 3.1 of Ref. 5) by assuming an exponential decay with increasing altitude, an  $e^{-1}$  altitude of 8 km, and relative densities of 78 and 21% for  $N_2$  and  $O_2$ , respectively. The average atmospheric temperature profiles for this model are shown in Fig. 1. Maximum variations are indicated by horizontal bars for summer and by shading for winter. Temperatures for the first 15 km (also omitted from Table 3.1 of Ref. 5) were determined from the average of the summer and winter values in Fig. 1.

The authors are with SRI International, Chemical Physics Laboratory, Menlo Park, California 94025.

Received 2 February 1987.

0003-6935/87/152988-07\$02.00/0.

© 1987 Optical Society of America.

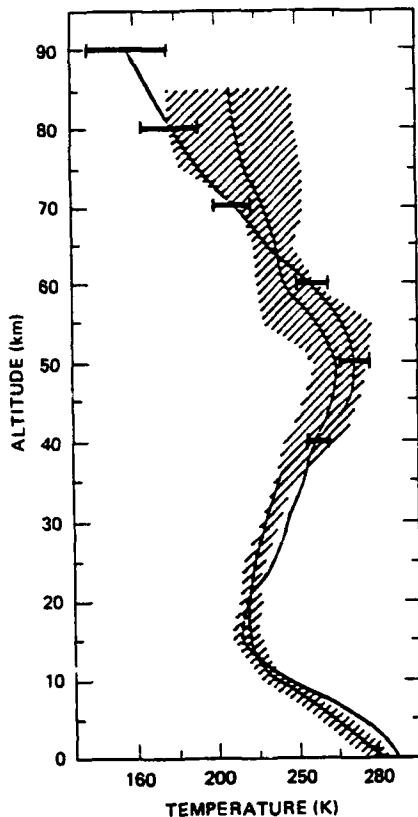


Fig. 1. Temperature profiles used in the Raman gain calculations. Maximum variations are indicated by horizontal bars for summer and by shading for winter (from Ref. 5).

### B. Raman Gain Model

The temperature dependence of the rotational Raman gain is described in Ref. 3 and summarized below. The steady-state plane-wave Raman gain coefficient is given by<sup>2</sup>

$$g = \frac{\lambda_S^2 \Delta N}{h\nu_S} \frac{\delta\sigma}{\delta\Omega} f(\delta\nu), \quad (1)$$

where  $f(\delta\nu)$  is the area-normalized Raman line shape and  $\delta\nu = \nu_p - \nu_S - \nu_R$ , where  $\nu_{p,S}$  are the pump/Stokes laser frequencies,  $\nu_R$  is the Raman transition frequency, and  $\lambda_S$  is the Stokes wavelength in the gain medium.

The spontaneous scattering cross section per molecule,  $\delta\sigma/\delta\Omega$ , is temperature independent, whereas the population difference  $\Delta N$  and the line shape  $f(\delta\nu)$  are the temperature-dependent factors. At the peak ( $\delta\nu = 0$ ) of a Lorentzian-shaped transition, Eq. (1) reduces to Eq. (1) of Ref. 3. Table I briefly summarizes the parameters used in the present Raman gain calculation.

The cross section is

$$\frac{\delta\sigma}{\delta\Omega} = \frac{2}{15} \left( \frac{2\pi\nu_S}{c} \right)^4 \frac{(J+1)(J+2)}{(2J+1)(2J+3)} \gamma^2 \quad (2)$$

for pump and Stokes polarizations that are linear and parallel, which is the only geometry considered in this work. The polarizability anisotropy  $\gamma$  is wavelength-dependent, and the details for determining the wavelength dependence are given in Ref. 3. All the results presented in this study are for a Stokes wavelength  $\lambda_S$  of 350 nm and a polarizability anisotropy of  $7.39 \times 10^{-25} \text{ cm}^3$ . We neglect the rotational quantum number  $J$  dependence of  $\gamma$ , an excellent approximation for  $N_2$ , as discussed in Ref. 3.

The population density difference is given by

$$\Delta N = N(J) - \left( \frac{2J+1}{2J'+1} \right) N(J') \quad (3)$$

$N(J)$  is the number density of molecules with rotational quantum number  $J$ , where primed and unprimed  $J$  denote the upper and lower state, respectively. The population difference  $\Delta N$  was calculated from a Boltzmann distribution using the  $N_2$  rotational constants in Ref. 8.

Only the high density limit was considered for the gain calculations of Ref. 3, and thus Lorentzian functions were used for  $f(\delta\nu)$ . For the present atmospheric model, we use a more general Voigt function for  $f(\delta\nu)$ . In the most general case, the Galatry (or other related line shapes<sup>9</sup>) line shape is a more accurate line profile for transitions that have line shapes with significant contributions from collisional narrowing. However, our use of Voigt line shapes is a good approximation for rotational  $N_2$  lines in the atmosphere for two reasons. First, at low altitudes (<20 km), pressure broadening dominates over Doppler broadening (5 MHz), and thus collisional narrowing is negligible. Second, at higher altitudes where Doppler broadening is appreciable, the

Table I. Parameters Used in the S(8) Gain Calculation for  $\lambda_S = 350 \text{ nm}$

Altitude (km)	Temperature (K)	$\Delta N/N$	Voigt $\Delta\nu_{FWHM}$ (MHz)	$f(\delta\nu = 0)$	Gain coefficient ( $\text{cm}^2 \text{ km}^{-1} \text{ MW}^{-1}$ )
0	285	0.0349	2960	0.000215	0.68
10	225	0.0441	784	0.000813	0.92
20	219	0.0451	180	0.00354	0.95
30	235	0.0424	39.8	0.0164	0.87
40	268	0.0373	10.5	0.0595	0.64
50	274	0.0365	5.7	0.121	0.36
60	253	0.0396	4.9	0.166	0.17
70	211	0.0464	4.5	0.209	0.067
80	197	0.0489	4.3	0.216	0.016
90	197	0.0489	4.3	0.218	0.0029
100	209	0.0468	4.4	0.212	0.00049

density is too small for significant collisional narrowing. Thus pure Voigt line shapes were used for all our results.

The width of the Lorentzian contribution to the Voigt was obtained by adding the linewidths due to self-broadening and to O<sub>2</sub> foreign-gas broadening. The linewidth measurements used here are summarized in Ref. 10. 'Self-broadening coefficients not given in Table I of Ref. 10 were determined by assuming a linear  $J$  dependence. Foreign-gas broadening coefficients for temperatures and  $J$  terms not given in Table V of Ref. 10 were determined by assuming that the foreign-gas values are 85% of the corresponding self-broadening values in Table I of Ref. 10. Finally, all broadening coefficients were assumed to have the linear temperature dependence described in Ref. 10. These three assumptions are based on the trends shown by the data of Ref. 10.

Our calculations assume that the laser linewidth is much smaller than the Raman linewidth. These calculations will also be valid if the laser linewidth is larger than the Raman linewidth, provided that the Stokes field is phase locked to the pump laser field.<sup>11-14</sup>

### III. Results

#### A. Altitude Dependence

Figure 2(a) shows the peak ( $\delta\nu = 0$ ) Raman gain coefficient of  $S(8)$  as a function of altitude for the temperature profile described in Sec. II.A. The two quantities  $\Delta N$  and  $\Delta\nu_T$  that combine to produce this altitude profile are also shown in Figs. 2(b) and (c) for the same temperature profile ( $\Delta\nu_T$  is the FWHM Raman linewidth.) The Raman gain is about constant below 40 km and drops to zero above 40 km. This occurs because the peak Raman gain depends on the ratio  $\Delta N/\Delta\nu_T$ . Below 40 km, Figs. 2(b) and (c) show that  $\Delta N$  and  $\Delta\nu_T$  decrease with altitude at about the same rate, yielding an approximate constant value of gain. Above 40 km, Fig. 2(b) shows that  $\Delta N$  continues to decrease, whereas Fig. 2(c) shows that  $\Delta\nu_T$  becomes constant with altitude; thus the Raman gain also decreases with altitude. The Raman linewidth is constant at high altitudes because the collisional broadening becomes negligible compared with the approximate constant Doppler broadening.

Because the Raman line shape is predominantly collisionally broadened over the 0-40-km region, a pure Lorentzian line shape should be a good approximation in the atmospheric gain calculation. For comparison, the dashed line in Fig. 2(a) shows the gain if the line shape function  $f(\Delta\nu)$  in Eq. (1) is calculated from a Lorentzian profile with a FWHM linewidth given by

$$\Delta\nu_T = (\Delta\nu_L^2 + \Delta\nu_G^2)^{1/2}. \quad (4)$$

The quantities  $\Delta\nu_G$  and  $\Delta\nu_L$  are the Doppler and collisional FWHM linewidths, respectively. The approximation is in good agreement with the full Voigt calculation except for a 20% discrepancy in the 50-70-km region. This small difference is important for the gain

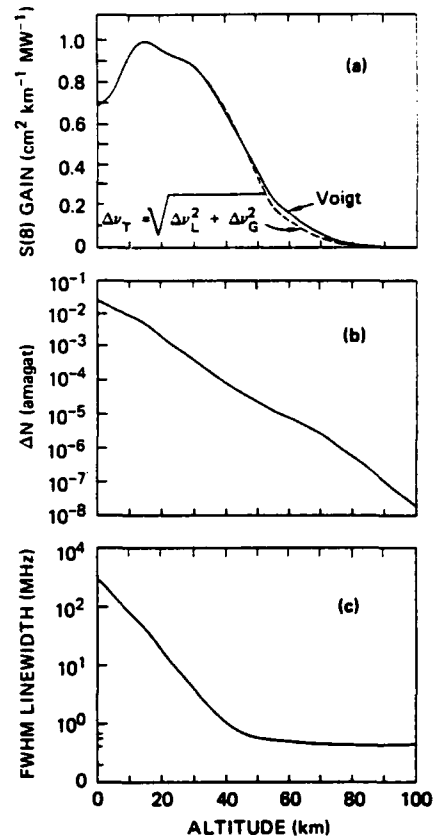


Fig. 2. Raman gain vs altitude. The solid curves show (a) the peak, steady-state plane-wave Raman gain coefficient; (b) the population difference  $\Delta N$ , and (c) the Raman linewidth (Voigt FWHM) as a function of altitude for  $S(8)$  in N<sub>2</sub>. The dashed curve in (a) shows the gain if the approximation,  $\Delta\nu_T^2 = \Delta\nu_G^2 + \Delta\nu_L^2$ , is used in place of the Voigt calculation of (c).  $\Delta\nu_T$ ,  $\Delta\nu_G$ , and  $\Delta\nu_L$  are the total, Gaussian, and Lorentzian linewidths, respectively.

calculation of the  $S(0)$  through  $S(4)$  transitions. The comparison of Fig. 2(a) shows that a simple approximation of the N<sub>2</sub> line shape is sufficient to predict accurately the atmospheric Raman gain for the most important transitions. However, we note that the rest of the results presented here were obtained with complete Voigt calculations.

The peak Raman gain coefficients for the strongest Stokes transitions are summarized as a function of altitude in Fig. 3. The difference between Figs. 3(a) and (b) is that the vertical scale of Fig. 3(b) is magnified by a factor of 3 to better illustrate the small gain coefficients of  $S(0)$  through  $S(4)$ . The number indicated next to each curve is the lower rotational quantum number  $J$  for that particular transition. Peaks and valleys that occur at an altitude of 15 km are due to the temperature minimum (200 K) that exists at this altitude. Decreasing temperatures tend to transfer molecules from the higher rotational levels to lower levels; thus  $\Delta N$  for  $S(14)$  and  $S(16)$  is decreasing while  $\Delta N$  for  $S(6)$  and  $S(8)$  is increasing at the temperature minimum. In Fig. 3,  $S(8)$  and  $S(10)$  have the largest gains at sea level, in agreement with the observation of

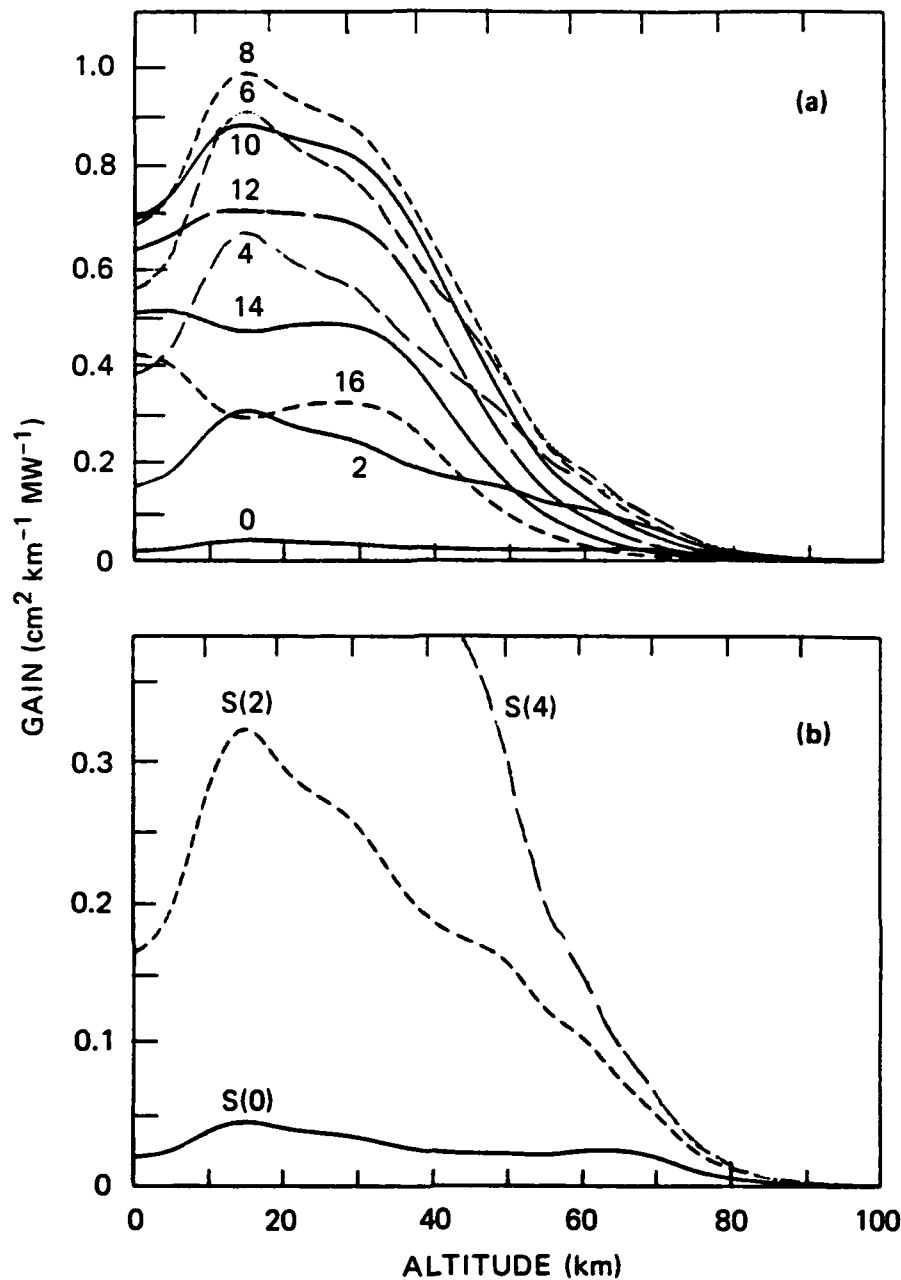


Fig. 3. Peak Raman gain coefficients for (a) the strongest transitions and (b) some of the weaker transitions as a function of altitude.

Henesian *et al.*<sup>2</sup> and our previous calculations.<sup>3</sup> The results of integrating the gain coefficients over the depth of the atmosphere (from sea level to 100 km) are tabulated in Table II, where we see that  $S(6)$ ,  $S(8)$ , and  $S(10)$  dominate the Stokes conversion process in the atmosphere. The odd-numbered  $J$  transitions are only half as strong as their adjacent even-numbered neighbors and are omitted from this investigation.

Raman gain coefficients for frequencies other than those at the peak [ $\delta\nu = 0$  in Eq. (1)] of the Raman transitions were also calculated. Figure 4(a) shows the  $S(8)$  gain coefficient as a function of altitude for detuning values of 0, 10, 100, and 800 MHz. The integrated (from 0 to 100 km in altitude) gain coeffi-

Table II. Peak Raman Gain Coefficients (Integrated from Sea Level to 100 km) for Stokes Rotational Transitions of  $\text{N}_2$

Transition $S(J)$	Gain coefficient ( $\text{cm}^2 \text{MW}^{-1}$ )
0	2.16
2	13.8
4	29.1
6	39.3
8	43.4
10	39.8
12	32.6
14	22.6
16	15.2

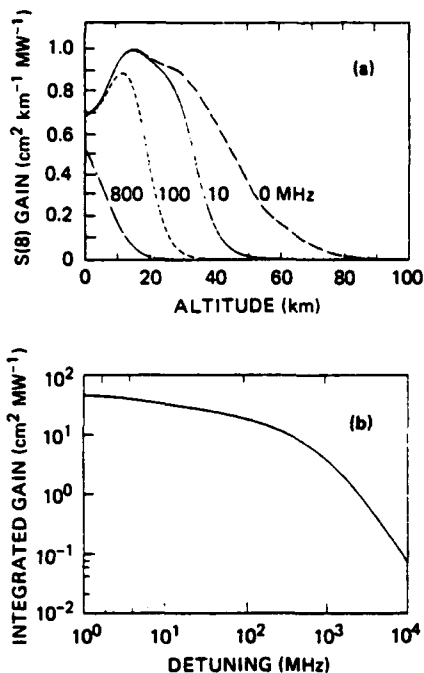


Fig. 4.  $S(8)$  Raman gain coefficient (a) as a function of altitude for detunings of 0, 10, 100, and 800 MHz from the line center and (b) integrated (from 0 to 100 km in altitude) gain coefficient as a function of detuning.

cient for  $S(8)$  is plotted vs detuning in Fig. 4(b). The information illustrated in Fig. 4 is useful for determining the effective bandwidth that experiences substantial gain over the entire lower 100 km of the atmosphere. This bandwidth is needed to calculate the pump laser intensity required to reach threshold.<sup>2,4</sup> We estimate this effective bandwidth from the detuning value, where the generated Stokes intensity is

down by a factor of 2. From Fig. 4(b), this bandwidth is 2 MHz and is to be compared to the value of  $\sim 3$  MHz that we estimate from Eq. (16) of Ref. 4.

#### B. Temperature Variations

All the results of Figs. 2–4 were obtained for the specific temperature profile of Table 3.1 of Ref. 5. The effect of atmospheric temperature fluctuations is summarized in the four curves of Fig. 5. The change in Raman gain of  $S(8)$ , due to seasonal variations of temperature, is illustrated with four different gain profiles. The four temperature profiles used in the calculations of Fig. 5 were determined from Fig. 1. The curves labeled maximum are the gains for the highest temperatures shown for that season, whereas those labeled minimum are the gains for the lowest temperatures shown for that season. Figure 5 shows that maximum variations in the Raman gain due to temperature changes in the atmosphere are  $\sim 10\%$  at all altitudes.

#### IV. Discussion

This is the first study to consider the effect of temperature variations on the Raman gain, and thus it is useful to compare the present work with a previous atmospheric gain calculation that neglects the temperature effects.<sup>4</sup> These two models are compared in Fig. 6, where the  $S(8)$  gain coefficient is plotted vs altitude for each model. Table III lists the most important parameters associated with the gain coefficient for both models. The two largest differences in these two models are the temperature distribution of the atmosphere and the density broadening coefficients that were used. Both the density broadening coefficients and the population difference change by 20–25% for  $S(8)$  when the temperature changes from

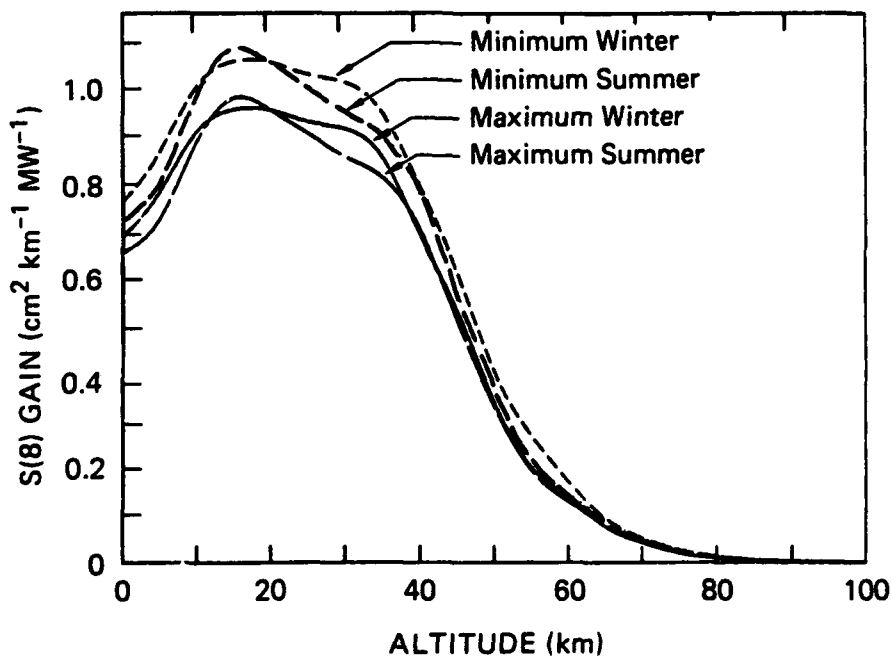


Fig. 5.  $S(8)$  peak Raman gain variations for typical variations in atmospheric temperatures.

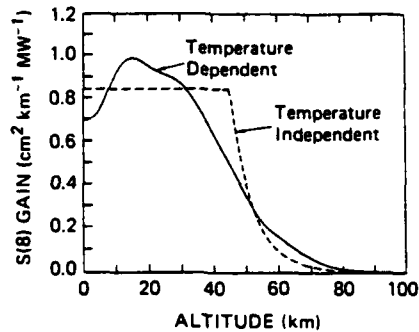


Fig. 6. Comparison of the temperature-independent model of Ref. 4 and the present temperature-dependent model of the atmospheric Raman gain coefficient for  $S(8)$ .

Table III. Atmospheric Rotational Raman Gain Coefficient and Associated Parameters for the  $S(8)$  Line in  $N_2$  at  $\lambda_s = 350$  nm

	Room temperature self-broadening coefficient (MHz/amagat)	Polarizability anisotropy ( $10^{-25}$ cm $^{-3}$ )	Sea level temperature (K)	Sea level $\Delta N/N$	Sea level gain coefficient (cm $^2$ km $^{-1}$ MW $^{-1}$ )	Threshold intensity (MW/cm $^2$ )
This work	3280	7.39	285	0.0349	0.68	0.85
Ref. 2					0.85 <sup>a</sup>	
Ref. 4	2600	7.47	300	0.035	0.83 <sup>a</sup>	0.86

<sup>a</sup> Gain coefficients were scaled to 350 nm using a  $1/\lambda_s$  dependence.

300 to 200 K. The combined effect of the atmospheric temperature variation on Raman gain coefficient is illustrated by the difference between the solid and dashed curves of Fig. 6. The broadening coefficients used in the present work<sup>10</sup> are  $\sim 20\%$  larger than those<sup>15</sup> used in Ref. 4, and this difference is the major contributor to the 15% difference in the two sea-level (or room temperature) gain coefficients of Fig. 6. To better visualize the effects on the gain due only to temperature variations, this 15% sea-level difference should be ignored. Thus the maximum difference between the temperature dependent gain and the temperature-independent gain occurs at 15 km, where the temperature-dependent model would give a gain coefficient 30% larger than the temperature-independent model.

Once the altitude dependence of the gain coefficients is known, the integrated gain can be computed and used to estimate the threshold intensity for appreciable Raman conversion. We calculate the threshold intensity with the expression

$$I_s = I_N \exp(-I_p \int g(z) dz), \quad (5)$$

where  $z$  is the atmospheric altitude,  $g(z)$  is the Raman gain coefficient,  $I_p$  is the pump intensity,  $I_s$  is the generated Stokes intensity, and  $I_N$  is the spontaneous noise intensity from the first gain length.<sup>2</sup> To compare with Ref. 4, we consider an atmospheric path perpendicular to the ground and define threshold to be  $I_s/I_p = 0.01$ . The threshold intensities for the two gain profiles shown in Fig. 6 are listed in the last column of Table III. The agreement between these two numbers illustrates the accuracy of the temperature-independent model when averaging over the entire depth of the atmosphere.

Other smaller differences between our work and that of Ref. 4 include the wavelength dependence of the polarizability anisotropy and the  $O_2$  foreign broadening. We have used the wavelength dependence of the rotational transitions,<sup>3</sup> and the results of Ref. 4 are based on the wavelength dependence of the vibrational transitions.<sup>16</sup> Another small difference is that we have accounted for the foreign-gas broadening contribution due to  $O_2$ . Each of these effects alters the gain coefficient by a few percent.

The uncertainties in the Raman gain coefficients reported for this study depend on how well the temperature of the gain medium is known. If the temperature is accurately known (e.g., laboratory conditions), the uncertainties in the gain coefficients are limited by the uncertainties in the linewidths and the polarizability anisotropy. Both of these uncertainties are  $\sim 1-2\%$ ; thus the gain coefficient uncertainties are  $\sim 5\%$ . In the atmosphere, where the temperature is not well known, the uncertainties in the gain coefficients are dominated by temperature uncertainties. Therefore, gain coefficient uncertainties are  $\sim 10\%$ , as illustrated in Fig. 5.

## V. Summary

The Raman gain of the Stokes rotational lines in  $N_2$  has been modeled as a function of altitude for the lower 100 km of the atmosphere. Calculations were completed for the even  $J$  transitions,  $S(0)$  through  $S(16)$ . The strongest lines,  $S(6)$  through  $S(10)$ , have maximum gain coefficients of  $1$  cm $^2$  MW $^{-1}$  km $^{-1}$  at an altitude of 15–20 km and smoothly decrease to zero over the 20–80-km region. Effects on the Raman gain are described for altitude and seasonal temperature

fluctuations in the atmosphere and detuning from the line center of the Raman transition. The results of this work provide useful input for simulation codes that model the stimulated Raman process in the atmosphere.

We thank David L. Huestis for stimulating conversation during this study. This work was supported by the Office of Naval Research under contract N00014-84-C-0256.

#### References

1. V. E. Zuev, *Laser Beams in the Atmosphere* (Consultants Bureau, New York, 1982).
2. M. A. Henesian, C. D. Swift, and J. R. Murray, "Stimulated Rotational Raman Scattering in Long Air Paths," *Opt. Lett.* **10**, 565 (1985).
3. G. C. Herring, M. J. Dyer, and W. K. Bischel, "Temperature and Wavelength Dependence of the Rotational Raman Gain Coefficient in  $N_2$ ," *Opt. Lett.* **11**, 348 (1986).
4. M. Rokni and A. Flusberg, "Stimulated Rotational Raman Scattering in the Atmosphere," *IEEE J. Quantum Electron.* **QE-22**, 3671 (1986); see correction to be published in *IEEE J. Quantum Electron.* **QE-23**, 000 (July 1987).
5. P. M. Banks and G. Kockarts, *Aeronomy* (Academic, New York, 1973), Chap. 3.
6. A. P. Hickman, J. A. Paisner, and W. K. Bischel, "Theory of Multiwave Propagation and Frequency Conversion in a Raman Medium," *Phys. Rev. A* **33**, 1788 (1986).
7. *U.S. Standard Atmosphere, 1976*, NOAA-S/T 76 1562 (National Oceanic and Atmospheric Administration, Washington DC, 1976).
8. K. P. Huber and G. Herzberg, *Molecular Spectra and Molecular Structure IV. Constants of Diatomic Molecules* (Van Nostrand Reinhold, New York, 1979), p. 420.
9. P. L. Varghese and R. K. Hanson, "Collisional Narrowing Effects on Spectral Line Shapes Measured at High Resolution," *Appl. Opt.* **23**, 2376 (1984).
10. G. C. Herring, M. J. Dyer, and W. K. Bischel, "Temperature and Density Dependence of the Linewidths and Lineshifts of the Rotational Raman Lines in  $N_2$  and  $H_2$ ," *Phys. Rev. A* **34**, 1944 (1986).
11. A. Flusberg, "Stimulated Raman Scattering in the Presence of Strong Dispersion," *Opt. Commun.* **38**, 427 (1981).
12. E. A. Stappaerts, W. H. Long, Jr., and H. Komine, "Gain Enhancement in Raman Amplifiers with Broadband Pumping," *Opt. Lett.* **5**, 4 (1980).
13. W. R. Trutna, Jr., Y. K. Park, and R. L. Byer, "The Dependence of Raman Gain on Pump Laser Bandwidth," *IEEE J. Quantum Electron.* **QE-15**, 648 (1979).
14. A. Flusberg, D. Kroff, and C. Duzy, "The Effect of Weak Dispersion on Stimulated Raman Scattering," *IEEE J. Quantum Electron.* **QE-21**, 232 (1985).
15. K. Jammu, G. St. John, and H. Welsh, "Pressure Broadening of the Rotational Raman Lines of Some Simple Gases," *Can. J. Phys.* **44**, 797 (1966).
16. W. K. Bischel and G. Black, "Wavelength Dependence of Raman Scattering Cross Sections from 200-600 NM," in *AIP Conference Proceedings, No. 100, Subseries on Optical Science and Engineering, No. 3, Excimer Lasers-1983*, C. K. Rhodes, H. Esser, and H. Pummer, Eds. (AIP, New York, 1983).

**Appendix N**

**CW STIMULATED RAYLEIGH-BRILLOUIN SPECTROSCOPY OF GASES**

**Third International Laser Science Conference  
1-5 November 1987, Atlantic City, NJ**

# THIRD INTERNATIONAL LASER SCIENCE CONFERENCE (ILS-III)

November 1-5, 1987

Harrah's Marina, Atlantic City, New Jersey

DO NOT WRITE IN THIS SPACE

Log number \_\_\_\_\_  
Accepted: Yes \_\_\_\_\_ No \_\_\_\_\_  
Session \_\_\_\_\_  
Program number \_\_\_\_\_  
Organizer \_\_\_\_\_

William K. Bischel 415-859-5129  
Corresponding Author *Phone Number*

SRI International Molecular Physics Laboratory  
Institution Department

333 Ravenswood Ave.  
Street Address or Box Number

Menlo Park, CA 94025  
City State (Country) Zip

poster preferred  oral preferred  no preference

Which author will most likely present this paper? Gregory Herring

Special requirements or comments \_\_\_\_\_

First choice of subject area \_\_\_\_\_ second choice \_\_\_\_\_

DO NOT TYPE IN THIS BOX →

PLEASE MAIL FLAT NOT FOLDED ESPECIALLY IN THIS AREA

THIS SPACE IS 10.5 cm

CW Stimulated Rayleigh-Brillouin Spectroscopy of Gases,\* G. C. HERRING, MARK J. DYER, and WILLIAM K. BISCHEL, SRI International, Menlo Park, CA 94025--We report the results of CW stimulated Rayleigh-Brillouin spectroscopy of gases at 568 nm. These are the first measurements that fully resolve the details of the line shapes and line shifts for the Brillouin doublet in Xe, SF<sub>6</sub>, and freons with a resolution limit of less than 10 MHz. The experiment consists of two single-frequency CW lasers, a Kr<sup>+</sup> laser at 568 nm and a tunable ring dye laser operating at 568 nm, that counter-propagate through a multipass SBS cell that refocuses the beams to common foci for 30-60 passes. The lasers are configured in a counter-propagating geometry to probe the backward SBS gain used in phase conjugation applications. The ring dye laser is amplitude modulated at 0.1-3 MHz. This modulation is transferred to the Kr<sup>+</sup> probe laser by SBS gain and is detected using a lock-in amplifier. The resulting line shapes are subsequently fit using line shape theories for Rayleigh-Brillouin scattering. The data presented here is important for applications involving phase-conjugation using stimulated Brillouin scattering.  
\*This work is supported by the Office of Naval Research.

TYPE ABSTRACT ENTIRELY WITHIN THIS RECTANGLE ONLY MATERIAL WITHIN THE LINES WILL BE PRINTED

Send this form to: Lynn Borders, Iowa Laser Facility, University of Iowa, Iowa City, Iowa 52242-1294; phone: (319) 335-1299; fax: 910-525-1398; Bitnet: BLAWCSPD@UIAMVS.

**Appendix O**

**HIGH RESOLUTION STIMULATED RAYLEIGH-BRILLOUIN  
SPECTROSCOPY OF Xe AND SF<sub>6</sub>**

# HIGH RESOLUTION STIMULATED RAYLEIGH-BRILLOUIN SPECTROSCOPY OF XE AND SF<sub>6</sub>

G. C. Herring,\* Mark J. Dyer, and William K. Bischel†  
Molecular Physics Laboratory  
SRI International, Menlo Park, CA 94025

## ABSTRACT

We have developed a high resolution (10 MHz) coherent Brillouin spectrometer that, for the first time, clearly resolves the Rayleigh and Brillouin components of the low frequency scattering spectrum of gases. Two narrow band cw lasers are used with a multi-pass cell to obtain signal-to-noise ratios of 100. We have used this apparatus to directly measure the stimulated Brillouin scattering (SBS) gain coefficients, linewidths, and line shifts for Xe and SF<sub>6</sub>. Our results improve the accuracy of previous measurements and illustrate the power of the technique for characterizing other potential SBS media for phase conjugation applications.

\* Current address: NASA Langley, Instrument Research Division, Mail Stop 235A  
Hampton, VA 23665-5225

† Current address: Coherent Inc., 3210 Porter Drive, Menlo Park, CA 94304

MP 90-126  
July 30, 1990

In recent years, phase-conjugate reflectors have generated much interest for a variety of applications.<sup>1</sup> Many nonlinear techniques can be used as phase-conjugators, but stimulated Brillouin scattering (SBS) is one of the techniques receiving the most attention.<sup>1-3</sup> Optimum design of phaseconjugate reflectors will require high resolution experiments to accurately measure the lineshape and related properties of Brillouin scattering. In the past,<sup>4</sup> the frequency resolution of SBS experiments in gases has been limited to 100 MHz by the Fourier limited bandwidths of the pulsed lasers used to drive the Brillouin interaction. More recently, a resolution of 4 MHz has been demonstrated using two cw single-frequency dye lasers,<sup>5</sup> but the signal-to-noise ratio (SNR) was too small to observe the Rayleigh component. In the present work, the combination of large SNR and high resolution has resulted in a clear separation of the Rayleigh and Brillouin components.

In this paper we report the development of a high resolution (10 MHz) SBS spectrometer to study backward SBS in gases. We have demonstrated our technique on Xe and SF<sub>6</sub>, two gases that have been previously studied because of their high SBS conversion efficiency. To achieve the highest resolution, two single-frequency cw lasers are used, while a multipass cell is used to increase the sensitivity. The high resolution of our system has allowed the direct measurement of the Brillouin linewidths and line shifts, while our high SNR and the relatively well-known Gaussian spatial profiles of the lasers has allowed accurate absolute gain coefficient measurements for both Xe and SF<sub>6</sub>.

The experimental set-up is shown in Fig. 1. The probe is a Kr<sup>+</sup>-ion laser operating at 568 nm and uses a temperature stabilized oven to reduce the bandwidth to about 10 MHz. The pump is a tunable ring dye laser that has a bandwidth of 1 MHz. Both of these laser beams are collimated to the same size (3 mm diameter) and then directed into a multipass cell (30cm focal length), where the beams are overlapped in a counterpropagating geometry. Both the pump and probe beams are passed through a Faraday isolator to prevent laser instabilities due to optical feedback. The pump beam is amplitude modulated at 100 kHz with an acousto-optic modulator that gives 85% depth of

modulation. This modulation is transferred to the probe through the SBS process when the angular frequency difference of the two lasers is equal to

$$\omega_B = 2 (\omega_1 v n/c) \sin (\Theta/2), \quad (1)$$

where  $\Theta$  is the crossing angle of the pump and probe beams,  $\omega_1$  is the probe laser angular frequency,  $v$  is the speed of sound, and  $n$  is the index of refraction. A small percentage of the probe is then picked off with a glass slide and monitored with an EG&G SGD-444 photodiode, where the 100 kHz SBS signal is detected with a lock-in amplifier.

An example of the SF<sub>6</sub> Rayleigh-Brillouin lineshape is given in Fig. 2. The dots are the data and the solid line is a fit to the data based on a Lorentzian lineshape model. The left-hand and right-hand peaks are the Brillouin loss and gain peaks respectively. The central structure is the Rayleigh gain/loss profile, seen in SBS as the derivative of the spontaneous Brillouin profile. Our best SNR is better than twice that shown in Fig. 2 and is about 100. The exact stimulated Rayleigh-Brillouin lineshape<sup>6</sup> for an atomic medium is actually more complicated than a Lorentzian, particularly at low pressures. However at the high densities used in most of this study, the Lorentzian approximation for the Brillouin profiles will not produce significant errors. At these high pressures the Rayleigh linewidth is substantially narrowed by collisions, thus the central Rayleigh profile can also be approximated as the derivative of a Lorentzian.

We have measured the pressure dependence of the Brillouin linewidths for pressures high enough that the Brillouin and Rayleigh components remain distinguishable. These measurements are shown in Fig. 3 along with the results of a Damzen et al.<sup>7</sup> who have recently measured the decay time of the acoustic intensity in pulsed SBS experiments. Their results yield the empirical relations,

$$\tau_B \text{ (ns)} \sim 0.65 \lambda^2 p \quad (2)$$

for Xe ( $p$  = pressure in atm and  $\lambda$  = laser wavelength (air) in  $\mu\text{m}$ ) and

$$\tau_{\text{B}}^{-1} (\text{sec}^{-1}) = \frac{5.9 \times 10^9}{\rho \lambda} + 1.6 \times 10^5 \rho \quad (3)$$

for  $\text{SF}_6$  ( $\rho$  = density in  $\text{kg m}^{-3}$ ), that give decay times as a function of pressure or density. In reproducing Eqn. (3) in Fig. 3, we have used the second and third virial coefficients for the equation of state.<sup>8</sup> We have converted the intensity decay times of Ref. 7 to FWHM linewidths using  $\Delta\omega = 1/\tau$ . The comparison in Fig. 3 shows good agreement between the decay time measurements and the linewidth measurements. At the highest pressures, the present linewidth measurements are about 10 MHz larger than the linewidths predicted by Eq. 3.

We have also used our signal levels to determine the absolute steadystate plane-wave gain coefficients. Assuming that the pump and probe beams have the same waist and confocal parameter, the plane-wave gain coefficient,  $g$ , is related to the multi-pass focused fractional gain,  $G$ , of the probe by<sup>9</sup>

$$G = (\Pi g P/\lambda) \frac{(1-R^N)}{(1-R)} + N \ln (R) \quad (4)$$

where  $P$  is the total power in the pump beam,  $N$  is the number of passes through the cell, and  $R$  is the mirror reflectivity. We determine  $G$  by directly measuring the ratio of the Brillouin signal and the probe power levels. This ratio is then corrected for pump and probe laser power changes. The results of our measurements are given in Fig. 4 by triangles for Xe and squares for  $\text{SF}_6$ .

The steady-state SBS gain coefficient can be calculated from<sup>10</sup>

$$g = \frac{\gamma_e^2}{\lambda^2 \frac{1}{T_B} n c v \rho} \quad (5)$$

where  $\gamma_e$  is the electrostrictive coefficient given by

$$\gamma_e = \rho (\partial \epsilon / \partial \rho)_T = \frac{1}{3} (n^2 + 1) (n^2 + 2). \quad (6)$$

Using the literature<sup>11,12</sup> values of the density dependence of the index of refraction to determine  $\gamma_e$ , we have calculated the gain for Xe and SF<sub>6</sub>. These results are plotted by the dashed lines in Fig. 4. This figure shows the agreement, within 10%, of absolute gain coefficient determinations using two different and independent methods. The agreement between the measurements and the calculations is remarkable given the uncertainties inherent in mode-matching and overlapping two counter-propagating laser beams for 50 passes. Thus we believe the present technique can be used to obtain absolute gain coefficients at the 10% uncertainty level for unknown gases and liquids.

Lastly, we have measured the Brillouin frequency shifts (center of Rayleigh line to center of Brillouin line) as a function of gas density. The data are plotted in Fig. 5. In SF<sub>6</sub>, the vertical spread in the data at 20.5 atm shows typical variations for three successive scans without any changes in the experimental apparatus, while the vertical spread near the 6 atm region shows the variations for data taken on different days with the frequency scale recalibrated between the two different days. These variations give an indication of the size of the systematic errors associated with our measurements. The Brillouin shift,  $\omega_B$ , is related to the sound velocity,  $v$ , by Eq. 1 and has been previously studied<sup>12</sup> in SF<sub>6</sub> with spontaneous Brillouin experiments. The result of Ref. 12, also shown in Fig. 5, consists of an empirical relation for the density dependence for the sound velocity and is consistent with the current measurement. In contrast, the current Xe measurements are larger than the

standard sound velocity equation (see caption) at 20 atm. We believe that this discrepancy in Xe is real since the difference is slightly larger than the error bars determined by the scatter in the SF<sub>6</sub> data.

In conclusion, we report the development of a high resolution, high sensitivity stimulated Brillouin spectrometer. The system has been demonstrated with gas phase Xe and SF<sub>6</sub>, in which we have measured absolute gain coefficients to 10% accuracy and lineshapes (linewidths and line shifts) to a few per cent accuracy. These types of measurements will be important for the modeling of the SBS process. In addition, with modest improvements in the signal-to-noise ratio and the frequency resolution, it should be possible to obtain lineshapes accurate enough to yield new information on the collision potentials<sup>13</sup> associated with atomic collisions.

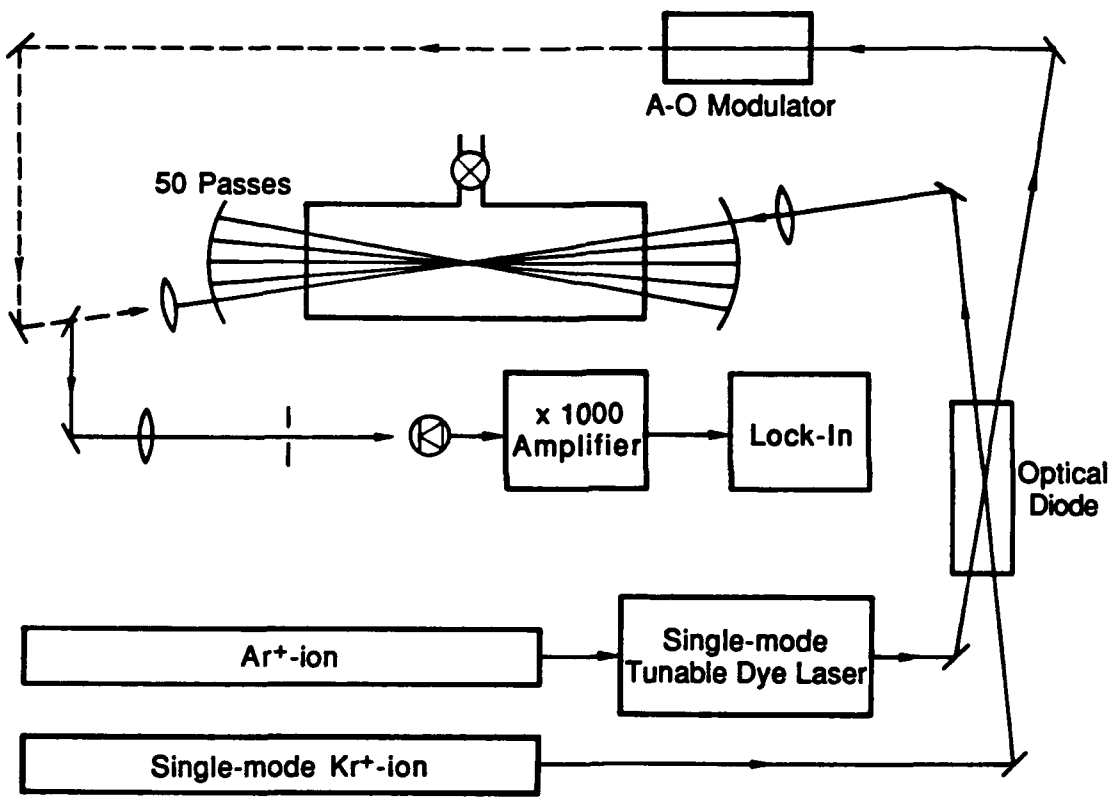
## REFERENCES

1. *Optical Phase Coniugation*, Robert A. Fisher, Ed. (Academic, New York, 1983)  
Chapter 1.
2. B. Ya. Zel'dovich, V. I. Popovichev, V. V. Ragul'skii, and F. S. Faizullov, *Sov. Phys. JETP* **15**, 109 (1972).
3. Marcy Valley, Gabriel Lombardi, and Robert Aprahamian, *J. Opt. Soc. Am.* **B3**, 1492 (1986)
4. C. Y. She, G. C. Herring, H. Moosmuller, and S. A. Lee, *Phys. Rev.Lett.* **51**, 1648 (1983).
5. S. Y. Tang, C. Y. She, and S. A. Lee, *Opt. Lett.* \_\_\_\_, (1987).

6. A. Sugawara, S. Yip, and L. Sirovich, *Fluids* **11**, 925 (1968)
7. M. J. Damzen, M. R. H. Hutchinson, and W. A. Schroeder, *IEEE J. Quantum Electron.* **QE-23**, 328 (1987).
8. J. H. Dymond and Smith, *The Virial Coefficients of Pure Gases and Mixtures*, (Oxford Univ. Press, New York, 1980) pp. 192 and 251.
9. W. R. Trutna and R. L. Byer, *Appl. Opt.* **19**, 301 (1980).
10. W. Kaiser and M. Maier, "Stimulated Rayleigh, Brillouin, and Raman Spectroscopy," in *Laser Handbook, Vol. 2* (North Holland, Amsterdam, 1972) pp. 1077-1150.
11. Landolt-Bornstien, *Zahlenwerte und Funktionen II. Band. 8. Teil, Optische Konstanten* (Springer-Verlag, Berlin, 1962).
12. C. M. Hammond and T. A. Wiggins, *J. Acoust. Soc. Am.* **52**, 1373 (1972).
13. N. A. Clark, *Phys. Rev. A* **12**, 232 (1975).

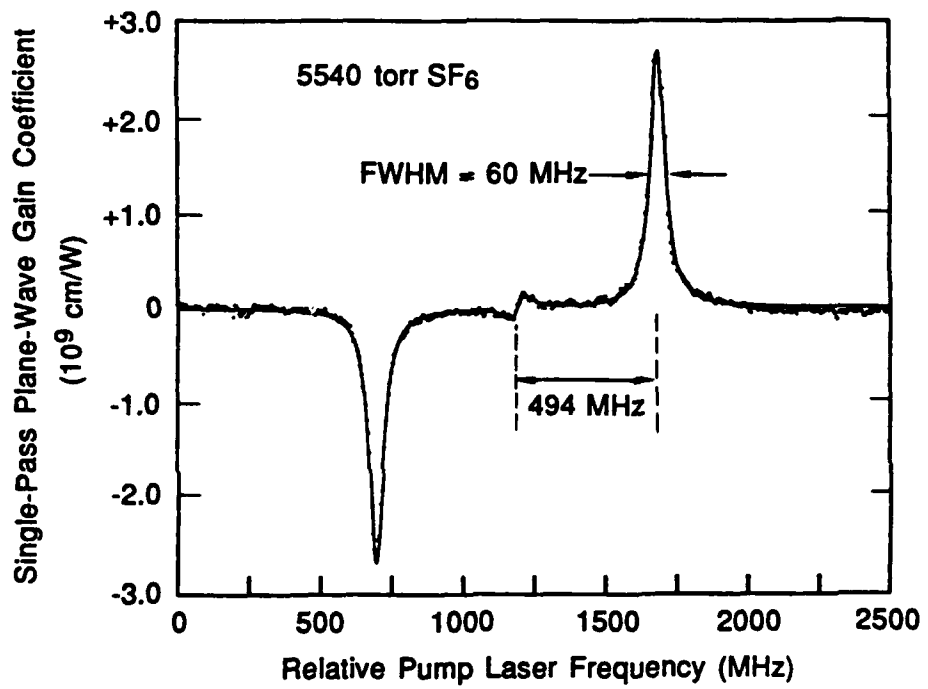
## FIGURE CAPTIONS

1. Experimental set-up for backward coherent Brillouin scattering. We use 50 passes in a multipass cell that has a single-pass transmission (window losses and mirror reflectivity combined) of  $R = 0.985$ . Laser powers into the cell are 70 and 150 mW for the pump (ring-dye) and probe (ion) respectively.
2. Rayleigh-Brillouin lineshape for 5540 torr of  $\text{SF}_6$  at room temperature. Dots show data, while the solid line shows a fit that consists of Lorentzians for the Brillouin gain and loss peaks and a Lorentzian derivative for the central Rayleigh peak.
3. Pressure dependence for Brillouin linewidths. The solid/dotted lines show linewidths derived from the decay time measurements of Ref. 7, while the direct measurements of this work are shown for Xe (triangles) and  $\text{SF}_6$  (squares).
4. Pressure dependence of Brillouin gain coefficients at 568 nm. The present results for Xe (triangles) and  $\text{SF}_6$  (squares) are shown along with calculations of Eq. 5 (dashed lines). The  $\text{H}_2$  Raman gain for the Q(1) vibrational transition (solid line) is shown for comparison.
5. Pressure dependence of the Brillouin shifts. Current results (squares for  $\text{SF}_6$  and triangles for Xe) are compared to the results of Ref. 12 (solid curve) for  $\text{SF}_6$  and the sound velocity equation (dotted curve),  $v = (\gamma dp/d\rho)^{0.5}$  S, for Xe, where  $\gamma$  is the heat capacity ratio  $C_p/C_v - 5/3$ .



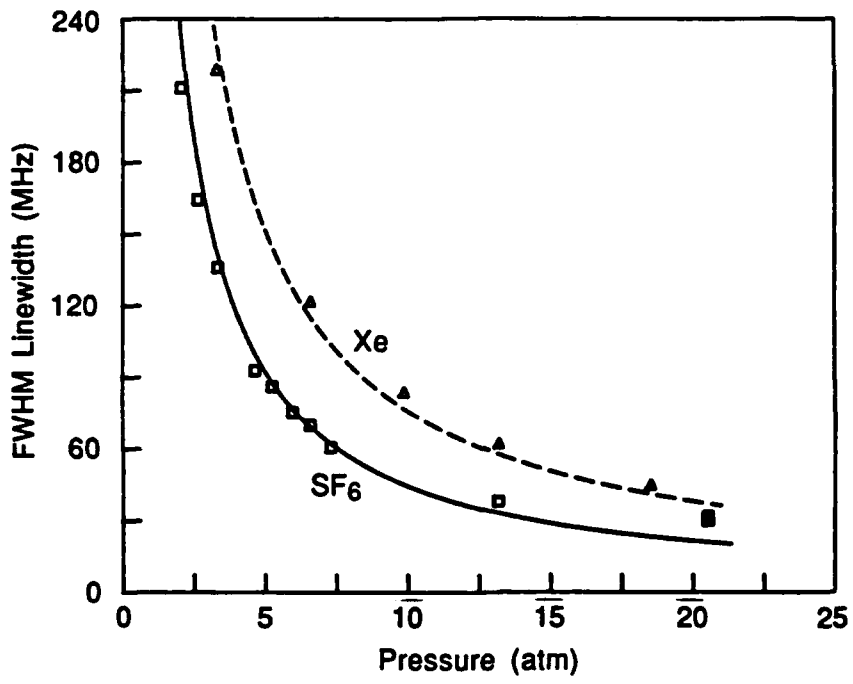
JA-m-7123-74

Fig. 1



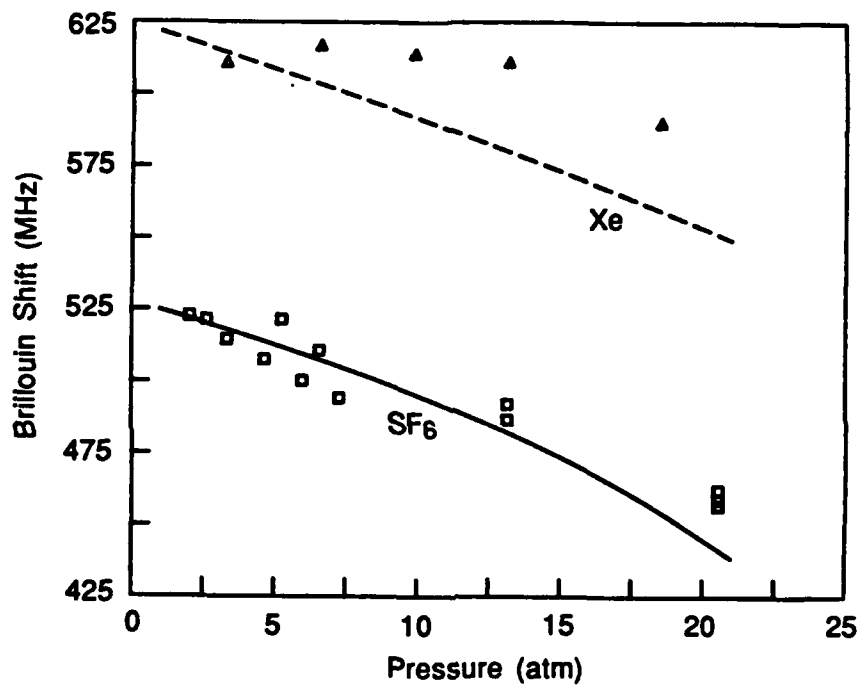
JA-7123-90

Fig. 2



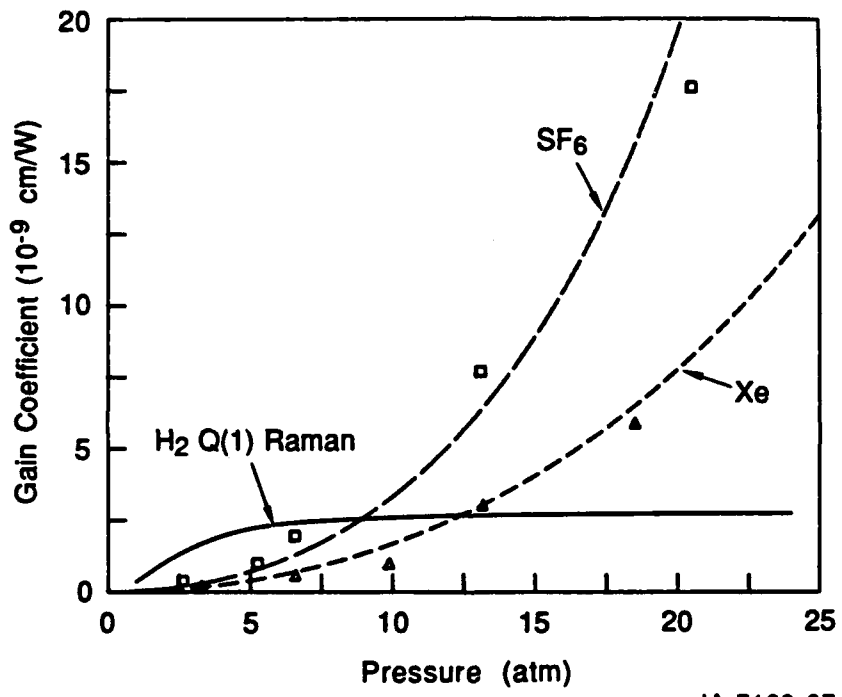
JA-7123-88

Fig. 3



JA-7123-89

Fig. 4



JA-7123-87

Fig. 5

**Appendix P**

**HIGH-POWER 80-ns TRANSFORM-LIMITED Nd:YAG LASER**

**SPIE 912, 32 (1988)**

## High-power 80-ns transform-limited Nd:YAG laser

Mark J. Dyer and William K. Bischel  
Chemical Physics Laboratory, SRI International  
Menlo Park, CA 94025

and

David G. Scerbak  
Electro-Optics Technology  
Fremont, CA 94538

### ABSTRACT

The construction and operation of a long pulse, single-mode Nd:YAG laser is described. The laser is configured around an injection-seeded, unstable oscillator/single amplifier and produces 80 ns pulses at 10 Hz with pulse energies of over 300 mJ. When frequency doubled, the infrared is converted to a 56 ns pulse at 532 nm with a Fourier-limited linewidth of 8 MHz. This approach brings the Nd:YAG source to within the bandwidth domain normally dominated by visible CW lasers, but at a considerably higher power, thus providing an attractive alternative for applications in high resolution spectroscopy and non-linear studies.

### 1. INTRODUCTION

The importance of narrowband laser light to high resolution spectroscopic studies is well recognized. While pulsed sources have found some application, the use of linewidth-narrowed and stabilized CW ion and dye lasers has long been the convention in fulfilling experimental requirements for narrow bandwidths of better than 10 MHz. Unfortunately, CW lasers rarely provide line-narrowed powers greater than several watts without extraordinary attention to stabilization and cooling requirements. For kilowatt or greater powers, pulsed sources appear far more practical and efficient, but only if the coherence properties of CW lasers can be emulated. With the recent development of laser-diode-pumped, single-mode Nd:YAG lasers<sup>1,2,3</sup> and the demonstrations of injection locking<sup>4,5</sup> Fourier-limited operation of high-power Nd:YAG lasers is now easily performed and commercially available. Though most attention has been directed toward highest power pulse durations of around 10 ns, to produce linewidths of less than 10 MHz, pulses of greater than 44 ns must be generated.

The production of long single mode pulses in Nd:YAG may be approached in several ways. Certainly the most versatile source would result from chain amplifying an acousto- or electro-optically shaped single mode CW laser emission. In order to compete with the power levels of other available continuous lasers, however, this method can become quite costly and complex, though multipass slab amplifier geometries promise to make this a more attractive technique.<sup>6</sup> Long pulses may also be generated in stable or unstable Q-switched Nd:YAG oscillator configurations. Lengthening the pulse build-up time or forcing the stimulated photons within the cavity to circulate longer before saturating the rod gain results in a longer ejected pulse. Furthermore, injection locking these longer pulses to a single mode master frequency yields narrowband light robust enough for immediate power amplification.

We have constructed a stable source of high power, Fourier transform-limited, 80 ns wide laser pulses using an injection-seeded unstable resonator and a single stage of amplification, which provides more than 300 mJ of output energy per pulse. The design is a slightly modified version of an earlier system,<sup>7</sup> but the technique may certainly be applied to virtually any Q-switched resonator.

### 2. SYSTEM DESCRIPTION

The entire system, illustrated in Fig. 1, consists of five principle stages: master oscillator, slave oscillator, isolation, amplification and frequency doubling. The master oscillator is a Lightwave Electronics S-100 Injection Seeding System. It is a compact package housing a well-stabilized, laser-diode-pumped, single-mode Nd:YAG ring laser, Faraday isolator and associated electronics, and provides almost 2.5 mW of CW power in a 1 mm diameter beam at its output. The seeder is directly mounted to the Invar resonator structure within a Molectron MY34-10 Nd:YAG laser. This modified chassis contains the slave oscillator, an adaption of a self-filtering unstable resonator<sup>8</sup> design, isolation and amplification stages, and frequency doubling and harmonics separation optics.

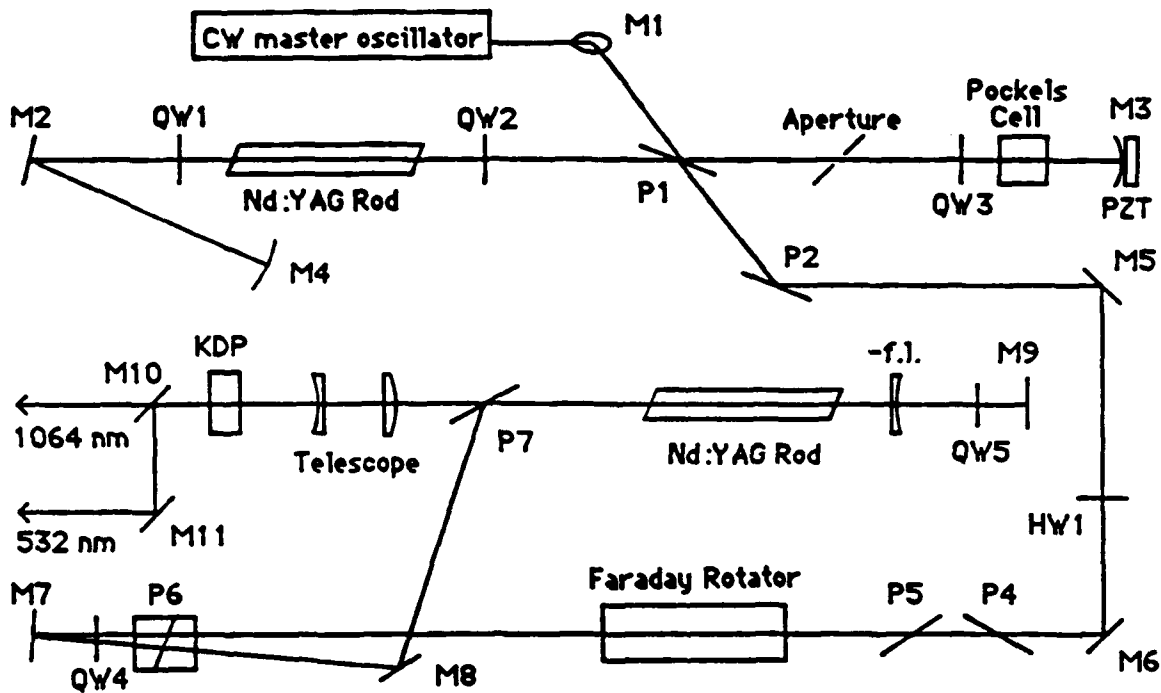


Figure 1. Component schematic for single-mode long pulse generation and amplification.

## 2.1 Master/slave oscillator

The master frequency from the seeder is polarization-coupled into the self-filtering unstable resonator (SFUR), where it effectively fills the entire volume of a 7mm X 110mm Nd:YAG rod housed in a Quantel SF51107 dual flashlamp pump chamber. When the flashlamps are fired, the rod gain is swept by approximately .65 mW from the seed laser until Q-switch action is initiated. At the peak of the rod gain, the Q-switch is opened, momentarily closing the cavity off to the seed and permitting the master frequency to be resonantly amplified within the slave. A piezo stack mounted behind the end reflector M3 and controlled by Q-switch buildup time (QSBUT) reduction electronics<sup>9</sup> in the S-100 seeder provides active stabilization of the slave cavity length in order to support the master frequency. Quarterwave plates on either side of the rod provide the necessary suppression of spatial hole burning<sup>10</sup> and adjustable outcoupling. When operated at high flashlamp energies near the limits of Q-switch hold-off, this resonator produces more than 200 mJ in 10 ns on a single axial mode and with near diffraction-limited beam quality.

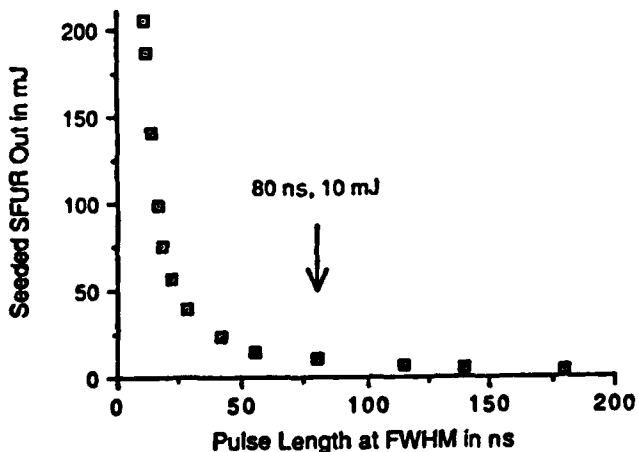


Figure 2. Plot of the energy per pulse as a function of pulse duration for the injection seeded SFUR cavity.

### 2.1.1 Long pulse generation

Stretching the pulses of a Q-switched resonator was rather straightforward. It could have been accomplished either by increasing the length of the oscillator, introducing higher intracavity losses, or by changing the gain of the active medium. Lengthening the slave cavity considerably to obtain 80 ns pulse widths was quickly dismissed due to considerations of mechanical stability and space limitations. We avoided introducing additional lossy elements into the cavity because they would also reduce the seed laser power presented to the rod and possibly degrade spatial performance. The two alternatives available to us to increase the losses, Q-switch control and quarterwave plate rotation to

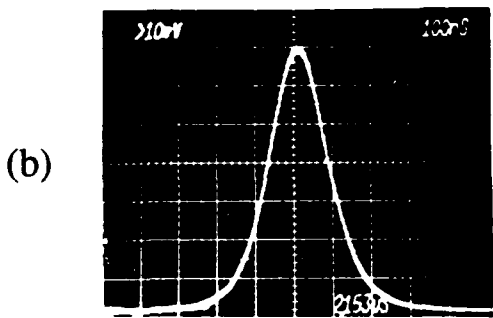
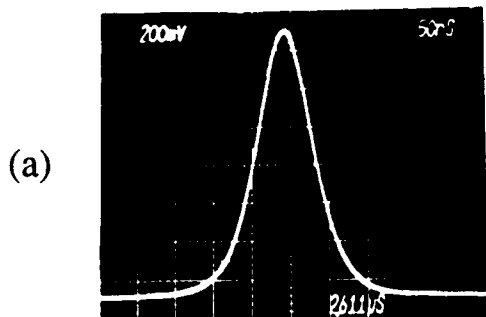


Figure 3. Oscilloscope traces of the injection-locked long pulses at  $1.064\mu\text{m}$  for (a) 80 ns and (b) 180 ns at FWHM.

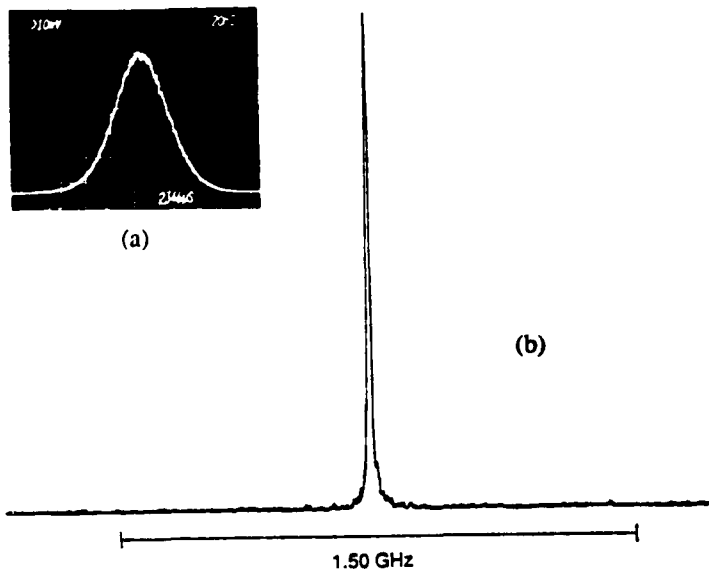


Figure 4. (a) Temporal profile of the second harmonic and (b) optical spectrum of the  $.532\mu\text{m}$  shows good agreement with the expected Fourier-transform bandwidth of 8 Mhz to within the resolution of the scanning confocal interferometer.

impossible. The isolation stage consists of a permanent magnet Faraday rotator manufactured by Electro-Optics Technologies and positioned between paired thin film polarizers and a Glan-laser polarizer. With AR-coatings and a clear aperture of 8.5 mm, the entire isolator

diminish feedback, met with limited success. Long pulses were created, but they proved more difficult to control and injection seed than those produced simply by lowering the applied flashlamp energy and, therefore, the gain of the rod. With some repositioning of end reflector M4 to compensate for differences in rod lensing, this master/slave combination yielded seeded pulses continuously variable in width from 10 ns to as much as 180 ns at FWHM, with relatively high energies. Fig. 2 shows the variation of output energy with pulse length and Fig. 3 illustrates the pulse shapes of the long pulses.

Active stabilization of the slave cavity for 80 ns pulse generation is only slightly more difficult than for 10 ns pulse operation. Because the 80 ns pulses emerge from the slave a few hundred nanoseconds past the Q-switch trigger, instead of less than 100 ns for the 10 ns pulse, a corresponding delay had to be introduced into the trigger of the seeder for its QSBUT reduction electronics to lock properly (this was less invasive than changing the dynamic range of the reduction circuit). Also, since the output timing of the slave is processed by the reduction electronics via a photodiode monitoring the weak back reflection off a polarizer in the seeder, the photodiode signal had to be boosted for the lower long pulse intensities. Taking precautions to isolate the slave resonator from mechanical vibrations was the last concern before long term stable operation was possible. The final output at 80 ns was 10 mJ at  $1.064\mu\text{m}$  with approx.  $\pm 10$  ns timing jitter, attributed mostly to pulse build-up statistics, and less than 2 MHz frequency dither, determined by the piezo movement and the slave cavity's free-spectral range, imposed on the bandwidth from the active stabilization by the seeder. Figure 4 presents a spectrum of the frequency doubled output at 532 nm taken with a scanning confocal interferometer.

## 2.2 Isolation

Of paramount importance to the stability of the seeded resonator for the purpose of power amplification is the insertion of an optical isolator between the oscillator and amplifier. This decouples the two stages, preventing spontaneous emission in the amplifier from propagating back into the oscillator, during the buildup of the long pulse, and competing with the injected frequency. Without adequate isolation, seeding is at best erratic and active locking

assembly furnishes an isolation of greater than 40 dB with less than 10% total insertion loss.

Tracing the optical path in Fig. 1, the linearly polarized output from the slave cavity is rotated 45° from vertical by the halfwave plate HW1, then transmitted through the thin film polarizers P4 and P5 before entering the Faraday rotator, where the polarization is rotated 45° back to the vertical and passed through the Glan-laser polarizer P6. The beam is then retroreflected through a quarterwave plate, used only for beam attenuation in this scheme, and presented to the amplification stage by polarization coupling off polarizer P7.

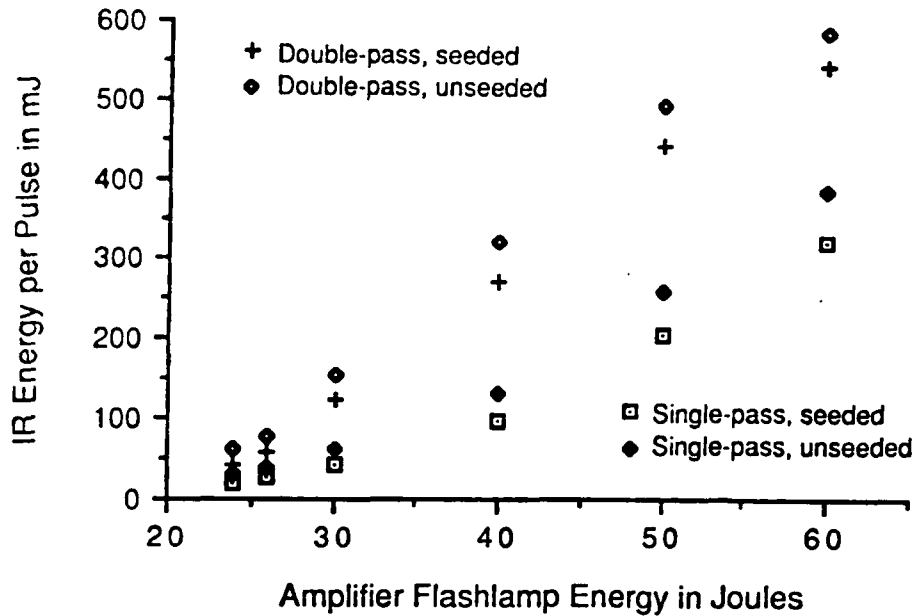


Figure 5. Single and double pass energy plots versus applied flashlamp energy for seeded and unseeded operation.

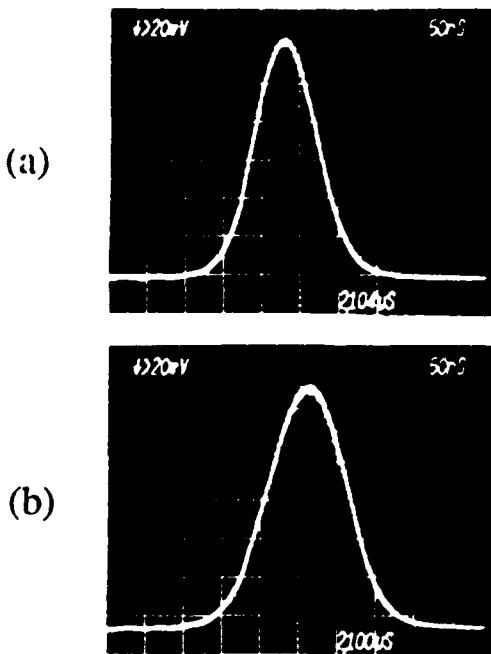


Figure 6. Pulse broadening related to gain saturation for (a) 450 mJ and (b) 540 mJ double-pass output at 1.064  $\mu\text{m}$ .

### 2.3 AMPLIFICATION

Amplified energies of several hundred millijoules were initially achieved with single-pass amplification through a Nd:YAG pump chamber identical to that used in the oscillator cavity. With less than 10 mJ into the rod, however, flashlamp-pumping the rod hard enough to reach these energies severely distorted the spatial quality of the output beam and left the gain unsaturated. A polarization-multiplexed, double-pass geometry was then adopted. The vertically polarized beam reflection from polarizer P7 passes through the rod, retroreflects off mirror M9 through a quarterwave plate, where it undergoes a full halfwave rotation, and then passes back through the amplifier. The amplified beam is then transmitted by P7 and down-collimated for frequency conversion. For this amplification scheme, the Faraday isolator was particularly valuable because it removed any undesirable energy rejected from P7 that might retrace the optical path back to the oscillator. The results of the single- and double-pass amplification schemes are shown in Fig. 5

We confirmed that gain saturation was occurring above 300 mJ for double-pass amplification but observed that the pulse broadened in time. As seen in Fig. 6, the pulse width increases by 150% for a flashlamp energy of 60 Joules and a total pulse energy of 540 mJ.

#### 2.4 Frequency doubling

Frequency doubling efficiencies of the high power pulses are under investigation at this time. With 50% down-collimation after the amplifier, we expect at least 10% conversion efficiency for the unbroadened 80 ns output. Spectral analysis of the doubled high power will determine if additional frequency components are created by the amplification and doubling stages, and significantly influence the bandwidth integrity of the unamplified emission.

### 3. DISCUSSION

We found that pushing this technique further to longer pulses appears possible, but owing to mechanical and thermal instabilities in our slave resonator, the extremely long pulse build-up times and subsequent timing jitter of the pulse evolution, the seeder could not maintain adequate lock for more than a few seconds for pulses greater than 100 ns. By modifying the dynamic range and time constant of the time-reduction circuit within the seeder, and improving the mechanical and thermal stability of the slave cavity, we hope to push this system as far as the master oscillator will successfully seed the SFUR cavity. With .65 mW of injected power, this limit appears to be just under 200 ns before mode-beating oscillations appear on the pulse waveform. This restriction, along with the relative pulse buildup times of different pulse lengths, is illustrated by Fig. 7.

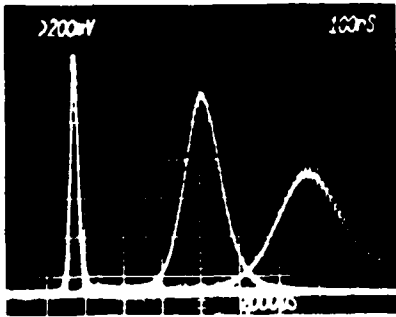


Figure 7. Oscilloscope traces superimposed to demonstrate the limits of this technique for .65 mW of injected seed power. Long pulses may be seeded from 10 ns to just under 200 ns before oscillations appear on the waveform.

### 4. CONCLUSION

We have demonstrated that long pulse, narrowband operation of injection-seeded Nd:YAG lasers is possible by varying the applied flashlamp energy to the slave oscillator. With minor modifications and the addition of optical isolation between oscillator and amplifier, the output is stable and may be power amplified directly to produce several hundred millijoules of 1.064  $\mu\text{m}$  radiation with a bandwidth of less than 10 MHz.

### 5. REFERENCES

1. B. Zhou, T.J. Kane, G.J. Dixon, and R.L. Byer, "Efficient, frequency-stable laser-diode-pumped Nd:YAG laser," *Opt. Lett.* **10**, 62-64 (1985).
2. T.J. Kane and R.L. Byer, "Monolithic unidirectional single-mode Nd:YAG ring laser," *Opt. Lett.* **10**, 65-67 (1985).
3. W.R. Trutna, Jr., D.K. Donald, and M. Nazarathy, "Unidirectional diode-laser-pumped Nd:YAG ring laser with a small magnetic field," *Opt. Lett.* **12**, 248-250 (1987).
4. Y.K. Park, G. Giuliani, and R.L. Byer, "Stable single-axial-mode operation of an unstable-resonator Nd:YAG oscillator by injection locking," *Opt. Lett.* **5**, 96-98 (1980).
5. R.L. Schmitt and L. Rahn, "Diode-laser-pumped Nd:YAG laser injection seeding system," *Appl. Opt.* **25**, 629-633 (1986).
6. T.J. Kane, W.J. Kozlovsky, and R.L. Byer, "62-dB-gain multiple-pass slab geometry Nd:YAG amplifier," *Opt. Lett.* **11**, 216-218 (1986).
7. M.J. Dyer, D.G. Scerbak, and W.K. Bischel, "Injection seeding of a self-filtering unstable resonator using a cw diode-pumped Nd:YAG ring oscillator," (in preparation, 1988).
8. P.G. Gobbi, S. Morosi, G.C. Reali, and A. Zarkasi, "Novel unstable resonator configuration with a self-filtering aperture: experimental characterization of the Nd:YAG loaded cavity," *Appl. Opt.* **24**, 26-33 (1985).
9. L.A. Rahn, "Feedback stabilization of an injection-seeded Nd:YAG laser," *Appl. Opt.* **24**, 940 (1985).
10. E.S. Fry and S.W. Henderson, "Suppression of spatial hole burning in polarization coupled resonators," *Appl. Opt.* **25**, 3017 (1986).

**Appendix Q**

**LASER FREQUENCY CONVERSION USING TWO-PHOTON EMISSION IN  
BARIUM VAPOR**

Conference on Lasers and Electro-Optics (CLEO 88)  
25-29 April 1988, Anaheim, CA

**VM34 LASER FREQUENCY CONVERSION USING TWO-PHOTON  
EMISSION IN BARIUM VAPOR**

James J. Silva, C. C. Liu, Kenneth Y. Tang, Western Research Corporation;  
David L. Huestis, SRI International

**ABSTRACT**

We calculate the nonlinear susceptibility for conversion of ultraviolet krypton fluoride excimer laser radiation to the visible using stimulated two-photon emission in barium vapor and discuss results of an experiment to measure this conversion.

# FREQUENCY HALVING

--- USES NONLINEAR MEDIUM (ATOMIC BARIUM VAPOR) TO GENERATE TWO VISIBLE PHOTONS FROM ONE UV PHOTON.

$$\omega_{\text{KrF}} - \omega_{\text{CO}_2} = 2\omega_{\text{F.H.}} + \Delta\varepsilon_{\text{Metastable}}$$

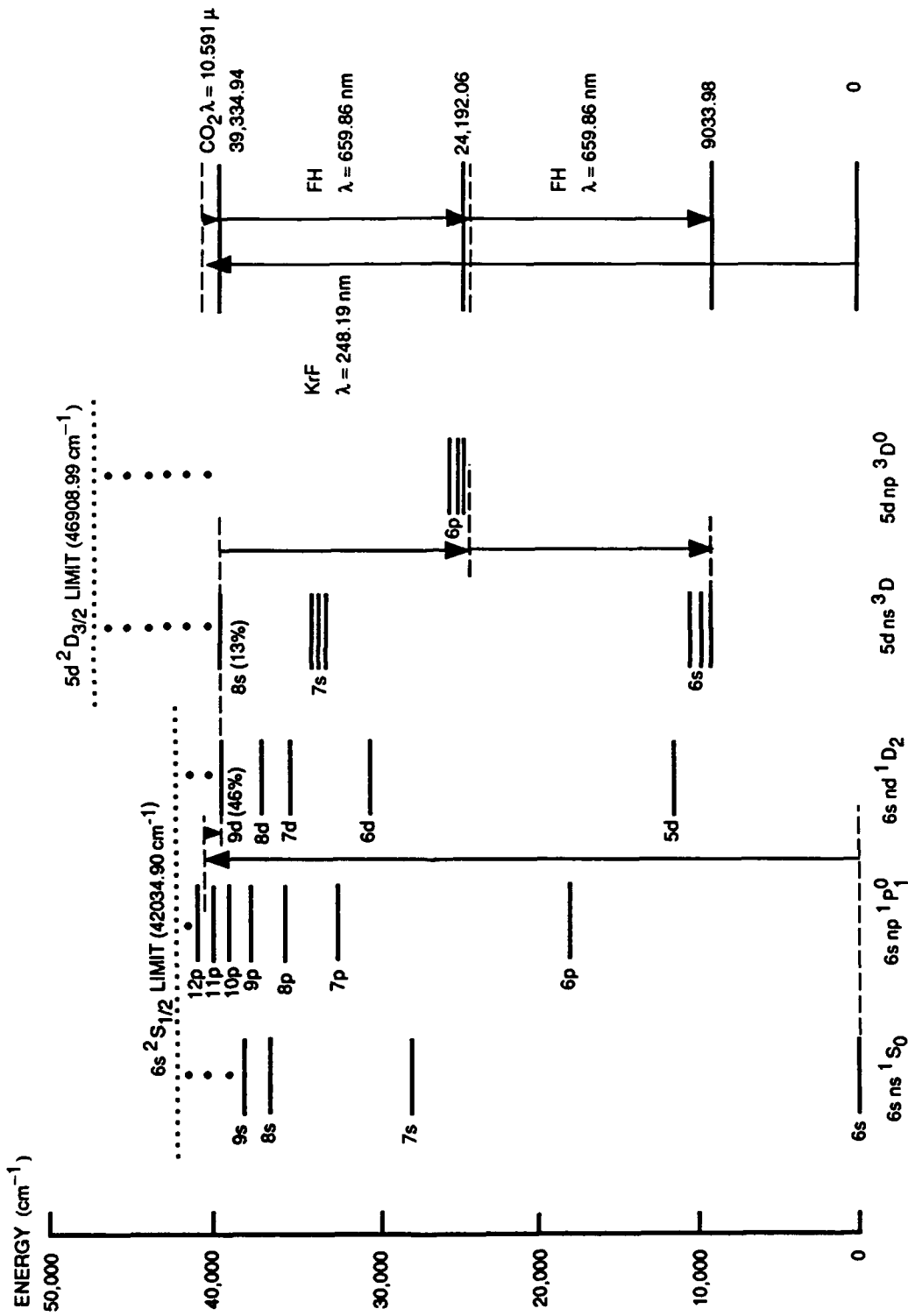
--- SCHEME IS A HYPER-RAMAN PROCESS. NO PHASE MATCHING IS REQUIRED, AND HIGH EFFICIENCY AND BEAM CLEANUP CAN BE EXPECTED.

--- LARGE FREQUENCY DOWNSHIFT FROM KrF (248nm) TO VISIBLE (660nm) DOES NOT RESULT IN LARGE ENERGY WASTE AS IT WOULD IN RAMAN SHIFTING BECAUSE TWO VISIBLE PHOTONS COME OUT FOR ONE UV PHOTON IN.

--- HIGH EFFICIENCY VISIBLE LASER POSSIBLE STARTING WITH EFFICIENT KrF EXCIMER LASER

--- OUTPUT AT 660nm IS IDEAL BECAUSE OF HIGH OPTICS DAMAGE THRESHOLDS AND LOW ATMOSPHERIC SCATTERING

## FREQUENCY HALVING: BARIUM ENERGY LEVEL SCHEME



# FREQUENCY HALVING GAIN EQUATION

--- FREQUENCY HALVING PROCESS INVOLVES A SEVENTH ORDER NONLINEAR SUSCEPTIBILITY

--- HIGH SUSCEPTIBILITY REQUIRES NEARLY RESONANT INTERMEDIATE LEVELS

--- KrF AND CO<sub>2</sub> LASERS CAN BE TUNED FOR STIMULATED RAMAN SCATTERING TO BARIUM LEVEL AT 39335 cm<sup>-1</sup>

--- SUBSEQUENT STIMULATED TWO-PHOTON EMISSION TO LEVEL AT 9034 cm<sup>-1</sup> IS DETUNED BY ONLY 7cm<sup>-1</sup> FROM INTERMEDIATE LEVEL AT 24192 cm<sup>-1</sup>

--- SUSCEPTIBILITY IS A FUNCTION OF LASER POLARIZATION. FOR LINEAR POLARIZATIONS, KrF AND CO<sub>2</sub> POLARIZATIONS MUST BE PERPENDICULAR TO EACH OTHER.

--- CALCULATION OF SUSCEPTIBILITY INVOLVES SUMS OVER INTERMEDIATE LEVELS OF PRODUCTS OF EIGHT TRANSITION DIPOLE MOMENTS DIVIDED BY PRODUCTS OF SEVEN DETUNINGS OR LINEWIDTHS

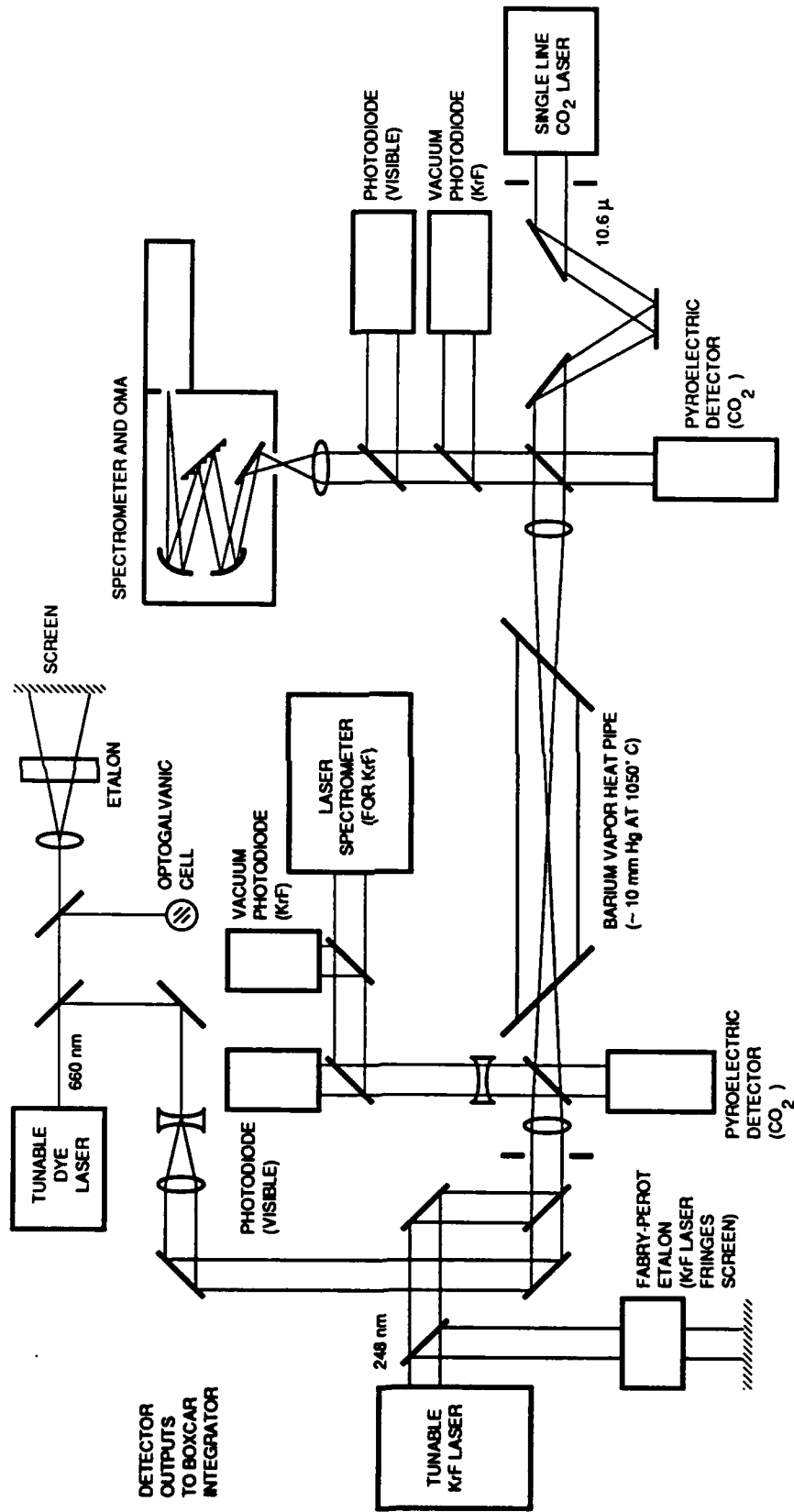
$$\chi^{(7)}(-\omega_{F.H.}; \omega_{KrF} - \omega_{CO_2} - \omega_{F.H.} \omega_{F.H.} \omega_{CO_2} - \omega_{KrF} \omega_{F.H.}) \\ = (N/i\Gamma\Delta^2)(2 \times 10^{-43}) \text{ cm}^9/\text{erg}^3$$

WHERE N=ATOMIC NUMBER DENSITY (cm<sup>-3</sup>),  
 $\Delta$ =DETUNING FROM S.R.S. RESONANCE (cm<sup>-1</sup>) AND  
 $\Gamma$ =LASER LINEWIDTH (cm<sup>-1</sup>)

--- GAIN EQUATION FOR VISIBLE SEED

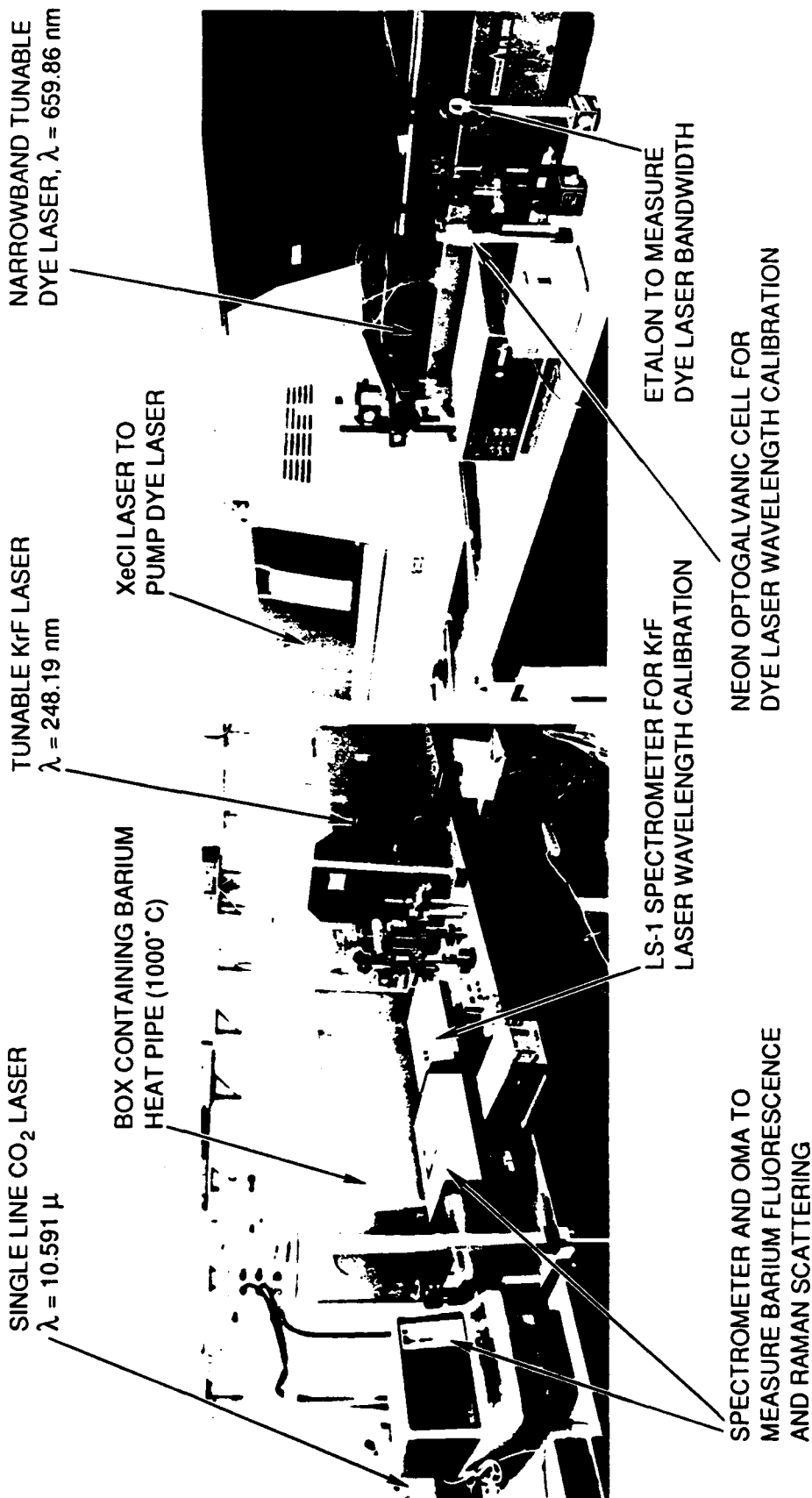
$$dI_{F.H.}/dz = (6 \times 10^{-42}) (N/\Gamma\Delta^2) I_{KrF} I_{CO_2} (I_{F.H.})^2 (\text{cm}^2/\text{watt})^3 (1/\text{cm})$$

## FREQUENCY HALVING: EXPERIMENTAL SET-UP



# TTC

## FREQUENCY HALVING: LABORATORY EQUIPMENT



# FREQUENCY HALVING EXPERIMENTAL PARAMETERS

--- TO AVOID OPTICAL DAMAGE TO COATINGS, FINAL EXPERIMENT INCORPORATED COLLIMATED BEAMS CROSSING AT VERY SMALL ANGLES IN BARIUM VAPOR

--- BARIUM VAPOR CONTAINED IN ALUMINA HEAT PIPE (TOP TEMPERATURE ABOUT 1200 CELSIUS) WITH ARGON BUFFER GAS (ABOUT 20 TORR) AND  $\text{BaF}_2$  WINDOWS TO TRANSMIT BOTH KrF (248nm) AND  $\text{CO}_2$  (10.6 $\mu$ ) LASER RADIATION

---  $\text{CO}_2$  LASER AND VISIBLE DYE LASER POLARIZED VERTICALLY AND INCIDENT FROM ONE END, KrF LASER POLARIZED HORIZONTALLY AND INCIDENT FROM THE OTHER END

--- LASER PARAMETERS FOR CENTRAL OVERLAPPING 50 cm IN BARIUM VAPOR (+/- 20%)

$\text{CO}_2$ : 1000 mjoule on 0.5  $\text{cm}^2$  in about 1  $\mu\text{s}$  with a peak intensity in first 100 ns of 3.3  $\text{MW}/\text{cm}^2$ . Single line bandwidth of 0.07  $\text{cm}^{-1}$

KrF: 55 mjoule on 0.2  $\text{cm}^2$  in 16.2 ns, with 75% narrowband in correct polarization for 12.7  $\text{MW}/\text{cm}^2$ . Bandwidth 0.05  $\text{cm}^{-1}$ , tunable in mode hopping increments of about 0.2  $\text{cm}^{-1}$

Visible: 0.52 mjoule on 0.005  $\text{cm}^2$  in 8.7 ns for 11.5  $\text{MW}/\text{cm}^2$ . Bandwidth 0.1  $\text{cm}^{-1}$ , tunable in 0.05  $\text{cm}^{-1}$  increments

# EXPERIMENTAL PROCEDURE

--- BEAM OVERLAP ASSURED BY CHECKING BEAM POSITIONS AT BOTH ENDS OF BARIUM CELL

--- KrF LASER TUNED TO GIVE MAXIMUM CO<sub>2</sub> STIMULATED RAMAN SCATTERING TO LEVEL AT 39335 cm<sup>-1</sup> DETERMINED BY MAXIMIZING SUBSEQUENT 470 nm AMPLIFIED SPONTANEOUS EMISSION TO LEVEL AT 18060 cm<sup>-1</sup>.

--- RELATIVE TIMING OF LASER PULSES SET TO MAXIMIZE A.S.E.

--- TIMING OF VISIBLE LASER SET SO THAT BEGINNING OF VISIBLE LASER PULSE ENTERS CELL WHEN BEGINNING OF KrF LASER PULES EXITS CELL (RELATIVE JITTER ABOUT 1 ns)

--- KrF LASER DETUNED SOME AMOUNT FROM PEAK OF S.R.S. TRANSITION

--- VISIBLE LASER SCANNED IN WAVELENGTH WHILE  $I_{OUT}/I_{IN}$  IS MONITORED ON BOXCAR INTEGRATOR AND PLOTTED AS A FUNCTION OF TIME

# EXPECTED FREQUENCY HALVING GAIN

--- FOR TEMPERATURE OF 1150 CELSIUS, BARIUM  
VAPOR PARTIAL PRESSURE IS ABOUT 28 TORR,  
CORRESPONDING TO  $N=2 \times 10^{17}/\text{cm}^3$

---  $I_{\text{KrF}} = 12.7 \text{ MW}/\text{cm}^2$ ,  $I_{\text{CO}_2} = 3.3 \text{ MW}/\text{cm}^2$ ,  
VISIBLE SEED LASER  $I_{\text{F.H.}} = 11.5 \text{ MW}/\text{cm}^2$

--- WIDTH OF KrF - CO<sub>2</sub> STIMULATED RAMAN  
TRANSITION WAS MEASURED TO BE ABOUT  $1.5 \text{ cm}^{-1}$   
(AT THIS TEMPERATURE WITH THESE LASER  
INTENSITIES). A DETUNING OF  $1 \text{ cm}^{-1}$  LEADS TO A  
QUADRATURE  $\Delta$  OF  $1.8 \text{ cm}^{-1}$ . LASER LINEWIDTH  $\Gamma=0.1$   
 $\text{cm}^{-1}$ .

--- GAIN EQUATION FOR VISIBLE SEED

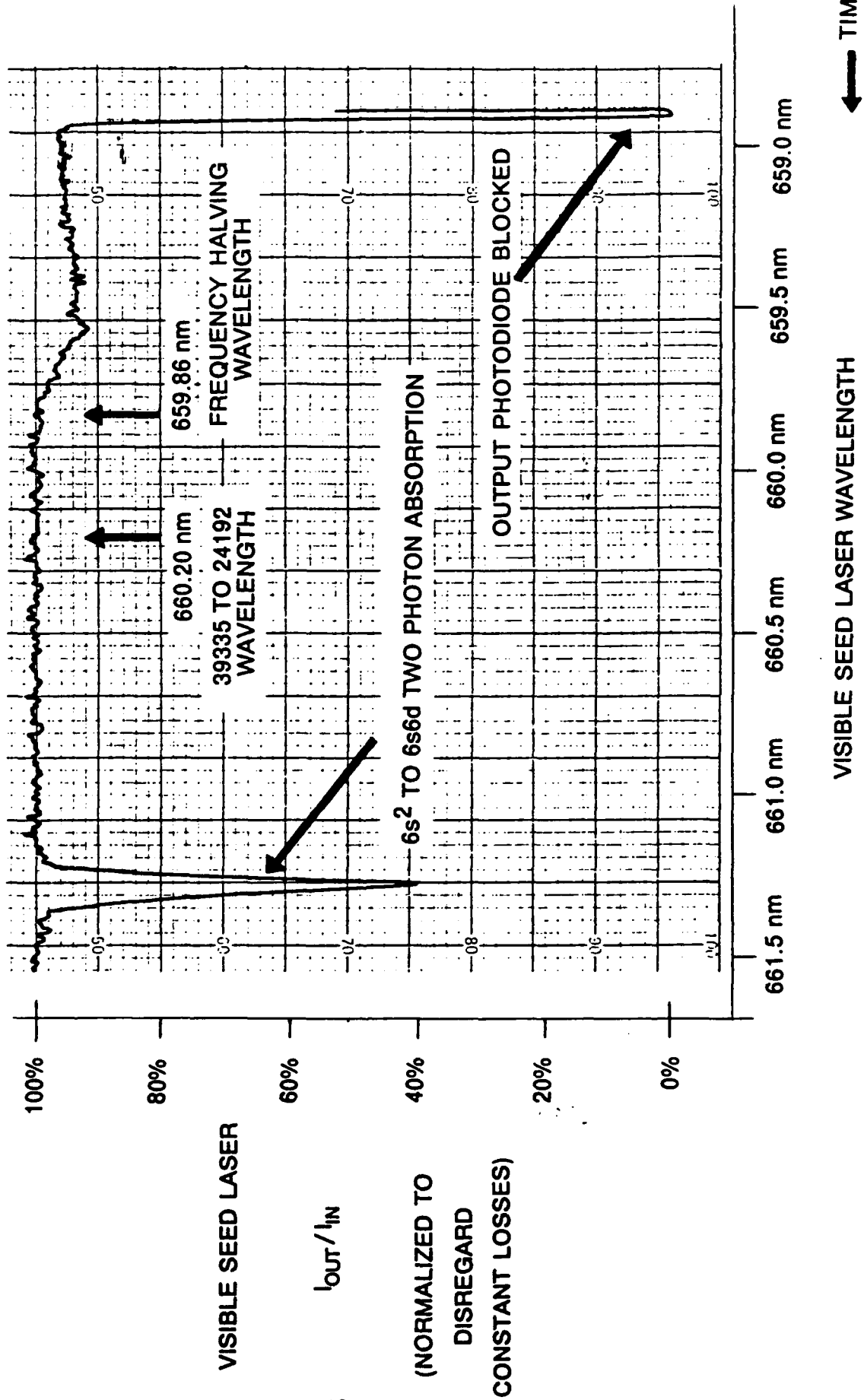
$$dI_{F.H.}/dz = (6 \times 10^{-42}) (N/\Gamma \Delta^2) I_{KrF} I_{CO_2} (I_{F.H.})^2 \text{ (cm}^2/\text{watt)}^3 (1/\text{cm})$$

LINEAR GAIN  $(dI_{F.H.}/dz)/I_{F.H.} = .18\%/cm$  GIVING  
MEASURABLE GAIN OF 9% FOR 50 cm INTERACTION  
LENGTH.

--- EQUATION  $dI/dz = aI^2$  HAS SOLUTION  
 $I(z) = (1/I(z=0) - az)^{-1}$  LEADING TO COMPLETE  
CONVERSION AT  $z = 560$  cm (IGNORING DEPLETION  
OF KrF PUMP BEAM)

--- NO EXPERIMENTS (2% SIGNAL TO NOISE) SHOWED  
GAIN

# TYPICAL FREQUENCY HALVING GAIN MEASUREMENT SPECTRUM



(7.5 PULSES/SEC, 0.6 STEPS/SEC, 30 SAMPLE AVERAGING, 0.2 INCH/MIN CHART SPEED)

# DISCUSSION OF EXPERIMENT

--- BARIUM CHOSEN AS FREQUENCY HALVING CANDIDATE ATOM BECAUSE OF NEAR INTERMEDIATE RESONANCES AND ADEQUATE VAPOR PRESSURE AT ACCESSIBLE TEMPERATURES

--- FAILURE TO MEASURE GAIN ON VISIBLE SEED LASER PROBABLY DUE TO TWO FACTORS: LARGER THAN EXPECTED TRANSITION LINEWIDTHS AND LOWER THAN EXPECTED DIPOLE TRANSITION PROBABILITIES

--- MEASURED STIMULATED RAMAN SCATTERING LINEWIDTH OF  $1.5 \text{ cm}^{-1}$  WAS A FACTOR OF THREE LARGER THAN EXPECTED. LARGE WIDTH OF RYDBERG TRANSITION MAY BE DUE TO STARK EFFECT FROM LARGE DENSITY OF IONS AND ELECTRONS CREATED FROM AUTOIONIZATION OF BARIUM ATOMS ABSORBING TWO KrF PHOTONS (AS EVIDENCED BY A.S.E. AT 650nm FROM  $\text{Ba}^+$ )

--- FREQUENCY HALVING LINEWIDTH  $\Gamma$  CALCULATED AS LASER LINEWIDTH OF  $0.1 \text{ cm}^{-1}$  MAY BE LARGER DUE TO ATOMIC EFFECTS

--- WHERE POSSIBLE, TRANSITION DIPOLE MATRIX ELEMENTS WERE CALCULATED FROM MEASURED EINSTEIN A COEFFICIENTS. FOR RYDBERG TRANSITIONS, CALCULATIONS WERE BASED ON THE COULOMB APPROXIMATION.

--- SUBSEQUENT EXPERIMENTAL MEASUREMENTS INDICATE THAT ONE CRITICAL TRANSITION MOMENT FROM THE LEVEL AT  $24192 \text{ cm}^{-1}$  TO THE LEVEL AT  $39335 \text{ cm}^{-1}$  MAY BE SUBSTANTIALLY LOWER THAN CALCULATED. IT WAS NOT SEEN IN AN ABSORPTION EXPERIMENT THAT DID MEASURE TRANSITIONS TO OTHER NEARBY RYDBERG LEVELS. THE CALCULATED TRANSITION MOMENT WAS BASED IN PART ON A PUBLISHED M.Q.D.T. CALCULATION SHOWING MIXING BETWEEN THE  $6s9d \ ^1D_2$  AND THE  $5d8s \ ^3D_2$  LEVELS.